The Pennsylvania State University

The Graduate School

The Graduate Program in Acoustics

INFRASONIC PISTONPHONE CALIBRATION

A Dissertation in

Acoustics

by

Timothy Merrill Marston

Submitted in Partial Fulfillment
of the Requirements
for the Degree of

Doctor of Philosophy

May 2009

The thesis of Timothy Merrill Marston was reviewed and approved* by the following:

Thomas B. Gabrielson
Professor of Acoustics
Senior Scientist
Dissertation Advisor
Chair of Committee

Steven L. Garrett
United Technologies Professor of Acoustics

Victor W. Sparrow
Professor of Acoustics

Martin W. Trethewey
Professor of Mechanical Engineering

Anthony A. Atchley
Professor of Acoustics
Head of the Graduate Program in Acoustics

*Signatures are on file in the Graduate School

ABSTRACT

Few options exist for calibration of transducers at infrasonic frequencies. A variable frequency infrasonic pistonphone is one option for calibration; however, thermo-viscous effects can decrease the accuracy of calibrations made using an infrasonic pistonphone. An infrasonic pistonphone is developed that produces calibration signals between 0.001 and 30 Hz. To decrease calibration uncertainty due to thermo-viscous effects, the pressure inside the constructed pistonphone chamber is calculated using Rott's continuity and momentum equations, readily accepted equations that model thermo-viscous effects in enclosures. The pressure response of the pistonphone chamber is measured, and compared with the pressure predicted by a model incorporating Rott's equations. Example calibrations and thermo-viscous effect corrections are conducted. Results show an increase in calibration accuracy, and demonstrate the potential usefulness of the pistonphone design for the calibration of acoustic transducers at infrasonic frequencies.

TABLE OF CONTENTS

LIST OF FIGURES

LIST OF TABLES

ACKNOWLEDGEMENTS

The author of this thesis would like to gratefully acknowledge the following individuals for the help and support they have contributed over the past five years: Dr. Keolian for the hours spent in the lab teaching circuit reliable circuit design, capacitor lore, and letting the author into the lab on the numerous occasions the he locked himself out. John Brady and Doug Wilcox for the conversation, book lending, and technical insights for various hardware problems. Matt Poese for a significant amount of expertise on various aspects of machining, hardware design, continual encouragement to finish strong, and interesting background music. Karen Brooks and Carolyn Smith for their patience with the author's many forgetful tendencies, as well as making the department run smoothly. Dr. Richard Stern, for allowing the author to begin his PhD research while in Japan, and also providing the author's funding through the ARL Educational and Foundational fund. The head of the Acoustics Department, Dr. Anthony Atchley, for aiding all Penn State acoustics students over the past 12 years, and bringing in funding.

The thesis committee is gratefully acknowledged for the ways in which they have individually contributed to the author's deeper understanding of acoustics: Dr. Garrett for the colorful and highly effective methods of teaching acoustics and vibration both in and out of class, and for taking personal interest in his students. Dr. Sparrow, for requesting the completion extremely interesting field measurements and measurement apparati. Dr. Trethewey for a deeper understanding of the word "spectrum." Most of all, the extremely patient, knowledgeable and good natured chair of the committee Dr. Gabrielson, who has instructed the author closely over the last 5 years, and has contributed more to the author's understanding of acoustics, signal analysis, and field measurement techniques than any other person.

The author wishes to acknowledge his father and mother, who have spent much time personally encouraging him, providing love and support, and being examples of integrity and practical wisdom. Finally and most of all, the author wishes to acknowledge his Lord and Savior Jesus Christ, whose glory is reflected in the intricate, amazing and awe inspiring workings of the universe.

Chapter 1

Introduction

1.1 Background, definition of terms and overview

Calibration of acoustic transducers at infrasonic frequencies is challenging. Condenser microphones, for example, are designed with pressure equalization leaks to reject very slow barometric pressure changes. These pressure leaks, however, significantly affect the response of a transducer at low frequencies. Calibration methods that do not expose both the active portion of the transducer and the pressure equalization vent to the calibration pressure signal do not provide an accurate representation of the free-field response at very low frequency. This problem can be avoided by totally immersing the transducer in the pressure field, subjecting both the diaphragm and equalization vent to the calibration signal [**17**]. The idea of building a pistonphone for total immersion is not new. A single frequency 13.8 Hz adiabatic infrasonic pistonphone [**26**], a "laser pistonphone" [**12**], a variable frequency pistonphone [**4**], and an electromechanical infrasonic calibration chamber [**2**] have been developed, with the results presented at meetings, but few articles concerning infrasonic calibration have actually been published in peer-reviewed journals. There are several difficulties with the pistonphone design that have prompted some to doubt the usefulness of the design [**1**]. Both the volume of the pistonphone and the movement of the piston need to be precisely measured and leaks in the chamber must be negligibly small or measured and compensated. In addition, pressure oscillations in the pistonphone chamber may not be simply adiabatic [**4**]. Depending on the frequency of operation and the pistonphone chamber geometry the pressure oscillations may be adiabatic, isothermal, or somewhere

in between, and the variance in amplitude can be as large as the ratio of specific heats - approximately 3 dB in air.

Difficulties not specific to the pistonphone design exist for infrasonic calibration as well. As is demonstrated in this thesis, high levels of infrasonic noise exist in the atmosphere. A calibrator must compensate either by attenuating this noise or increasing the amplitude of the calibration signal. An infrasonic calibration may require a large amount of time because the periods of oscillation of the calibration signals are long. This increases the possibility of calibration error from changes in conditions that are normally assumed constant, such as temperature and ambient pressure. If, for example, the temperature of the pistonphone chamber fluctuates, the static pressure follows the change in temperature and this fluctuation appears as noise. Furthermore, changes in ambient pressure result in changes in the calibration signal amplitude for fixed piston displacement amplitude. Finally, the calibrator must be designed to accommodate many different types of transducers used to measure infrasonic signals.

This thesis describes the theoretical modeling, mechanical construction, and operation of a total-immersion pistonphone designed for both "relative" and "absolute" calibrations over a frequency range of 0.001 Hz (roughly 15 minutes per cycle) to 30 Hz. The terms "relative" and "absolute" are significant. In a relative calibration two transducers are used, one of which has a known sensitivity. The sensitivity of the second transducer is calculated by subjecting both transducers to the same signal, and comparing the magnitude and the phase response of the second with the reference. The quality of the comparison calibration depends directly on the accuracy of the reference transducer. Any calibration error in the reference will carry over into the calibration of the other transducer. Furthermore, the reference transducer must be calibrated.

If a calibration is "absolute," it means that only one transducer is used in the calibration process: the transducer being calibrated. The sensitivity is not calculated by comparison with a reference, but rather by calculating the magnitude and phase of the calibration signal from (in this case) the ideal gas law and knowledge of thermo-viscous effects. Making an accurate absolute calibration with a pistonphone is of chief importance in this thesis. Making an absolute calibration of an acoustic transducer is not

difficult in many circumstances. A Bruel & Kjaer type 4228 pistonphone operates by varying the volume of a small chamber a known amount, at approximately 250 Hz. At this frequency, for the volume of the pistonphone, the pressure can be calculated directly by measurement of the change in volume and with the assumption that the pressure oscillations are adiabatic. In the case of the infrasonic pistonphone, however, the adiabatic assumption can not be made and equations for the thermal and viscous effects on acoustics in tubes are needed to maintain accurate calibrations. Fortunately, many papers have been published concerning thermal and viscous effects, and models describing their effects are well established and utilized especially in the field of "Thermoacoustics" [**18**] [**20**] [**21**]. Thermo-viscous models can be used to predict the calibration signal amplitude and phase in the pistonphone chamber through the transition from adiabatic to isothermal pressure oscillation [**16**]. This pistonphone is designed to measure the phase response as well as the magnitude response of transducers because it has been previously demonstrated that the phase response of transducers near the low-frequency cutoff may have significant effect on the captured waveform of signals having a significant amount of energy in the infrasonic spectrum [**8**].

The calculation of chamber pressures is based on a Tee-section electrical analogy [**6**], [**19**] with elements defined to satisfy a finite-difference approximation to Rott's wave equation [**21**]. Rott's thermo-viscous *f*-function for cylindrical ducts is used to account for the thermal and viscous effects of the chamber walls on the internal acoustic field. This predicted pressure can then be used as the reference pressure for transducer calibration.

1.2 Thesis statement, goal, and scope

Despite the difficulties associated with the construction of an infrasonic pistonphone calibrator, good infrasonic calibrations of many types of acoustic transducers can be made using the pistonphone design scheme. The goal of this thesis research is to make a total-immersion pistonphone calibrator capable of calibrating acoustic transducers at infrasonic frequencies without the use of a reference transducer, and to demonstrate

such a design through actual calibrations. An integral part of this goal is to improve the accuracy of infrasonic pistonphone calibration by accounting for thermo-viscous effects. Linked with this goal, therefore, is the design and application of an algorithm that can calculate the internal pressure of the pistonphone chamber in the presence of thermo-viscous effects.

A wide variety of modeling and measurement techniques have been used throughout this thesis research. To limit the size of the main body of the thesis the scope of the main body has been reduced to descriptions of the mechanical construction of the pistonphone, the theory behind the model used to predict the characteristics of the calibration signal, results of model/measurement comparisons, steps that were taken to eliminate model errors, and actual calibration examples. The scope of the appendices is considerably broader, covering in more detail some of the previously mentioned topics but also applications for the thermo-viscous model that include propagating infrasonic signals through more complicated duct networks, data-processing algorithm details, and techniques for modeling the thermal properties of duct walls.

1.3 Chapter summaries

The thesis begins in Chapter 2 with a complete mechanical description of the presently used design. This chapter gives the reader an understanding of the term "infrasonic pistonphone" as it is used in this thesis, and shows the reader what exactly is being modeled in the thermo-viscous theory section. Chapter 3 establishes the theory and techniques used to model the pressure response of the pistonphone chamber. Chapter 4 compares the pressure predicted by the theory developed in Chapter 3 to measurements of the pressure inside the pistonphone chamber. The measurement process is outlined and a significant portion of the chapter is focused on isolating model and measurement discrepancies. Chapter 5 describes the calibration process, using a calibration case study with a *Brüel & Kjaer* 4193 half-inch measurement microphone. Additional calibrations follow the example, showing the different types of measurements that can be made with the pistonphone. Chapter 6 is a summary of the findings from the research. Readers are

encouraged to begin by reading Chapter 6 for an overview of the research then locate the appropriate sections of interest in the table of contents.

As a final introductory note, this thesis contains a lengthy appendix with additional calibration examples, Matlab code explanations, and in particular, a detailed explanation of Tee-section theory. The Tee-section theory used for modeling the pressure inside the pistonphone is simple and very powerful. Appendix **C** contains a more lengthy discussion of some of the calculations that can be done with the technique, and provides many examples of interest.

Chapter 2

Pistonphone design

2.1 Design evolution

This chapter is a description of the mechanical and electrical components of the pistonphone. Several pistonphone designs preceded the currently used design. Through several models, the generated SPL was optimized and different displacement sensors were implemented to measure the location of the piston. An LVDT was the final choice for piston displacement measurement. The chamber of the pistonphone was shaped to match the theoretical model in a more ideal manner, and have less flow losses, and the transducer immersion system was refined. The development process is covered in detail in Appendix **F**.

2.2 Pistonphone design description

2.2.1 Chamber measurements and description

Figure **2-1** is a cross section of the pistonphone, showing the most significant aspects of its construction. The piston, manufactured by *AirPot* is 23.93 ± 0.025 mm in diameter, made of graphite, and precision ground to slide in a glass tube. The glass tube is joined to a truncated polyvinylchloride (PVC) cone having an opening diameter matching that of the glass tube. The glass tube is held to the PVC cone by means of a separate PVC fixture, and sealed by an O-ring. The PVC cone changes diameter linearly beginning with the inner diameter of the glass tube and ending with the inner diameter of a 4-inch Schedule 80 PVC tube (actual measured inner diameter: 95.75 ± 0.25 mm). The taper of the interior of the cone is approximately 8 degrees. The slow taper minimizes

losses associated with flow separation or diameter discontinuities that would not be accounted for in the theoretical model. The cone is connected and sealed to the 4-inch PVC tube by means of a clamp and o-ring.

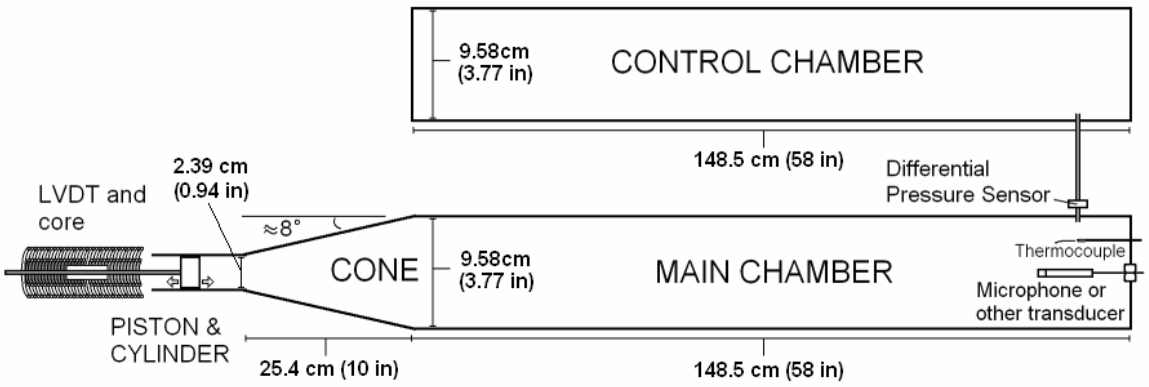

Figure **2-1**: Pistonphone cutaway, top-view, depicting significant aspects of the pistonphone design.

The length of the 4-inch PVC tube is 148.54 ± 0.15 cm. The 4-inch PVC tube (hereafter referred to as the "chamber" of the pistonphone) is surrounded by three PVC rings having the same outer diameter as the clamp ring holding the cone to the main chamber. These rings support the body of the pistonphone and act as spacers to keep the body of the chamber from having significant thermal contact with the laboratory bench. The cone section is supported by a similar spacing ring. The end of the pistonphone chamber opposite the piston is sealed by a PVC plug with a hole in the center. Transducers are inserted into the body of the pistonphone chamber through this hole. The hole is sealed by various adapters designed to accommodate the transducer cable. The back plug has a separate hole for insertion of a thermocouple into the pistonphone chamber.

2.2.2 Control chamber

The purpose of the control chamber pictured in Figure **2-1** is to provide a reference for a differential pressure sensor that measures the pressure inside the

pistonphone chamber. The control chamber also significantly reduces measurement noise. Because it is a similar size to the main chamber, changes in pressure due to ambient temperature fluctuation become common mode "noise" rejected by the differential sensor. The stiffness of the chamber walls also contributes to attenuation of ambient external pressure fluctuations. Figure **2-2** compares the background signal from two sensors mounted in two configurations: (1) venting to the laboratory, and (2) venting to the control chamber.

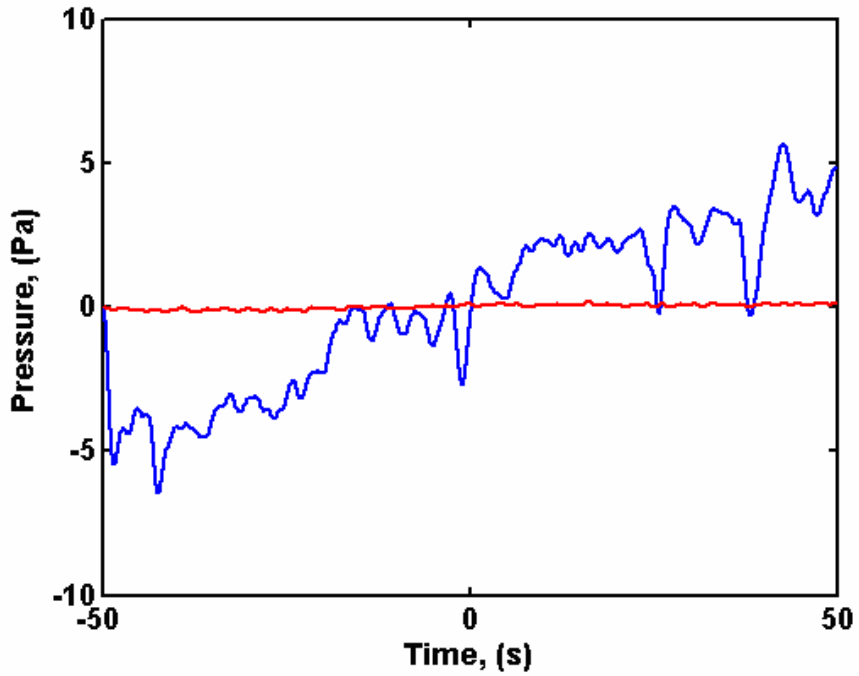

Figure **2-2**: Background pressure fluctuations as measured by the differential sensor vented externally to the lab (the jagged curve that trends upward with time), and vented to the control chamber (the horizontal smooth curve).

2.2.3 Differential pressure sensor

A 0.8 PSI differential piezo-resistive pressure sensor sold by Omega (model # PX74-0.8DV) is the primary sensor used to measure the pressure inside the pistonphone main chamber. The sensor is mounted inside an aluminum casing which screws into the main chamber, and is connected with tubing and compression (Swagelok™) fittings to the control chamber. A cutaway of the transducer is shown in Figure **2-3** :

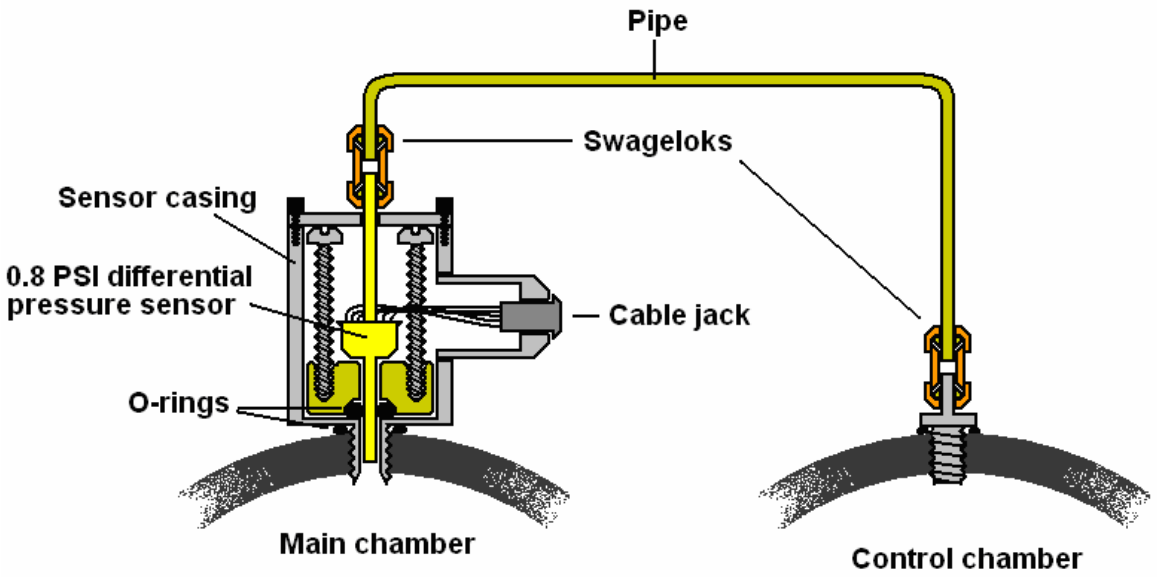

Figure **2-3**: Cutaway illustration of the pressure sensor. The front side of the pressure sensor is exposed to the pressure of the main chamber. The back side of the pressure sensor is exposed to the pressure of the control chamber via a Swageloked tube. A chassis surrounds the pressure sensor to provide strain relief.

The pressure sensor is powered and amplified by a custom-built preamplifier. The circuit schematic is shown in Figure **2-4**. The front end of the preamplifier is an Analog Devices 621AN instrumentation amplifier. This instrumentation amplifier has a fixed gain of either 10 or 100. The signal-to-noise ratio generally increases when the gain is

increased on an instrumentation amplifier, and the preamplifier is set for a gain of 100 during normal operation.

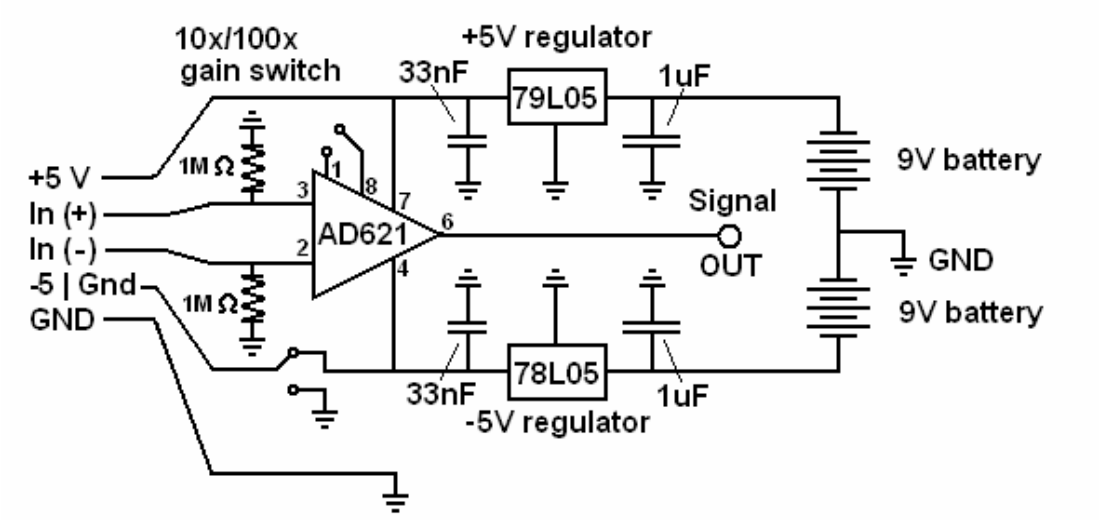

Figure **2-4**: Piezo-resistive preamplifier schematic. The preamplifier is shielded inside an aluminum project box, and the output is connected to a data-acquisition system via a BNC jack.

2.2.4 Piston displacement measurement

Piston displacement is measured with a custom-built linear-variable-differential-transformer (LVDT). The mount used to hold the piston cylinder to the mouth of the cone also houses a set of LVDT coils. Figure **2-5** is a cross-section of the piston/LVDT assembly. The two secondary coils are both 38 mm long, and are located inside a 76 mm primary coil. A 38 mm cylindrical ferrite bead, which acts as the core of the LVDT, is mounted on the shaft of the piston. As the piston moves back and forth, the displacement of the core is decoded from the output of the secondary coils. A Teflon washer with an inner diameter matching the diameter of the piston rod is placed at the end of the LVDT mount to ensure that the motion of the core is parallel to the axis of the LVDT.

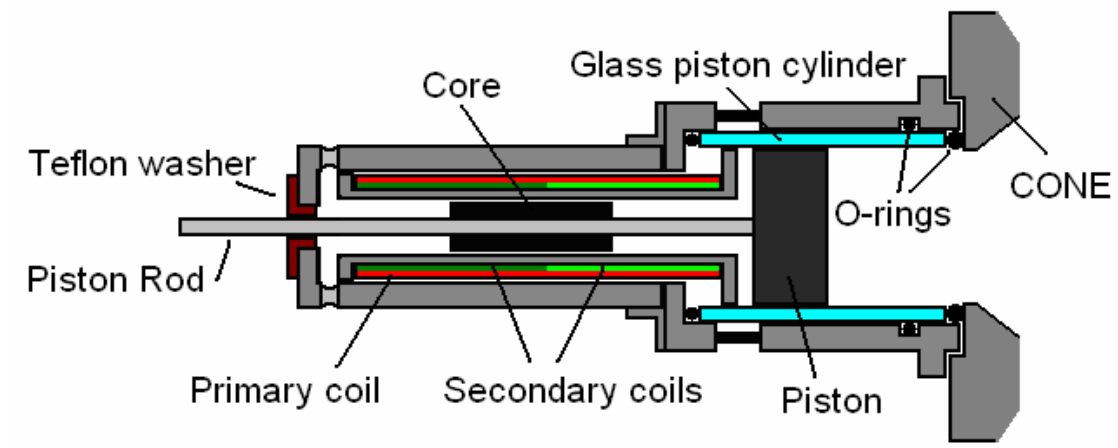

Figure **2-5**: Piston, PVC fixture and LVDT. Mounting screws and other small mechanical components have been omitted to retain figure clarity.

Significant error can be introduced into the displacement measurement if mechanical play exists between the graphite piston head and the core of the LVDT. The LVDT core is glued solidly to the piston rod but mechanical play exists in the ball-and-socket joint connecting the rod to the piston head. Without modification, the motion of the core does not precisely follow the displacement of the piston because of this play. To eliminate the play a stiff spring is compressed between the rod and the head of the piston, as is illustrated in Figure **2-6**.

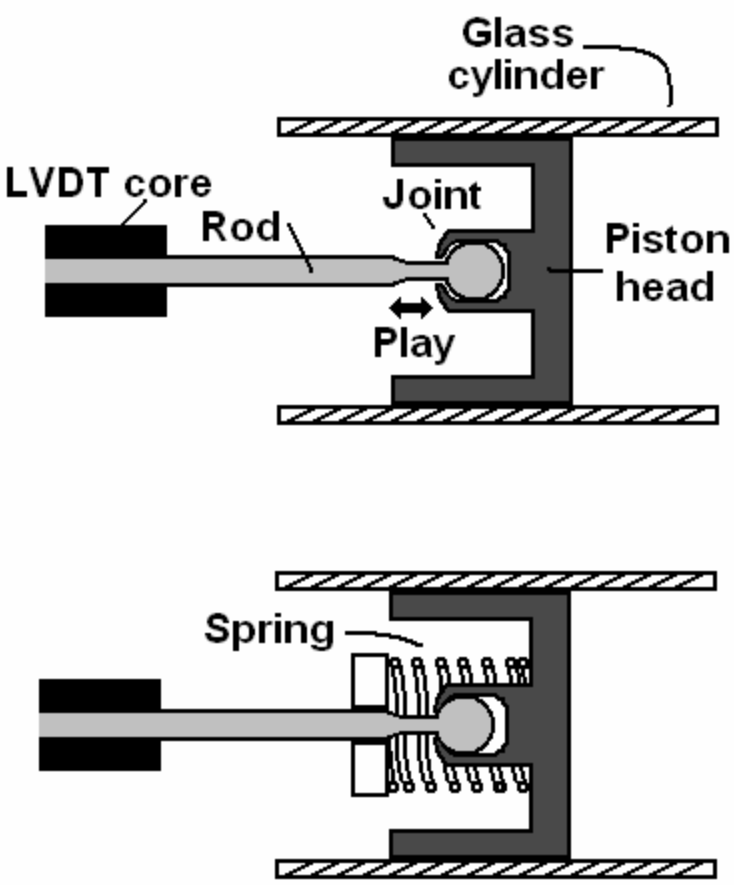

Figure **2-6**: Cutaway view of the piston cylinder with and without a spring. The spring keeps the ball and socket joint under tension. Without the spring, mechanical play between the rod and piston head introduce significant error in piston displacement measurements.

Another source of error in displacement measurements occurs if the coil assembly of the LVDT and the pistonphone chamber are not rigidly coupled. Relative motion between the LVDT coils and the body of the pistonphone appears in the displacement measurement as spurious motion of the piston head. To prevent this type of error the LVDT coil assembly is attached directly to the piston cylinder as shown in Figure **2-5**. This rigid connection ensures that the true motion of the piston head relative to the pistonphone chamber is recorded.

Several methods can be used to decode the output the signal from the LVDT coils. Figure **2-7** is the pattern for the circuit schematic used with the pistonphone's

LVDT. A 15 kHz, 0.45 Vrms signal is applied to the primary coil surrounding the secondary coils. The magnitude of the signal across a secondary coil depends on the core location. The output of the signal is full-wave rectified by precision rectifier circuits shown in the figure below.

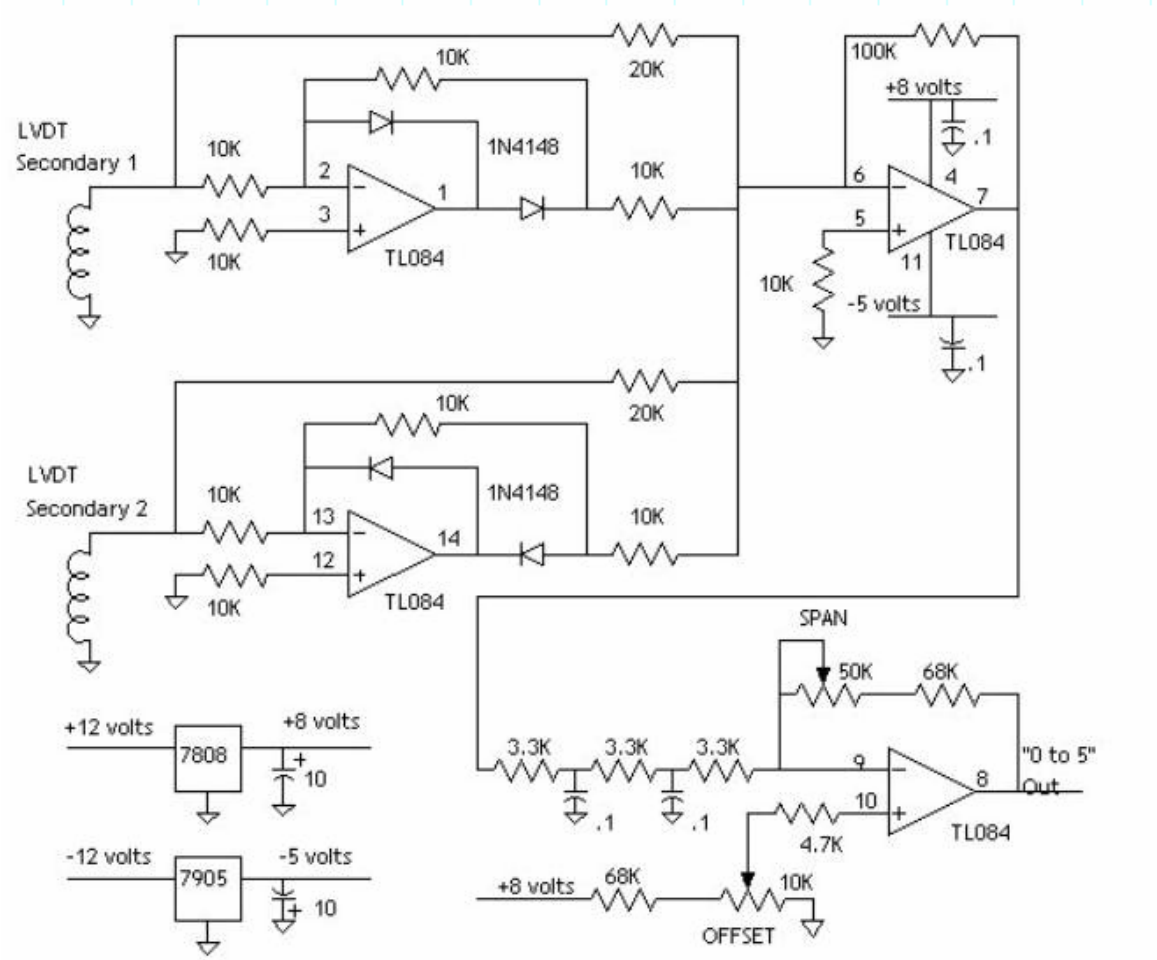

Figure **2-7**: Circuit schematic upon which the LVDT circuit used for the pistonphone is based. Source and copyright are found in the bibliography [**27**]. Minor differences in components, filtering, and powering schemes are used in the actual circuit.

The output of the first coil is positive rectified, and the output of the second coil is negative rectified, so that when the core is at the center of the LVDT the DC terms cancel when the signal is summed. Following the rectification, the signals from the two coils are summed and low-pass filtered to eliminate the remnants of the carrier harmonics resulting from rectification. Within the region of linear operation, the DC offset of the filtered data

represents the location of the core with respect to the null point in the middle. The low-pass filter used in the circuit is a second order Sallen-Key Butterworth low-pass filter [**11**]. The phase response has a small effect on calibration phase response near 30 Hz and to correct this phase error, the response of the filter has been simulated in Matlab and divided out of the calibration. The LVDT itself is calibrated using a micrometer fixture. The calibration process used for the LVDT is given in detail in **4.2**, "Displacement calibration."

The effect of the LVDT on the data-processing is enormous. Figure **2-8** shows a portion of pressure response data that has been enhanced by the use of the LVDT. A major benefit of the LVDT is that it allows good measurements to be taken quickly. Before the LVDT was installed, extremely long measurements had to be made to improve data quality. The recording time can be cut down by a factor of ten in some cases, with a significant improvement in data spread still visible, when the LVDT is used. The techniques for implementation of the LVDT displacement data into the signal processing algorithm are discussed in Chapter **4**.

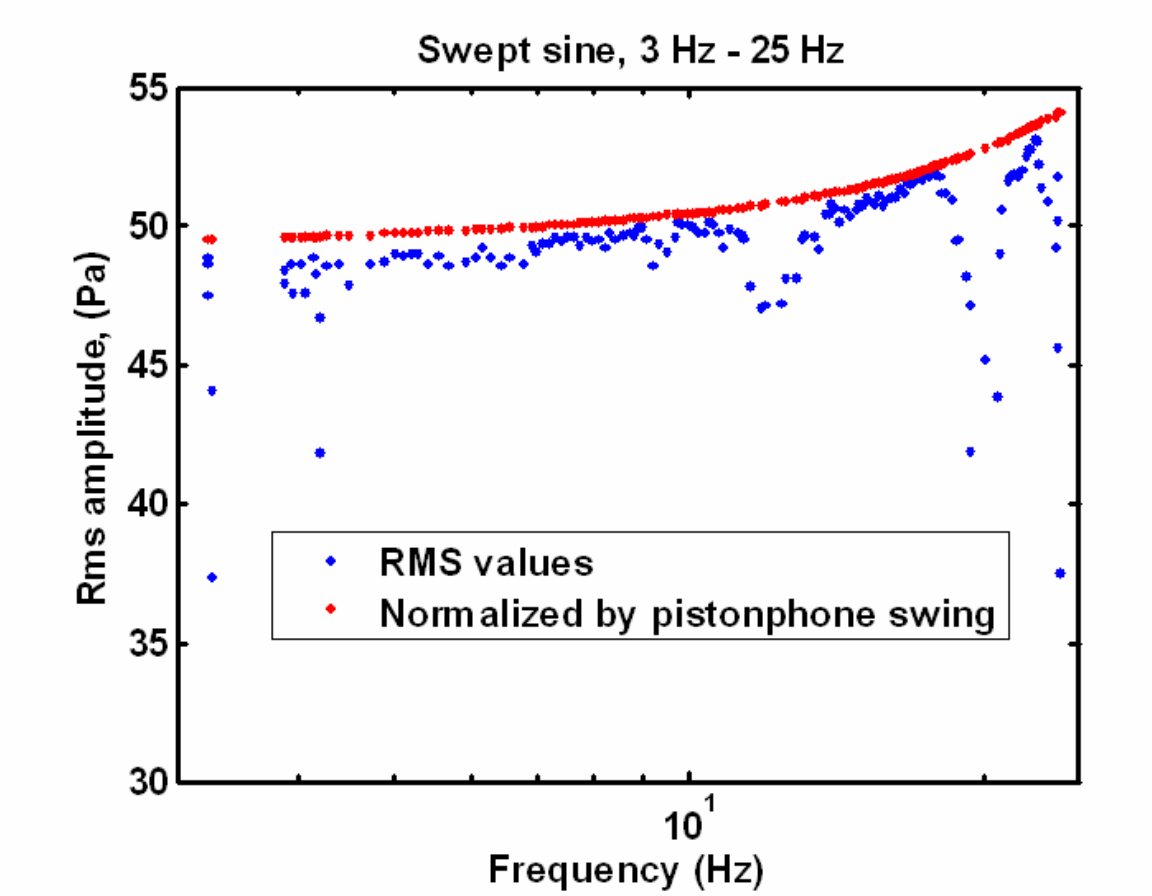

Figure **2-8**: The smooth, upper set of points in the graph is the data set enhanced by the LVDT measurements. Using displacement information from the LVDT output significantly improves the data spread of response measurements made with the pistonphone.

2.2.5 Pressure estimation

The measured volume of the pistonphone chamber is 11,520 ± 75 cm^3. The majority of the uncertainty with regard to predicting the internal pressure amplitude results from the variation in the radius of the 4-inch PVC tube. A more accurate value for total volume could be obtained by filling the chamber with water then draining and measuring the volume of liquid. When the acoustic wavelength is much larger than the

largest chamber dimension, the root-mean-square (rms) pressure amplitude in the chamber is ?*P*(? V_{rms}/V) where ? is the ratio of specific heats (1.402 for air) for adiabatic oscillation, and unity for isothermal oscillation. P is the measured local atmospheric pressure, V is the total chamber volume, and ? V_{rms} is the rms volume change produced by the piston. At sea-level, with the given piston dimensions and displacement this equates to approximately 50 Pa_{rms} for adiabatic pressure oscillation and approximately 36 Pa_{rms} for isothermal pressure oscillation. Most of the calibration frequency range occurs between the adiabatic and isothermal regions, and the actual calibration pressure is somewhere between 36 and 50 Pa_{rms}. Toward the upper end of the frequency range, as the first resonance is approached, the pressure amplitude is not uniform lengthwise in the chamber, and will exceed 50 Pa_{rms} near the end-cap.

2.2.6 Motor and gearing

The pistonphone is driven by a DC motor that has sufficient torque to operate from approximately 40 to 1800 RPM under the load imposed by the gear assembly. To increase the frequency range of the pistonphone, several gearing configurations are used. Figure **2-9** shows the major components of the gearing system. The motor may be directly connected to the shaft of the wheel cranking the piston; in this configuration a 1 to 30 Hz range of operation is achieved. To shift the frequency range to 0.1 Hz to 3 Hz, a 10:1 reducer using cogs and a timing belt is attached to the motor. For lower frequencies ranging from 0.001 Hz to 0.7 Hz, a worm-gear/cog assembly attached to the wheel shaft is engaged. This worm gear has a reduction ratio of 40:1, which can be further reduced by attaching it to the 10:1 reducer. The decreased load on the motor under the fully geared (400:1 reduction) configuration lowers the motor's minimum rotation-per-minute rating, and pushes the lowest frequency of operation to 0.001 Hz. Each range has a significant amount of overlap with the adjacent gearing configuration. Vibration isolation is achieved by using torsionally stiff but flexurally limp wires and tubes to join the shafts of the motor and various gear assemblies to each other. Gear jitter is reduced by using a clamp to apply a constant resistive load to the worm-gear cog fixed to the axle.

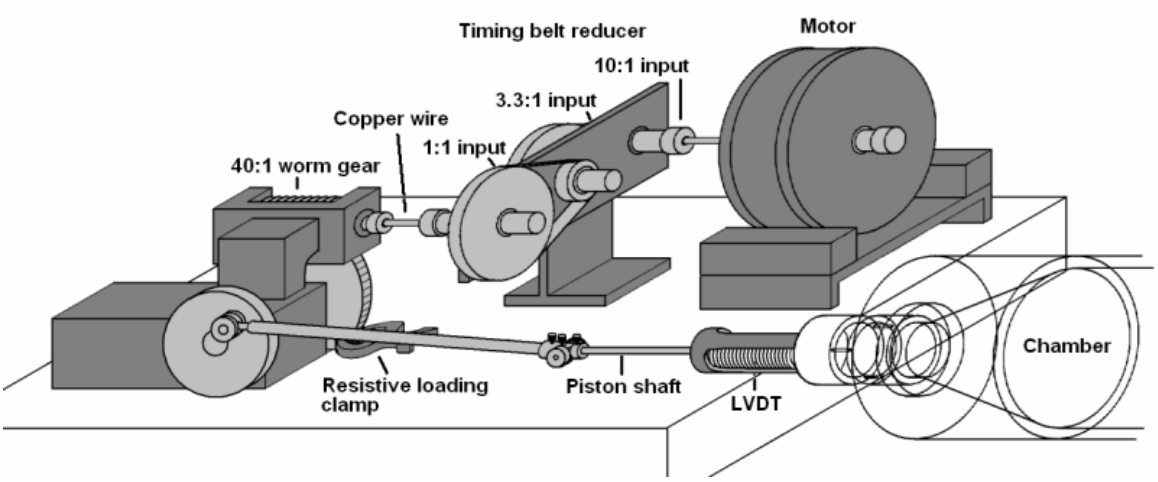

Figure **2-9**: Major components of the gearing and motor assembly, showing some of the connections that can be made. When the worm gear is engaged, the axis of the motor shaft and reducer shafts are parallel with the axis of the worm gear

As is typical for a crankshaft-driven piston, the piston motion is not perfectly sinusoidal. The amplitude of the second harmonic is generally about a factor of 100 below the fundamental. The error introduced by harmonic distortion is minimized by subsequent data processing (to be discussed in Chapter **4)**.

2.3 Chapter 2 summary

The following is a list of the major mechanical characteristics of the pistonphone design.

- Schedule 80 PVC chamber
    - Inner diameter = 95.75 ± 0.25 mm, volume = 11,520 ± 75 cm^3.
    - Diameter tapers set to eight degrees, to prevent flow separation.
- AirPot™ piston head and cylinder
    - The graphite and glass construction provide low friction, while maintaining a tight seal with low leakage.

  - Play in the ball-and-socket joint between the shaft and head is reduced by using a spring.
  - Approximate SPL generated by the piston is 127 ± 1.5 dB.
- Control chamber and differential pressure sensor
  - Cuts down on ambient noise.
  - Noise from thermal fluctuations becomes common mode.
- Linear-variable-differential-transformer (LVDT) displacement measurement
  - Measures piston head displacement, relative to chamber location.
  - Output is decoded using a precision rectifier circuit.
- Motor and gearing
  - Timing belts and a worm-gear provide gear reduction.
  - 0.001 to 30 Hz range using four different gearing configurations.

Chapter 3

Model for the internal acoustic field

3.1 Overview

Thermo-viscous effects can play an important role in acoustic propagation through ducts [**6**]. These effects are the dominant source of loss in many duct systems and how much loss they cause is determined by the diameter of the tube in comparison to the "thermal" and "viscous" penetration depths. Another less obvious thermo-viscous effect is the alteration of the lumped element acoustic compliances and inertias that describe a duct. If unaccounted for, these effects can cause major deviations from simplistic pressure field predictions based only on adiabatic changes in volume. This chapter describes the application of a well established thermo-viscous theory to the prediction of the pressure generated inside a pistonphone. After a breakdown of the theory, assumptions concerning pistonphone wall thickness and chamber end-cap effects are examined.

3.2 Rott's equation and the multi-element "Tee-section" model

An electrical equivalent-circuit analogy for the pistonphone chamber is used to predict the amplitude and phase of the calibration signal as a function of piston displacement. A finite-difference approximation for the thermo-viscous Rott equations[1] leads naturally to an equivalent-circuit representation in the form of a "Tee." The horizontal branch of the Tee contains electrical elements that represent acoustic inertial and viscous effects in a segment of duct, and the vertical branch of the Tee contains elements that represent acoustic compliance and thermal-conduction effects in a segment

[1] Derivation, discussion, and applications of Rott's equations can be found in references [**18**] and [**21**].

of duct. Even the lossless version of this model can be used to improve estimates of, for example, resonance frequencies in Helmholtz resonators, or the pressure response in tubes to plane-wave excitation. When a multi-segment, lossless Tee-section model is used for one-dimensional propagation in a pipe, the resonance frequencies can be calculated accurately, but predicting the quality factor of the resonances requires the addition of viscous and thermal wall losses.[2] This is the strength of the thermo-viscous Tee-section model based upon Rott's equations. Other approaches based on Rott's equations are used extensively in the thermo-acoustics community, and some precise measurements have been undertaken to verify the accuracy of the model [**23**]. For the infrasonic calibrator, the particular utility of the model based on Rott's equations is the ability to model the continuous transition from adiabatic oscillation to isothermal oscillation. Another point of view is that this approach works whether the acoustic boundary layer is small or large compared to the tube radius. These equations incorporate a function (called the "*f*-function") that modifies the acoustic compliance and inertance, and adds thermal and viscous wall losses of a segment of pipe as a function of the viscous and thermal penetration depths. Rott's equations and the *f*-functions are developed in detail in [**21**]. In Chapter 4 of the same reference, derivations for the impedances used in the Tee-section model can be found, as well as *f*-functions for various duct geometries – in this case the circular cross-section duct is used.

The relevant Rott's equations for the Tee-section model are the differential forms of the momentum and continuity equations:

$$dp = \frac{i\omega\rho_0 dx}{A(1-f_m)}U \qquad \textbf{3.1}$$

$$dU = -\frac{i\omega A dx}{\gamma P_0}\left[1+\frac{(\gamma-1)}{(1+\varepsilon_s)}f_k\right]p \qquad \textbf{3.2}$$

[2] When high volume-velocities are involved, other non-linear losses may be present. See references [**19**] and [**14**] for discussions.

where p is acoustic pressure, U is acoustic volume velocity, r_0 is the mean gas density, A is the cross-sectional area of the tube, g is the ratio of specific heats, P_0 is the local atmospheric pressure, e_s is a factor to account for finite heat capacity in the tube wall, and f_m and f_k are the viscous and thermal f-functions. Figure **3-1** is an illustration of the Tee-section analogy, followed by definitions of the circuit component values that are derived from Eq. **3.1** and Eq. **3.2**.

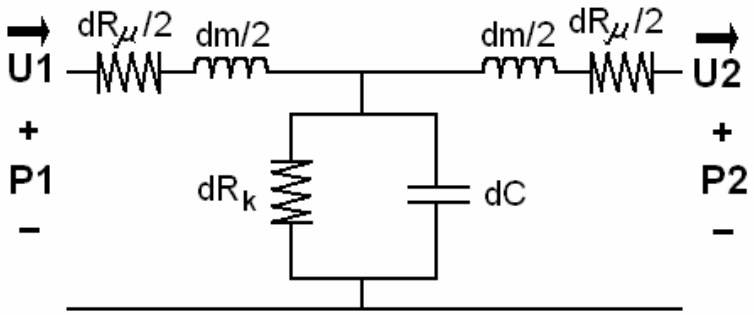

Figure **3-1**: The Tee-section used to model a segment, *dx*, of the pistonphone chamber, showing individual components.

The Tee-section model is symmetric: the acoustic inertance *dm* and viscous resistance dR_μ are split into equal parts in the right and left sides of the horizontal branch. The elements *dC* and dR_k represent the acoustic compliance and the thermal loss, respectively.

$$dm = \frac{r_0 dx}{A}\frac{1-\mathrm{Re}[f_m]}{\left|1-f_m\right|^2} \qquad \textbf{3.3}$$

$$dC = \frac{A dx}{g P_0}\left[1+\frac{(g-1)}{(1+e_s)}\mathrm{Re}[f_k]\right] \qquad \textbf{3.4}$$

$$dR_m = \frac{w r_0 dx}{A}\frac{\mathrm{Im}[-f_m]}{\left|1-f_m\right|^2} \qquad \textbf{3.5}$$

$$dR_k = \frac{1}{dx}\frac{(1+e_s)g}{(g-1)}\frac{r_0}{wA\,\mathrm{Im}(-f_k)} \qquad \textbf{3.6}$$

Equations **3.3** and **3.4** model the inertance and compliance of a duct segment having length *dx*. Equations **3.5** and **3.6** are real resistances that model viscous and thermal losses in the duct segment. Equations **3.1** – **3.6** can all be found in [**21**]. In this reference, terms are added to the continuity and compliance equations that represent the effects of a thermal gradient in the duct. Including thermal gradients in the analysis is important if the gradients are large (as they are in thermoacoustic engines and refrigerators); however, gradients are negligibly small in the calibrator so these terms are dropped in this instance. Equations **3.4** and **3.6** include an e_s term in the continuity and compliance equations not found in [**21**]. The e_s term modifies the compliance and continuity equation according to the available heat-capacity of the wall. The term assumes infinite wall thickness and is defined in Eq. **3.7**:

$$e_s = \frac{r_{air}C_{air}d_{k(air)}}{r_{wall}C_{wall}d_{k(wall)}} \qquad \textbf{3.7}$$

The numerator of Eq. **3.7** is the product of the density, constant-pressure specific heat capacity and thermal penetration depth of air, and the denominator is the product of the density, specific heat capacity and thermal penetration depth of the duct wall material. Rott's equations including this term can be found in [**20**]. The term was left out in [**21**] because, in that treatment, the assumption that the walls have infinite heat capacity is reasonable. The effect of finite wall thickness on this term is calculated in **4.7.9**. For the calibrator, the assumption of infinite heat capacity in the tube wall would lead to an error of 0.13 dB in the isothermal region of operation. This error is small but is within the resolution of the calibration, and would represent a systematic and removable error.

The form of the *f*-functions in the equations above depends on the geometry of the duct; for cylindrical ducts, the *f*-functions are:

$$f_{m,k} = \frac{2J_1\left[(j-1)a/d_{m,k}\right]}{J_0\left[(j-1)a/d_{m,k}\right](j-1)a/d_{m,k}} \qquad \textbf{3.8}$$

where a is the duct radius and $d_{m,k}$ are the penetration depths, viscous or thermal. The f-function approaches the value of one in the isothermal limit. Practically speaking, this occurs when the thermal penetration depth is much larger than the radius. The f-function approaches zero in the adiabatic limit, which occurs when the penetration depth is much smaller than the radius. The thermal and viscous penetration depths d_k and d_μ are defined as:

$$d_k = \sqrt{\frac{2k}{wrC_p}} \text{ (thermal)} \qquad \textbf{3.9}$$

$$d_m = \sqrt{\frac{2m}{wr}} \text{ (viscous)} \qquad \textbf{3.10}$$

where k, μ, and *?* are the thermal conductivity, dynamic shear viscosity, and density of the gas, and C_p is the specific heat of the gas at constant pressure.

At the low end of the frequency range of the calibrator, a simple lumped-element approximation (a single Tee section, that is,) would suffice; however, at the high end of the frequency range, the chamber is a significant fraction of the acoustic wavelength. To preserve the accuracy of the model as the frequency increases, the chamber is modeled as many individual slices with each slice represented by a Tee-section, as depicted in Figure **3-2**. This is similar to the concept of an electrical “transmission line.” In the theoretical pistonphone model, more than 100 segments are used for each portion of the chamber (piston cylinder, cone, and main chamber). In principle, the number of segments could be assigned as a function of frequency to reduce computation time but the model is sufficiently fast without this added complexity.

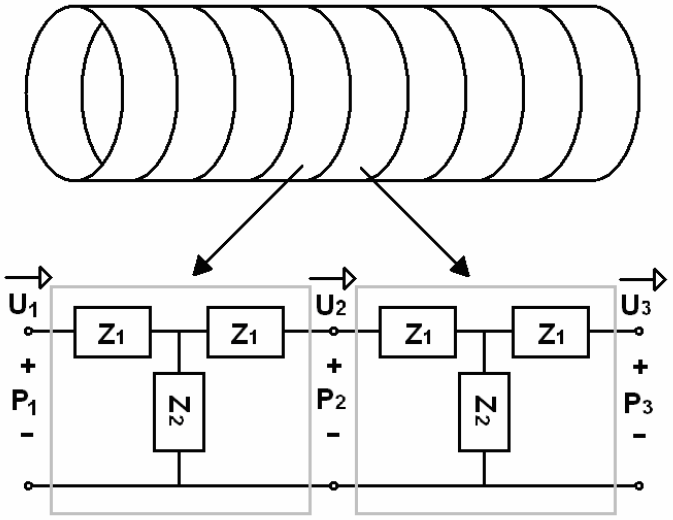

Figure **3-2**: Partitioning of the pistonphone chamber into multiple Tee-sections. Impedances Z_1 and Z_2 are the combinations of the impedances found in the circuit of Figure **3-1**.

3.3 Pressure calculation at the location of the transducer

The multiple-segment Tee-section model allows calculation of the pressure at any point in the calibration chamber; however, for calibration, the pressure at the location of the sensing element of the immersed transducer is the important quantity. Because many segments are used and the spatial variation of the field is slow, this pressure is estimated to be the pressure at the nearest Tee-section junction in the model. The calculation of the pressures and volume velocities at the junctions of the Tee-sections proceeds as follows. The pressure, P_1, and volume velocity, U_1, on one side of any Tee-section element can be written in terms of the pressure, P_2, and volume velocity, U_2, on the other side using a 2x2 transfer matrix:

$$\begin{bmatrix} P_1 \\ U_1 \end{bmatrix} = T \begin{bmatrix} P_2 \\ U_2 \end{bmatrix} \qquad \textbf{3.11}$$

The transfer matrix, T, captures the behavior of the Tee segment:

$$T = \begin{bmatrix} 1 + Z_1 / Z_2 & 2Z_1 + \dfrac{Z_1^2}{Z_2} \\ \dfrac{1}{Z_2} & 1 + \dfrac{Z_1}{Z_2} \end{bmatrix} \qquad \textbf{3.12}$$

To relate the pressures and volume velocities across multiple segments, simply replace the individual-segment transfer matrix with the transfer matrix for the sequence of segments. This aggregate transfer matrix is calculated by multiplying the transfer matrices of the individual segments. Considering Figure **3-2**, P_1 and U_1 could be related to P_3 and U_3 by means of the matrix product of two of the individual-segment transfer matrices. In the constant-diameter section of the calibration chamber, all of the segment transfer matrices are identical; in the cone section, each segment transfer matrix depends on the local radius.

To solve for pressure at the microphone location, the end conditions of the pistonphone are used. The volume velocity at the rigid end of the pistonphone chamber opposite the piston is zero. At any given frequency, the amplitude of the volume velocity of the piston is $jw\dfrac{dV}{2}$, where j indicates that the volume velocity is 90 degrees out of phase with the displacement. The volume change, *dV*, is the peak-to-peak volume excursion as calculated from the piston cylinder dimensions and LVDT stroke displacement measurement. The pressure at the location of the transducer sensing element can be found from the two transfer matrices, T_1 and T_2:

$$T_1 = \begin{bmatrix} a_1 & b_1 \\ c_1 & d_1 \end{bmatrix} \qquad \textbf{3.13}$$

$$T_2 = \begin{bmatrix} a_2 & b_2 \\ c_2 & d_2 \end{bmatrix} \qquad \textbf{3.14}$$

T_1 is the transfer matrix for the portion of the pistonphone chamber between the piston and the sensing element, and T_2 is the transfer matrix for the portion of the pistonphone chamber between the sensing element and the rigid end of the pistonphone. Together they

relate the pressure and volume velocity at the transducer to the conditions at the ends of the pistonphone. The two transfer matrices impose the following relationships:

$$\begin{bmatrix} P_{pist} \\ U_{pist} \end{bmatrix} = T_1 \begin{bmatrix} P_{mic} \\ U_{mic} \end{bmatrix} \quad \textbf{3.15}$$

$$\begin{bmatrix} P_{endcap} \\ 0 \end{bmatrix} = T_2 \begin{bmatrix} P_{mic} \\ -U_{mic} \end{bmatrix} \quad \textbf{3.16}$$

Writing the equation for U_{pist} from the upper relationship and the equation with zero on the left-hand side from the lower relationship,

$$\begin{aligned} U_{pist} &= c_1 P_{mic} + d_1 U_{mic} \\ 0 &= c_2 P_{mic} - d_2 U_{mic} \end{aligned} \quad \textbf{3.17}$$

another matrix equation can be written,

$$\begin{bmatrix} U_{pist} \\ 0 \end{bmatrix} = \begin{bmatrix} c_1 & d_1 \\ c_2 & -d_2 \end{bmatrix} \begin{bmatrix} P_{mic} \\ U_{mic} \end{bmatrix} \quad \textbf{3.18}$$

Define this new 2x2 matrix as T_3, and inverting the equation,

$$T_3 = \begin{bmatrix} c_1 & d_1 \\ c_2 & -d_2 \end{bmatrix} \quad \textbf{3.19}$$

$$\begin{bmatrix} P_{mic} \\ U_{mic} \end{bmatrix} = T_3^{-1} \begin{bmatrix} U_{pist} \\ 0 \end{bmatrix} \quad \textbf{3.20}$$

gives a direct relationship for either the pressure at the microphone or the volume velocity at the microphone in terms of the matrix, T_3, and the volume velocity of the piston. The matrix, T_3, is determined entirely by the dimensions of the chamber and the properties of the air and of the chamber wall.

This Tee-element technique is implemented in a Matlab function called "*pfunc.m*," which is used to predict the pressure in the chamber. An overview of the code is given in **4.5.1**, and a line-by-line explanation given in Appendix **A**.

From the piston displacement and the multiple-segment equivalent-circuit analogy for the pistonphone chamber, the response in Figure **3-3** is obtained. In the vicinity of 0.001 Hz the pressure response appears to converge to the isothermal limit. Above 1 Hz the pressure oscillations appear to converge to the adiabatic limit but this convergence is obscured by the increase in amplitude as the first resonance of the chamber is approached. A peak in the phase response of approximately 7 degrees occurs near 0.01 Hz; for cylindrical ducts this peak appears consistently near the frequency for which the hydraulic radius (hydraulic radius = area/perimeter = radius/2 for a circular cylinder) equals the thermal penetration depth.

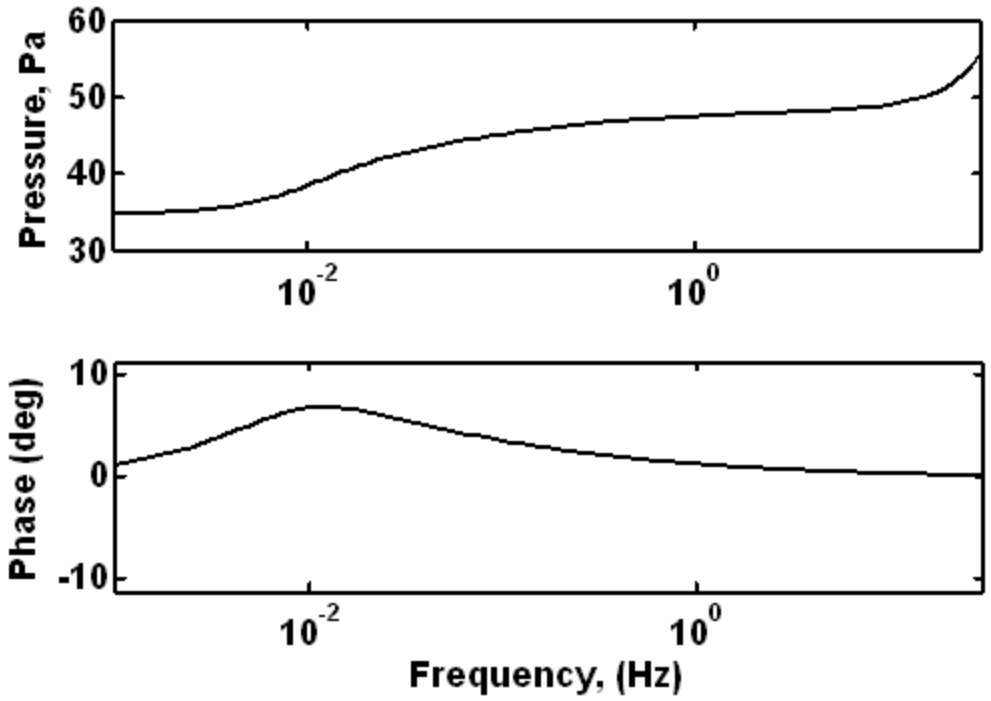

Figure **3-3**: Pressure response in the pistonphone chamber at the location of the differential piezo-resistive pressure sensor, as predicted by the Tee-section model incorporating thermo-viscous effects. The phase is relative to the piston volume displacement.

3.4 Model comparisons: Delta-E and finite-length cylinder exact solution

A software package called "DeltaE[3]" can be used to solve for the field in the calibration chamber including thermo-viscous effects. DeltaE is commonly used in the thermo-acoustics community for the design and performance prediction of thermo-acoustic engines. DeltaE is a powerful software tool but is not predominately used for the modeling of the pistonphone chamber for several reasons. Constant-displacement sources are inefficient to work with in DeltaE models and the program does not communicate easily with Matlab. Furthermore, writing a finite-element simulation in Matlab allows for certain types of simulations pertaining to this research to be completed that are either difficult or impossible to complete with DeltaE.

One advantage of the DeltaE code over the currently used Tee-section model, however, is that the losses due to the end-caps of the pistonphone chamber are simulated in addition to the wall losses. The DeltaE code is used to both 1) verify the Tee-section model's ability to accurately calculate pressure predictions in a pistonphone chamber, and 2) estimate the loss of accuracy due to neglecting the end effects of the tube in the Tee-section model. To further test the assumption that end effects may be neglected, the exact solution for the pressure in a finite annulus with hard ends is compared to the solution predicted by a Tee-section model for the same geometry.

Figure **3-4** is a direct comparison of the DeltaE pressure response prediction with a Tee-section prediction, for the geometry of the most recent pistonphone design.

[3] Information and free download available at http://www.lanl.gov/thermoacoustics/DeltaEC.html

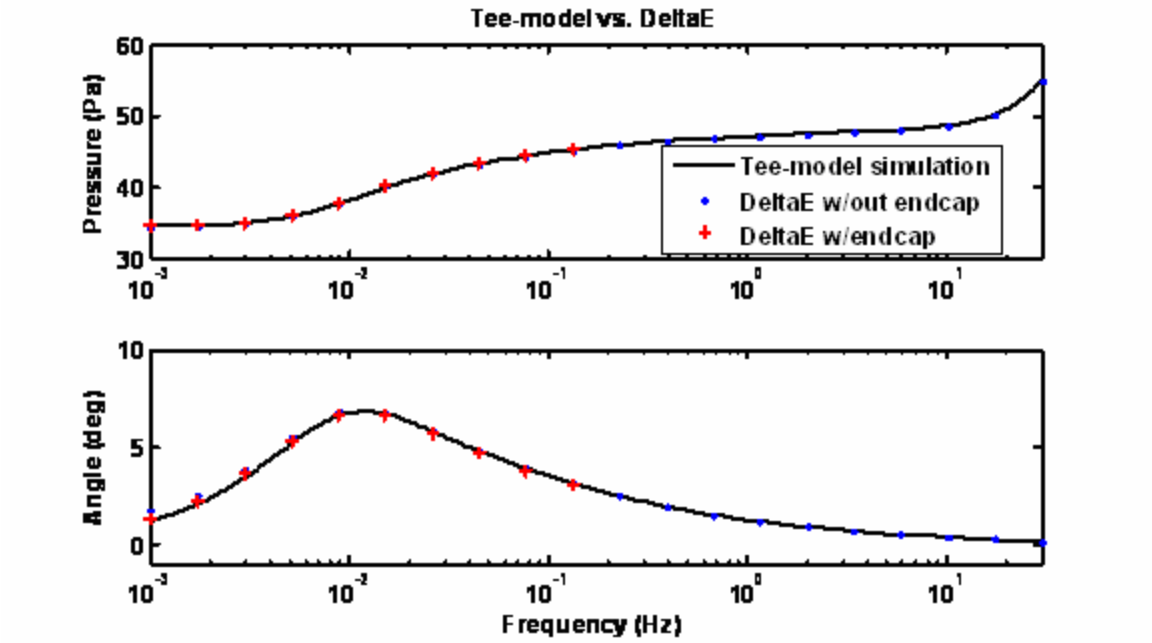

Figure **3-4**: Pressure response of the pistonphone as predicted by Tee-model, and DeltaE simulations including and excluding end-cap losses. The inclusion of the end-cap losses appears to have very small affect.

In the DeltaE code, including the end-cap causes approximately one quarter of a degree of change in phase at frequencies below 0.01 Hz, while the magnitude response varies by 0.3% in the same region. The end-cap losses therefore appear to have very small effect on the overall accuracy of the Tee-model calculations.

The exact solution for the pressure response of a cylindrical enclosure, including thermo-viscous effects and end-cap losses has been solved in the form of an infinite series by several authors (see references [**3**], [**5**] and [**22**]). The actual pistonphone chamber does not look like a perfect cylinder because one end has a cone and separate, smaller diameter cylinder fixed to it. To compare the Tee-element and exact solution predictions, the Tee-element model is re-programmed to look like a perfect finite-length cylinder, with no cones or changes in diameter. The pressure response inside the same cylinder is predicted using both the exact and Tee-element methods.

Consider the hollow cylindrical tube depicted in Figure **3-5**:

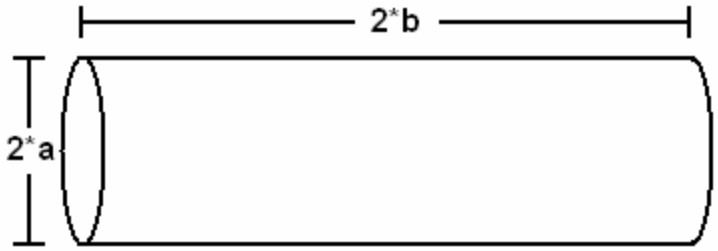

Figure **3-5**: Example cylindrical tube with radius *a* and length *2*b*. The ends are closed.

The acoustic compliance of this cylindrical tube can be calculated from the impedance solution presented in Thompson's paper on thermal boundary layer effects on the acoustic impedance of enclosures [**22**]:

$$Z = \frac{Z_a}{\left(g - (g-1)\frac{\overline{T}}{T_a}\right)} \qquad \textbf{3.21}$$

Z_a is the adiabatic compliance of a volume V at atmospheric pressure P_0:

$$Z_a = \frac{gP_0}{jwV} \qquad \textbf{3.22}$$

$\overline{T}/T_a$ is the ratio of the oscillatory temperature amplitude to the amplitude for purely adiabatic compression:

$$\frac{\overline{T}}{T_a} = \frac{32b^2}{p\left(1-s^2\right)} \sum_{m,n=1}^{\infty} \frac{\left[G_m(a_m) - sG_m(sa_m)\right]}{\left[b^2 + \frac{a_m^2}{r_0^2} + \frac{n^2p^2}{4b^2}\right]\left[G_m(a_m) + sG_m(sa_m)\right]} \qquad \textbf{3.23}$$

The other variables have the following definitions:

$$b^2 = \frac{jwr_0C_p}{k} \qquad \textbf{3.24}$$

$$s = \frac{r_i}{r_o} \qquad \textbf{3.25}$$

$$G_m = J_1(a_m) - C_m Y_1(a_m) \qquad \textbf{3.26}$$

and *a* is the radius, *2b* is the total length of the pipe, r_i is the inner radius, and r_o equals the outer radius, *a*. In this circumstance r_i is zero, causing *s* to equal zero, G_m to equal J_1, and setting a_m equal to the zeros of the J_1 function. This allows the above equation to be reduced to a simpler form, and the final total compliance of the cylinder is:

$$Z_{total} = \frac{\frac{gP_0}{jwV}}{\left\{ g - (g-1)\left[\frac{32b^2}{p^2} \sum_{m=1,2\ldots,\, n=odds}^{\infty} \frac{1}{b^2 + \frac{n^2 a_m^2}{r_o^2} + \frac{n^2 p^2}{4b^2}} \right] \right\}} \qquad \textbf{3.27}$$

Equation **3.27** can be compared to equation 11 from Biagi and Kook [**3**], a calculation of the same impedance, for confirmation. Figure **3-6** represents the pressure in a closed cylindrical tube as calculated by the infinite series exact solution for the lumped element compliance of a tube with a radius of 4.8 centimeters and length of 1.5 meters. The equivalent Tee-section comparison is plotted along-side the exact solution.

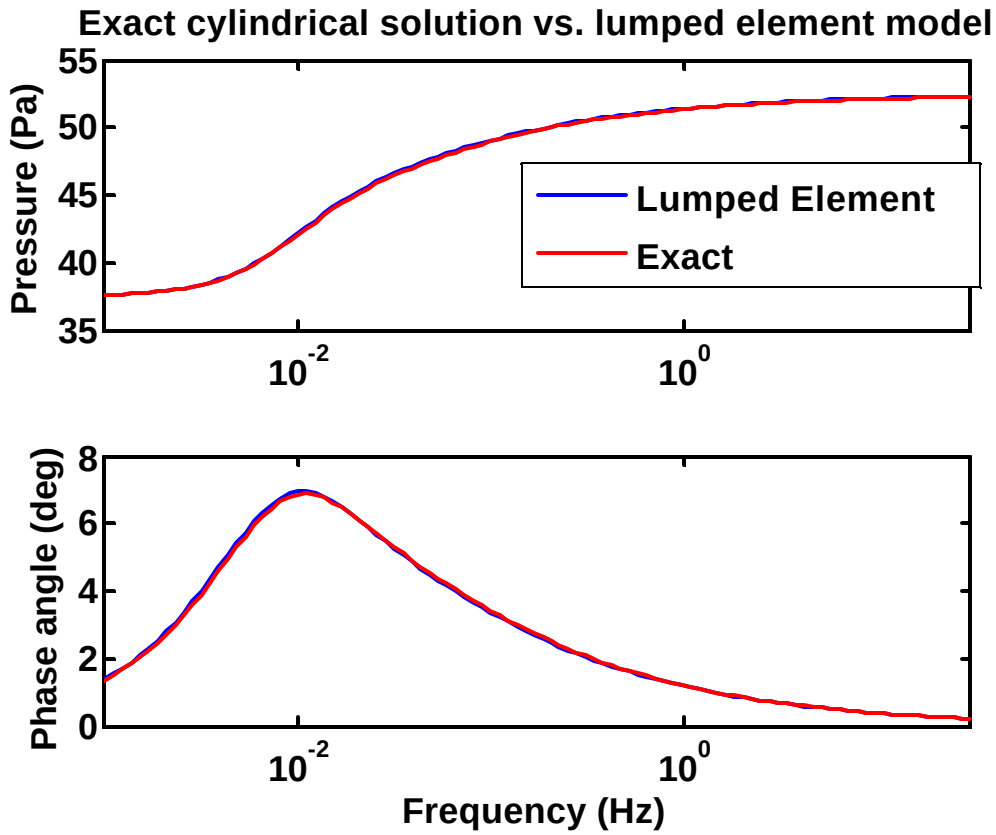

Figure **3-6**: Exact solution, including end-cap effects, vs. Tee-model solution, for cylinder geometry similar to the pistonphone main chamber.

A useful check for the exact solution is to compare the pressure response of a squashed[4] cylinder having surface area dominated by the end-caps, to the pressure response calculated for an enclosed space trapped between two parallel plates. Figure **3-7** compares these two responses and shows that, as expected, the exact cylinder solution is nearly identical to the parallel plate solution. This demonstrates that the end-cap losses are accurately being modeled by the exact solution.

[4] I.e. letting *b* in Figure **3-5** approach *0*. In this simulation *b = 0.018 m*.

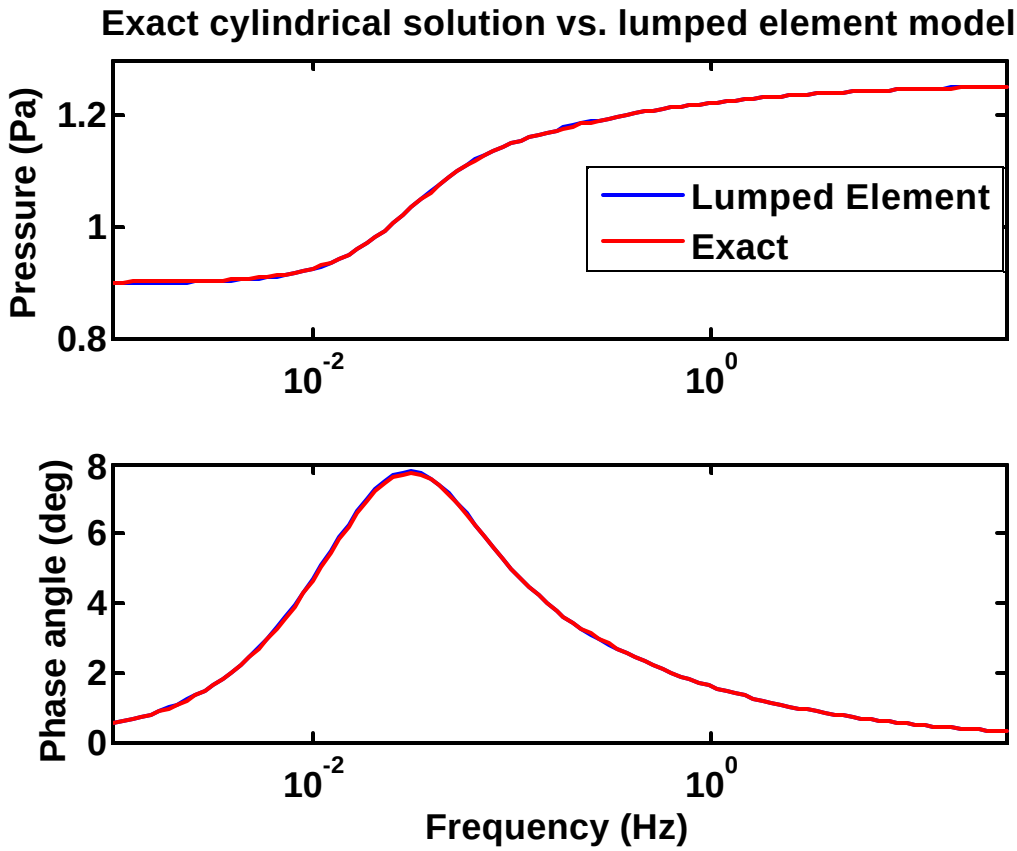

Figure **3-7**: End-cap loss verification. The pressure response of a cylinder with a length of 0.036 m and radius of 2 m, compared to the pressure response of an equivalent volume having losses dominated by two parallel plates and calculated using the parallel plate *f*-function.

The conclusion can be drawn from the above examples that the losses at the ends of the pistonphone chamber do have some effect on the response of the tube; however, the effect is small, and the pressure response of an enclosure is not severely affected by neglecting the losses in a pressure response simulation.

3.5 Wall assumptions

3.5.1 Wall material

For many applications, the material and thickness of duct walls is considered irrelevant when calculating thermo-viscous effects. The heating and cooling of the gas due to pressure oscillations, and the transfer of heat energy to the walls in the isothermal regime is assumed to have no effect on the temperature of the wall itself. In reality, the heat generated by compressing the gas will slightly elevate the temperature of the walls. In the isothermal region of operation, the result is that the pressure generated in the tube will be slightly higher than predicted, because the temperature of the gas will not completely cool to the initial temperature of the walls. Calibrations require pressure predictions to have accuracy beyond that of many other applications, and the extent to which the wall material and wall thickness may affect the pressure predictions is not immediately apparent. As stated in section **3.2**, the parameter e_s is used to account for the finite heat capacity of the walls. The definition for e_s as written in section **3.2** makes an additional assumption, however, namely that the wall is infinitely thick. This model is therefore not perfectly accurate, either. The viability of the "infinite thickness" model can be examined, however, by comparing the thermal penetration depth in the material to the thickness of the tube.

Figure **3-8** is a plot of the adiabatic-to-isothermal transition predicted for the pistonphone geometry, assuming various types of wall material. In the "air" example, a hypothetical situation is assumed, in which the walls are perfectly stiff, but infinitely thin, so that the thermal properties of the wall are determined by the air surrounding the wall.

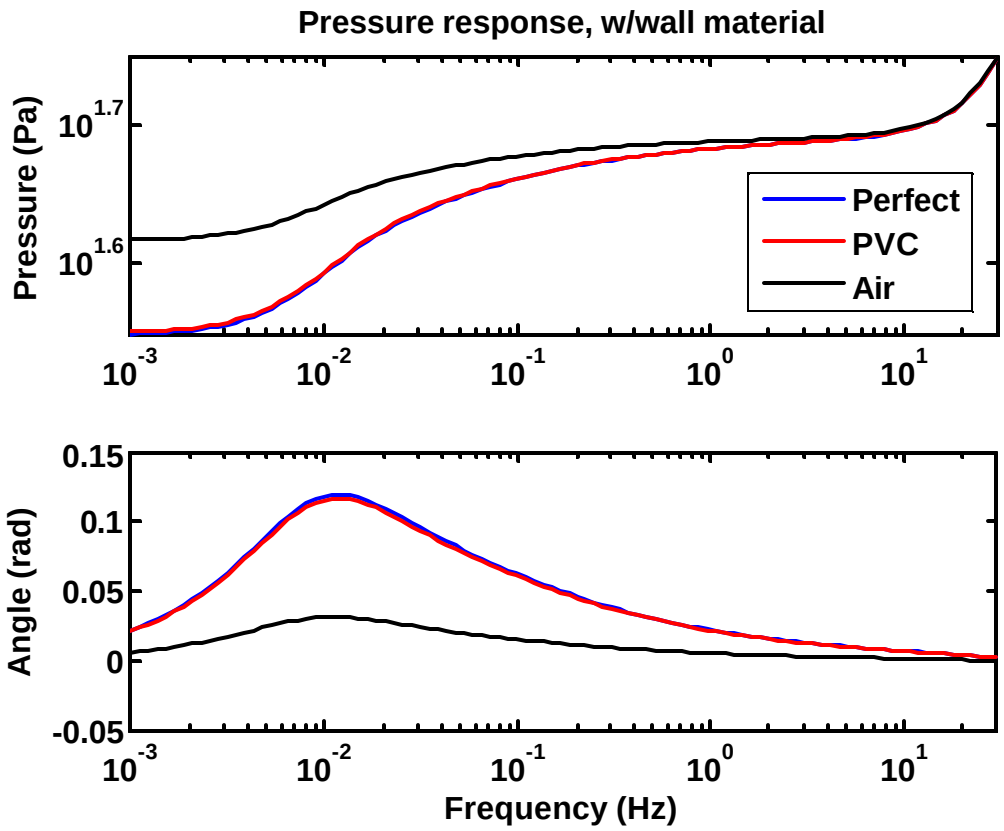

Figure **3-8**: Pressure response in the pistonphone chamber, predicted for various wall materials. The effect of the wall material is most prevalent in the isothermal region of operation.

The pressure magnitude prediction for PVC walls varies from the ideal wall prediction by a maximum of 0.4%, a small amount. The air-wall example is useful for showing what would happen in the limiting case that the walls get extremely thin. As is clearly shown, the effect of finite heat capacity in the walls on the phase is to *lower* the height of the phase peak. This observation becomes important when trying to isolate the source of measurement vs. model discrepancies.

3.5.2 Wall thickness

To examine the validity the infinite wall thickness assumption, the thermal penetration depth is compared to the thickness of the chamber wall. Beyond one thermal penetration depth, changes in temperature that occur at the surface of the PVC wall will have negligible effect. For this reason, if the wall is thicker than a penetration depth, the wall can be considered, for all practical purposes, an "infinitely thick" wall. Figure **3-9** plots the thermal penetration depth vs. wall thickness.

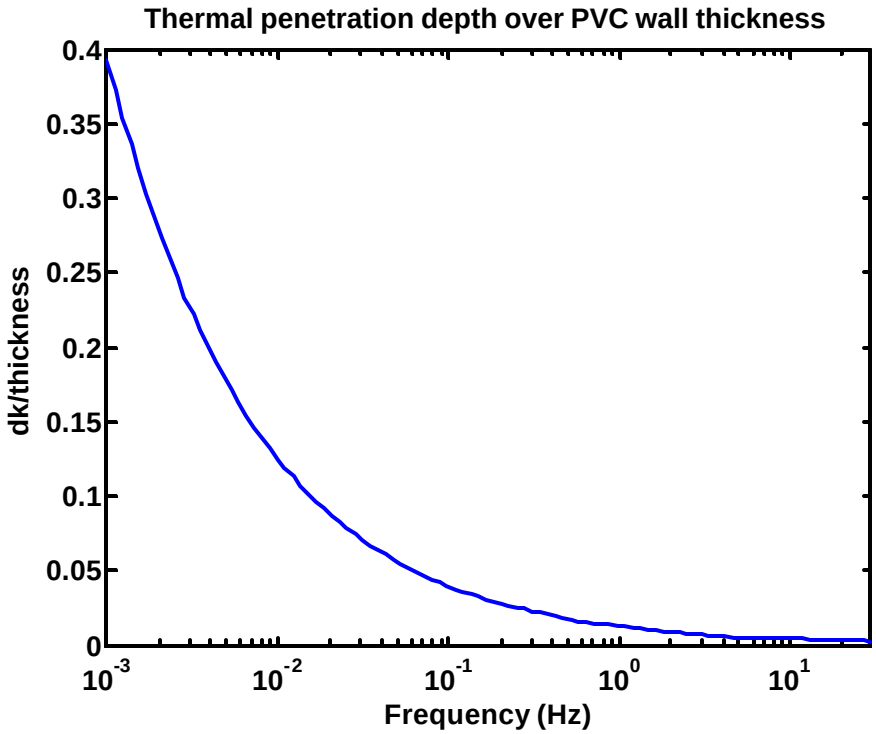

Figure **3-9**: Thermal penetration depth divided by wall thickness for the current pistonphone design and schedule 80 PVC pipe. The ratio stays well below one, implying that the infinitely thick assumption is reasonable.

According to the thermal penetration depth calculation for PVC, the thermal penetration depth is shorter than the thickness of the tube throughout the range of calibration frequencies. This would seem to validate the "infinitely thick" wall assumption.

Wall assumptions are re-examined, during error isolation, in the next chapter, and for a more in-depth discussion of the effects of wall thickness see the next chapter, **4.7.9** "finite wall thickness."

3.5.3 Wall compliance

The final wall assumption that will be examined is that the wall has "zero compliance." This means that the wall does not bend in a manner such as to alter the acoustic stiffness of the chamber as perceived by the piston. If the walls or any portion of the chamber add significant compliance, the effect is to reduce the pressure generated within the chamber to a lower value. A faulty assumption regarding wall compliance could have disastrous effects on the accuracy of calibrations completed inside the pistonphone chamber.

The effect of non-zero compliance on the acoustics of ducts is worked out in reference [**7**]. The compliance of a cylindrical wall is found to be:

$$C_{wall} = V \frac{1 - s^2}{Y} \frac{2a}{t} \qquad \textbf{3.28}$$

Y represents the Young's modulus of the material (in this case PVC), s represents the Poisson's ratio, a represents the radius, V is the volume, and t represents the thickness of the wall. The wall compliance can be electrically represented as a capacitance in parallel with the capacitance representing the acoustic compliance of the segment of tube. Assuming a Poisson's ratio of 0.42, Young's modulus of 10^9 Pa and calculating the compliance for a PVC tube having a thickness of 1.6 centimeters, radius of 9.6 centimeters and a length of 1.5 meters, the compliance of the wall will be 0.05% the acoustic compliance of the chamber. The effect is negligible by the standards of this thesis. Additional confidence in this assumption comes from the probability that this value represents an upper bound on the compliance. The stiffness of the tube is enhanced by the presence of rings around the outside of the container, as well as an end-cap cemented to the end of the pistonphone chamber.

3.6 Matlab script

A detailed breakdown of the workings of the Matlab script used to model the pistonphone is given in Appendix **A**, along with instructions on how to modify the code to predict the pressure response of pistonphones having different design parameters.

3.7 Chapter 3 summary

A transmission line analogy for the pistonphone chamber is constructed using "Tee-sections," which are networks of lumped electrical impedances that represent the acoustic impedance of a portion of the chamber, and include changes in impedance due to thermal and viscous effects. The Tee-sections are strung together to represent the entire pistonphone chamber as an electrical transmission line, where current is analogous to volume-velocity, and voltage is analogous to pressure. The calibration pressure is calculated by deriving a function that relates the known volume velocity generated by the piston to the pressure generated at the location of the transducer. This function is derived by calculating four-element "transfer matrices" that relate the pressure and volume velocity at opposite sides of each Tee-section. The pressure and volume velocity relationships between arbitrary points in the pistonphone chamber can be calculated by multiplying the matrices between these points together to form a single, composite transfer matrix. Because the volume velocity is known at both sides of the pistonphone chamber, the pressure at any arbitrary point in the chamber can be calculated using this method.

Assumptions made about wall compliance and thermal properties were examined. It is found that accounting for the non-infinite heat capacity of the actual chamber walls affects the pressure predictions significantly enough to include in the pressure-prediction algorithm. Finite wall thickness and wall stiffness do not contribute significantly enough to merit inclusion into the pressure prediction algorithm, and the effect of the chamber end-cap on the isothermal-to-adiabatic transition is insignificant.

Chapter 4

Model/Measurement comparisons

4.1 Overview/assumptions

Though the equations used to model the thermo-viscous effects are well accepted and have been verified for many duct geometries (see a series of papers [**23**] [**24**] [**25**] by L. Wilen for a published set of good experimental measurements), it is necessary to experimentally confirm the applicability and accuracy of the thermo-viscous model for the pistonphone chamber. This chapter describes the experimental processes used to compare actual pressure measurements made inside the pistonphone chamber with the theoretical model used to calculate the pressure. The pressure response of the chamber when filled with different gases is also measured and compared to a theoretical model that has been adjusted to include the different properties of each gas. Helium, for example, is used because it raises the frequency range of the adiabatic-to-isothermal transition region well above that of air, and has a different ratio of specific heats.

An assumption made throughout this section is that the responses of all pressure sensors used to measure the pressure inside the pistonphone calibration chamber are flat. Justification for this assumption is that the piezoresistive (PZR) sensors used to measure the pressure are DC-coupled, and their resonance frequencies are far above the 0.001 to 30 Hz measurement region.

4.2 Displacement calibration

Critical to the calibration process is an accurate measurement of the displacement of the piston. Displacement measurement is important because it provides a phase reference for the calibration, but also because the magnitude of the pressure response is

calculated directly from the change in displacement. The displacement is the variable in the calculation of the change in volume, and any error in this measurement will directly affect the accuracy of the calibration sensitivity result.

The LVDT used to measure displacement is described in Section **2.2**. To calibrate the LVDT, a micrometer is placed with the axis parallel to the motion of the piston shaft. A misalignment of the shaft and axis of the micrometer will result in a small calibration error. The axes are estimated to be parallel within 5 degrees, which would add an additional 0.3% in uncertainty to the final calibration result.

Figure **4-1** is a diagram of the apparatus used for calibrating the LVDT and Figure **4-2** is a photo of the apparatus in use.

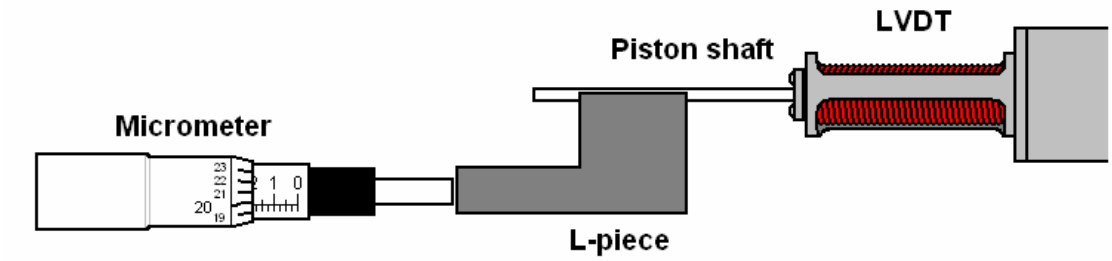

Figure **4-1**: Top view of LVDT with calibration equipment in place. The L-piece snaps to the piston shaft by means of a machined groove.

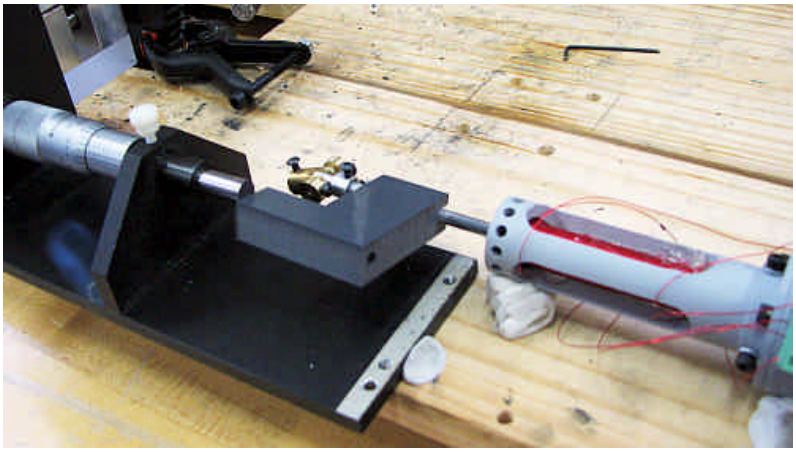

Figure **4-2**: Photo of the calibration process in operation. The micrometer base and clay used to fix it in place are visible.

To calibrate the LVDT, the micrometer is fixed to the same platform the axle block is attached to. Because of the size of the micrometer, the barrel of the micrometer can not be placed directly in front of the shaft of the piston. To allow the micrometer to be moved to the side, an L-shaped PVC block that snaps to the shaft is used. This piece is used to make contact with the tip of the micrometer barrel. The micrometer and L-piece are positioned such that the reading of the micrometer is 0 when the piston shaft is most fully inserted into the LVDT.

Before the first voltage measurement is made, the LVDT circuitry is powered for at least 30 minutes. This is merely a precaution, but is advisable because a small amount of drift has been observed in the output, and this tends to stabilize after a half hour period of warm-up. Additionally, despite precautions used during the fabrication process of the LVDT, the axis of the ferrite beads used to make the core are not perfectly in line with the axis of the shaft. Furthermore, the axis of the shaft is not perfectly in line with the coil axis. For this reason, it is important that the same rotational position of the shaft used during calibration also be used during pistonphone operation. Lastly, it is important that the same carrier signal frequency and voltage are used during the measurement process as is used during the LVDT calibration process. For measurements made in this thesis, the carrier frequency used is 15 kHz, and the amplitude of the signal is 450 mVrms.

When the LVDT has warmed up and the "0-inches" mark has been determined by positioning the micrometer and making contact with the L-piece, the calibration process begins. The DC offset of the signal is measured either by multi-meter or oscilloscope and recorded, along with the corresponding displacement on the micrometer. An oscilloscope is used for most of the calibration measurements in this thesis. The micrometer is then backed out by 50 mil[5]. The L-piece is brought into contact with the face of the barrel again, (displacing the shaft by 50 mil in the same direction), and the DC offset of the signal is once again measured and recorded.

[5] 1 mil = $1/1000^{th}$ of an inch, or $2.54*10^{-6}$ m.

This process is repeated such that the entire displacement traveled by the piston during operation is calibrated. Figure **4-3** is a graph of one of the calibration curves measured for the piston:

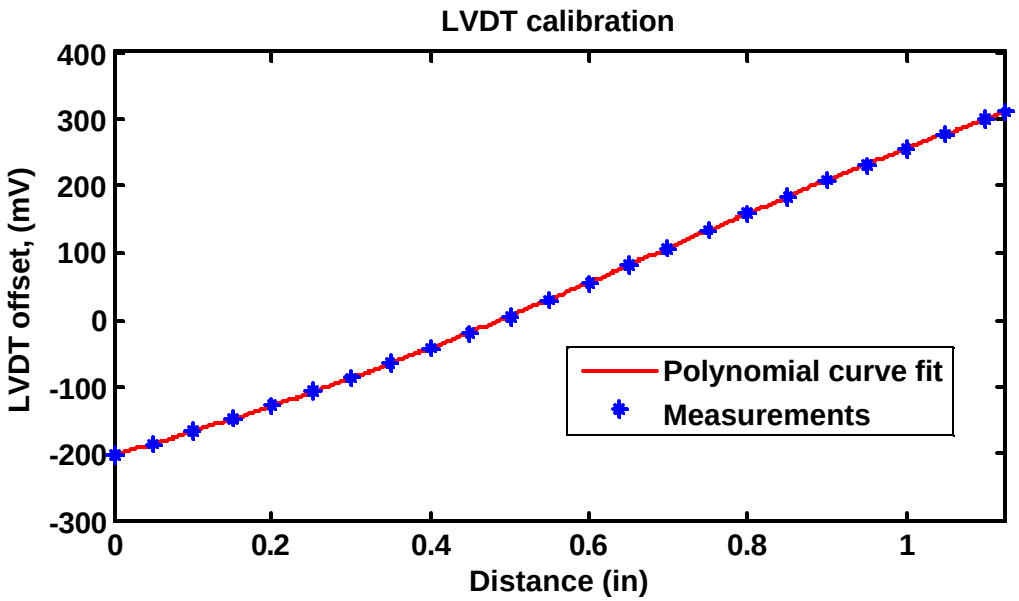

Figure **4-3**: LVDT displacement calibration curve and polynomial curve fit for the data.

After the curve has been measured, a 4^{th} order polynomial curve is obtained that fits the data. After a data-acquisition system has been used to measure the output of the LVDT during pistonphone operation, this polynomial is used to map the LVDT output voltages to displacements, which are then used to calculate the pressure inside the pistonphone chamber. The code for this operation is discussed in more detail in section **4.4** of this chapter, and Appendix **B**.

4.3 Pistonphone operation

Operation of the pistonphone is not a complicated procedure; however, there are a large number of steps involved. The motor can not directly drive the piston across the entire 0.001 to 30 Hz frequency span. Four gearing configurations are used to cover this

range, and a detailed description of the steps involved in changing gears and operating the pistonphone is given in Appendix **G**.

4.4 Data processing

The data from the pistonphone can be post-processed in a variety of ways. In this case a special Matlab code is written to work with the data recorded by a digital instrumentation recorder (TEAC GX-1). The Matlab code quickly processes the data and returns easily readable results. In this section, the post-processing accomplished by this program will be outlined. The final part of this section will be a comparison of the pressure response results measured using this data processing method with other data processing methods.

4.4.1 HEBI: data processing code

Figure **4-4** is a screen shot of the HEBI[6] code during operation. The code has been developed to provide a quick and accurate method of retrieving pressure response information from the swept sine signals measured using the TEAC recorder. It provides a number of variables that can be tuned to adjust for changes in the number of channels, the gain on each channel, the number and types of transducers used, and the sensitivity of the reference pressure sensor. In this section, the data-processing method used in the code will be outlined. For an actual breakdown of the code and variable descriptions see Appendix **B**.

[6] The program was named HEBI ("snake" in Japanese) because the graph updated during code execution looks like a snake crawling across the screen.

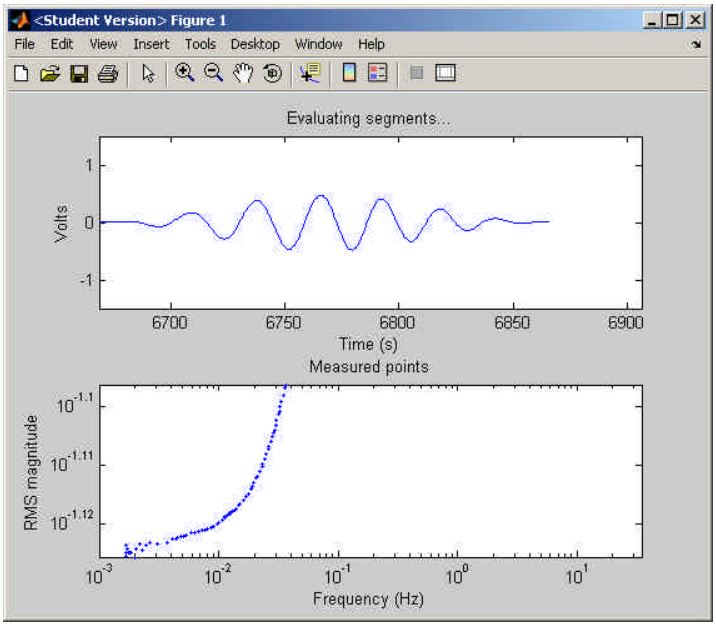

Figure **4-4**: HEBI display, updating information as pistonphone data is being processed. The top window shows the current segment of the time data being processed by the algorithm. The bottom graph shows the portion of the response that has been calculated.

4.4.2 Data processing outline

The basic strategy used behind the HEBI code is to calculate a spectrogram for both the pressure transducer and the LVDT output, and trace the ratio of the peaks for each segment of the spectrogram. The window-size, window type, and overlap percentage can all be specified in the HEBI command script, and may be varied appropriately for the particular sweep range (e.g., the overlap may be set to 95% for the very low frequency sweep, but 25% for the 3.5 to 30 Hz sweep). The code automatically assembles the data from the individual sweep sets into one final data-set that contains the pressure response in the tube for the entire range of the pistonphone: 0.001 Hz to 30 Hz. The code does this by processing the data in batches, where each batch is the recorded information for a single sweep. Each batch is composed of 3 wav-files (4 if an ambient-pressure sensor is used) containing the information of the 15 PSI PZR, 1 PSI PZR, and

LVDT transducers. The code reads the data for a particular batch, perhaps representing the 0.001 to 0.087 sweep, processes it, and stores it in a variable while it evaluates the other batches. The final results for each batch are compiled into one large matrix representing the entire spectrum from 0.001 Hz to 30 Hz, and presented at the completion of the data processing.

The first portion of the code is the section where all variables are set that determine overlap, "bin range" (discussed in the next paragraph), and gain for each channel to appropriately adjust for the TEAC settings. Because the data-sets may be hours in length, the code decimates the data to a set length that is also defined in this section (normally 10000 points, but increased for the last sweep to preserve high frequencies). The decimation is not necessary, but it increases the speed of the data processing.

The signal processing begins by taking a short-time window (the length of which is user defined) of the LVDT data, and calculates the spectrum, similar to what would be done in a spectrogram. As the short-time window shifts, the dominant frequency will shift because the calibration signal is swept from low to high. At the start of the program the user defines a range of bin values[7] that the peak of this spectrum must lie between. If the segment is too short, the peak in the spectrum will lie below the specified range, and the code will compensate by lengthening the window until the peak of the spectrum lies inside the bin range. If the peak lies above the range, the window length is truncated until the peak lies within the bin range. In this way, the code breaks up the data very much like a spectrogram, except that the window size automatically optimizes itself for measurement of the dominant frequency. Figure **4-5** through **4-8** graphically illustrate the bin-range and truncation/elongation process.

[7] It is important to note that, because the length of the windows change, the bin-range does *not* correspond to a specific frequency range, for the entire data set. Another way of thinking about how the program divides up the signal is that it forces a particular number of *oscillations* to occur, per window.

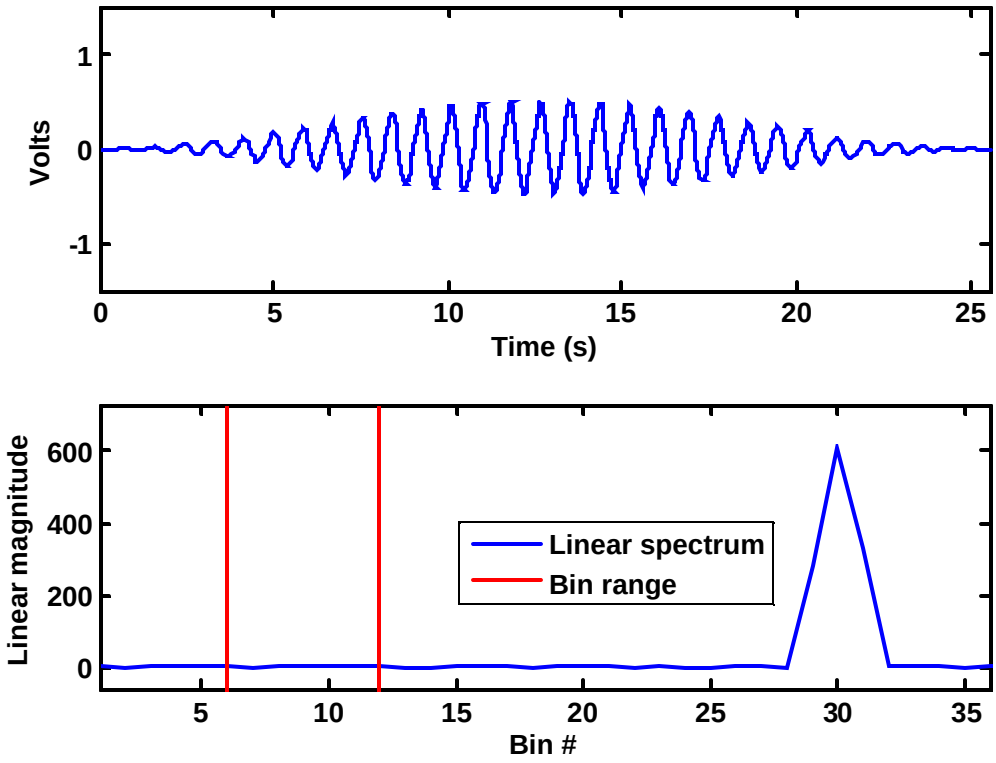

Figure **4-5**: The length of the segment is roughly 26 seconds. The frequency is about one hertz, and the resulting peak in the linear spectrum lies on the 30^{th} bin. The bin range is the portion of the response between the vertical lines. The peak lies above the bin range, so the segment will be trimmed. (The data in the upper plot has been windowed by a Hanning window).

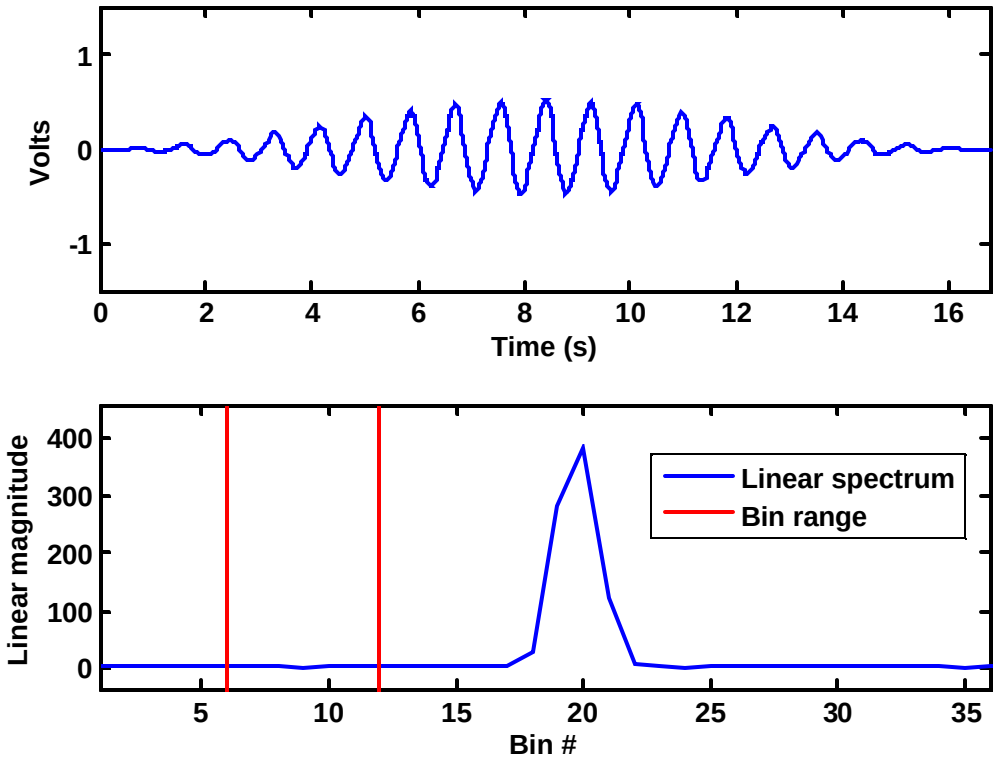

Figure **4-6**: Several trims later the bin number has been lowered to bin 20, and the length of the segment is 17 seconds. The peak is still outside of the bin range.

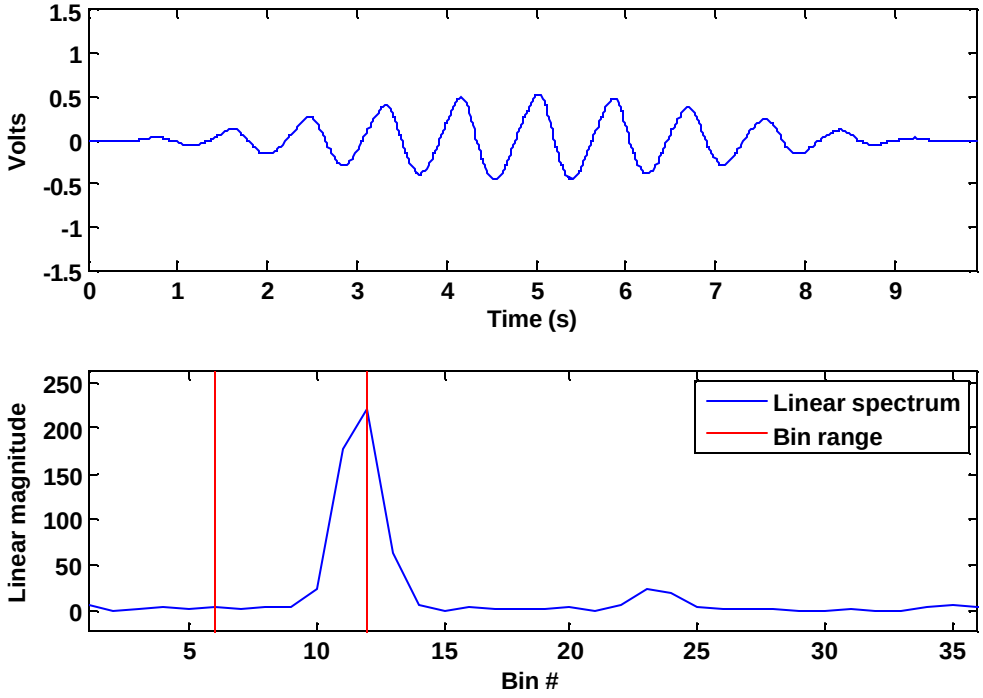

Figure **4-7**: After several more trims, the peak finally falls within the bin range. The length has been trimmed to 10 seconds. The high distortion of the wave-form is due to the low-torque of the motor at the operating frequency: 1 Hz in direct connection configuration. Under normal circumstances the distortion of the wave-form is much less obvious.

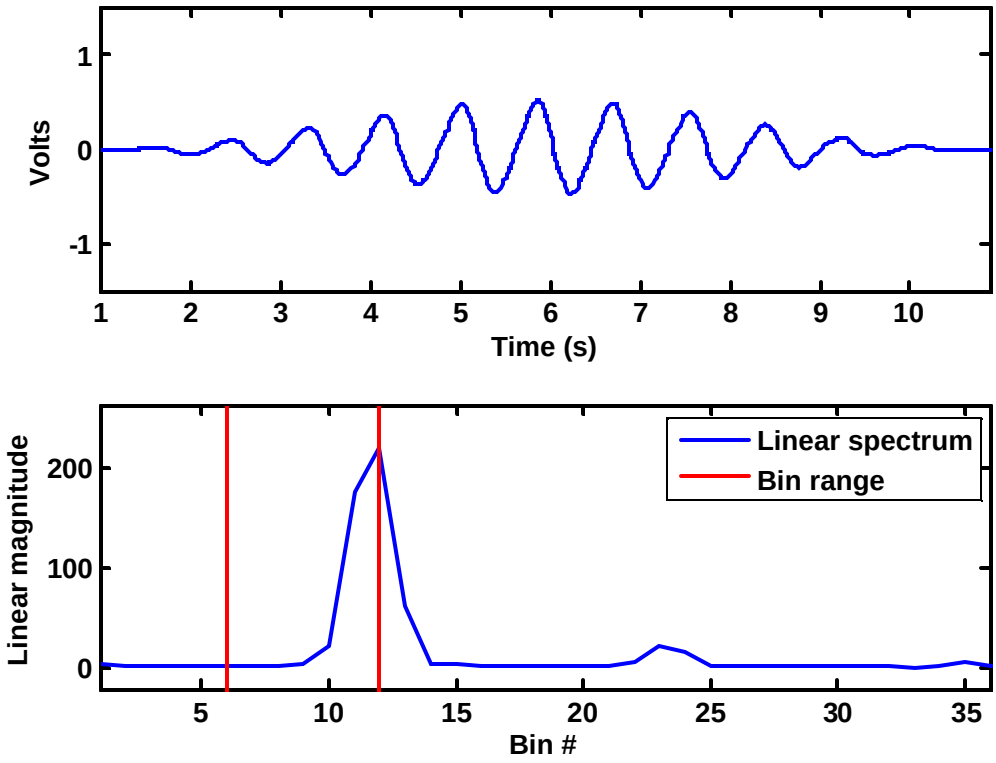

Figure **4-8**: A new segment is evaluated. Because the peak of the previous segment was within the bin range, the appropriate calculations were made, and the window was shifted by the overlap percentage to spanning from 1 second to 10 seconds. The peak of the spectrum still lies within the bin range for this window as well, and no adjustments are made.

This window-size optimization greatly increased the quality of the results. A drawback is that sometimes the code can get stuck in a loop. To save time, the truncation and elongation functions resize the window by a specific percentage (10%) rather than sample-by-sample. If the bin-spacing is tight, the peak can miss the bin region and bounce back and forth between elongation and truncation. To alert the user to such glitches and to monitor the progress of the code, a graph is updated in real-time during which the segment of data being processed is displayed.

After the appropriate window-size has been found, the true frequency of the peak is determined. The truncation of the data into a small window results in a large loss of

frequency resolution. The LVDT output always has a high signal-to-noise ratio, and the location of the peak can be recovered accurately by zero-padding. A frequency spectrum corresponding to the new, padded length is generated, and the peak of the resultant spectrum is matched to the appropriate frequency and stored. This technique for frequency measurement greatly improved the quality of graphs resulting from the data-processing used in this code.

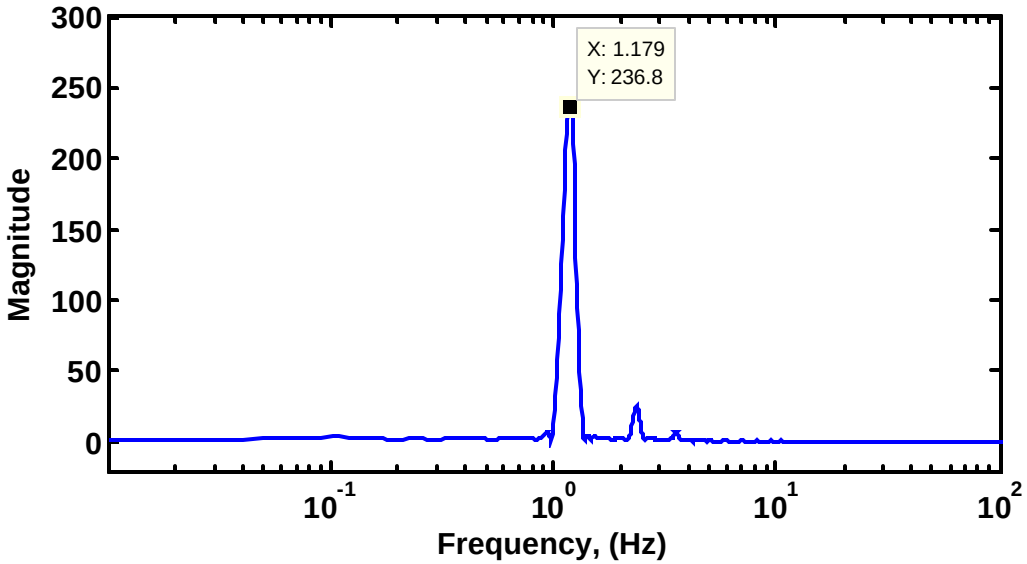

Figure **4-9**: Linear spectrum of the windowed segment, with zero-padding equal to 10 times the length of the segment.

Once the true frequency has been determined, the spectrum of the LVDT data clip is calculated without zero padding. The spectrum is also calculated for the corresponding window of data taken from the differential pressure sensor. In this linear spectrum calculation the data is windowed with a Hanning window. This window consistently returns the best results for data with peaks in the 5 to 15 bin range.[8] The power spectrum is then calculated, adjusting appropriately for the effects of the length and type of window. The root-mean-square of the signal is found by calculated by integrating the

[8] A bin range of 5 to 15 is chosen because only a few cycles are normally measured at the lowest frequencies, and raising the minimum bin to high will cause that very low frequency information to be lost. A maximum of 15 is chosen because it gives good measurement density at the higher frequency portions of the data set.

power spectrum several bins below the peak to several bins above the peak, as is seen in Figure **4-10**:

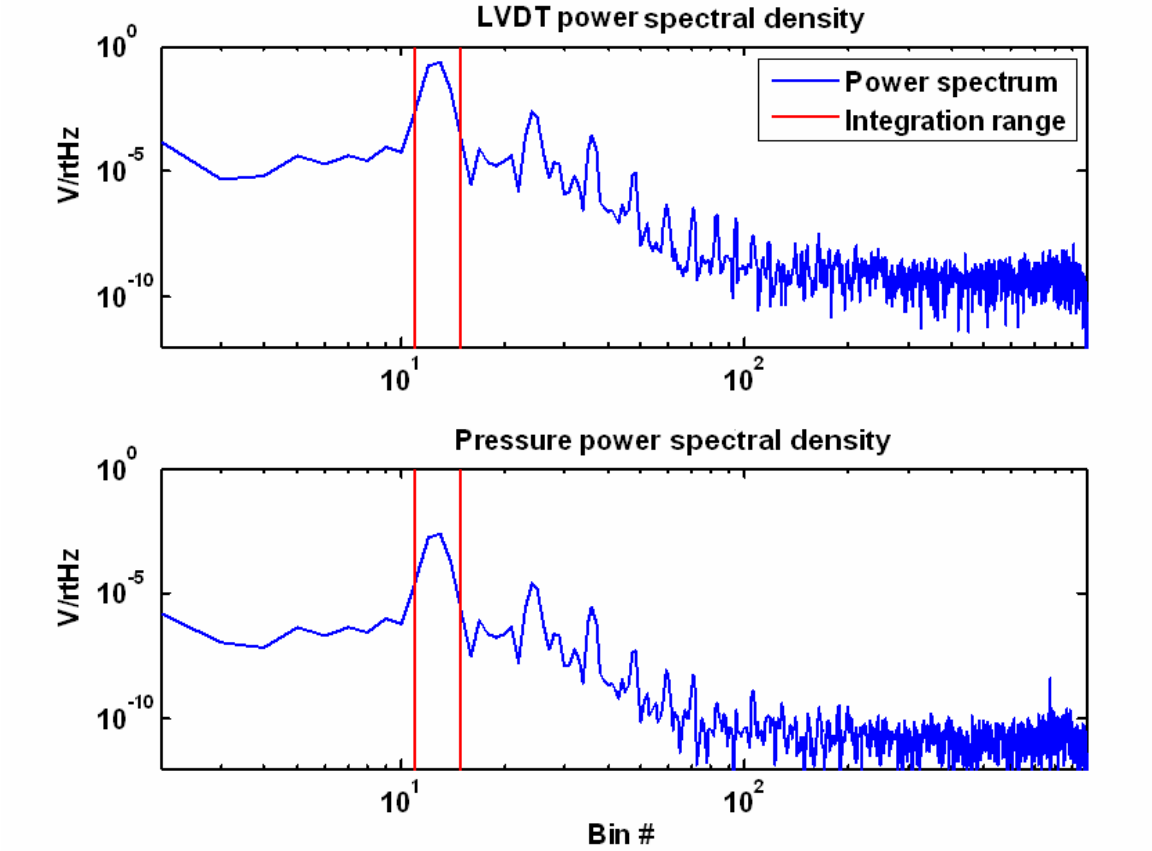

Figure **4-10**: Power spectral densities of the LVDT and pressure sensor data. "rt—" indicates the square root of a quantity. The x-axis is listed as "Bin #" instead of frequency, and the vertical stripes lie indicate the bin range over which the power spectral density is integrated.

It is important to note, from the figure above, that though the power-spectra are noisy, the noise is similar. If the graphs are scaled to account for the different sensitivities and overlaid, the plots are nearly identical at lower frequencies. The fact that the graphs are similar is important because it means many troublesome signal processing and noise artifacts divide out of the spectrum when the ratio of the two spectra is taken, as will be discussed in more detail later.

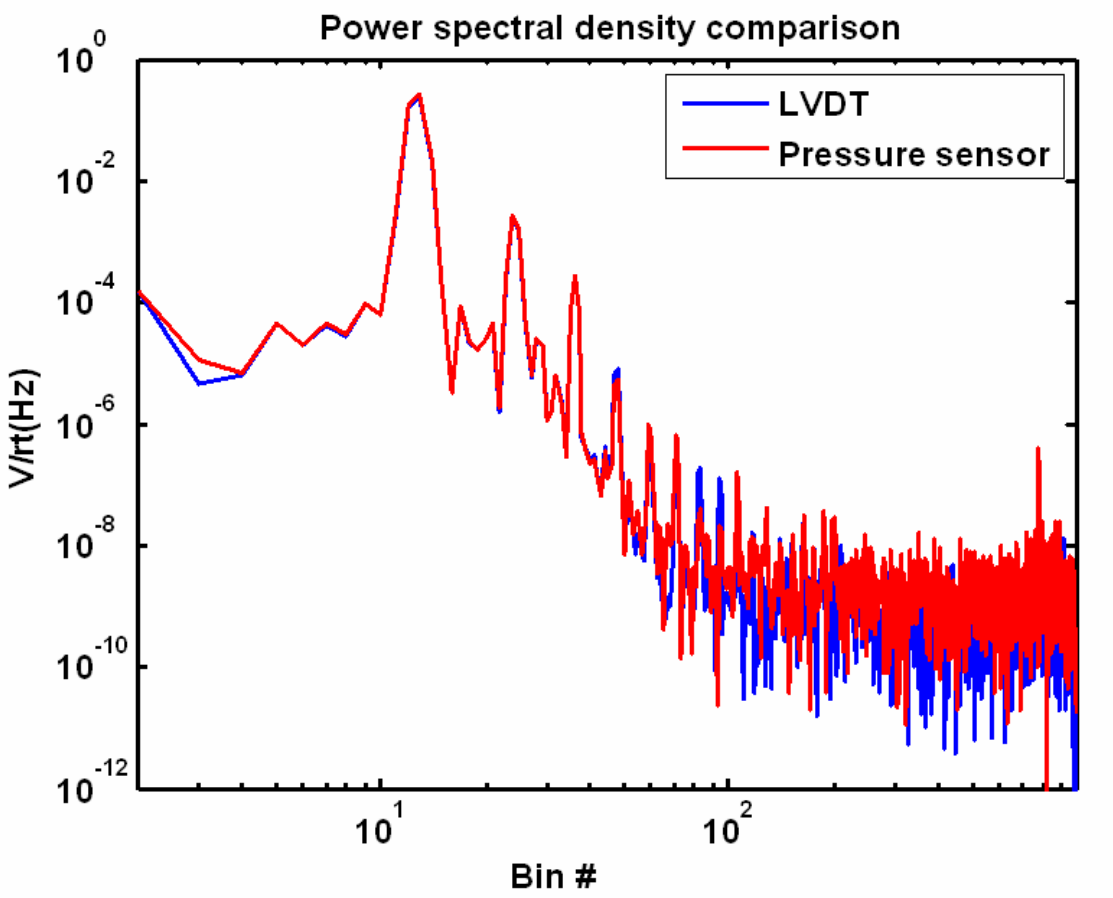

Figure **4-11**: Power spectrum comparison, LVDT data vs. pressure sensor data. The spectra are nearly identical in the region surrounding the peak, indicating that scalloping loss and noise are common to both signals.

The narrow integration shown in Figure **4-10** has the effect of tightly filtering the data around the peak frequency so that the effects of the upper-harmonics are not included in the measurement of the pressure response at a particular frequency. This is especially important because the method of driving the piston results in a signal that is guaranteed to be non-sinusoidal. The root-mean-squared values are stored in variables, and the phase difference between the LVDT and the pressure sensor is then calculated.

To find the phase of the pressure-sensor with respect to the displacement, the linear spectrum is once again calculated, but is zero-padded by a factor of 10 as in the case of the precision frequency measurement. The phase of the peak of the LVDT is

measured from the linear spectrum, and the difference between it and the phase at the same bin in the pressure sensor data is calculated and stored.

At this point, a graph updates on the screen revealing the ratio of the peak pressure sensor magnitude to the peak LVDT magnitude. The shape of the pressure-response curve is traced out as the code progresses, allowing the user to see if the code has stalled, or if any serious measurement errors have occurred, so that the program may be stopped prematurely if such errors become visible. Figure **4-12** is a snapshot of the code working through a pressure response curve measured for air.

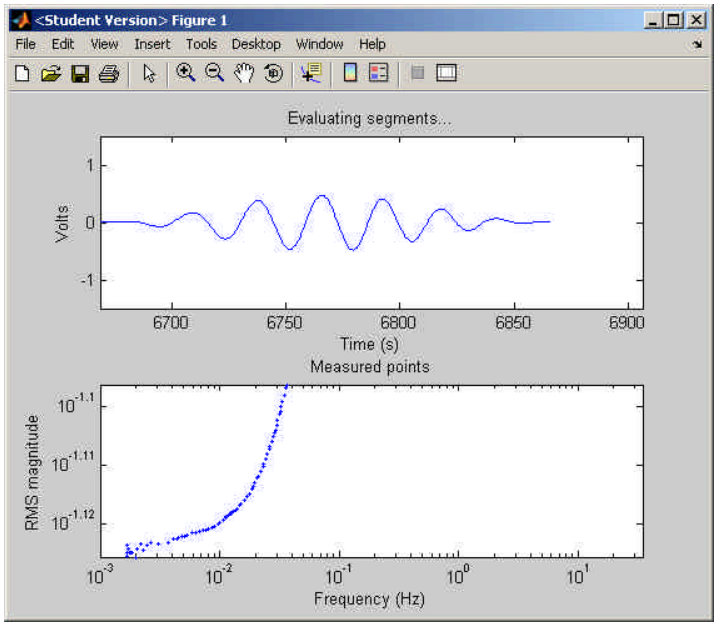

Figure **4-12**: Screenshot of the HEBI update window during data processing. The top graph shows the current segment, and the bottom graph shows the response points.

Following the successful completion of a magnitude and phase measurement for a single window, the window is shifted by a user-specified percentage. This percentage is with respect to the *current window size* rather than the size of the window initially defined. So, for example, the window size may have been initialized to 3000 points. This may get truncated to 1000 points to place the peak in the specified bin range. If the overlap has been specified as 90 %, the next window will be 1000 points long, and shifted by 100 points.

After a batch (representing one sweep range) has been completed, the code loads the batch of data representing the next sweep. The process is repeated until all the specified batches have been evaluated.

The final major step in the data-processing involves normalization with the LVDT data. This is a critical step, and of all previous data-processing steps, this one seems to improve output quality the most. The LVDT and the pressure sensor experience many of the same signal distortions. Because these distortions are common to both measurements the effects of the distortion divide out when the ratio of the pressure sensor values and the LVDT values is calculated. Furthermore, the effects of the Hanning window and leakage from harmonics are common to both transducers and these also divide out of the spectrum. The total response resulting from normalization with the LVDT data is much cleaner, as can be seen from Figure **4-13**, which is a comparison of the response measured without normalization and with normalization:

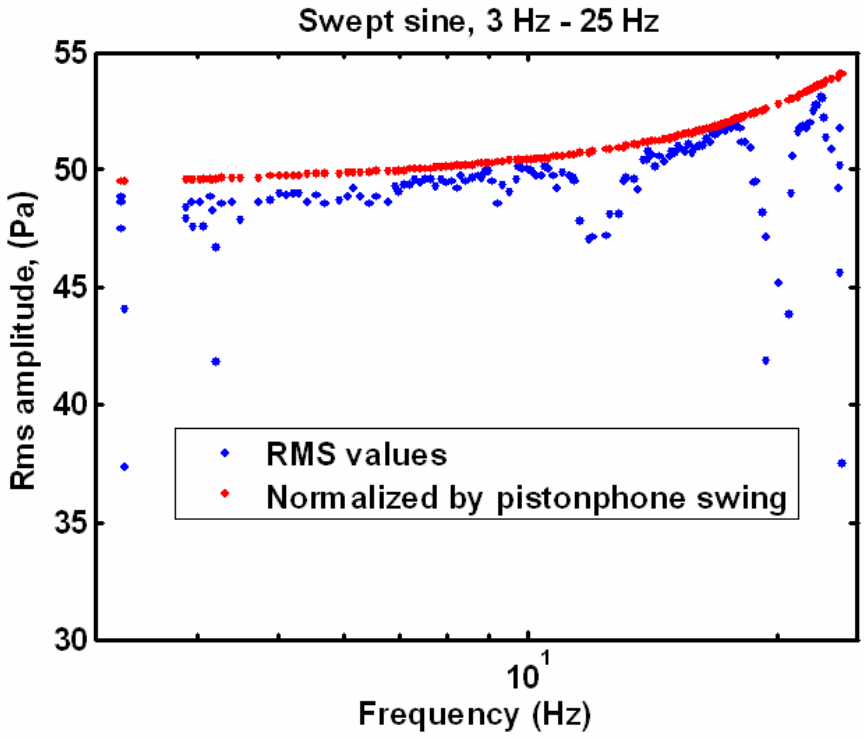

Figure **4-13**: Comparison of the HEBI code output before and after dividing by the normalized LVDT displacement measurements.

Following the normalization, the data is organized, plotted, and saved as a variable which can be opened, modified, and compared to theoretical models in a different m-file devoted to plotting data. Figure **4-14** is an example of the data after it has been entirely processed by the code. Each point represents the RMS of the pressure amplitude at the peak-frequency for a specific slice of the data sets.

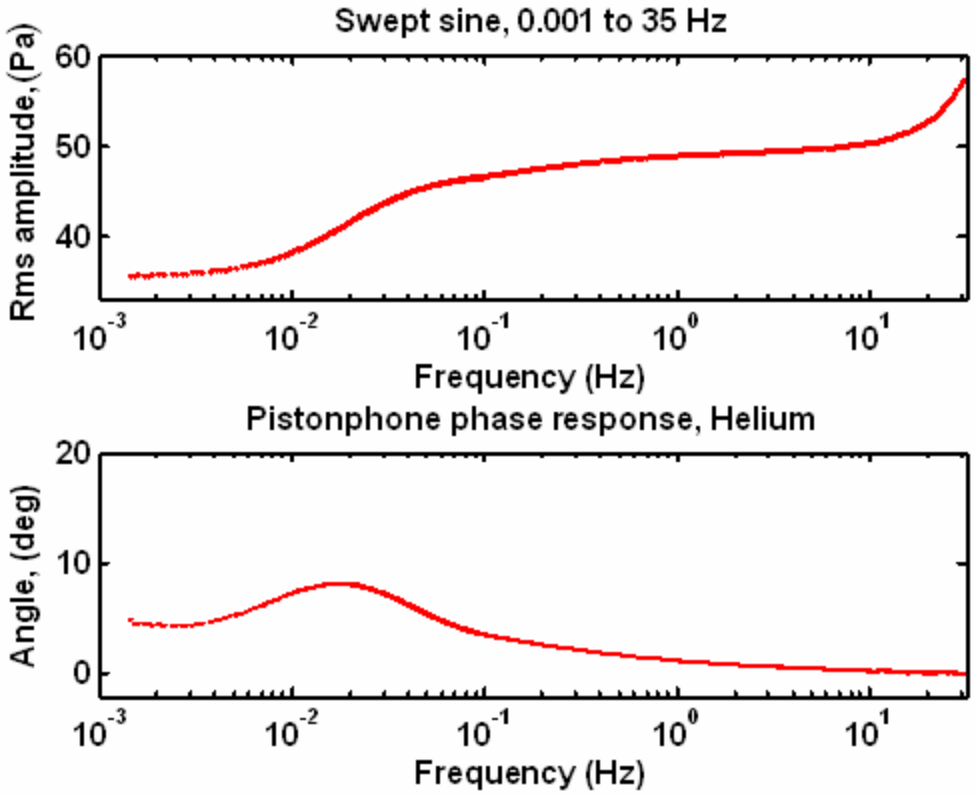

Figure **4-14**: Example data set processed by HEBI code.

Several distinct regions can be seen in the phase and magnitude plots shown in Figure **4-14**. The far left of the magnitude plot shows a region in which the pressure magnitudes appear to converge on a lower value, approximately 35 Pa. The gas is compressed isothermally in this region. The slope from 0.01 to 0.1 Hz is the transition region, in which the compression of the gas is switching from isothermal to adiabatic. At higher frequencies, 0.1 to 10 Hz the pressure oscillations are very nearly adiabatic. The

upward bend in magnitude that occurs above 10 Hz is due to the proximity to the quarter-wavelength resonance of the tube, at approximately 55 Hz.

The phase plot shows a gradual increase towards a peak that occurs near 0.01 Hz. The peak in the phase occurs in the same frequency region as the adiabatic-isothermal transition in the magnitude plots. After the peak, the phase starts to head back to zero degrees, but there is a small upturn that indicates a slow leak in the chamber. Compensation for chamber leaks is described in **4.6**.

4.5 Pressure Prediction

The previous section explained the algorithm used to process the data. In this section, the pressure prediction code is introduced. The theory for thermo-viscous losses and the lumped-element Tee-section has already been described in Chapter **3**, and a detailed code break-down is given in Appendix **A**. This section will provide an overview and outline of the code in the same way that the previous section described the HEBI code.

4.5.1 Pfunc.m

Pfunc ["Pressure function"] is the function name of the m-file script used to predict the pressure in the tube. It predicts the pressure generated inside the tube for a set of passed parameters: frequency range, piston stroke length, the location of the microphone in the chamber, atmospheric pressure (in mBar), and whether the response returned should be a correction type (in which case the returned response is normalized by the adiabatic-compliance pressure value and unit-less), or an absolute pressure value, in which case the response is returned with the units of pascals. Several variations of the program have been written to allow modification of the wall material or gas properties in the simulation. Once the values have been passed to the function, the pressure response

inside the tube is calculated at the specified location for a range of frequencies, and returned as a complex vector.

The function begins by initializing atmospheric constants, and specifying the volume velocities associated with the user-determined values for stroke length and frequency range. The function then sets up the geometrical parameters for the pistonphone chamber. The method used to define the shape of the pistonphone chamber makes re-definition of the chamber shape simple, and will be discussed shortly. The chamber is composed of several segments, each of which has an opening diameter, closing diameter, length, and "slice number." If the segment is a cone, the diameter of the mouth of the cone is used as the opening diameter and the diameter of the other side of the cone is used as the closing diameter. If it is a tube, the opening and closing diameters are both set equal to the diameter of the tube. The slice number is the number of differential segments used to represent the tube segment.

These four values – opening diameter, closing diameter, length, and slice number, are put into a column of a matrix representing that specific segment. The columns for the segments are then concatenated to form one large matrix, the far left column of which describes the piston-cylinder, and the far right column of which describes the segment of the chamber farthest from the piston. A script has been written that plots the cross-section of the pistonphone according to the defined geometry. For example, a piston defined by the following matrix *a*,

```
a =

    0.0120    0.0120    0.0480
    0.0120    0.0480    0.0480
    0.0478    0.2453    1.4843
   10.0000  100.0000  100.0000
```

would have the following cross section:

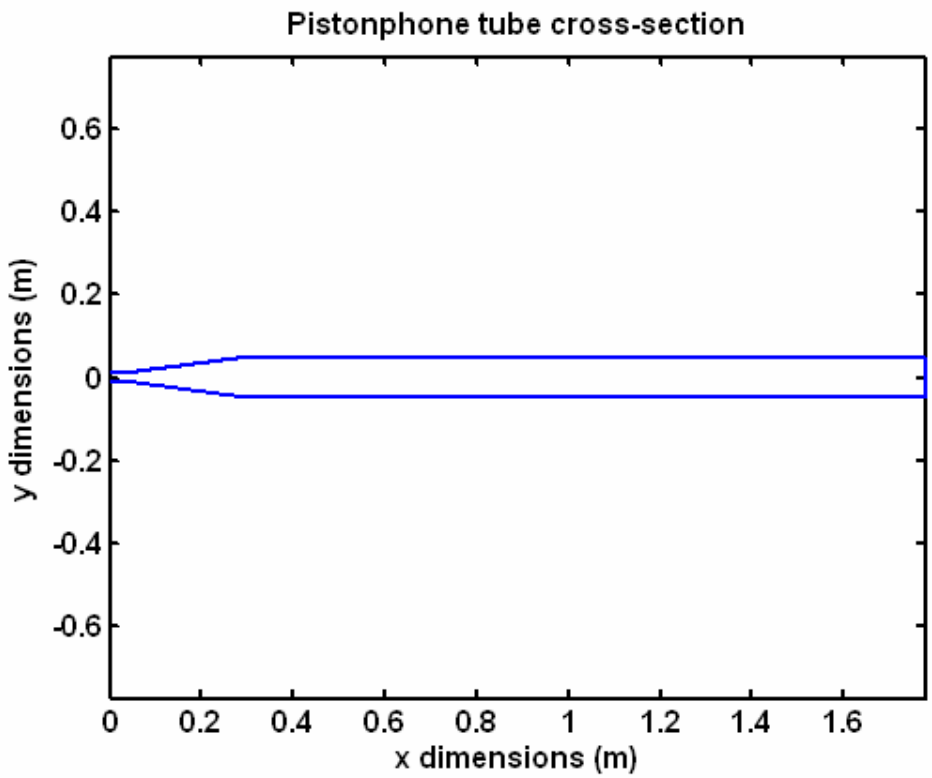

Figure **4-15**: The piston phone chamber defined by the numbers in segment definition matrix *a*.

The figure above is a plot of the pistonphone cylinder defined by the measurements made of the real pistonphone geometry. The design was intended to be simple, but the pistonphone evaluation code can just as easily predict the pressure in an acoustic chamber with the cross section defined below:

```
a = [
    0.015   0.015   0.1     0.3     0.33    0.33    0.25    0.04    0.02    0.25    0.25
    0.015   0.1     0.3     0.3     0.33    0.25    0.04    0.02    0.25    0.25    0.05
    0.05    0.08    0.01    0.2     0.05    0.1     0.1     0.1     0.05    0.08    0.02
    10      10      10      10      10      10      10      10      10      10      10 ];
```

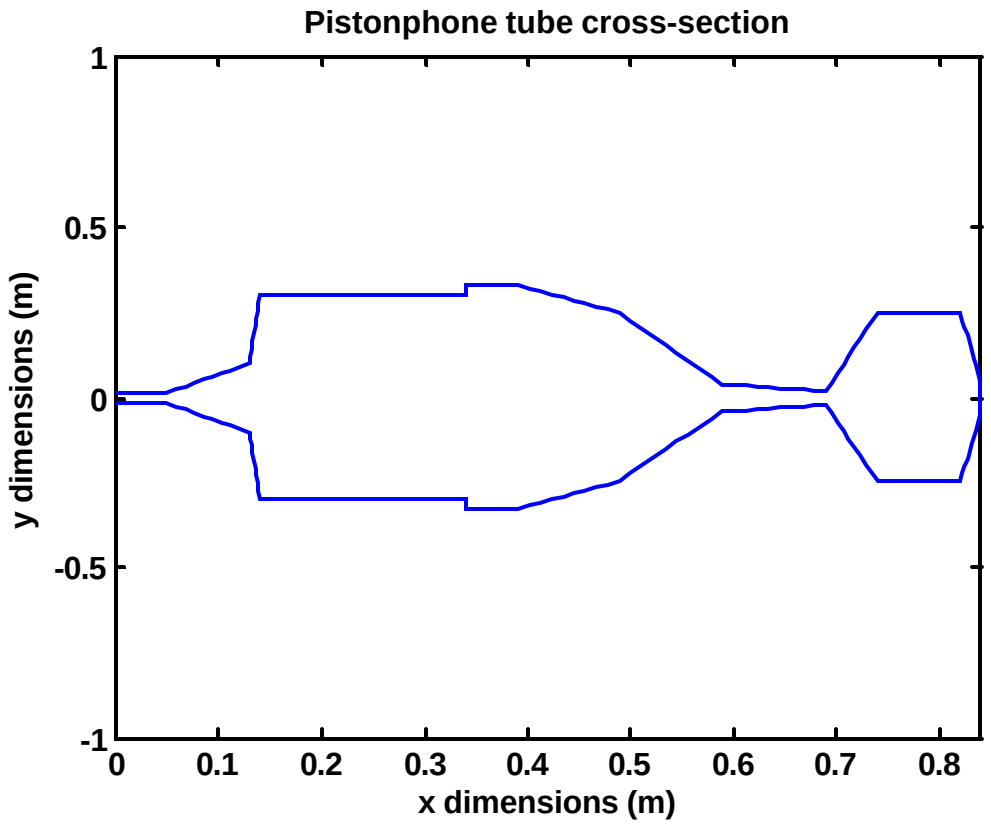

Figure **4-16**: A more complicated pistonphone cross section that can be modeled by the code. Turbulence losses from the sharp diameter transitions would not be predicted, and at velocities where these losses become significant the total system losses would be under-predicted.

In fact, the Tee-sections can be used like building-blocks to simulate the acoustics of much more complicated systems involving multiple acoustic pathways, external links, walls with finite compliance, and many other properties not considered here. Examples of using the Tee-sections to simulate the acoustics in more complicated duct networks, porous hoses, and infrasonic arrays are found in Appendix **C**.

Some extra matrix calculations are included to speed up the execution of the code, but essentially what occurs next is that Tee-sections are formed for every slice of every segment of the tube, at every frequency. At each frequency the calculated transfer matrices corresponding to the Tee-sections are multiplied together in the appropriate order (this is critical, especially in the case of cones), and the boundary conditions (U =

piston volume velocity at x = 0, and $U = 0$ at the x = end-cap) are used to solve for the complex pressure at the location of the microphone at the particular frequency. The complex pressure is evaluated at the microphone location at each frequency, and returned to the function caller as a complex vector of pressures.

4.6 Model vs. measurement comparisons

From the piston displacement and the multiple segment equivalent-circuit analogy for the pistonphone chamber currently in use, the response in Figure **4-17** is obtained. In the vicinity of 0.001 Hz the pressure response appears to converge to the isothermal limit. Above 1 Hz the pressure oscillations appear to converge to the adiabatic limit but this convergence is obscured by the increase in amplitude as the first resonance of the chamber is approached. A peak in the phase response of approximately 7 degrees occurs near 0.01 Hz; for cylindrical ducts this peak appears consistently near the frequency for which the hydraulic radius (hydraulic radius = area/perimeter = radius/2 for a circular cylinder) equals the thermal penetration depth.

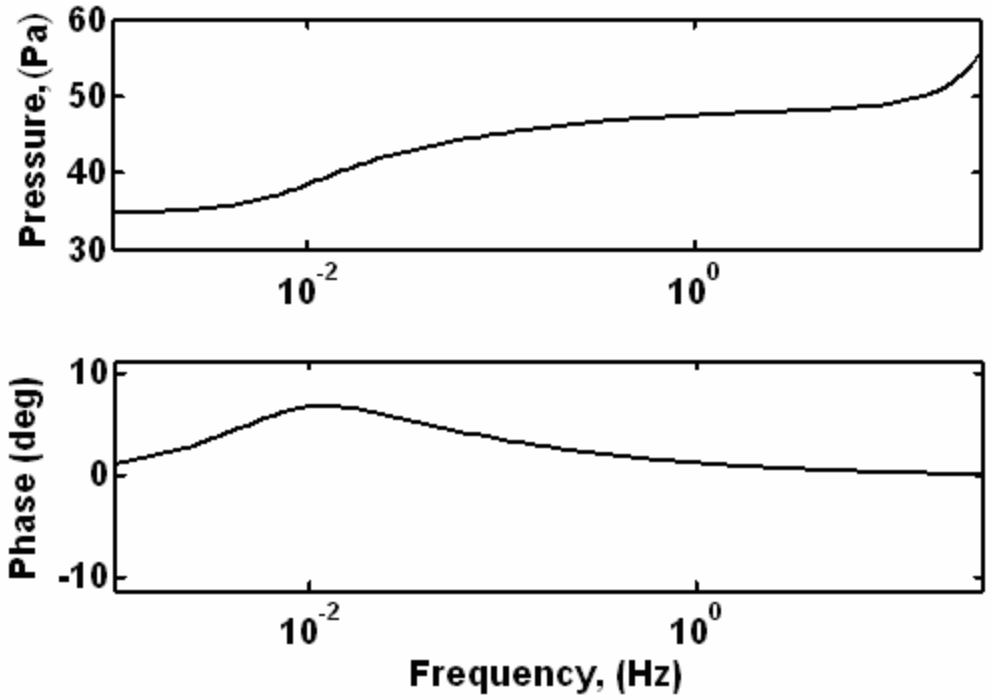

Figure **4-17**: Predicted pressure response in the pistonphone chamber at the location of the differential piezo-resistive pressure sensor, as predicted by the Tee-section model incorporating thermo-viscous effects. The phase is relative to the piston volume displacement.

The predicted pressure can be compared to the output of the differential pressure sensor that is vented to the control chamber. The absolute sensitivity of this differential pressure sensor is only known to within about 2%, but the comparison of the phase is unaffected by scaling errors introduced from the uncertainty in pressure sensor calibration. In Figure **4-18**, measurements of the pressure magnitude and phase inside the pistonphone are overlaid on the prediction. There are no free parameters in the model; all the required inputs are measured. The differential piezo-resistive pressure sensor (PZR) is calibrated using a separate plane-wave tube and a ¼'' B&K reference microphone. The response of the reference microphone at 250 Hz is checked with a standard B&K Model 4228 pistonphone.

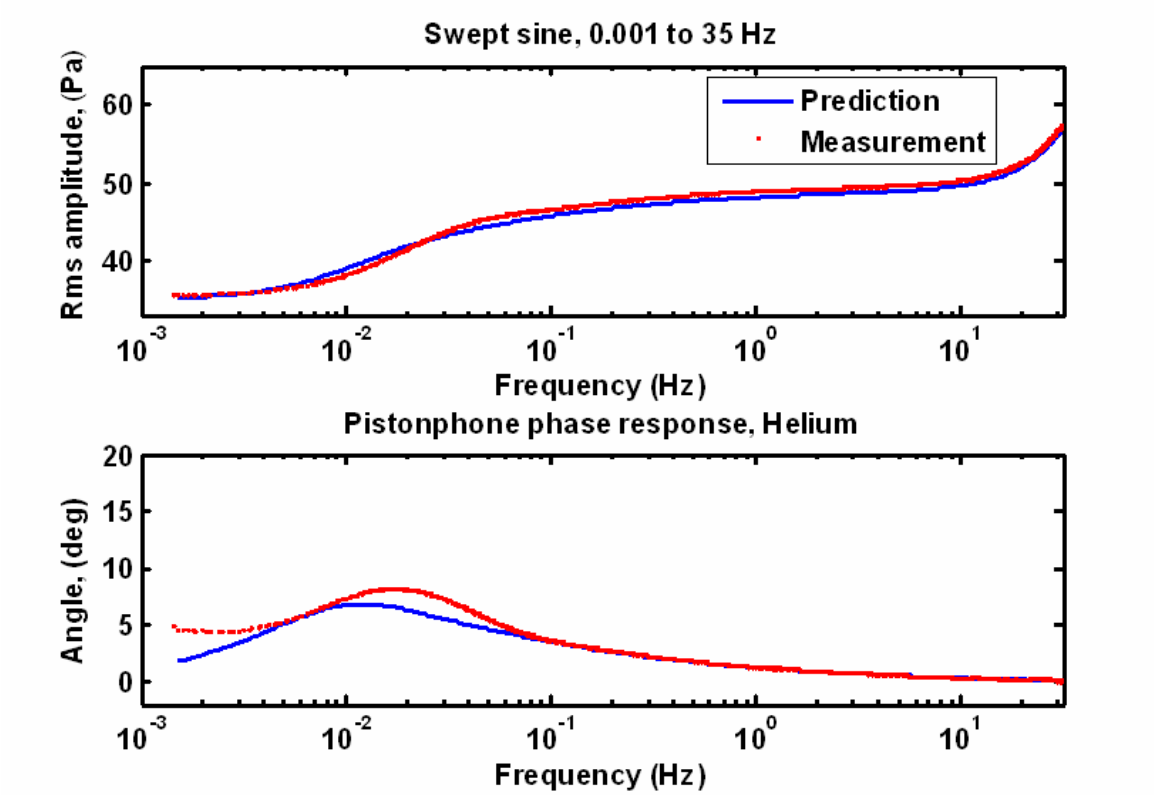

Figure **4-18**: Measurements of the chamber pressure overlaid on the prediction calculated by the model.

As can be seen in the plot above, the shape of the measured and theoretical curves do not match precisely. The large deviation in phase at the lowest frequencies is due to the presence of a slow leak in the chamber that is not included in the model, but can be corrected for. The deviation in magnitude and phase between 0.01 and 0.1 Hz will be examined. Figure **4-19** is a difference plot of the phase and the magnitudes:

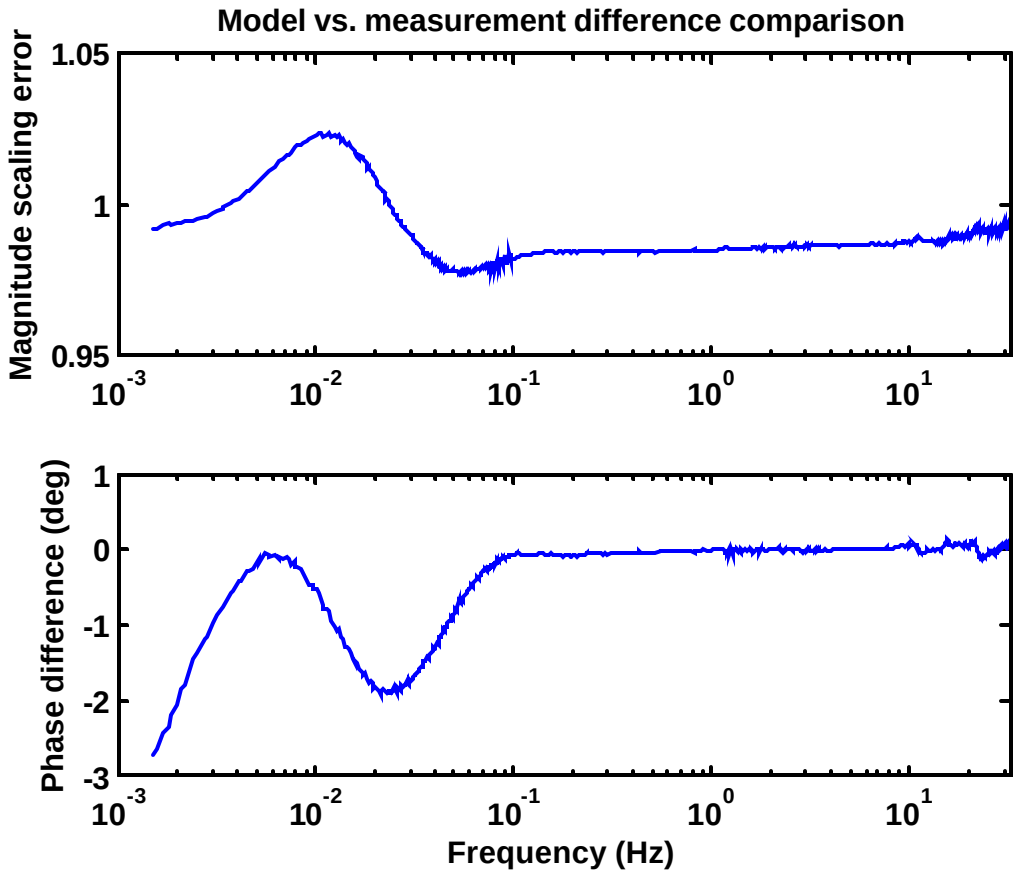

Figure **4-19**: Model vs. measurement, the upper graph is |model|/|measurement|, and the lower graph is the phase of the measurement subtracted from the phase of the model.

In the magnitude scaling error plot in the above figure, the deviations between the model and the measurement seem to peak around 0.01 Hz. The magnitude measurement remains within 5% of the prediction, and is significantly lower than the 30% error that would have occurred without adiabatic/isothermal correction. In Figure **4-20**, the difference plots are adjusted to correct for a small leak in the chamber.

To correct for the leak the chamber is over-pressurized by 1 PSI using a tank of compressed nitrogen. The time constant resulting from the slow leak is recorded. The acoustic compliance of the chamber is known, and using the relationship **t** = R*C a leak resistance can be calculated. The frequency response of the high-pass filter formed by the compliance and resistance is calculated, and this response divided from the measured pressure response of the pistonphone chamber.

The magnitudes of the measurements are scaled by 1.5% to bring the curves together in the 0.01 – 30 Hz region and give a better curve comparison.

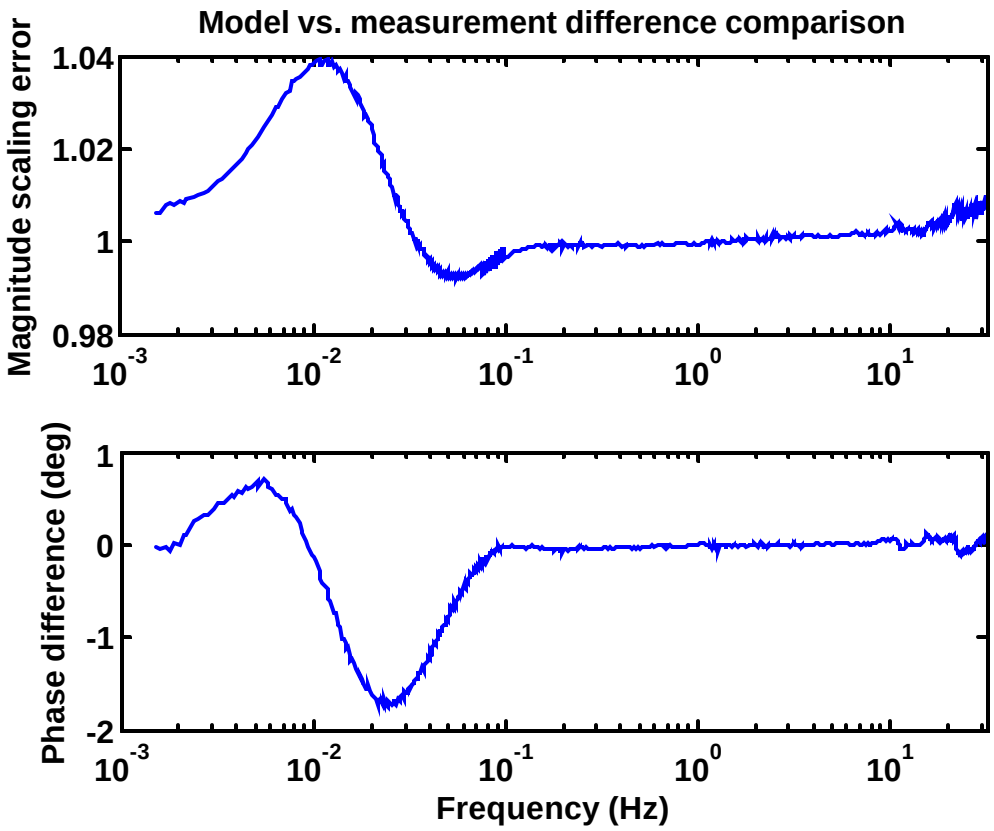

Figure **4-20**: Magnitude error scaled to see the maximum curve fitting error. From the graph it appears that the curve of the graph deviates by a maximum of nearly 4%. The phase plot has been corrected for a small leak in the chamber. The maximum phase error is nearly 2 degrees.

This measurement has been carried out many times, and the prediction deviation occurs in a consistent way every time. The size of the deviation varies, however. Figure **4-21** compares three different measurements completed at different times. As can be seen from the graph, the size of the deviation varies but the shape and location are consistent.

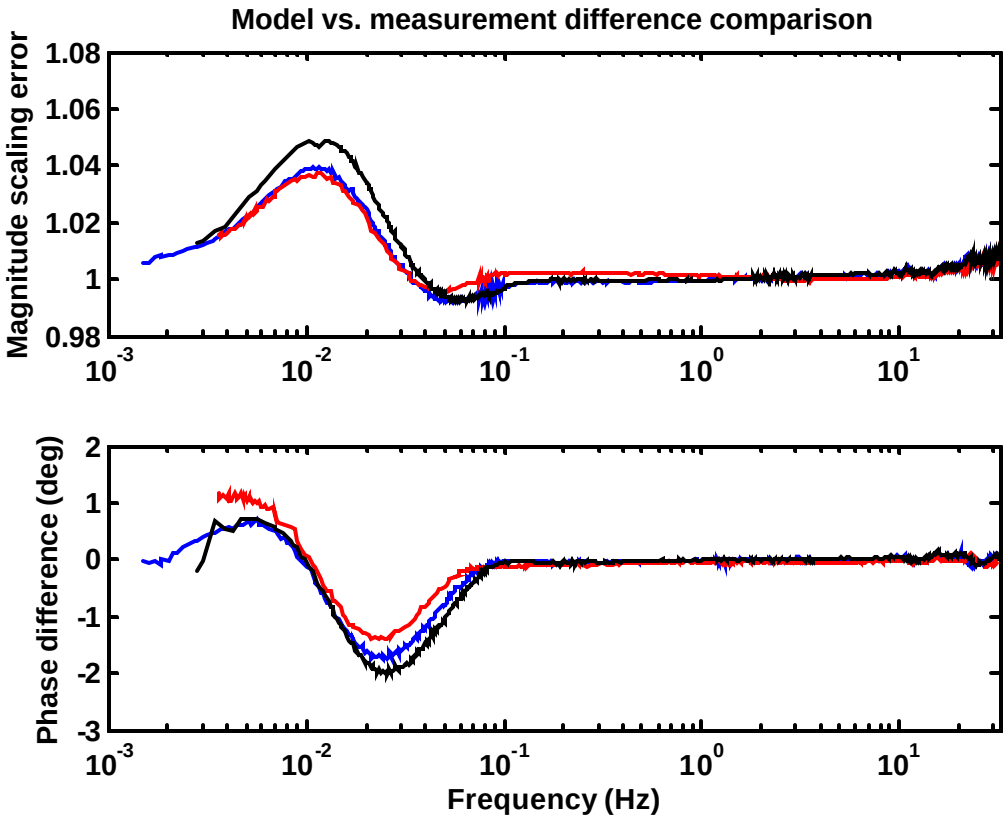

Figure **4-21**: Magnitude error and phase difference plots for three separate chamber pressure response measurements. The error magnitudes in the top plot are ratios, (prediction/measurement).

4.7 Error isolation

Although the pressure prediction model drastically increases the accuracy of the calibration over an adiabatic-only model, the consistency of the error that occurs at 0.01 Hz indicates that some repeatable aspect of the system is being neglected by the pistonphone model. If the source of error could be eliminated or incorporated into the model, calibration accuracy would increase. Many attempts were made to isolate the source of the error. Although all of them were unsuccessful, the results of some of them (particularly the use of Helium gas) were extremely informative. Furthermore, a list of

ideas that have already been tried is useful should anyone try to locate the source of error in future research.

The error could be coming from one of three sources: signal processing (if the data is being processed in an incorrect way), electrical (transducer responses may not be flat or may be being influenced by something that occurs at low frequencies), or mechanical/acoustical (the response measured with the transducers *is* the true pressure response of the chamber, and something such as gas, piston, or mechanical chamber properties is causing the response discrepancy).

4.7.1 Early measurement results

An early test of the pressure response of the tube did not show the kind of error that is now being measured every time the pistonphone is used. The following measurement was taken early spring of 2008:

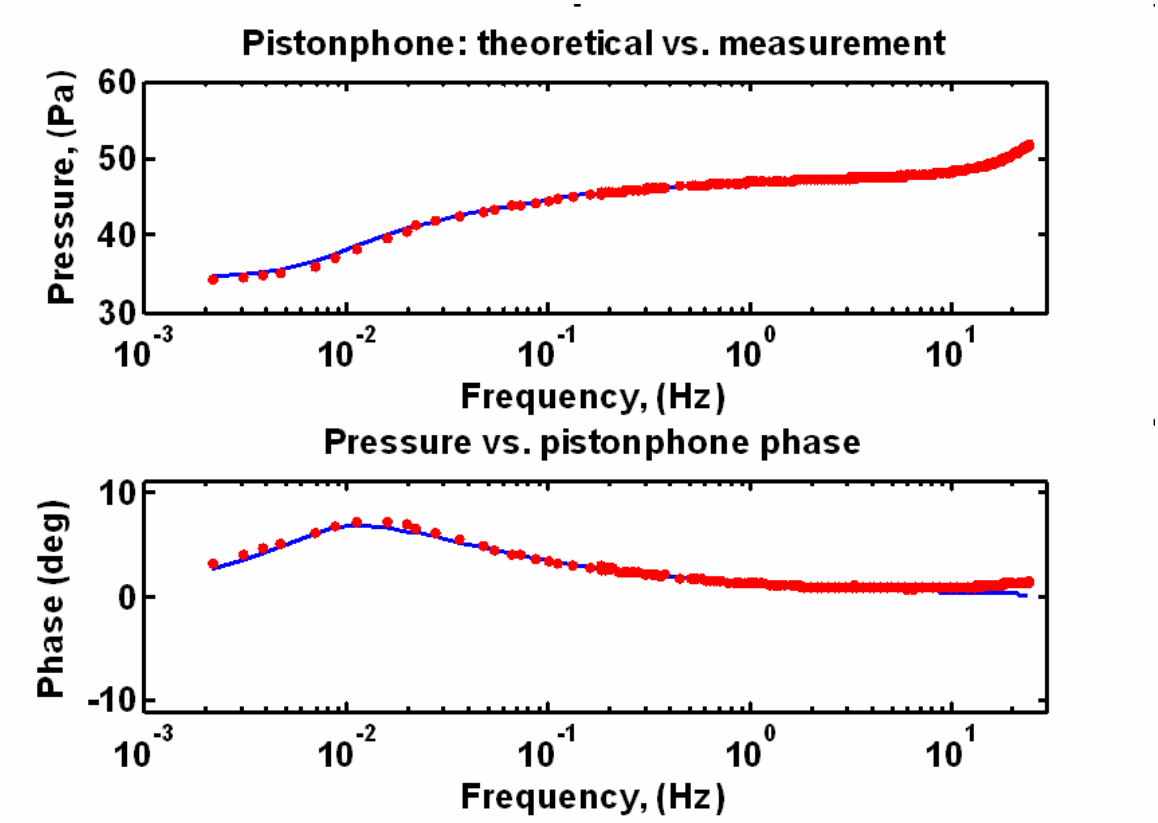

Figure **4-22**: Graph showing an early measurement for chamber pressure response.

The most significant thing about this graph is that it does not exhibit the same response deviations as the one consistently measured in the apparatus now. The measurement differed from the measurements being made now in the following ways:

1) The measurements below 0.1 Hz were made discretely, and not using a swept-sine source.
2) The signal processing used to evaluate the data was slightly different.
3) The LVDT was slightly different (though the circuitry and operating principle was the same).
4) The humidity level was lower.

Because the error that is so consistently present in current measurements appears to have been absent at the time of this measurement, one of these differences listed above could be the cause of the deviation. There could be other, unlisted changes, but temperature is not one of them. The temperatures of all the measurements are within a few degrees of 20 C.

4.7.2 Signal processing

Several tests are run to see if the signal processing methods used now are the cause of the deviation. The same measurement method used to make the graph in Figure **4-22** is used again to see if the results are error-free. The responses at a large number of frequencies between 0.001 and 0.25 Hz are measured by dialing particular frequencies on the motor and letting the piston pump at these frequencies for long periods of time. The following graph is the result of this experiment:

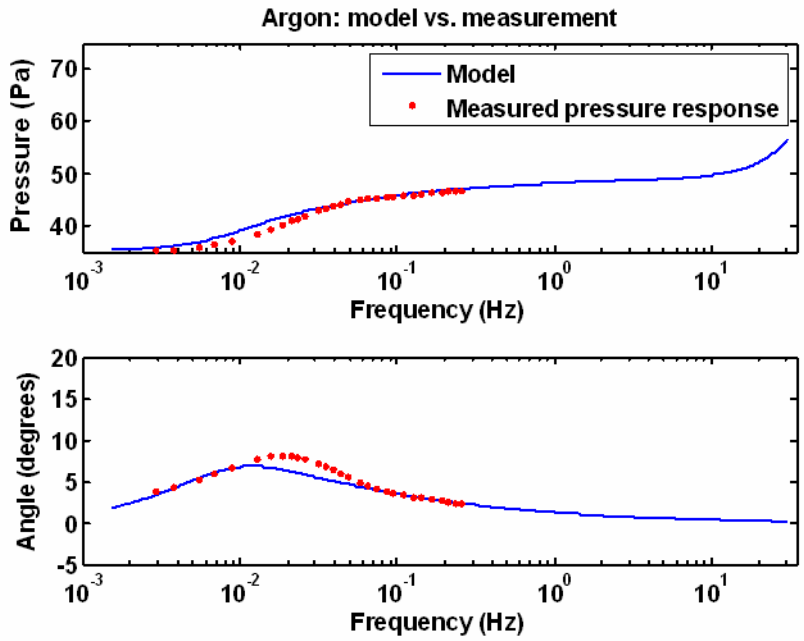

Figure **4-23**: Results of making pressure response measurements at a set of discrete frequencies between 0.001 and 0.25 Hz. The response still exhibits the deviations from the model that are seen using the swept-sine measurements.

A method for testing the HEBI data evaluation program is to synthesize a linear chirp that covers the entire spectrum of the pistonphone operational range and apply the frequency response of the pistonphone to the chirp. This modified chirp is written to a wave file which is then processed using the HEBI code. The following figure plots the model and the synthetically created pistonphone data:

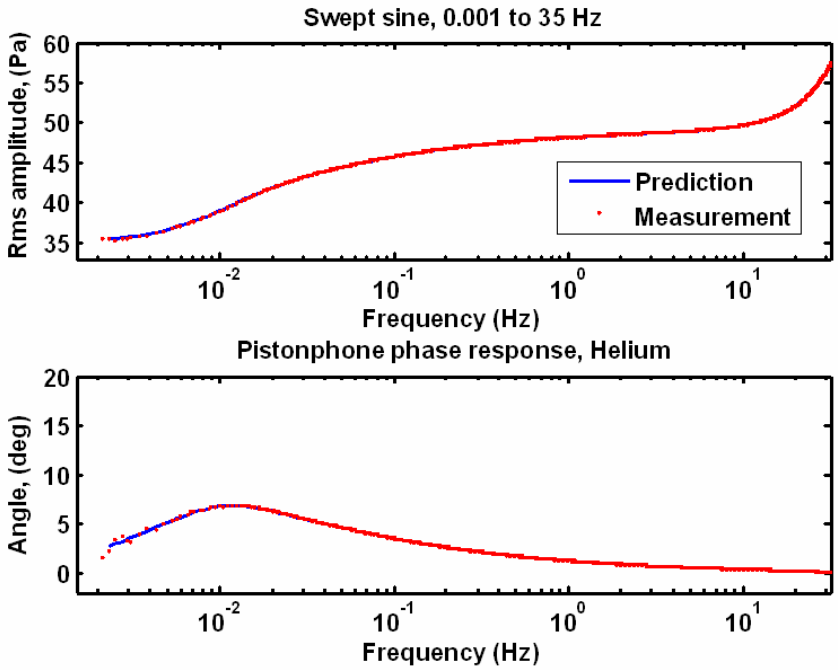

Figure **4-24**: Data synthesized in Matlab, with the response of the pistonphone applied to the signal and processed by the HEBI code, vs. the prediction. The results of this test indicate that the HEBI code is accurately processing the data.

The results of this test indicate that the signal processing is highly unlikely to be the source of error.

4.7.3 Electrical/Transduction error

Error can also be introduced into the measurements through the transduction process. If the piezo-resistive pressure sensors do not have a flat response, or the LVDT

does not have a flat displacement response with respect to frequency, the effects will be seen in the measurement of the pressure response. To test the flatness of the response of the transducers, swept-sine measurements of the pistonphone pressure response are made using multiple transducers to measure the same quantity.

To test the flatness of the LVDT displacement response at different frequencies, the displacement of the piston is measured using both the LVDT and the potentiometer system used in older models of the pistonphone design. The potentiometer displacement sensor is not fastened as securely to the piston head as the LVDT. Additionally, the output of the potentiometer is more nonlinear than the LVDT with respect to piston displacement and there are more ways for mechanical noise to affect the system. The reason for using the potentiometer as a reference is that the electrical systems used in the potentiometer and LVDT are completely de-coupled, and work on very different principles. If the deviation is caused by the LVDT circuitry it should not affect the potentiometer, and the response deviation should be resolvable when comparing the potentiometer and LVDT outputs.

Figure **4-25** is a comparison of the LVDT and potentiometer displacement responses between 0.01 and 0.3 Hz, exactly where the error is most prominent in the measurements. If the LVDT is the source of the error, the same phase response error occurring in the pressure measurements will show up in a phase difference plot between the LVDT and potentiometer measurements.

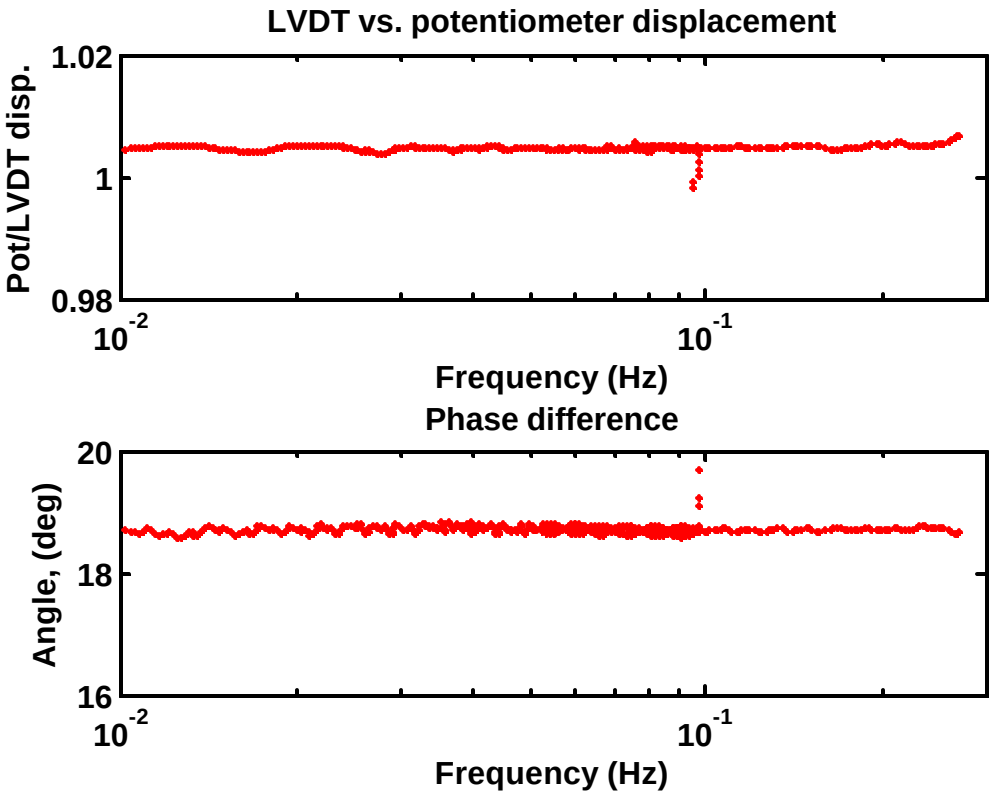

Figure **4-25**: Potentiometer/LVDT magnitude response plot, and phase difference plot.

From Figure **4-25** it is clear that the LVDT and potentiometer systems do not differ from each other in a way that would indicate that the LVDT is a source of the problem. For this reason, the LVDT circuitry is not suspect in causing the response measurement discrepancies. Piston-head and piston shaft connection faults have not been ruled out, however, because these are not measured by the LVDT or the potentiometer circuit.

The other major transducer being used to measure the pressure response of the tube is the 1 PSI piezo-resistive sensor that is mounted on the side of the chamber and vented to the control chamber. The possibility exists that this sensor may not have a flat response near 0.01 Hz, and this response error is being superimposed on the pressure measurements. It would be highly unlikely that the pressure transducer would coincidentally have a response error lying precisely at the same location as the adiabatic-

isothermal transition of the gas in the pistonphone chamber; however, it should be checked. To test for response error a second transducer is used to make a simultaneous measurement of the pressure inside the chamber. The sensitive PZR that is normally used is a "PX70" differential 1 PSI[9] transducer sold by Omega. The extra transducer used simultaneously is a 15 PSI Endevco piezo-resistive pressure sensor, vented externally to the laboratory. The low sensitivity implies that the measurement made by the Endevco is noisier than the measurement made by the PX70. A trend is still visible in the measurement made by the Endevco sensor, however. Figure **4-26** overlays plots of the phase response as recorded by both pressure transducers:

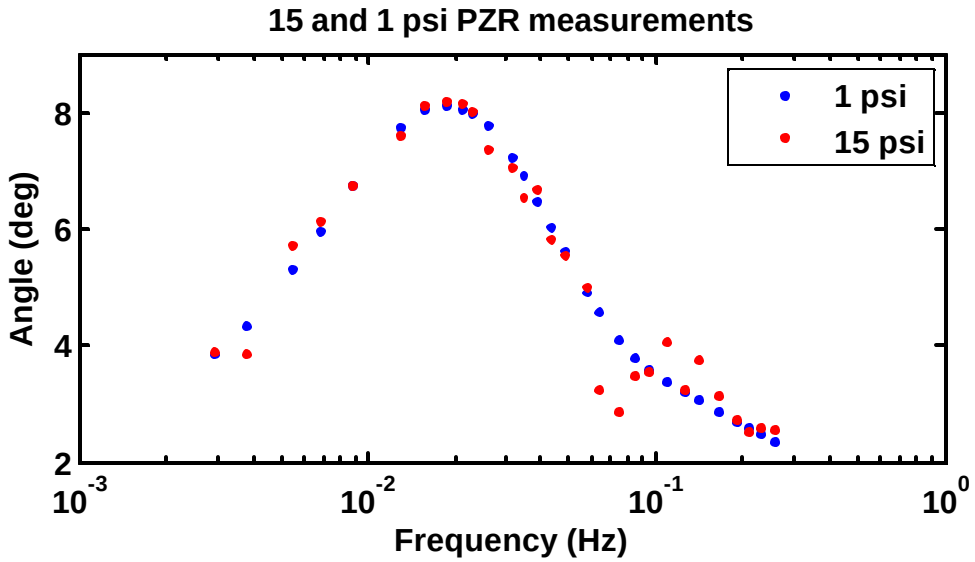

Figure **4-26**: Phase response of the pistonphone chamber as measured by two different transducers. Except for an excess of noise in the measurement made by the 15 PSI Endevco sensor, the results nearly match.

The measurements indicate that the shapes of the responses of the two sensors are nearly identical over the measurement frequency range, and both measure the deviation. This would imply that the frequency response of the PX70 is not the source of error.

[9] The sensor is marketed as a "0.8 PSI" sensor, but this value is rounded to 1 in this thesis, when the sensor is referenced.

4.7.4 Acoustical/Mechanical modeling error

If the frequency responses of the displacement and pressure transducers are correct, and if the signal processing code is returning the true response results, then the likeliest possibility is that the observed discrepancy between the measured pressure and the modeled pressure actually exists. This would indicate that something about the system is not being modeled accurately. Several possible causes for the discrepancy are hypothesized.

4.7.5 Humidity

The first hypothesis is that humidity is the cause of the error. This hypothesis stems from the fact that the one measurement that does *not* exhibit the discrepancy (Figure **4-22**) was made when the relative humidity of the room was much lower than it is now. The effects of humidity on the adiabatic-to-isothermal transition are unknown, as are the effects of moisture in the wall cavities. To isolate humidity as the problem, two tests are conducted.

The first test is to lower the humidity of the pistonphone chamber, and observe the effect on the size of the deviation. To do this, the air in the pistonphone chamber is evacuated, and replaced with nitrogen. The diaphragm of the differential sensor is relatively fragile (it will rupture if it is subject to a differential pressure equal to atmospheric pressure); therefore, the control chamber must be evacuated and replenished simultaneously with the pistonphone main chamber so as not to put a large pressure differential across the transducer. To do this a network of tubes and valves was added to the system. A diagram of the new setup is shown in Figure **4-27**:

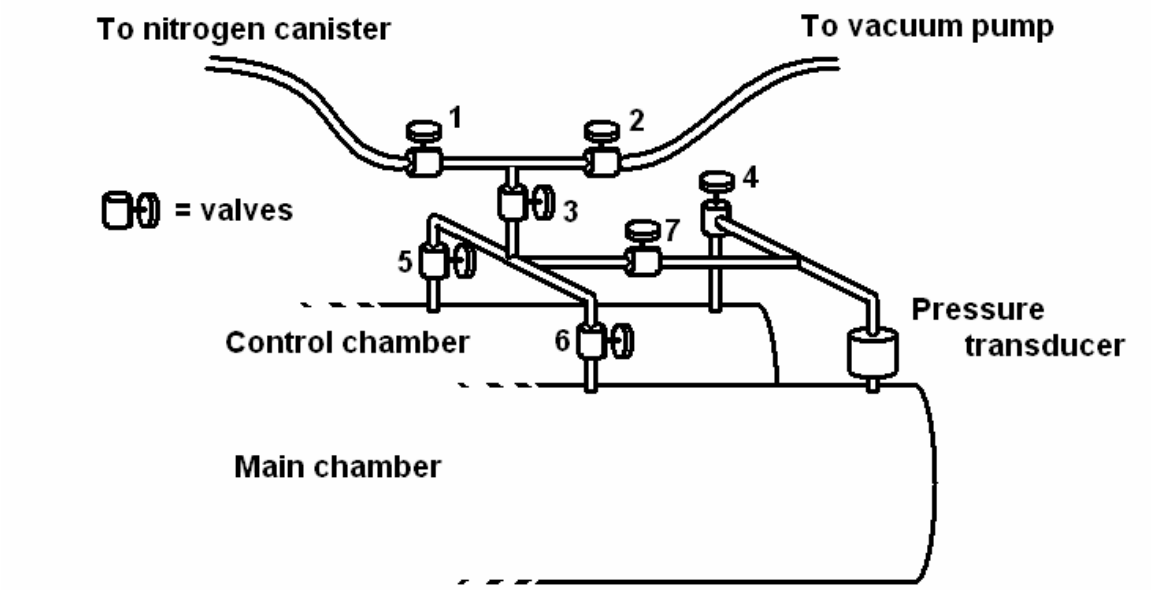

Figure **4-27**: The pistonphone chamber and control chamber valved to allow for evacuating the chambers and refilling them with another gas.

. To evacuate the chamber, the brass hinge connecting the piston shaft to the wheel must be loosened, and the collar around the shaft tightened. Placing the system under vacuum will suck the shaft inward, so that the collar is forced against the LVDT mount. In the setup shown in Figure **4-27** the evacuation and replenishing process is controlled by a system of valves, (labeled 1 – 6 in the figure). To prevent irreparable damage to the transducer, care must be taken when choosing the opening and closing order of the valves. Valves 2, 3, 4, 5, and 6 must all be open. Valve 1 is closed because it is attached to the nitrogen canister. Valve 7 is closed because the pressure differential across the transducer can exceed the transducer tolerance while the tanks are filling if it is open. During the evacuation process, the pressure inside the main chamber is checked via a gauge fixed to the vacuum pump. Once the chambers have been evacuated, valve 3 is closed. The vacuum pump is turned off and the vent on the pump is opened to re-pressurize the hose attached to the vacuum pump up to valves 1 and 3.

To refill the chambers, the regulator of the nitrogen tank is set to 5 PSI. The output pressure is set this low to prevent damage to the pistonphone if the chamber is accidentally over-filled. Valve 1 is then opened, while valve 3 remains closed. Nitrogen

is allowed to flow through the hose and out the vacuum pump vent, to prevent any gas impurities that may be contained in the section of hose between valve 1 and the nitrogen chamber from re-entering the chambers. After a few seconds, valve 2 is closed, preventing Nitrogen from escaping to the atmosphere. Valve 3 is then gradually opened. Fully opening valve 3 while the nitrogen tank is hooked up to the system can cause the two chambers to fill at different speeds, risking damage to the differential pressure sensor. To prevent damage, valve 3 is opened very slowly and the differential pressure sensor output is monitored on an oscilloscope screen to make sure that the transducer output is not saturating.

It is hypothesized that if the system is flushed by evacuating the chamber several times, and the chamber is left under vacuum for an hour, that a significant amount of the water absorbed into the walls of the chamber can be extracted. Replenishing the system with pure nitrogen lowers the humidity levels equal to or below the level they were at when the measurement of Figure **4-22** was made.

Using this process, the measurement shown in Figure **4-28** is made:

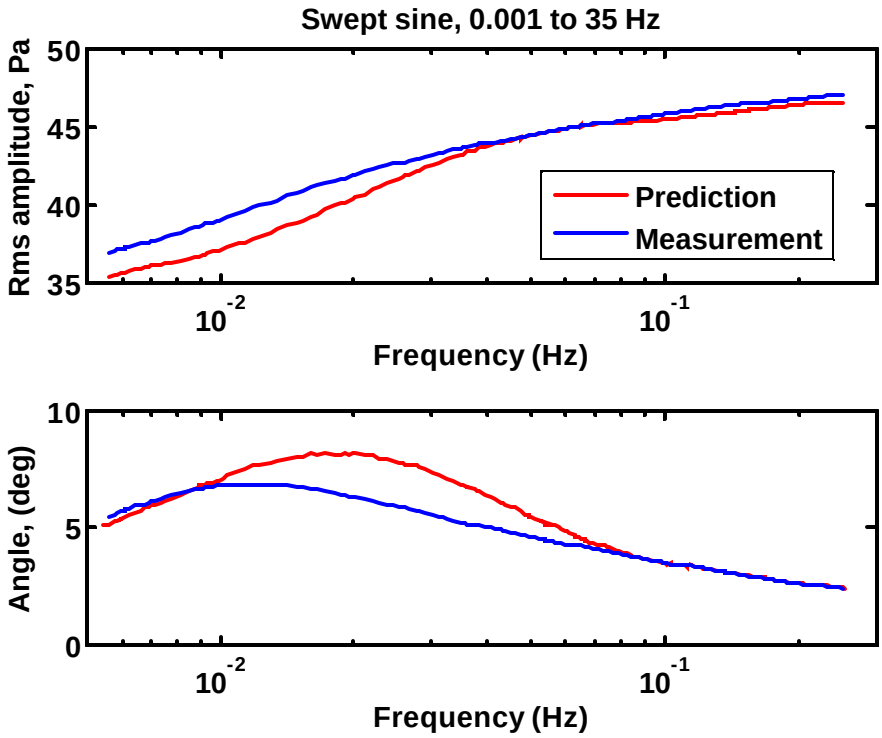

Figure **4-28**: The pressure magnitude response of the pistonphone chamber when filled with pure nitrogen.

An examination of the scaling error and phase difference between the model and the measurement reveals that filling the chamber with Ultra High Purity (UHP) Nitrogen has no effect on the transition, when compared to standard air.

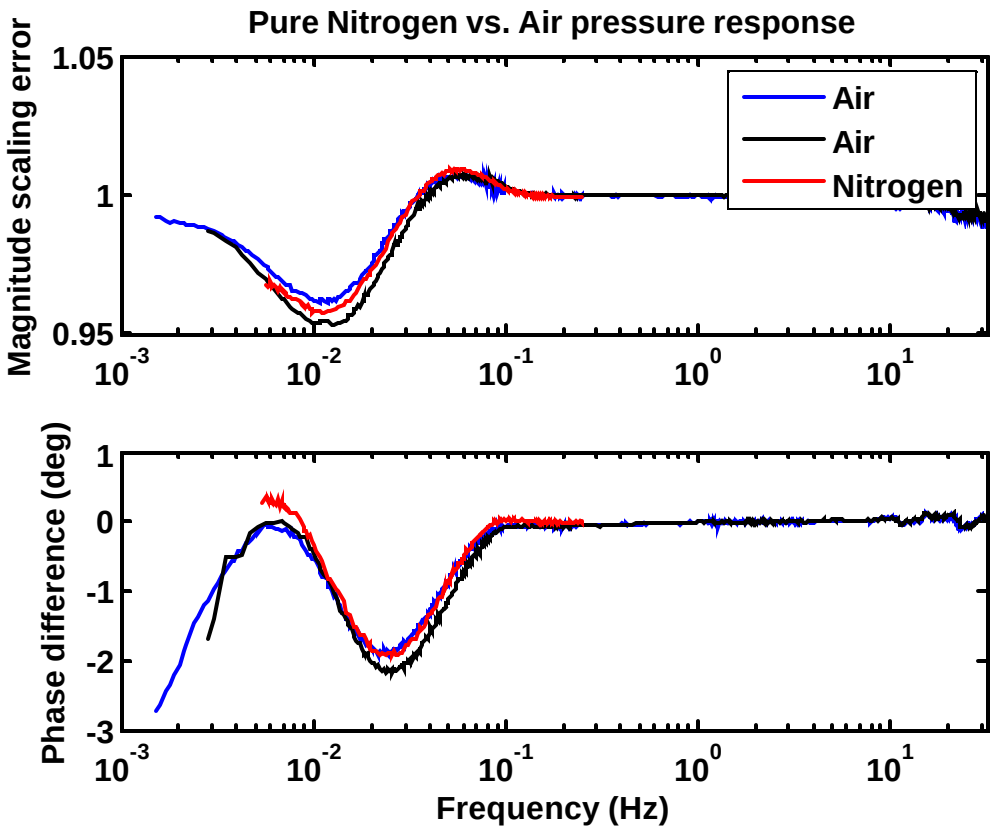

Figure **4-29**: The scaling error and phase difference between the measurement and model for two measurements using normal air (humidity ~55%) and pure nitrogen.

The conclusion to be drawn from this experiment is that reducing the humidity in the chamber appears to have no effect on the measurement discrepancy.

4.7.6 Molecular relaxation

The addition of the valves to the pistonphone apparatus makes inserting other gases into the pistonphone chamber simple. Replacing the gas in the tube with pure nitrogen appeared to have no effect on the shape of the transition. It is hypothesized that replacing nitrogen (which has properties virtually identical to air) with argon or helium will eliminate some aspects common to both nitrogen and air as a source of error. Argon and helium are both monatomic gases, and if the deviation in the adiabatic-to-isothermal

transition is influenced by some diatomic property of nitrogen then the problem will disappear when either helium or argon is used. Furthermore, because the thermal penetration depths differ for the different gases, the transitions occur at different frequencies. If the discrepancy occurs at the same frequency, even if the transition is moved, then it can be disassociated with the thermo-viscous model and attributed to some other modeling deficiency.

4.7.7 Helium

The first gas used is helium. The density of helium at standard temperature and pressure is 0.178 kg/m^3 (compared to 1.23 kg/m^3 for air), the thermal conductivity is 0.14 W/(m*K), (compared to 0.026 W/(m*K) for air), and the specific heat capacity is 5230 J/(kg*K) (compared to 1010 J/(kg*K) for air). The thermal penetration depth is defined as:

$$d_k = \sqrt{\frac{k}{wrc_p}}$$

At the same frequency the thermal penetration depth in helium is about 3.4 times that in air. For constant chamber diameter, the adiabatic-isothermal transition will occur at higher frequency in helium.

Two other properties of helium will drastically alter the pressure response curve from that of air. The sound-speed of helium is much higher than air (955 m/s vs. 341 m/s), which means that the first resonance of the tube will be pushed to a higher frequency. This means that near 30 Hz the effects of the first resonance will be greatly reduced when helium is used.

The other property that will drastically alter the shape of the pressure response curve is the ratio of specific heats. The ratio of specific heats in air is approximately 1.4, however, in helium it is 1.667. For isothermal compression, the pressure generated by the piston will be equal in air and helium, as the pressure/volume relationship reduces to Boyle's law for both gases. However, for adiabatic compression, the pressure produced in

the pistonphone chamber will be higher than in air for the same piston displacement. The pistonphone model is modified to account for the properties of Helium, and Figure **4-30** plots the predicted pressure responses of the calibration chamber for both gases:

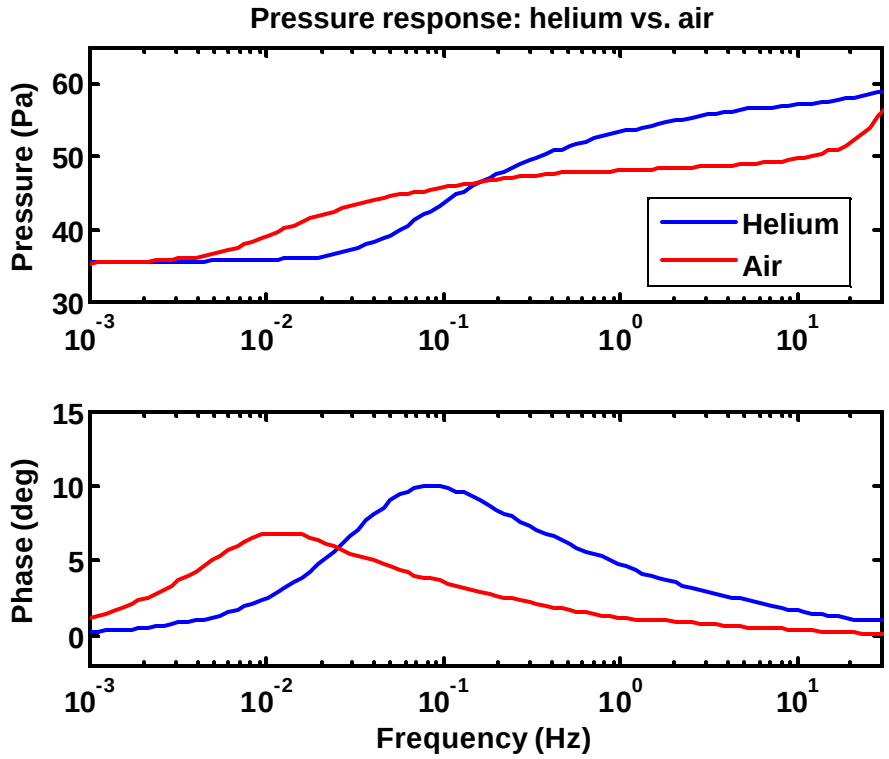

Figure **4-30**: Comparison of the pressure response of the chamber, helium vs. air.

Using the same procedure for evacuating the chamber and filling with nitrogen, the chamber is evacuated and filled with helium. From previous experiments it has already been discovered that the pistonphone chamber is not perfectly airtight. The leak rate is even higher with helium. Using the same leak correction techniques described previously for the UHP nitrogen example, the results in Figure **4-31** are obtained:

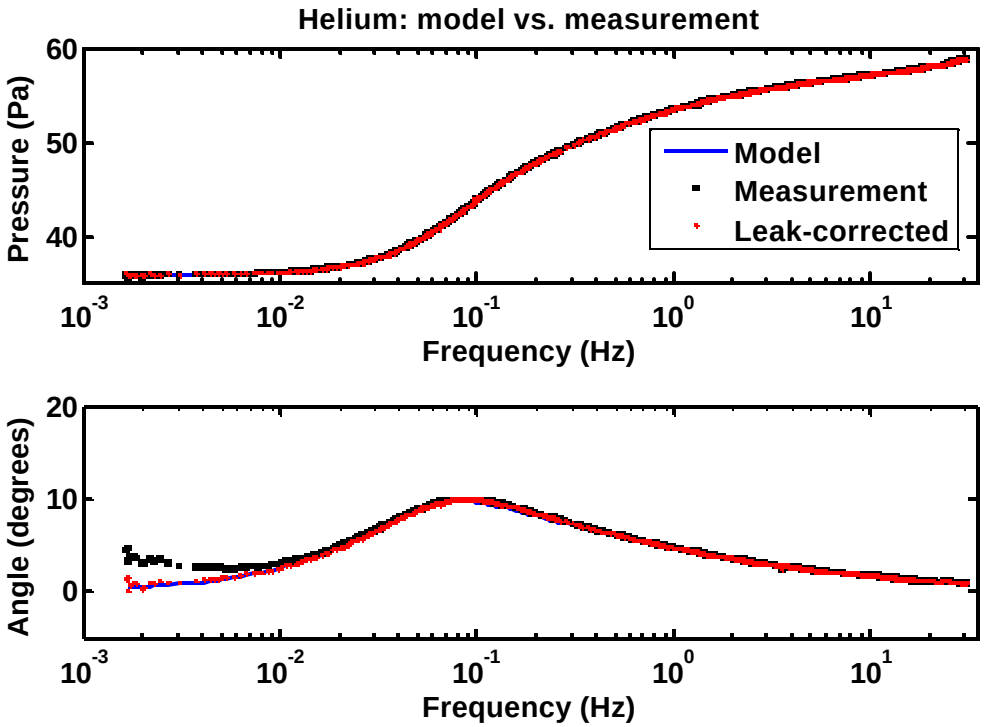

Figure **4-31**: Comparison of the model updated for helium properties, vs. an actual measurement in which the chamber was filled with helium.

The helium measurement and model display extremely good agreement – considerably better than any of the results in air. Figure **4-32** shows the difference between the helium measurement and model, and compares it to the difference plots obtained from measurements made in air:

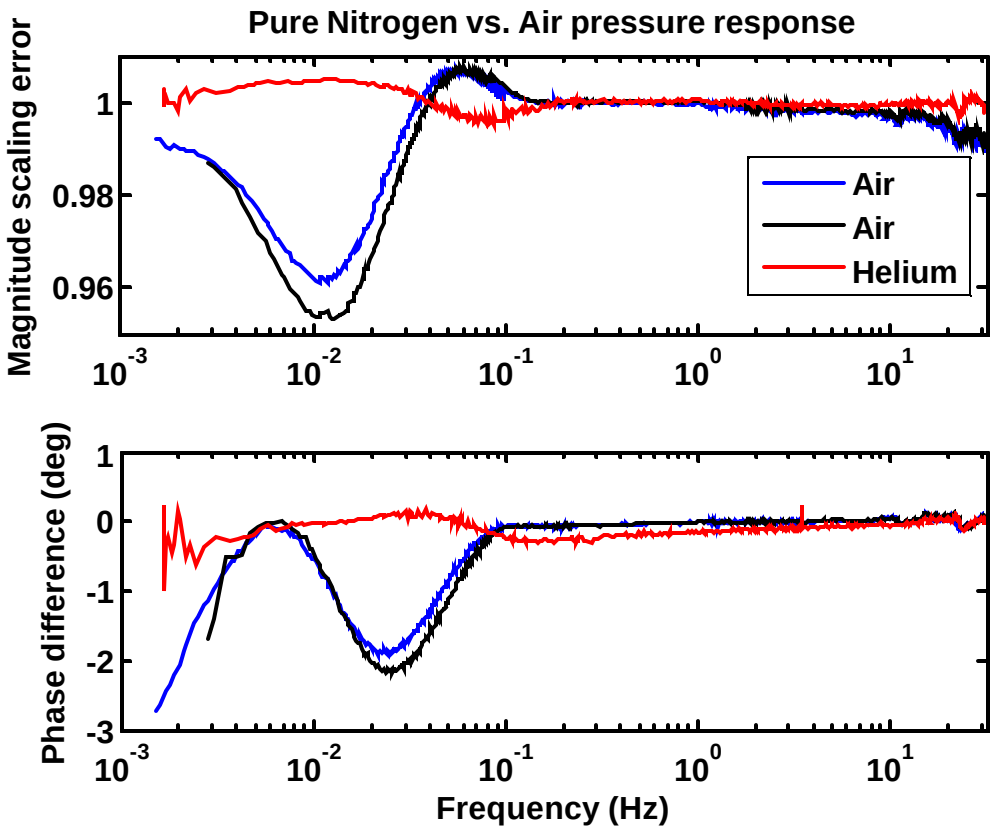

Figure **4-32**: Helium measurement error vs. air measurement error. The peak error in magnitude is around 0.005%.

Because of the small leaks in the pistonphone chamber, and the inability to perfectly evacuate all the gas in the chamber prior to refilling, the gas inside the chamber is not pure helium. The magnitude plots still correspond extremely well with the model, and the error peaks near 0.005%. This is roughly ten times better than the peak error in the magnitude plots for measurements made in air. Oddly, the error that does exist seems to have a similar but reversed shape to the error that occurs in air graphs.

Several new hypotheses for the cause of the discrepancy in air arise from the completion of the helium experiment. The error that exists in the air measurements might be a result of using a diatomic gas, a gas with a smaller thermal penetration depth, or a gas that has a different ratio of specific heats. To explore the discrepancy further, argon, another monatomic gas is used.

4.7.8 Argon

Argon has a thermal penetration depth approximately 0.9 times that of air. This places the transition region in the vicinity of the transition for air; however, the ratio of specific heats is the same as helium and argon is monatomic. Figure **4-33** is a model of the pressure response of the pistonphone chamber, modified to match the properties of argon:

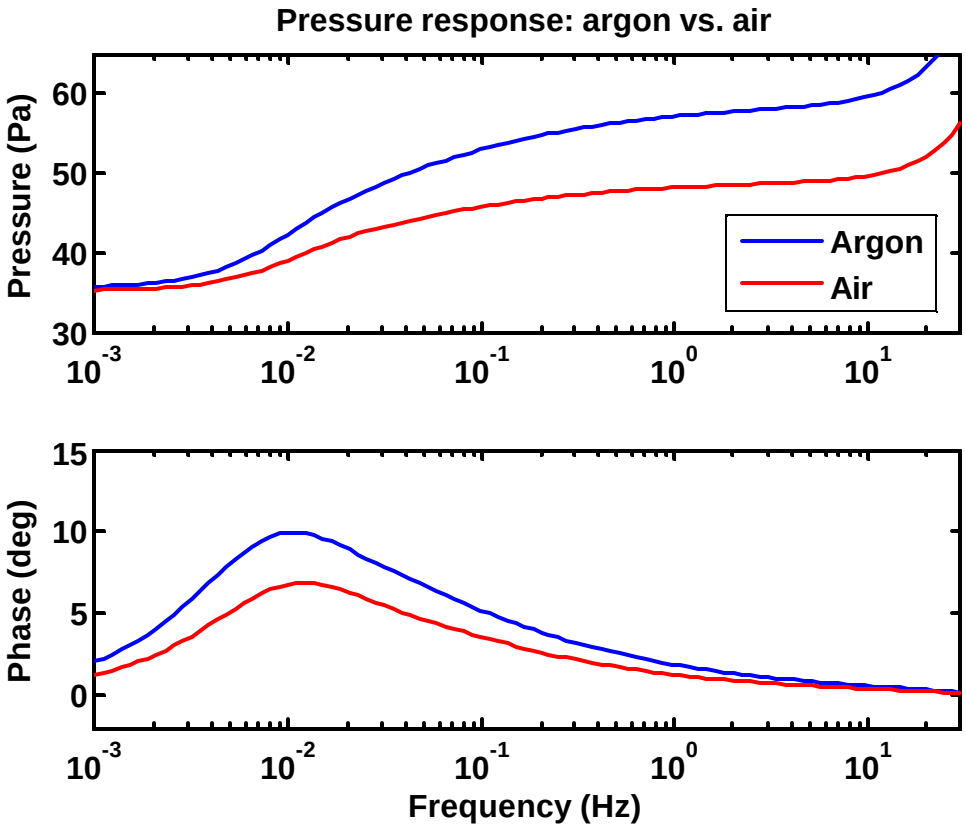

Figure **4-33**: Pressure response of the chamber, air vs. in argon. The adiabatic-to-isothermal transition occurs at nearly the same frequency as in air, but the gas is monatomic and the ratio of specific heats is greater.

The pistonphone is once again over pressurized, so that the leak time-constant may be measured and the effects on the pressure response divided out of the spectrum. Figure **4-34** shows the modeled pressure response, the raw measurement, and the leak-corrected measurement:

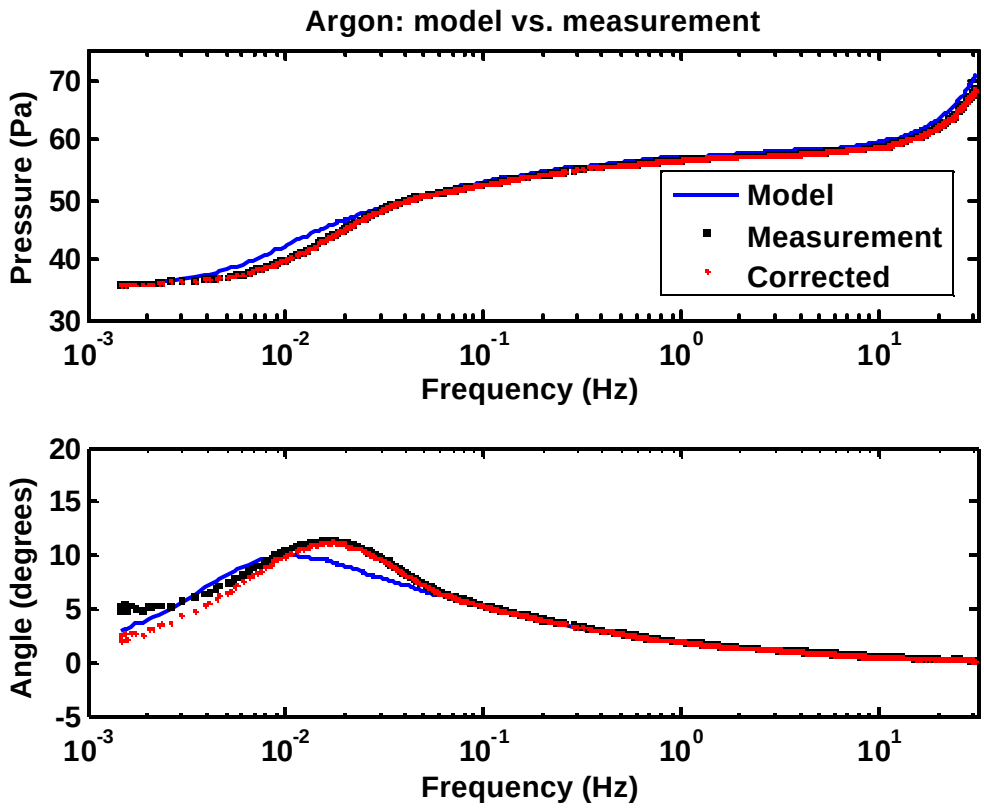

Figure **4-34**: Measured pressure response for the pistonphone chamber when filled with argon, compared to the model adjusted for the properties of argon

The effects of the discrepancy have returned. The fact that Argon is a monatomic gas with a different ratio of specific heats than air implies that neither of these properties contribute significantly to the deviation. Figure **4-35** compares the model-versus-measurement difference plot for argon with the model-versus-measurement difference plots made for air:

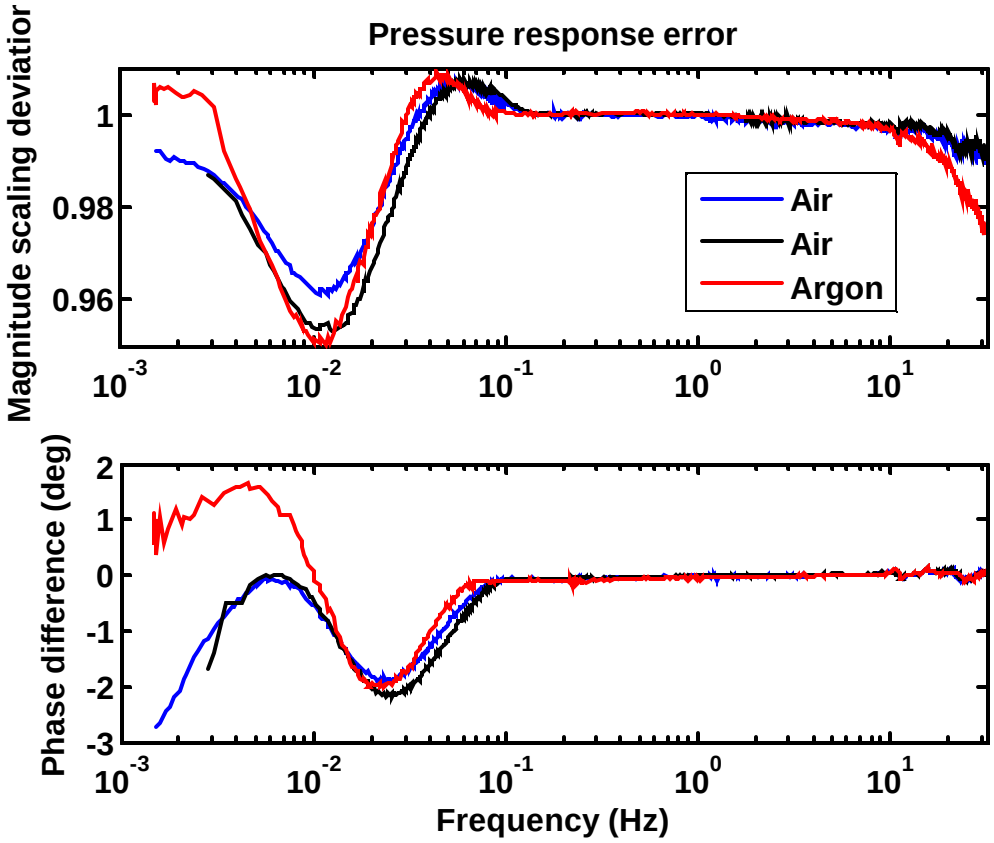

Figure **4-35**: Measurement-versus-model deviation plots for argon and air measurements.

The model-versus-measurement deviation found in argon has a very similar shape to the deviation in air, with the exception that the deviation in the argon measurement seems to have been shifted slightly lower in frequency, and increased in magnitude.

From the experiments with monatomic gases it is found that the discrepancy occurs in both monatomic (argon) and diatomic (nitrogen) gases. Shifting the transition region higher in frequency, however, seems to eliminate the deviation, as can be seen from the helium measurement.

4.7.9 Finite Wall Thickness

Another hypothesis is that the finite thickness of the wall material influencing the pressure response in the tube. If this is true, one might expect to see more consistency in

the magnitude and phase of the measured phase discrepancy, because the wall material and thickness is unchanging. However, the hypothesis ought to be considered.

One way of examining the problem is from the perspective of thermal penetration depth. A treatment of thermal penetration depth in the wall itself is given in **3.5.2**, and it is found that the thermal penetration depth remains smaller than the thickness of the pipe walls for all frequencies of pistonphone operation. The effects of finite thickness on the pressure response can also be calculated using the heat equation. A calculation for the effects of finite wall thickness has been done by the author, and is based on the calculation for finite thickness effects in parallel plates that can be found in Swift [**20**] and can be found in Appendix **H**. The following two equations describe the temperature profile in the wall of the chamber, and the gas inside the chamber:

$$T_s = T_{b1}\frac{K_1(Mr_o)I_0(Mr)+I_1(Mr_o)K_0(Mr)}{K_1(Mr_o)I_0(Mr_i)+I_1(Mr_o)K_0(Mr_i)} \qquad \textbf{4.1}$$

$$T = \frac{bT_m p_{acs}}{(e_s-1)}\frac{I_0(Mr)}{I_0(Mr_i)r_m C_p}+\frac{bT_m p_{acs}}{r_m C_p} \qquad \textbf{4.2}$$

T_{b1} in Eq. **4.1** is the temperature at the gas/solid boundary, which can be calculated using Eq. **4.2**. The e_s term is a correction factor that is used to modify the lumped element impedances based on the available heat capacity of the wall, and is equal to:

$$e_s = \left(\frac{\frac{\sqrt{krC_p}}{\sqrt{k_s r_s C_{ps}}}\frac{I_1(Mr_i)}{I_0(Mr_i)}}{\frac{K_1(Mr_o)I_1(Mr_i)+I_1(Mr_o)K_1(Mr_i)}{K_1(Mr_o)I_0(Mr_i)+I_1(Mr_o)K_0(Mr_i)}}\right) \qquad \textbf{4.3}$$

Eq. **4.2** can be used to plot the temperature profile through the gas and the wall as a function of frequency. Figures **4-36** through **4-38** show the temperature profile of the pistonphone chamber using the solution derived above, for 0.001 Hz, when the

oscillations are nearly isothermal, 0.01 Hz, where the transition is taking place, and 0.1 Hz where the pressure oscillations are beginning to appear adiabatic. The temperature oscillations in the graphs are the oscillating temperature magnitudes in degrees Celsius. The phase of the oscillations is not shown.

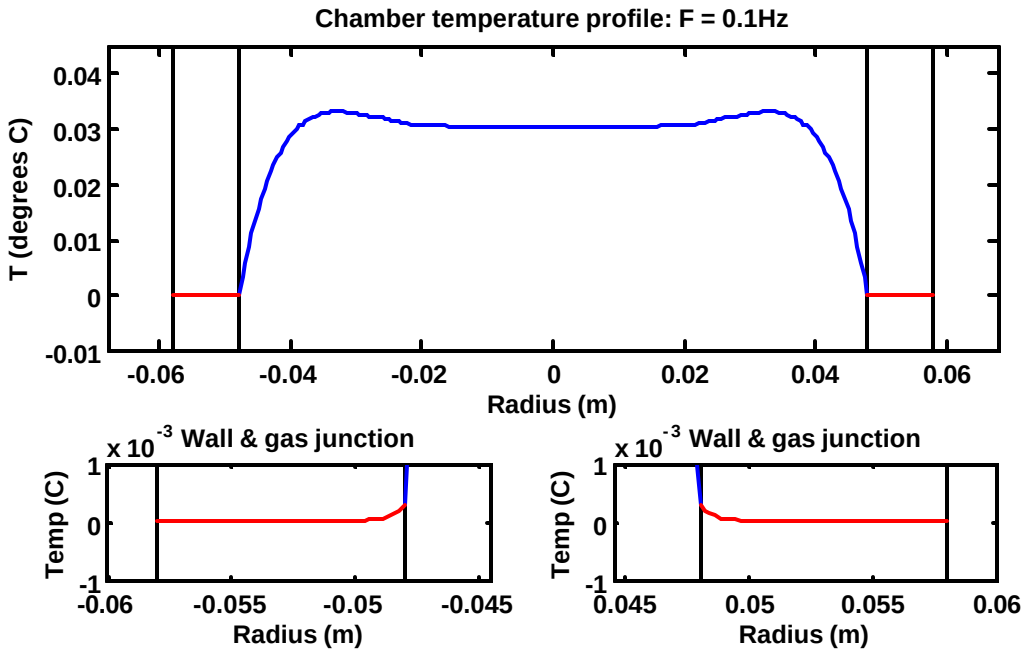

Figure **4-36**: Temperature oscillation magnitude for a 0.1 Hz, 50 pascal acoustic signal in a cylindrical duct with the Pistonphone's dimensions. The temperature in the center of the duct is largely un-affected by the temperature of the walls

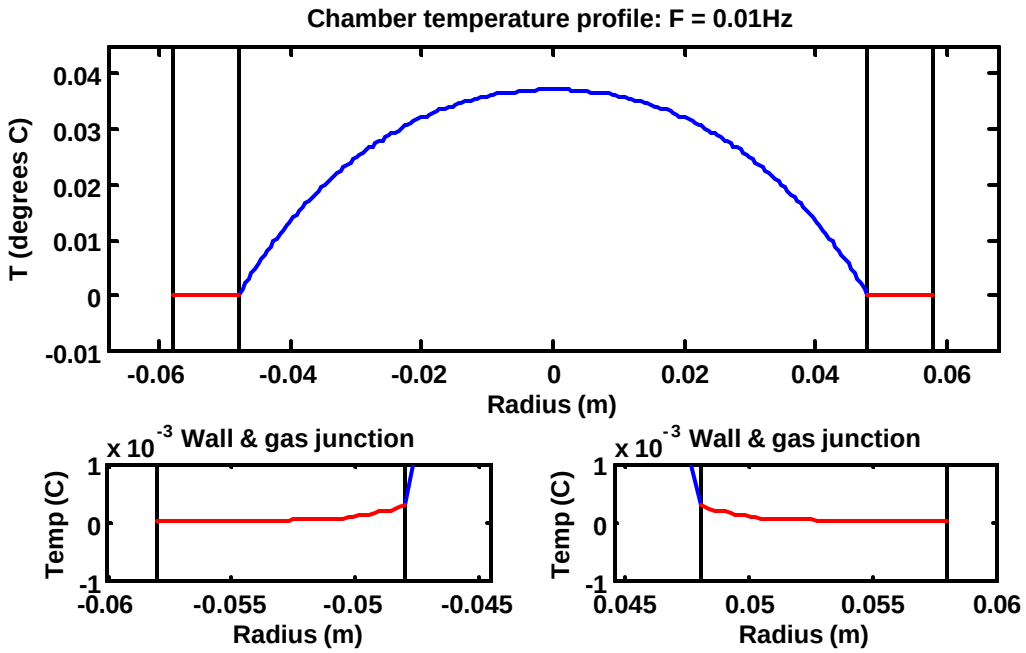

Figure **4-37**: Temperature profile at 0.01 Hz. The wall is affecting the entire thermal profile.

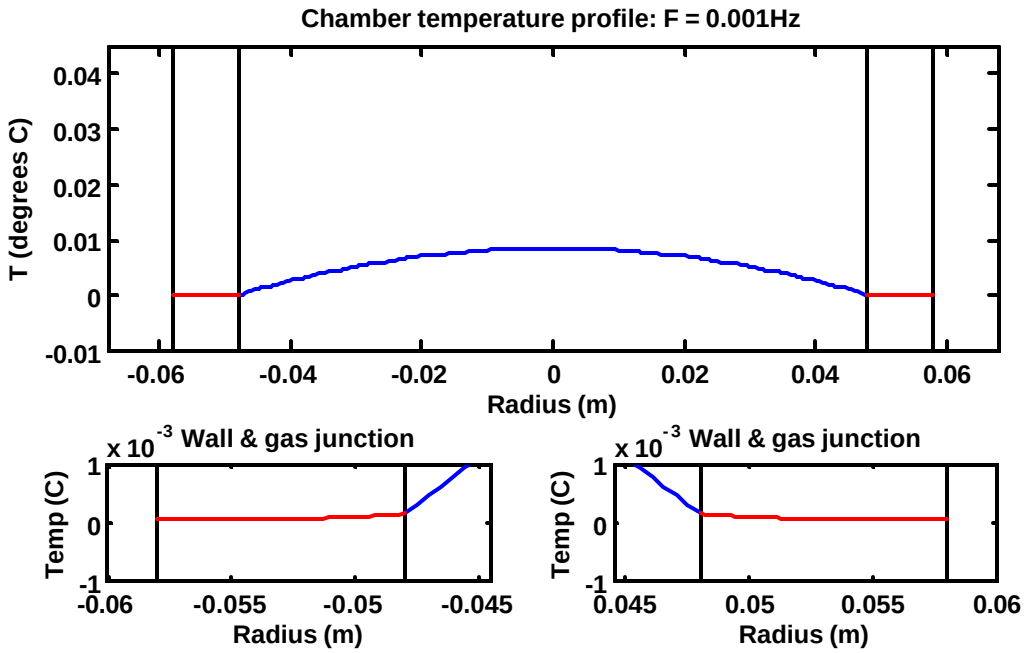

Figure **4-38**: Temperature profile at 0.001 Hz. The pressure oscillations are nearly isothermal, and the temperature profile is largely determined by the temperature of the wall.

The curves of the temperature profiles agree well with the parallel plate version, which has already calculated in [**20**]. Figure **4-39** is an example of a thermal profile calculation for a 0.1 Hz signal between parallel plates. The same assumptions applied to the calculation above (i.e. no thermal gradient, velocity is negligibly small, the plates are insulated on the outside) are used in the calculations for the profile plot in the figure. The temperature profiles in both the gas and the wall are very similar to the cylindrical tube calculation.

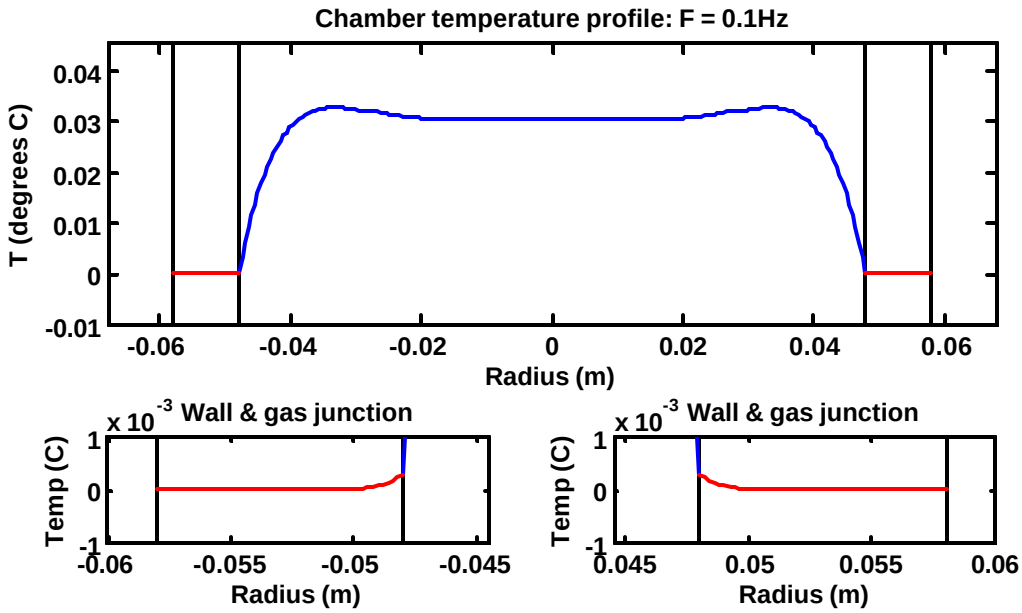

Figure **4-39**: Temperature profile for an 0.1 Hz acoustic signal between two parallel plates with a spacing equal to the diameter of the pistophone chamber. The temperature profile is very similar to the cylindrical case.

This finite wall thickness calculation is useful because, in addition to visualizing the effects of wall properties on the temperature profile, the e_s term can be used as a wall correction factor for the pressure response. This wall correction factor can be used to modify the lumped impedance terms to account for the heat capacity of the walls and simulate the resulting effects on the pressure response in the chamber. Figure **4-40** is a plot of the e_s correction factor for the pistonphone geometry. It is also compared with the correction factor for the parallel plate version, to show the similarities and differences.

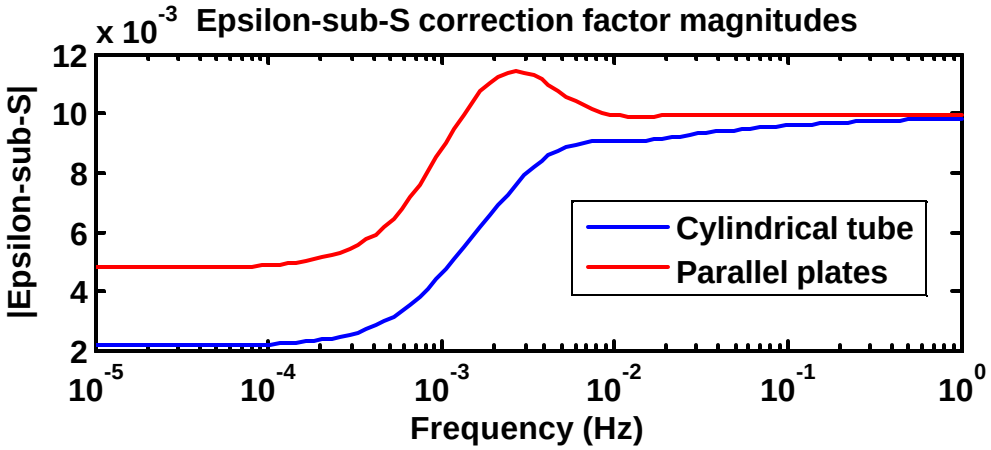

Figure **4-40**: Comparison of the magnitudes of the e_s correction factor. The factor is unit-less.

From Figure **4-40** it can be seen that e_s reaches both high and low frequency limits, the high frequency limit of which is determined by:

$$e_s = \frac{\sqrt{krC_p}}{\sqrt{k_s r_s C_{ps}}},$$

This is the e_s value used in the infinite-thickness assumption.

The modifications to the lumped element impedances are found from the continuity and momentum equations in [**21**], but with e_s retained throughout the derivation of Rott's wave equation. When the e_s term is retained, the lumped element compliance and thermal loss are modified from those given in [**21**] to become:

$$dC = \frac{Adx}{gP_0}\left[1 + \frac{(g-1)}{(1+e_s)}\mathrm{Re}[f_k]\right] \qquad \textbf{4.4}$$

$$dR_k = \frac{1}{dx}\frac{(1+e_s)g}{(g-1)}\frac{r_0}{wA\,\mathrm{Im}(-f_k)} \qquad \textbf{4.5}$$

To calculate the effect of the finite wall thickness, the infinite thickness version of the e_s term is modified to match the version found in the finite cylinder calculation. This new e_s is applied to the lumped impedances in the pressure calculation model. The

response of this model is then divided by the response of the model assuming that the wall is infinitely thick. Figure **4-41** plots the results of this comparison.

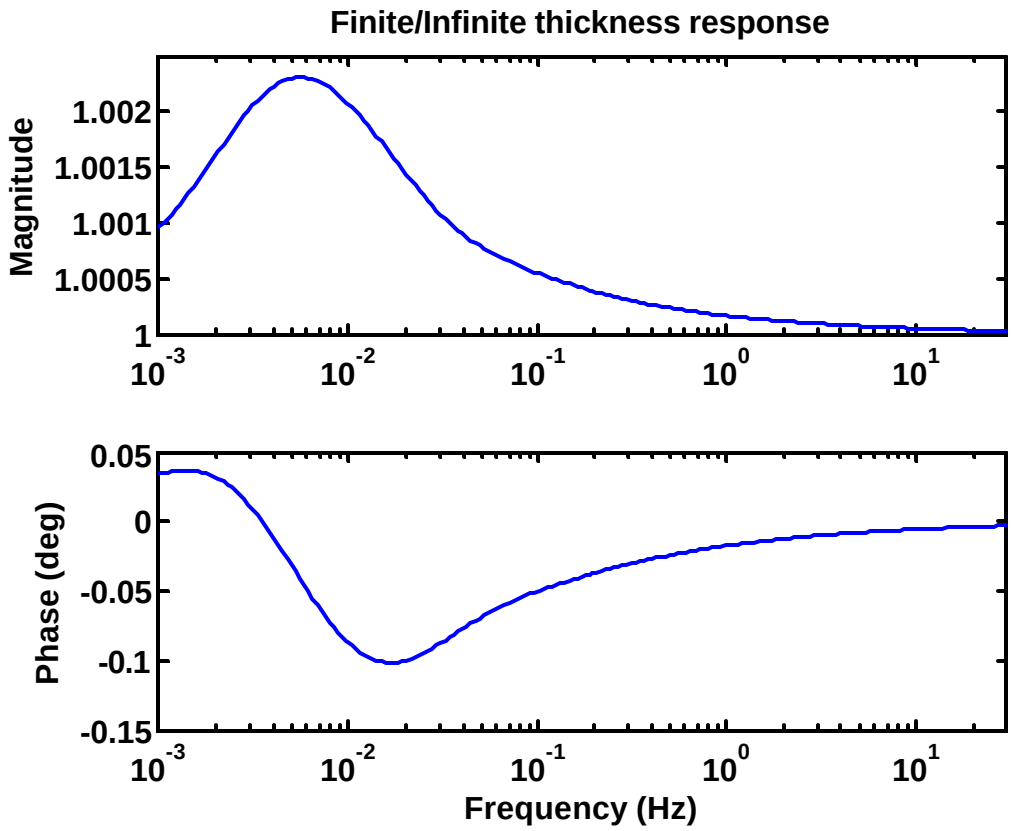

Figure **4-41**: Results of the actual response change caused by the finite thickness of the walls. The magnitude correction stays below 0.3%, and the peak phase is less than a tenth of a degree.

The results appear to indicate that the effect of finite wall thickness is an order of magnitude smaller than the error currently being analyzed, which has peak errors ranging from 3 to 6%. Therefore, finite wall thickness does not appear to be the cause for the observed model/measurement deviations.

To confirm that the e_s term is being correctly implemented into the lumped equations, the adiabatic-to-isothermal transition predicted by the lumped impedance model can be compared with an adiabatic-to-isothermal transition for the same geometry calculated directly from the thermal profile for a gas filled tube with finite wall thickness.

To calculate the adiabatic transition from the thermal profile of the tube, the average temperature of the tube is calculated as a function frequency. This is done by three-dimensionally rotating the thermal profile of the gas around the *z*-axis.

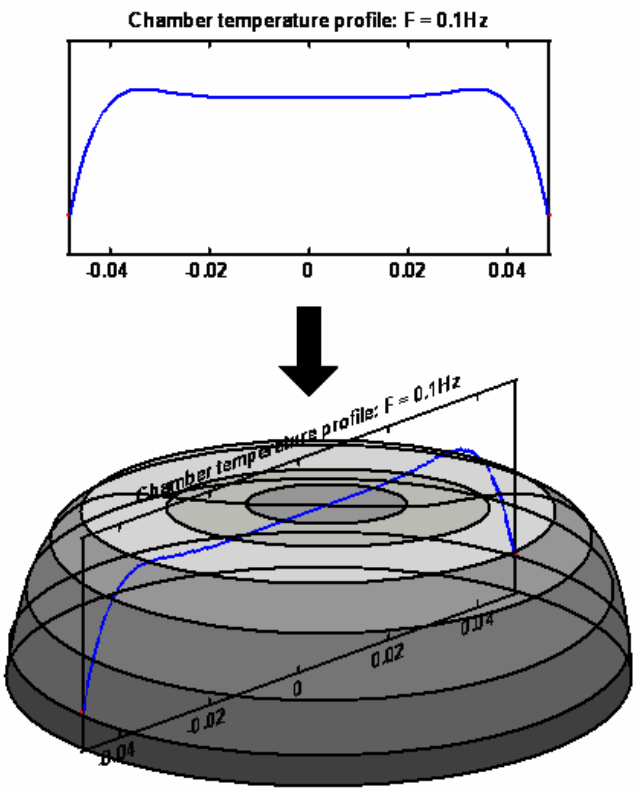

Figure **4-42**: Rotating the thermal profile around the *z*-axis. The average temperature in the tube is calculated from this three-dimensional temperature rotation.

The average temperature is then found by calculating the average height of the shell formed by the rotation. A number of numerical methods exist for doing this. The method used in this thesis is to take two points of the thermal profile, T_{n-1}, and T_n, having distances from the center r_{n-1} and r_n. The temperature $(T_{n-1} + T_n)/2$ is weighted by the area of the ring calculated by subtracting $p*r_n\text{^}2 - p*r_{n-1}\text{^}2$. This is done for all points on the thermal profile, which are summed and then normalized by $p*r_{max}\text{^}2$.

One of the terms in equation **4.2** is the acoustic pressure amplitude. The temperature profile calculation assumes that the pressure oscillations in the tube are

constant over all frequencies. Assuming a constant pressure excitation amplitude and using the ideal gas law, the variation in density required to achieve constant pressure is calculated, given the temperature profile. Starting with the differentiated ideal gas law [**21**]:

$$dp = r\Re dT + \Re T dr$$

$$dp = r\Re dT + \Re T \frac{dV}{V}$$

$$dV = \frac{V}{\Re T}\left(dp - r\Re dT\right) \qquad \textbf{4.6}$$

The complex, averaged temperature is plugged into *dT* of equation **4.6**, and the acoustic pressure amplitude used for the calculation is plugged into *dp*. *V* represents the volume of whatever length of pipe is being simulated, and the resulting *dV* is the change in volume necessary to achieve the defined acoustic pressure for the given volume and thermal profile. The volume changes will be largest for isothermal pressure oscillations, and the isothermal change in volume can be found by setting *dT* to zero.

The adiabatic-to-isothermal transition of the pressure amplitude in a tube with a displacement source, a pistonphone for example, can be found using equations **4.6** and **4.2**. To begin, the pressure amplitude resulting from the change in volume is calculated assuming the pressure oscillations are adiabatic:

$$dp_{adb} = gp_0 \frac{dV}{V}$$

dp_{adb} is then plugged into equation **4.2** to solve for the thermal profile, *dT(r, ?)*. The change in volume necessary to keep the pressure at dp_{adb} is then calculated by plugging *dT(r, ?)* and the volume of the chamber into equation **4.6**:

$$dV(w) = \frac{V}{\Re T}\left(dp_{adb} - r\Re dT(r,w)\right)$$

The pressure resulting from the constant displacement dV_{adb} can be found by multiplying dp_{adb} by $\frac{dV(w)}{dV_{adb}}$:

$$dV_{adb} = gV\frac{dp_{adb}}{p_0}$$

$$dp(w) = dp_{adb}\frac{dV(w)}{dV_{adb}} \qquad \textbf{4.7}$$

This will be the pressure amplitude in the tube assuming purely compliant acoustic impedance. This pressure prediction will not show resonances or any effects from viscous losses. However, because the region of the adiabatic transition is dominated by compliance and thermal effects, the transitions calculated using both the lumped impedance and the heat equation methods should overlap well in the transition region. Figure **4-43** is a plot of the pressure response predicted using the lumped element model incorporating the e_s term, and the pressure response calculated directly from the thermal profile of the gas inside the tube:

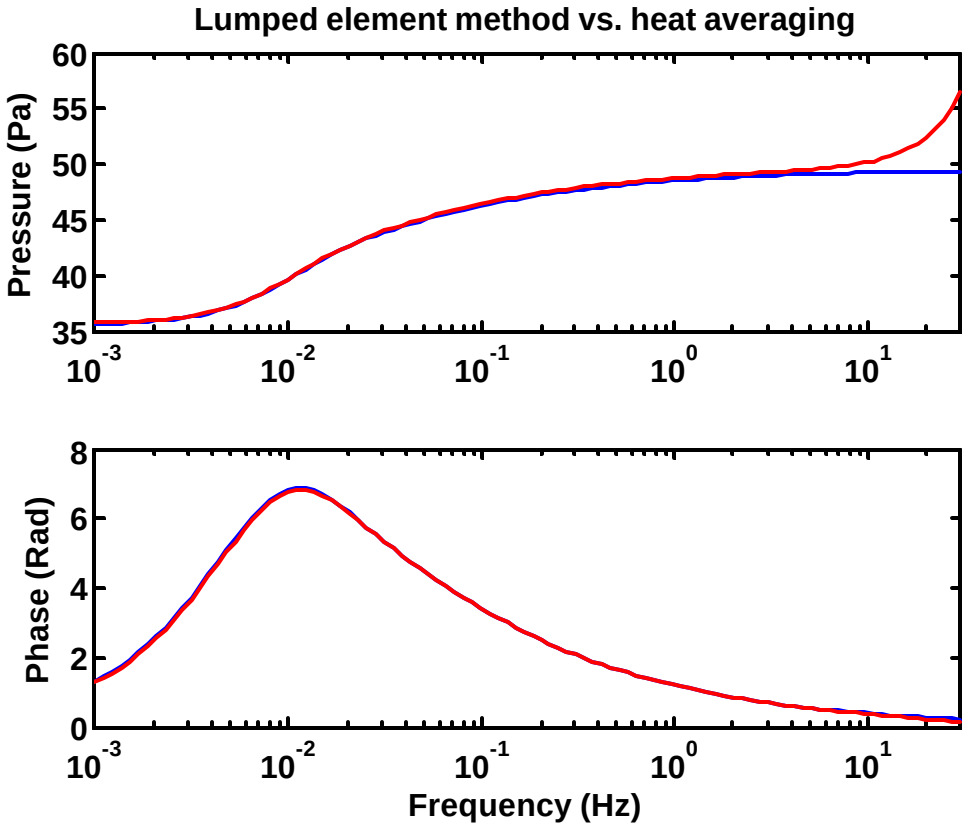

Figure **4-43**: Comparison of the adiabatic-to-isothermal transition predicted directly from the heat equation with the lumped element model incorporating the e_s term calculated for a cylindrical wall with finite thickness.

For unknown reasons a scaling error of 0.003% appears between the lumped element model and the heat-equation calculation; however, the phase plot demonstrates that the two models are nearly identical through the entire transition region. This provides confirmation that the e_s term is being correctly applied to the lumped-impedance model.

A final note about the effect of finite wall thickness: using a material with a higher thermal conductivity than PVC, such as aluminum or copper, decreases the accuracy of the "infinite wall thickness" assumption. At the same time, however, it appears to greatly increase the correspondence between the ideal model, (in which case e_s is equal to zero), and the model including e_s, because using a material with a high thermal conductivity reduces the overall value of e_s. Figure **4-44** exaggerates the affect of finite thickness by simulating a pistonphone chamber with impractically thin (0.1mm) walls. From the plots it can be seen that using a wall material with a high density and thermal conductivity (such as copper), reduces the effect of finite thickness, even though the penetration depth in the wall is far greater than the thickness of the wall.

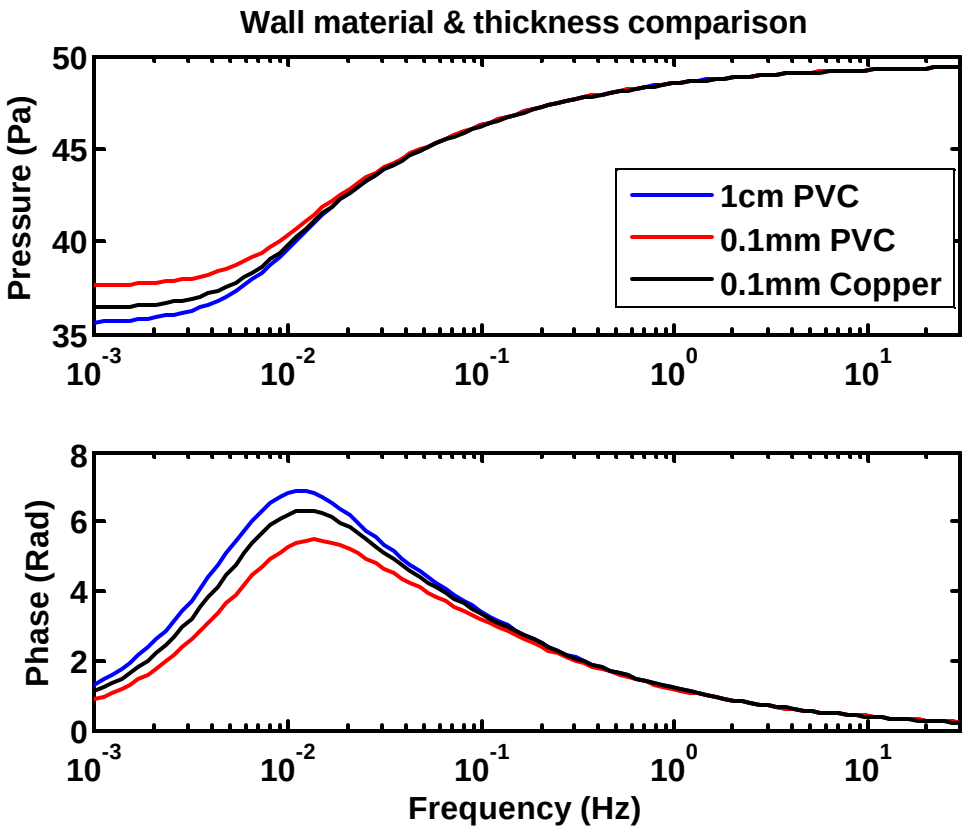

Figure **4-44**: Comparison of the adiabatic-to-isothermal transition in a cylindrical tube having 0.1 mm, when the wall material is changed from PVC to Brass. The 1cm PVC plot is included as a reference.

Because metals generally have a high density and thermal conductivity, a metal wall may be desirable in situations where the finite heat capacity of the wall could be an issue.

4.7.10 Additional tests

The PVC cement used for assembly of many of the chamber components has a lingering oder. In order to test whether the fumes from PVC cement may have contributed to the measurement/model discrepancy, a PVC cap filled with a large quantity of wet PVC primer and cement is inserted into the chamber, which is then

sealed. The fumes are left to diffuse through out the chambers for a day. The pressure response of the tube is measured; however, there was no change in response. To further test the influence of humidity on the measurements, the humidity was increased artificially. A paper towel is soaked and left in the chamber over night. The next day, it is removed and the pressure response measured. Boosting the humidity also apparently has no significant impact on the size and location of the deviation.

4.7.11 Error isolation conclusion

A deviation between the pressure response predicted by the model for the pistonphone chamber, and actual measurements made in the device consistently appears in response comparisons. The general location and size of the deviation is consistent; however, there is some small variability. Sometimes the deviation between predicted and measured magnitudes peaks as high as 6%, sometimes as low as 3%. An early measurement made with a different LVDT and different measurement methods shows drastically reduced model-versus-measurement discrepancies. This early measurement is not repeatable using the current pistonphone design.

To try to isolate the source of error, several experiments were conducted. It is concluded from these error-isolation experiments that neither the swept-sine measurement method, nor the algorithms used to process the recorded data are the source of the deviation. The transducers were checked for response errors by using different transducers to measure the same quantity. In the case of the displacement, both a potentiometer-based displacement sensor and the LVDT were run simultaneously. The response difference between both displacement measurement devices is very small, and does not match the error seen in the pressure response plots. The flatness of the response of the primary pressure sensor was tested by comparing the measured pressure response with the response measured by a sensor having a different make and vastly different sensitivity. The pressure response results agree, reducing the likelihood that the pressure transducer is the source of error.

The gas in the chamber was replaced with nitrogen to simulate dry air, but no improvements are found in the correspondence between the measurement and the model. More ideal gases, helium and argon, were used, to attempt to eliminate the discrepancy. The discrepancy completely disappears in the helium measurement and a very good curve fit can be attained; however, the adiabatic-to-isothermal transition frequency range is shifted to a much higher frequency when helium is used. It is unknown why this would affect the shape of the transition. The deviation reappears when argon is used, and the frequency of the discrepancy seems to track with the lower frequency range of the adiabatic-to-isothermal transition resulting from using this gas. The size of the discrepancy is only slightly larger than that in air. The fact that the deviation occurs when a monatomic gas is used reduces the likelihood that the discrepancy is a result of air not being monatomic.

Several possibilities for the cause of the discrepancy have been eliminated, but the cause remains unknown. Several other experiments could be done to probe the question further: the piston could be swapped with another piston, the tension in the piston head lock could be altered, and the inside of the chamber could be glossed to prevent air from leaking through cracks.

4.8 Chapter 4 summary

The pressure inside the pistonphone chamber is predicted using a Matlab script called *"pfunc.m"*, that applies the transmission line analogy constructed in Chapter **3**. The data from the LVDT and side-mounted pressure sensor are processed using a Matlab script called *"HEBI.m."* This code breaks the output into many smaller segments, and calculates the root-mean-square pressure amplitude of each segment and phase with respect to piston displacement.

A comparison of measurement results with the output of the pressure response prediction code *pfunc* shows good correspondence throughout the range of the calibrator with the exception of the region during which the pressure amplitude is changing most

swiftly due to thermo-viscous effects – approximately from 0.1 to 0.01 Hz. A discrepancy of consistent shape and size consistently appears between model and measurement in this region. Tests were conducted to find and eliminate the source of the discrepancy. Tests included replacing the gas inside the chamber with pure nitrogen, argon, and helium, using different pressure and displacement sensors, using different measurement techniques, and testing the data processing algorithm for errors. None of these tests revealed the source of the problem, however, it was found that the discrepancy disappeared when helium was used. The measurement and model correspondence was greatly enhanced through the use of helium. Despite the presence of the model/measurement discrepancy when air is used in the chamber, the scaling error between model and measurement remains below five percent.

Chapter 5

Calibration examples

Chapter 4 focused on experimental verification of the theoretical model used for predicting the pressure inside the pistonphone. This chapter will walk through the steps involved in calibrating an actual transducer, including correcting the calibration for thermo-viscous and resonance effects. The example calibrations are carried out on condenser microphones, although the transducer types that may be calibrated by the pistonphone are not limited to condenser microphones. Examples of microphone response stability, model consistency, mechanical response and accessory performance measurements are given at the end of the chapter to illustrate some additional calibration measurements that can be made with the pistonphone.

5.1 Experimental setup

5.1.1 Hardware

Figure **5-1** is a diagram of the experimental setup, showing all the important pieces of hardware involved in the calibration process. Cables and the insulation surrounding the main and control chambers have been omitted from the diagram for the sake of clarity:

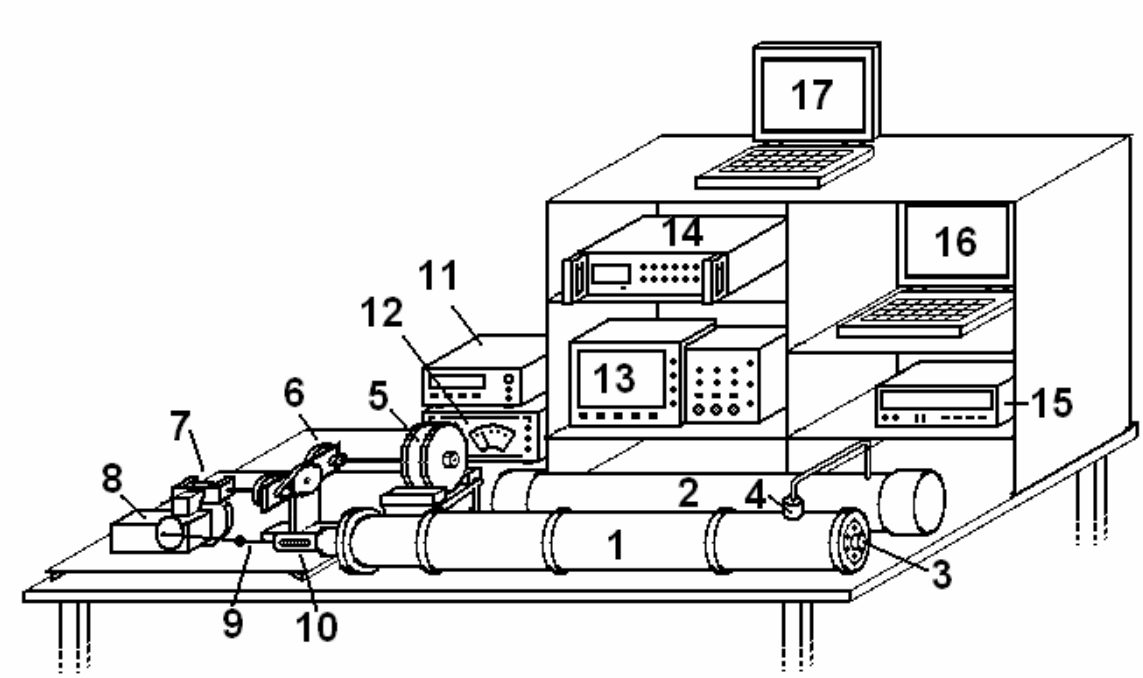

Figure **5-1**: Calibration measurement experimental setup showing most of the equipment. The numbers are labeled below. Not shown: Chamber insulation, LVDT processing circuit board, PZR amplifier, amplifier power supply, and barometric pressure sensor.

Illustration key:

1. Main chamber
2. Control chamber
3. Transducer cable seal
4. Differential pressure sensor (unused in absolute calibrations)
5. DC motor
6. 10:1 reducer
7. 40:1 worm gear reducer
8. Aluminum axle block with shaft wheel
9. Piston shaft
10. LVDT and fixture
11. LVDT signal source
12. DC Motor power supply
13. Tektronix 4 channel oscilloscope

14. Teac GX data recorder
15. Multiplexer/temperature sensor
16. Multiplexer memory dump laptop
17. GX controller laptop

The cables are connected in such a way as to allow the pressure/displacement signals from all transducers to be recorded by the GX and monitored simultaneously on the oscilloscope. Figure **5-2** is a diagram of the cable connections made during normal pressure measurement operations.

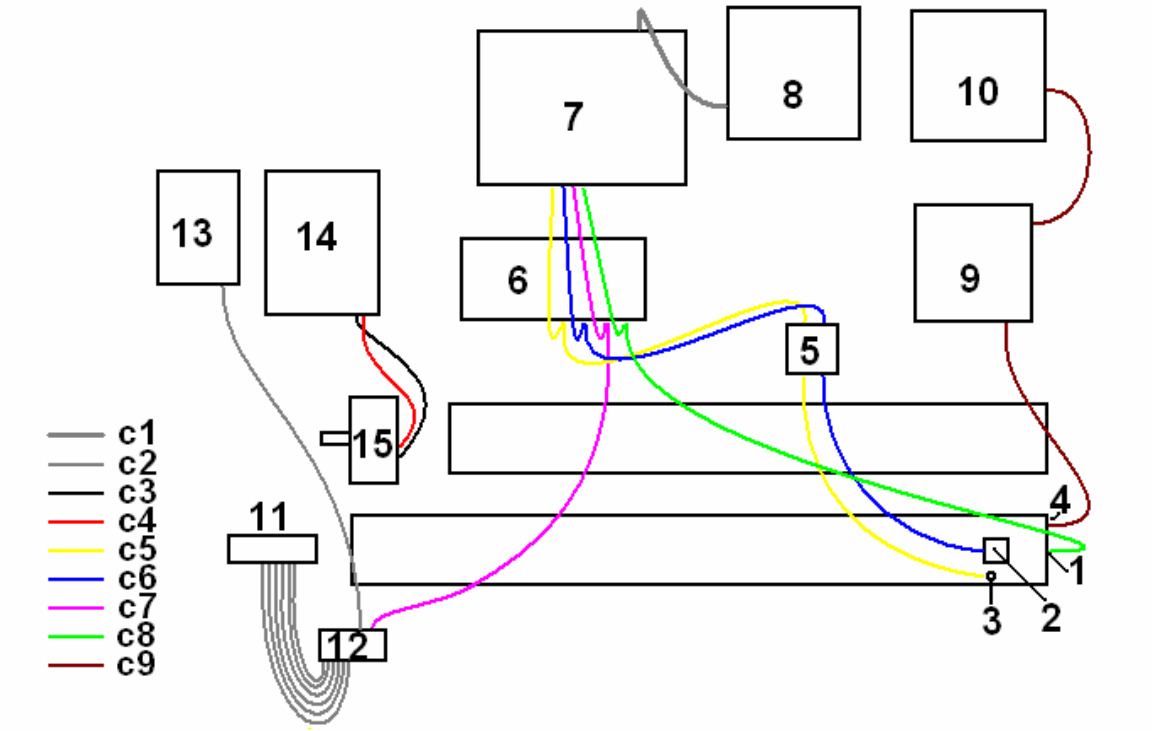

Figure **5-2**: Cable diagram for experimental setup.

Illustration key:

1. Transducer insertion point
2. High sensitivity differential piezo-resisitive pressure sensor
3. 15 PSI piezo-resistive pressure sensor
4. Thermo-couple

5. PZR amplifier box
6. Oscilloscope
7. Teac GX data acquisition system
8. GX controller laptop computer
9. Multiplexer/thermocouple recorder
10. Multiplexer memory dump
11. LVDT
12. LVDT decoder
13. Function generator/LVDT carrier signal source
14. DC motor power supply
15. DC motor

Cable color key:

c1: Teac/Laptop SCSI communication cable
c2: LVDT signal cables
c3: -Vs, DC motor
c4: + Vs, DC motor
c5: 15 PSI PZR analog signal
c6: Differential PZR signal
c7: LVDT displacement signal
c8: Immersed transducer signal (may require other items in the signal path)
c9: Temperature data

A step-by-step description of the swept sine measurement process is given in Appendix **G**. The only difference with transducer calibration is that the TEAC GX data-acquisition system needs to communicate with the immersed transducer. Unless the transducer is remote and the output broadcast over radio frequencies, calibration via infrasonic pistonphone requires sealing the transducer cable in a way that no leak is introduced into the system. Also, the cable and transducer must not be damaged by the

cable sealing method. Figure **5-3** is a photo of the cable seal used in the present pistonphone apparatus:

Figure **5-3**: Transducer cable seal used in the pistonphone. The seal compresses a soft rubber material around the transducer cable as a nut is tightened, making the insertion airtight.

The cable sealing method pictured in Figure **5-3** has been successfully implemented. It accepts cables of varying sizes without introducing leaks in the system that significantly affect the phase or magnitude pressure response in the 0.001 to 30 Hz frequency range.

The HEBI code described in **4.4** is used to make absolute calibrations of inserted transducers. The input signal used by HEBI is swapped from the signal of the differential piezo-resistive pressure sensor to the signal from the inserted transducer. To make an absolute calibration, the *pfunc.m* function is called from within HEBI, after the voltage response of the transducer has been measured. The voltage response of the transducer is divided by the pressure response predicted by *pfunc.m*, giving an output in volts-per-pascal.

HEBI can also return a relative calibration. Instead of calculating the voltage response of the transducer and dividing by a pressure response prediction, the input normally used for LVDT data is switched to PZR pressure sensor data, and the relative response is calculated directly. This works because when the LVDT data and PZR data sets are swapped, the transducer data is divided by the pressure response of the chamber as measured by the PZR, instead of the displacement response.

5.1.2 Volume corrections

The pistonphone works by comparing the voltage output of an immersed transducer with a pressure calculation based on the change in density of the air inside the pistonphone chamber. The change in density will be slightly different when a transducer is immersed, because the presence of an immersed transducer alters the volume of the pistonphone chamber.

For most transducers, the size of the correction factor needed to account for the change in volume is negligible compared to other sources of error. The volume of the pistonphone chamber is 11520 ± 75 cm^3. A typical half-inch measurement microphone may be 1.3 cm in diameter and 6.5 cm long. Add a 0.4 cm diameter, 75 cm cable into the chamber, and the change in volume due to the immersion of the transducers is about 70 cm^3. This is pushing the limits of the accuracy of the volume measurement of the chamber. It will, however, increase the pressure signal by about half a percent from what it would otherwise have been without the transducer present in the sound field. The effect will be larger for large transducers. If a large infrasonic microphone, such as the one shown in Appendix **E**, is being calibrated, the volume correction may be several percent. When the size of the transducer is a concern, the volume of the transducer is estimated, and the calibration amplitude adjusted slightly.

The additional surface area of the transducer, and any compliances it adds to the system will also slightly affect the calibration curve. Extra surface area will tend to push the adiabatic-to-isothermal transition to a higher frequency, and additional compliance will decrease the overall pressure. No measurement microphone calibrated to date has measurably altered the adiabatic-to-isothermal transition or the pressure response of the tube.

5.2 Calibration example

5.2.1 Bruel & Kjaer 4193 half-inch microphone

In the summer of 2008 NASA Dryden flight research center sent four *B&K* 4193 half-inch microphones to the Penn State acoustics laboratory to be calibrated by the infrasonic pistonphone. This section will focus on the method used to calibrate one of these microphones; however, all measured responses and calibration recording notes are available in Appendix **D**.

The microphone is a *B&K* 4193 half inch measurement microphone, with serial number 2571624. Using a *B&K* type 4228 pistonphone, the sensitivity of the microphone is determined to be 5.07 ±0.06 mV/Pa at 250 Hz. The response chart for these microphones indicate that the sensitivities of a *B&K* 4193 microphone at 30 and 250 Hz are very nearly equal, so the *B&K* type 4228 250 Hz pistonphone calibration serves as a sanity check for the infrasonic pistonphone calibration.

The microphone is fully immersed in the pistonphone chamber. If carefully positioned, the effects of the resonance on the pressure field generated at the microphone can be reduced. The microphone is placed 84 ±3 cm from the solid end of the pistonphone chamber. After positioning, the cable is sealed using the plug pictured in Figure **5-3**.

Before any measurements are taken, the environmental factors, channel setup, and any transducer amplifier gain settings (*B&K* "Nexus" microphone amplifier in this example) are recorded:

Table **5-1**: Table of recorded environmental conditions, equipment gain and range settings

Microphone SN:	2571624
Start time:	2:36 PM
Relative Humidity:	58%
Barometric Pressure:	967.2 mBar

Ch.1 input range	+/- 1V
Ch.2 input range	+/- 2V
Ch.3 input range	+/- 1V
Ch.4 input range	+/- 5V
Nexus sensitivity:	31.6 mV/Pa

Beginning at low frequencies and working upwards, the transducer is subject to a piston-generated swept-sine signal. The steep low frequency roll off of the *B&K* 4193 microphone results in very poor calibration quality near 0.001 Hz; therefore, the swept sine in this example begins at 0.0035 mHz. It extends through several gearing configurations and finishes near 30 Hz. The gearing configurations and pistonphone operation details can be found in Section **4.3**.

Using the lumped element model, the pressure response of the pistonphone is calculated over the same frequency range as the pistonphone sweep signal. The lumped element model is modified to calculate the pressure at the location of the transducer immersed inside the pistonphone chamber to increase the accuracy of the calibration as the frequency approaches the chamber resonance.[10] The calculated pressure response is used as the calibration reference, and the sensitivity in *V/Pa* is calculated by dividing the response of the microphone recorded in volts by the pressure response of the pistonphone predicted in pascals. Because the adiabatic-to-isothermal transition is accounted for in the tube, sensitivity error in the calibration is greatly reduced.

For comparison, a simultaneous relative calibration using the differential piezo-resistive sensor as a reference is also completed in this example. The major drawback of the relative calibration method is that calibration error in the reference sensor carries over to the transducer being calibrated. Furthermore, to make a relative measurement in this instance requires calculating the transfer function relating two points along the length of the pistonphone chamber. The microphone diaphragm is located approximately 0.83

[10] *Pfunc.m* has been modified so that transducer location along the inside of the chamber is a passed input parameter.

meters from the end of the chamber, while the piezo-resistive pressure sensor is located 0.1 meters from the end of the chamber. Near 30 Hz the pressure response at the locations of the transducers are different, and the relative calibration resulting from the dividing the responses will reflect this difference.

To compensate for transducer location the lumped impedance model is used to calculate the pressure responses at both locations. The transfer function relating the microphone immersion point to the differential pressure sensor mounting point is used to correct for the location of the microphone. When this correction is made to the microphone data, it appears as if it had been measured at the location of the differential pressure sensor.

The relative calibration is completed by dividing the output of the immersed transducer by the pressure in the tube as measured by the reference sensor and its known sensitivity. The result of this location correction and relative calibration are shown in Figure **5-4** alongside the absolute calibration made simultaneously.

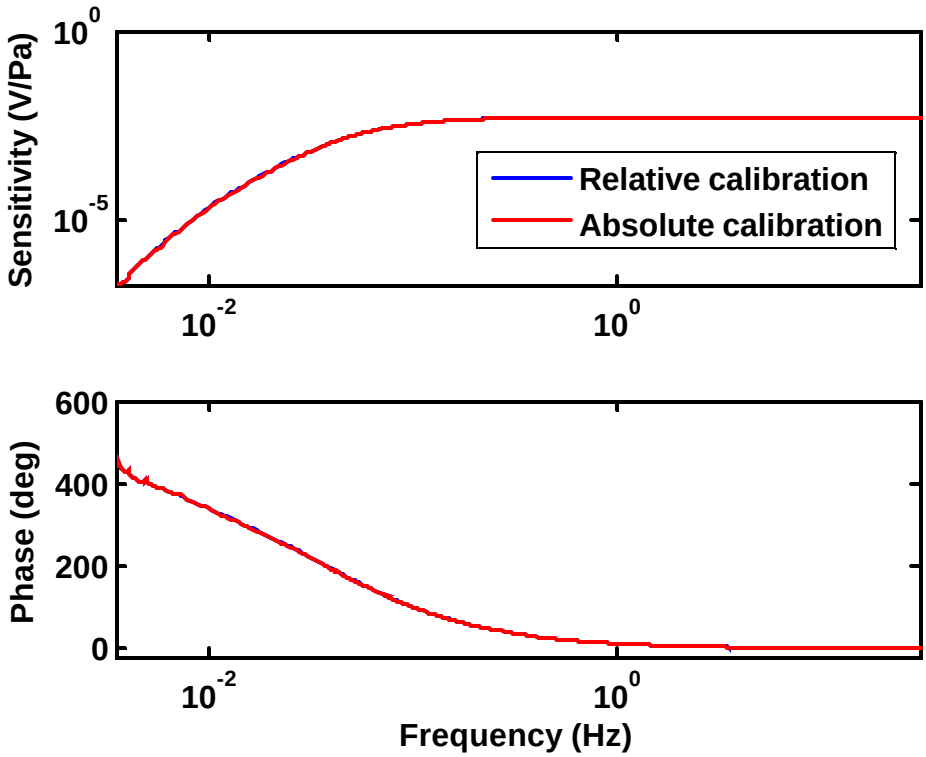

Figure **5-4**: Comparison of the 0.0035 to 30 Hz microphone response calculated by two different methods: "relative," using the response of a piezo-resistive pressure sensor as a reference, and "absolute," using the calculated pressure response of the pistonphone.

The results of relative and absolute calibration appear to be nearly identical. Figure **5-5** is a plot of the calculated pressure response inside the pistonphone chamber verses the pressure measurements made in the pistonphone chamber during the calibration example, and Figure **5-6** is a plot of the difference between the measurement and prediction. Calibration uncertainty is frequency dependent. At 30 Hz, the sensitivity error is increased to +/-2% due to the resonance of the tube and uncertainties in the location of the transducer. From 0.1 to 20 Hz the error is +/-1%, due mostly to the pistonphone geometry uncertainties specified in **2.2**. The measurement and prediction diverge in the vicinity of 10 mHz, increasing the error to nearly 5%. The prediction and measurements remain below 5% as the measurement and prediction both converge upon the isothermal limit.

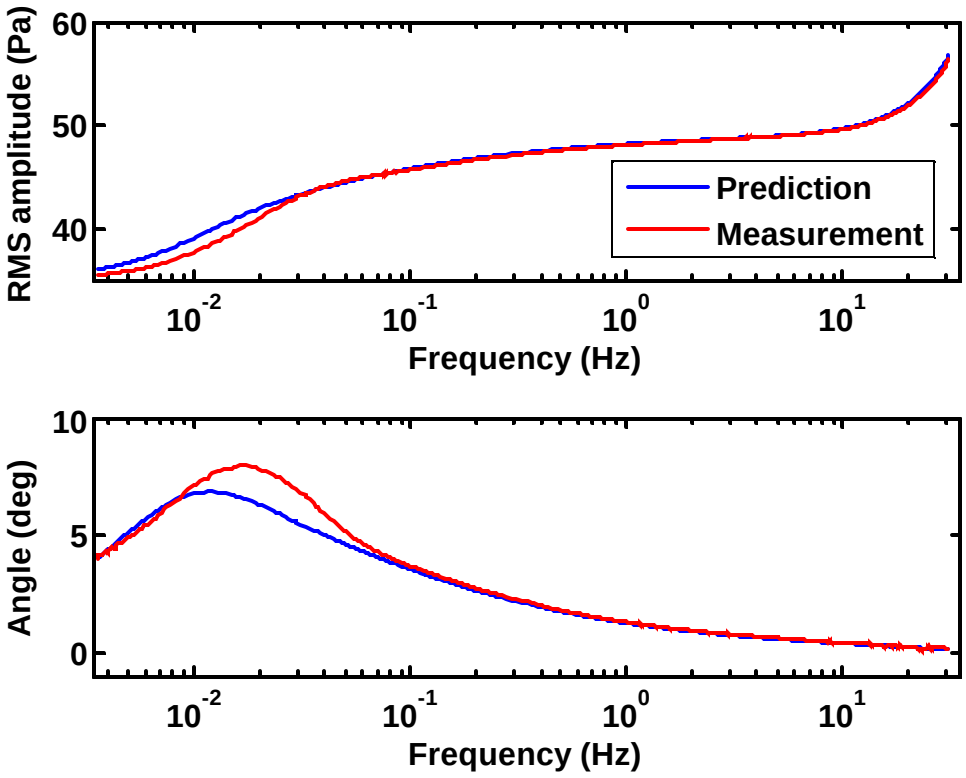

Figure 5-5: A comparison of the pressure response of the pistonphone chamber measured during the calibration example, vs. the calculated pressure response used in the absolute calibration process.

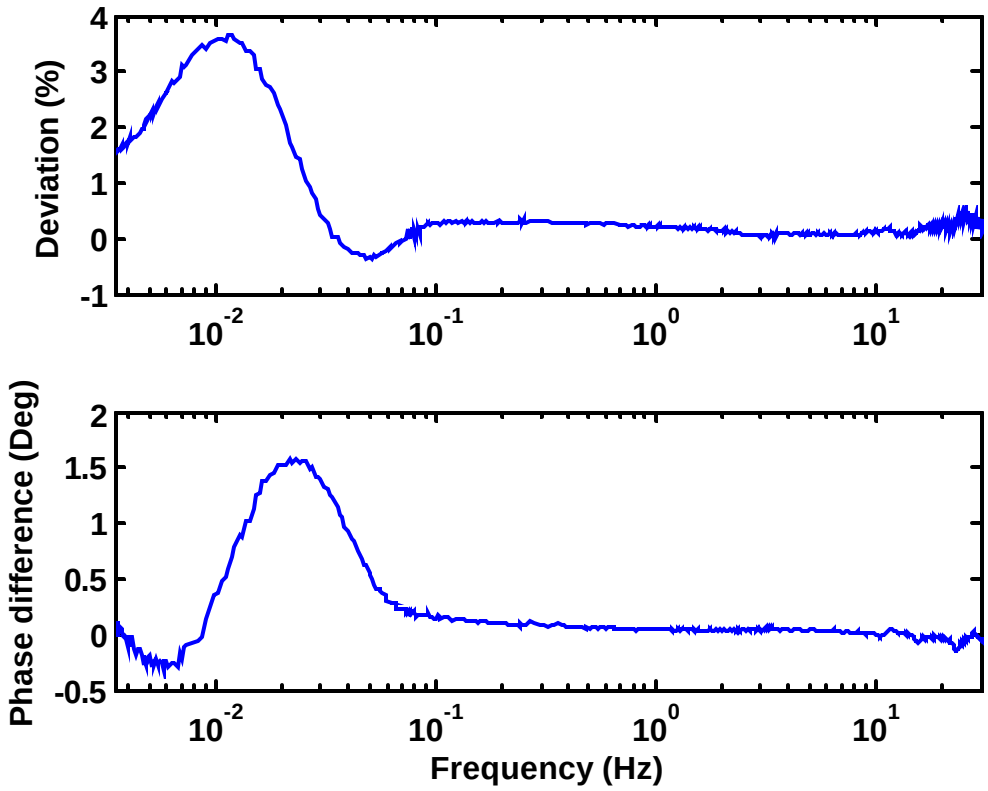

Figure **5-6**: Difference plot showing the deviation between the prediction and measurement of the pressure response inside the pistonphone chamber. The plot may also be seen as the difference between the relative and absolute calibration results.

The measured sensitivity of the microphone at 20 Hz is 5.03 ±0.1 mV/Pa, which compares to the 5.07 ±0.06 mV/Pa sensitivity measured at 250 Hz. A disadvantage of the present low frequency pistonphone design is that the maximum frequency lies significantly below the frequency of the *B&K* type 4228 pistonphone operation frequency, so the calibrations can not be made at the same frequency for comparison.

Generally calibration measurements beginning near 0.001 Hz take 3 to 8 hours, depending on how much low frequency data is required to make a good calibration. For the *B&K* 4193 microphone, the sensitivity at 0.0035 Hz is so low that the low frequency portion of the data sweep took nearly 5 hours. When transducers are more sensitive, less time needs to be spent recording low frequency data, and the sweep speed can be increased.

5.2.2 Stability and other useful measurements

When appropriate measures are taken to adjust for changes in barometric pressure, the pistonphone generates extremely consistent calibration signals. As a result, it may also be used for learning more about the mechanics of microphone construction, evaluating the performance of certain additions to the microphone design, and testing the stability of the response of a particular microphone. The following are some examples of calibration measurements that were used to evaluate microphone accessories, or reveal more subtle characteristics of microphone responses.

5.2.2.1 Bandwidth extension capsule evaluation

B&K and *G.R.A.S.*, well respected manufacturers of measurement microphones, market accessories that decrease the low frequency cutoff[11] location of half-inch microphones.[12] This is accomplished by increasing the capacitance between signal and ground before the signal is sensed by the preamplifier. This increases the RC time constant of the high-pass filter formed by the capacitance of the capsule and the input resistance of the preamplifier input. More detail about this kind of bandwidth extension can be found in reference [**15**].

This technique is limited in the extent to which it can be applied. Increasing the capacitance between the signal and ground will lower the frequency only of the preamplifier cutoff. There is at least one other source of low frequency attenuation present: the mechanical attenuation formed by the inclusion of a leak behind the diaphragm of the microphone capsule. The cutoff of this filter is unaffected by the inclusion of a coupling capacitor, and once the preamplifier cutoff has been pushed below

---

[11] "Cutoff," as used in this thesis, refers to a specific point on the response, i.e. the -3dB down point.
[12] Part numbers: The *B&K* UC-0211 adaptor is marketed with the 4193 half-inch microphone, and the *G.R.A.S.* RA0016 is marketed as a "20 dB Attenuator for externally pre-polarized half-inch microphones." A version for un-polarized microphones is also available.

the mechanical cutoff, the coupling capacitor does not increase the bandwidth of the microphone further.

The addition of a coupling capacitor decreases the sensitivity of the microphone, and decreases the total available dynamic range (though, due to preamplifier limitations, some headroom may be gained with high amplitude signals). The amount of dynamic range sacrificed is directly proportional to the gain in bandwidth. A decrease in sensitivity by a scale factor of 10 (20 dB) will result in a decrease of the RC cutoff frequency by a factor of 10.

The low frequency pistonphone is used to measure the response of a *B&K* 4139 microphone with the bandwidth extending accessory installed. The performance of the accessory is evaluated by measuring the gain in bandwidth and the magnitude of attenuation compared to the normal microphone configuration. Figure **5-7** is a comparison of the responses with and without the accessory installed.

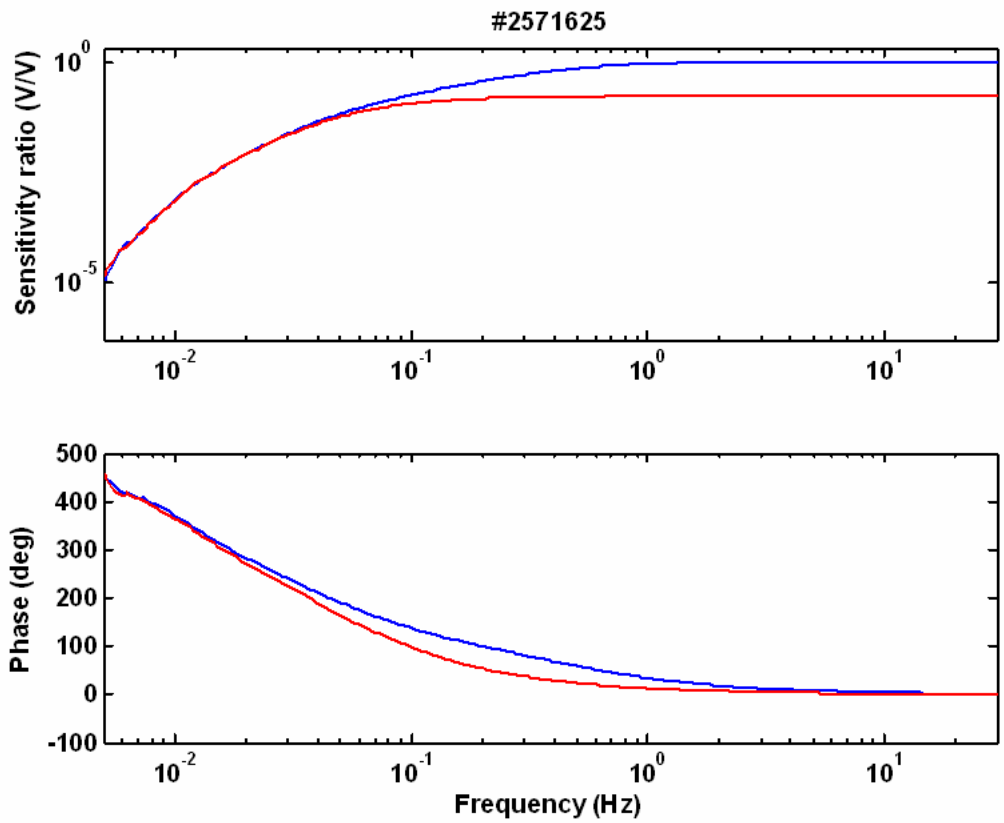

Figure 5-7: Response of *B&K* 4139, serial number #2571625, with (red) and without (blue) a bandwidth-extending accessory (part # UC-0211) installed.

The attenuated response of the bandwidth-extended microphone is 0.163 V/V at 30 Hz. The pass-band sensitivity of the microphone appears to have been decreased by about a factor of six. The -3dB down point of the normal microphone is 0.49 Hz, and the -3dB down point of the extended microphone has been reduced to 0.10 Hz, roughly a factor of 5. The bandwidth extending capability of the accessory has been confirmed, and the extension capability is nearly equal to that which would be predicted from a gain-bandwidth standpoint.

5.2.2.2 Mechanical leak localization

Using the infrasonic pistonphone and a capsule simulation accessory it is possible to isolate and measure the response of the mechanical leak in a microphone. An accessory may be purchased from *G.R.A.S.*[13] that simulates the capacitance of a microphone capsule and simultaneously allow a signal to be fed into the preamplifier via a function generator. Conveniently, the accessory is also compatible with the *B&K* half-inch preamplifier models.

Using this accessory, it is possible to isolate the electrical component of the frequency response of a microphone from the mechanical component. Measurements of the electrical responses of the *B&K* 4193 microphones using this accessory were made by Gabrielson [**9**]. The total microphone response measured via infrasonic pistonphone was divided by the purely electrical response, to isolate the mechanical response. Figure **5-8** shows the results for two different microphones. The mechanical response was evaluated for both the bandwidth-extended and normal configurations for the microphones.

[13] Part number: RA0052, "20 pF Preamplifier-input adapter for ½'' preamplifier"

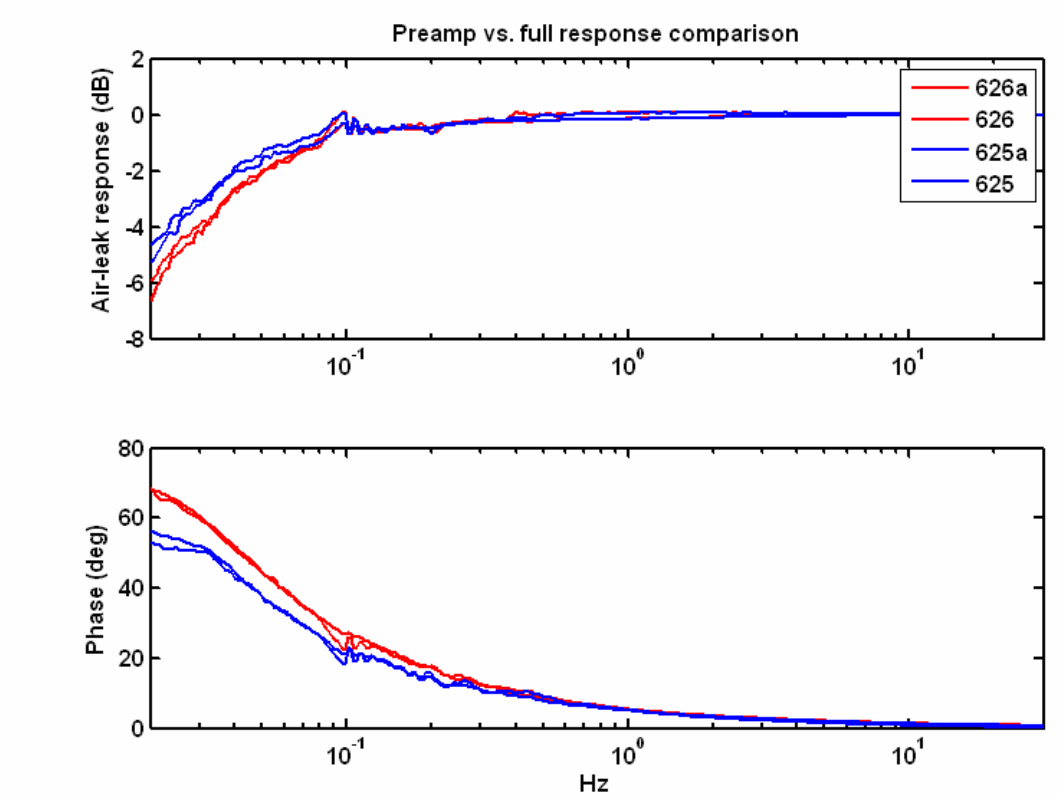

Figure **5-8**: Mechanical leak response, found by dividing the measured preamplifier response from the total response measured in the pistonphone chamber. The magnitude plot shows the decibel level with respect to the 30 Hz value. The subscript *a* in the legend refers to the presence of an attenuation coupler in the microphone, during the response measurement.

Evident from both graphs is that the mechanical leak cutoff is lower than the preamplifier cutoff, which in un-modified microphones consistently occurs in the vicinity of 0.5 Hz. The -3dB mechanical cutoff is located approximately an order of magnitude below the electrical value. Effects of the mechanical roll-off can be seen in the vicinity of 0.1 Hz, which is perhaps why the attenuators do not achieve the full bandwidth extension predicted by the gain-bandwidth product.

5.2.2.3 Stability

Provided barometric pressure changes are accounted for, pistonphone calibration is an ideal method for subjecting a microphone to a repeatable acoustic calibration signal. As such, infrasonic pistonphone calibration can be used to test the consistency of the response of a transducer in the infrasonic band. Repeatability measurements were made for both a *B&K* 4193 microphone, and a *G.R.A.S.* 40AN microphone. Figure **5-9** is a plot of two response measurements made on two different days, for a *B&K* 4193 microphone, and Figure **5-10** is a comparison of three calibration curves made for the same *G.R.A.S.* 40AN microphone.

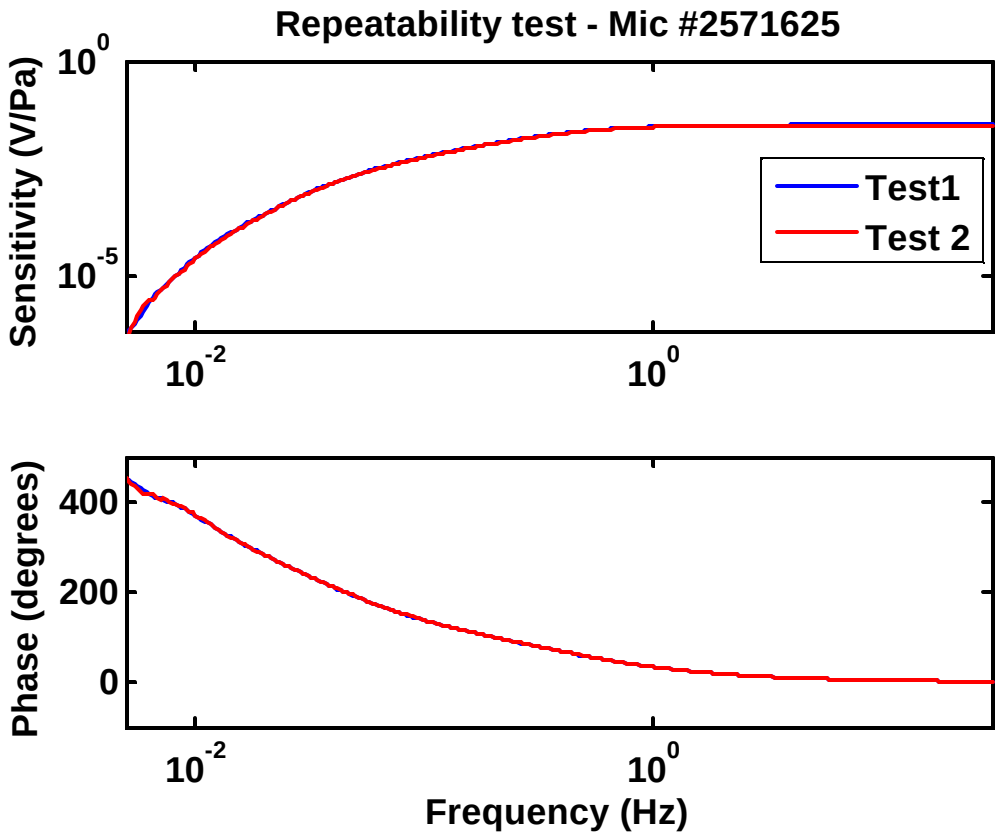

Figure **5-9**: Repeatability test, *B&K* 4139 microphone, serial number 275625. The calibration curves are nearly identical, between calibration instances. This is the only microphone of the set for which repeatability measurements were made.

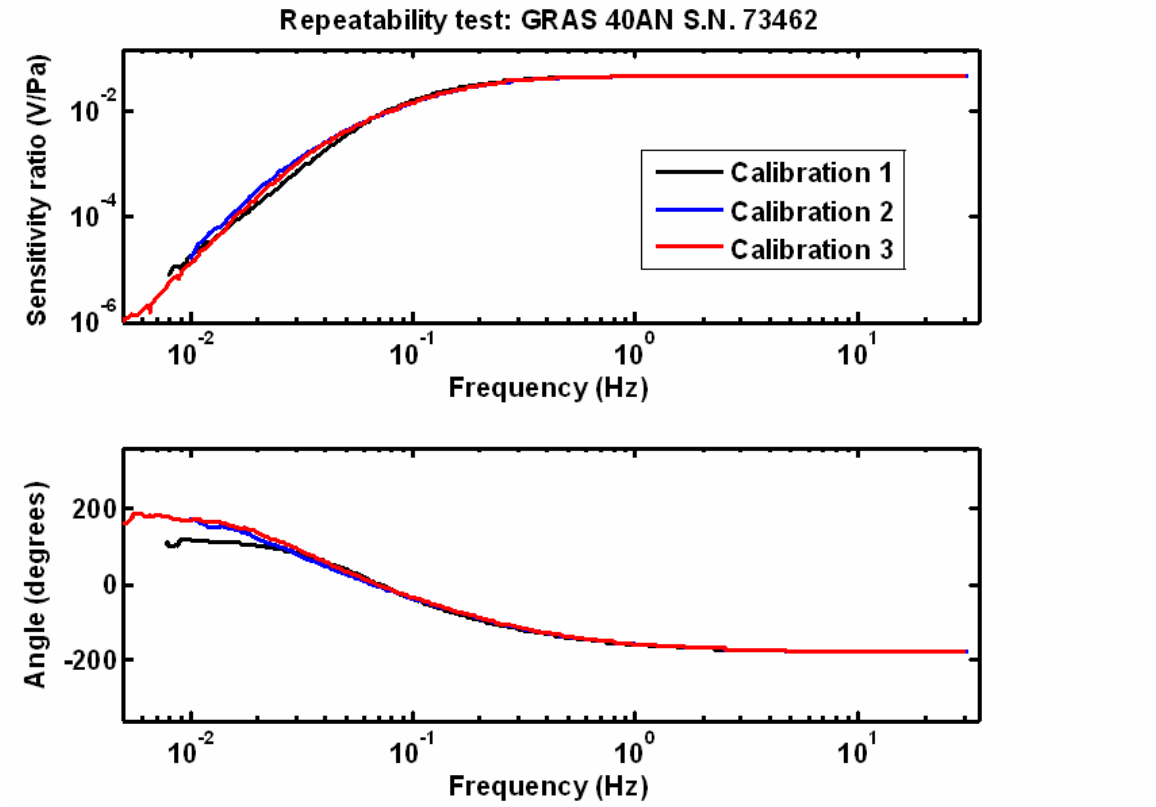

Figure **5-10**: Three calibration measurements for the same *G.R.A.S.* 40AN microphone, plotted on the same axis.

All *B&K* microphones showed extremely consistent response calibration curves. The author is hesitant to make any claims about the superiority or inferiority of any particular microphone model or brand over another, each having their strengths and weakness; however, it becomes apparent from the calibration curves in Figure **5-10** that the *G.R.A.S.* 40AN microphone does not have the same low frequency response stability that the *B&K* microphones do. Additionally, the *B&K* calibration curves showed smoother response curves for the same length of calibration time, possibly indicating amplifiers have less low frequency noise. It ought to be noted, however, that the *G.R.A.S.* 40AN and the *B&K* 4193 microphones are not equivalent models, and a different *G.R.A.S.* microphone and preamplifier may deliver performance and stability similar to that of the *B&K* microphones.

5.2.2.4 Microphone model consistency

Tests of the response uniformity between individual microphones of the same make and model are also made with the infrasonic pistonphone. Figure **5-11** compares the response curves of four *B&K* 4193 microphones on the same axis (the legend is the serial number associated with the curve color): Figure **5-12** and Figure **5-13** show the response measurements with different vertical axes.

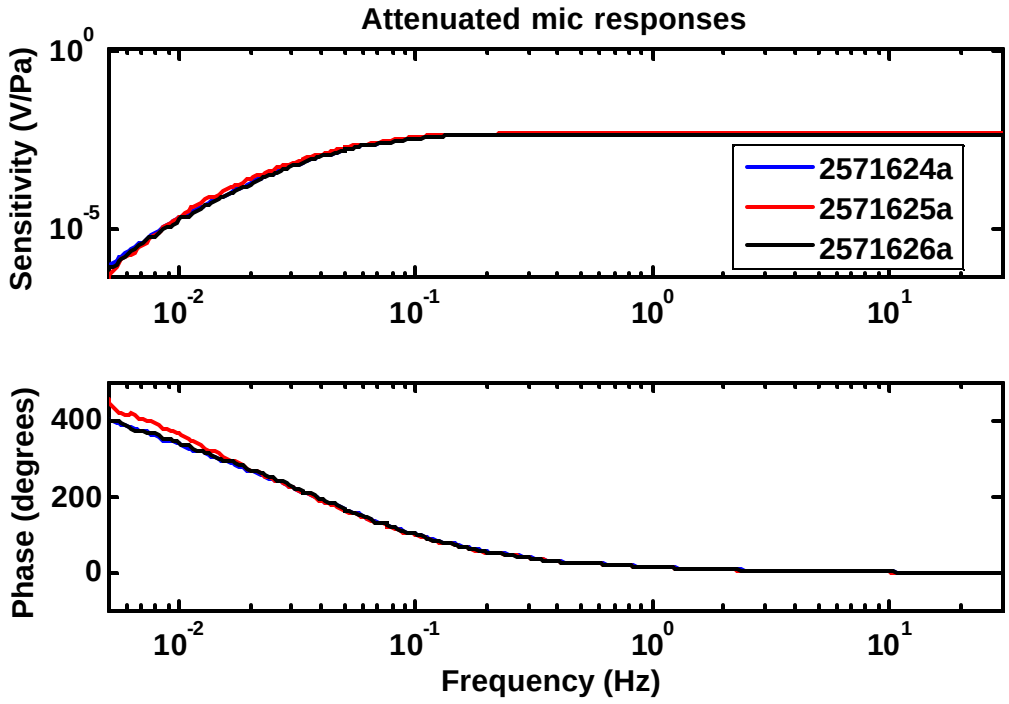

Figure **5-11**: Calibration curves compared for three different microphones, normalized by the 30 Hz sensitivity.

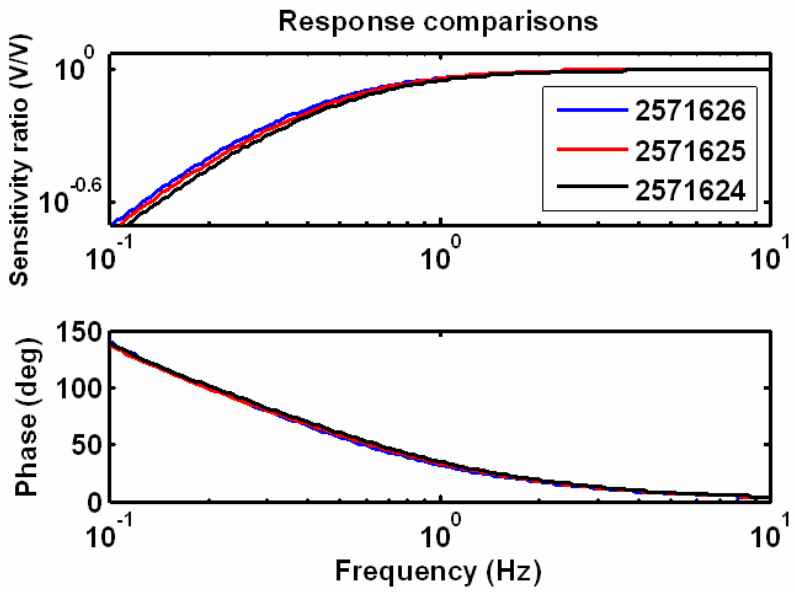

Figure **5-12**: Response comparisons zoomed in to 0.1 to 10 Hz, to make the differences between microphones visible.

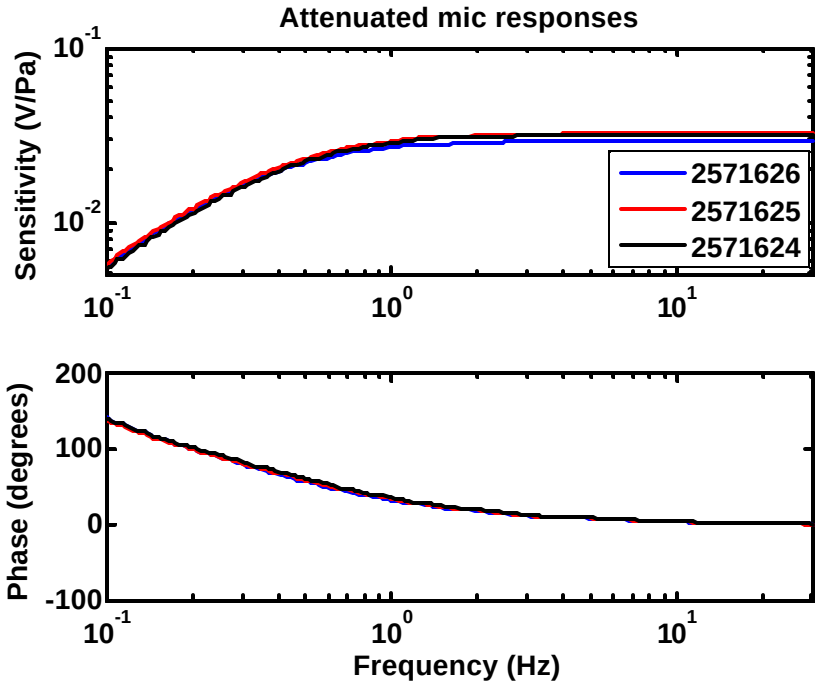

Figure **5-13**: The same graph as Figure **5-12**, but in V/Pa.

Figure **5-11** shows that above 0.01 Hz the *B&K* 4193 microphones have consistent frequency responses. From Figure **5-12** and Figure **5-13** small differences can be seen in the -3dB down point. Serial number 2571626 is the least sensitive of the three microphones, according to Figure **5-13**; however, it also has the lowest -3dB down point, as can be seen in Figure **5-12**. The less sensitive microphone therefore has a slightly wider bandwidth, which makes sense from a gain-bandwidth standpoint: the bandwidth can be extended by sacrificing gain. Perhaps the capsule of 2571626 has a source of stray capacitance.

5.3 Chapter 5 summary

The present infrasonic pistonphone design is capable of calibrating measurement microphones in a highly repeatable manner, over a wide range of frequencies. For the *B&K* 4193 measurement microphones characterized, useful response measurements extended as low as 0.0035 Hz.

A method for evaluating the performance of bandwidth-extending accessories is presented, as well as methods for characterizing the mechanical roll off of the microphone diaphragm. Additional calibration results made using the infrasonic pistonphone are found in appendix **D**.

Chapter 6

Conclusions

6.1 Conclusion overview and goal fulfillment

As stated in Chapter 1, the goal of this thesis research has been to make a total-immersion pistonphone calibrator capable of calibrating acoustic transducers at infrasonic frequencies without the use of a reference transducer, and to demonstrate such a design through actual calibrations. The principal challenge in this approach is accurately accounting for thermal and viscous effects due to chamber walls. This thesis has described the mechanical design of a pistonphone that produces a controlled calibration signal across a large range of frequencies (0.001 to 30 Hz). The pistonphone functions in conjunction with a theoretical model that predicts the pressure inside the pistonphone chamber in the presence of thermal and viscous effects.

Comparisons have been made with actual measurements. Though a discrepancy consistently exist between the model and measurements around the adiabatic-to-isothermal region of operation, the discrepancy appears to vanish when helium is used, confirming the thermo-viscous model in nearly ideal circumstances. Despite the loss in calibration accuracy due to the discrepancy, the magnitude of the calibration error caused by the discrepancy consistently remains at roughly 5% or below, and is significantly less throughout most of the calibration range. This is a large improvement over the 30% peak error that can occur if no thermo-viscous model is used.

Several models of microphones have been calibrated using the pistonphone described in this paper, and comparisons with relative calibrations and 250 Hz calibrations using standard pistonphones compare favorably. These calibration measurements verify the pistonphone as a potentially useful design for accurate calibration of acoustic transducers at infrasonic frequencies.

6.2 Research summary and findings

The infrasonic pistonphone calibration process developed in this research works by predicting the pressure generated inside the tube and comparing it to the voltage output of a transducer fully immersed inside the pistonphone chamber. The pressure is computed from a direct measurement of the displacement of the piston via a linear-variable-differential-transformer (LVDT) and a thermoviscous acoustic model for the relationship between the volume change and the chamber pressure. For the geometry of the present pistonphone design, the pressure oscillations at the lowest frequencies are nearly isothermal and nearly adiabatic at the highest frequencies.

Because the source of the acoustic signal is a displacement source rather than a pressure source, the pressure generated inside the tube is a function of frequency. The acoustic pressure amplitude changes by a factor of gamma (1.402 for air) as the pressure oscillations cross the adiabatic-to-isothermal transition. In the developed calibration process, this transition is mimicked by modeling the pistonphone chamber as an electrical transmission line with a current source. The impedance elements of the transmission line model vary with frequency according to the values predicted by Rott's momentum and continuity equations.

The dominant impedance in the frequency range of the adiabatic-to-isothermal transition for the present pistonphone geometry is acoustic compliance. The change in compliance predicted by Rott's equations is confirmed by predicting the change in compliance directly from the heat equation describing the thermal profile in the tube as a function of frequency:

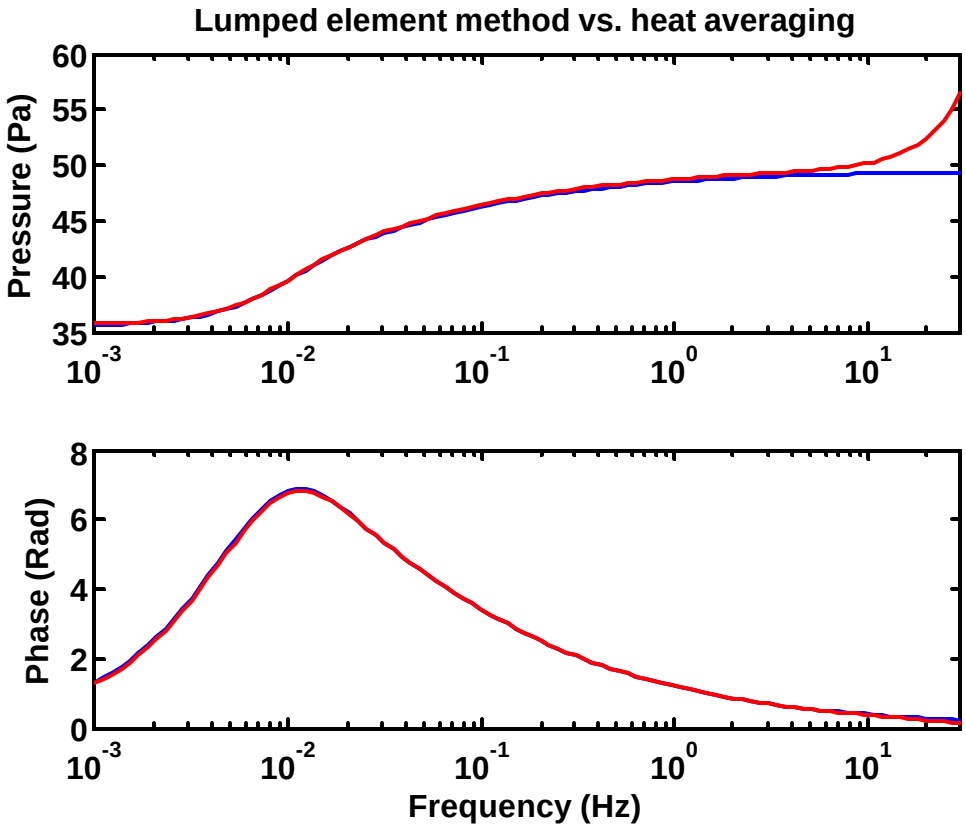

Figure **6-1**: Confirmation of the lumped element adiabatic-to-isothermal transition, by comparison with the same transition predicted using the heat equation and the ideal gas law. The heat equation prediction assumes only compliance and thus exhibits no resonance effects.

The lumped impedance model is additionally confirmed in this thesis through extensive experimental testing. This is done by comparing the predicted pressure response with the pressure response measured directly by a differential pressure sensor. Figure **6-2** is an example of a model vs. measurement comparison made in a chamber filled with air:

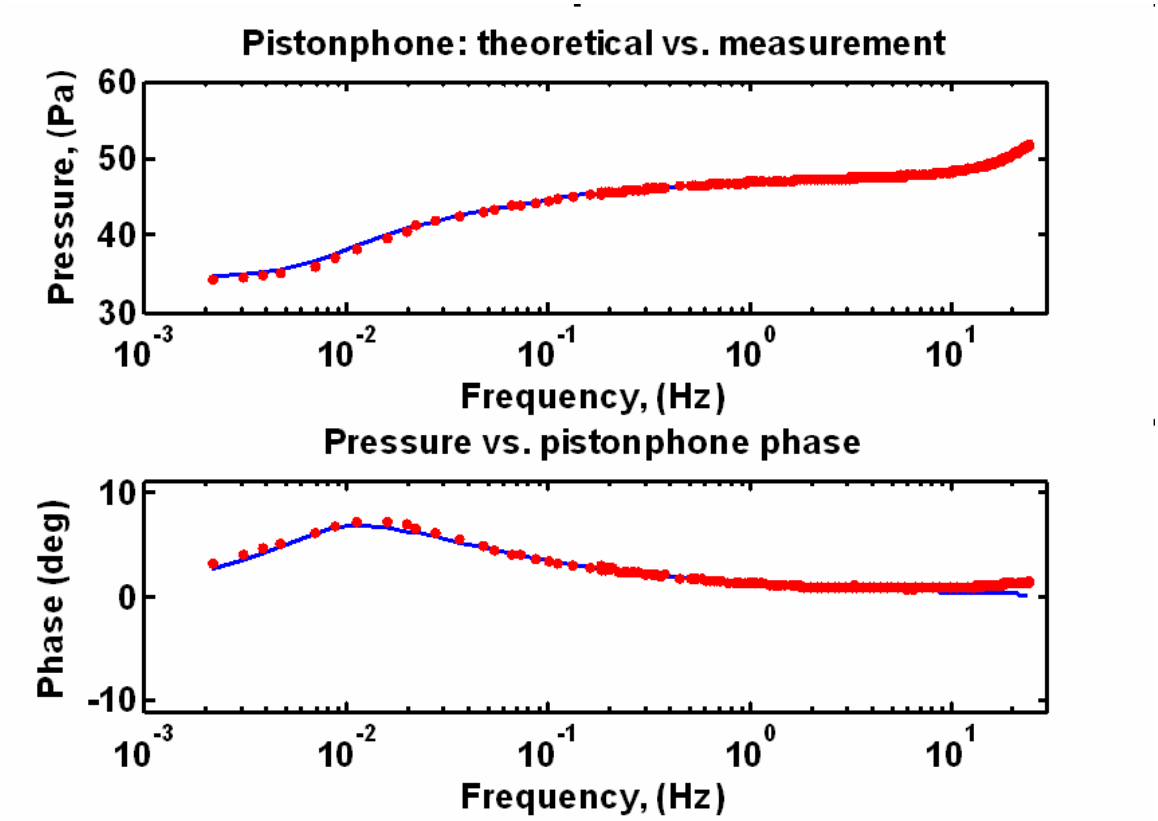

Figure **6-2**: An early measurement of the pressure response inside the pistonphone, compared to the pressure response predicted by the model.

The earliest measurement of the adiabatic-to-isothermal transition in the present pistonphone design, plotted in Figure **6-2** , shows excellent correspondence with the prediction made for the pistonphone geometry using the lumped element model. Subsequent to this measurement, an improved LVDT was installed and several other adjustments were made to the system. After these modifications, a relatively small but repeatable derivation was observed between the measured and modeled chamber pressure. Figure **6-3** shows the pressure response inside the most recent version of the pistonphone calibrator:

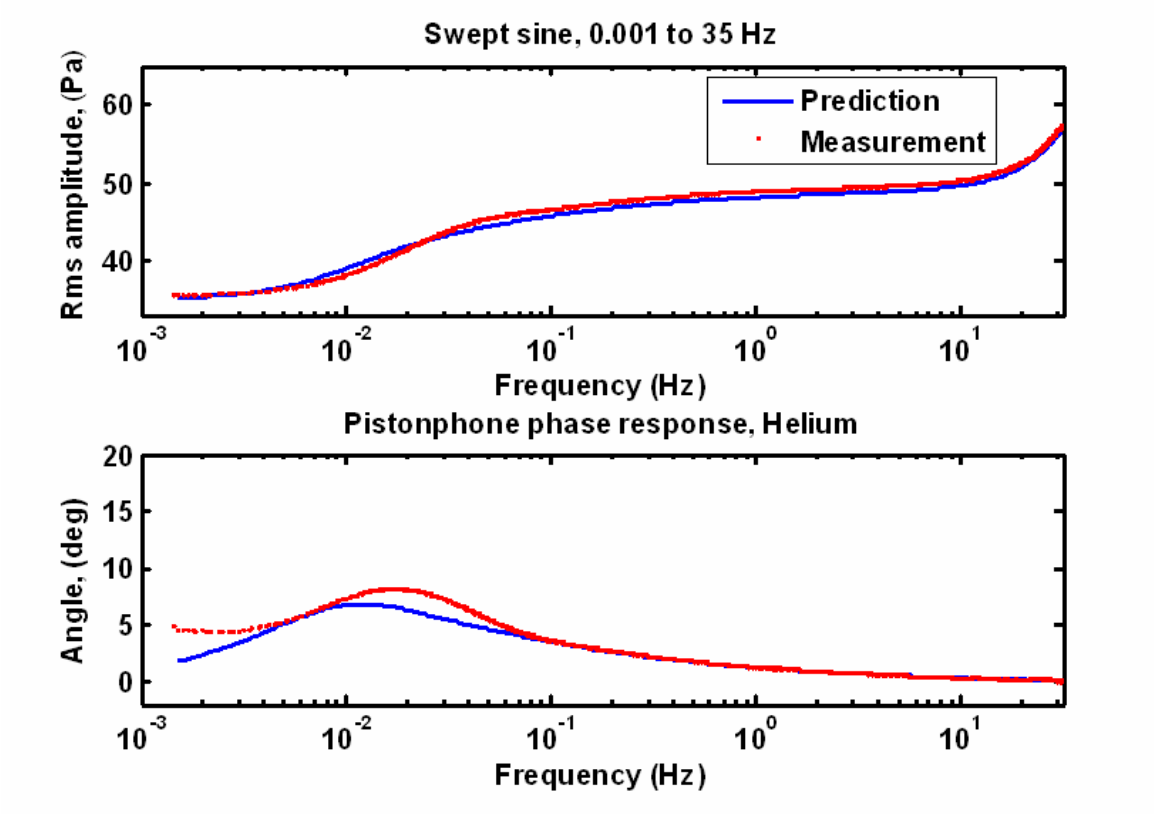

Figure **6-3**: Most recent version of the pistonphone pressure measurement results.

Visible in Figure **6-3** are deviations between model and measurement in both the magnitude and phase response. These deviations are not visible in Figure **6-2**. The phase and magnitude deviations that appear in Figure **6-3** consistently appear in all measurements made in both air and other gases having a similar penetration depth. Figure **6-4** shows the magnitude scaling and phase difference errors between the model and measurements for various calibrations in air:

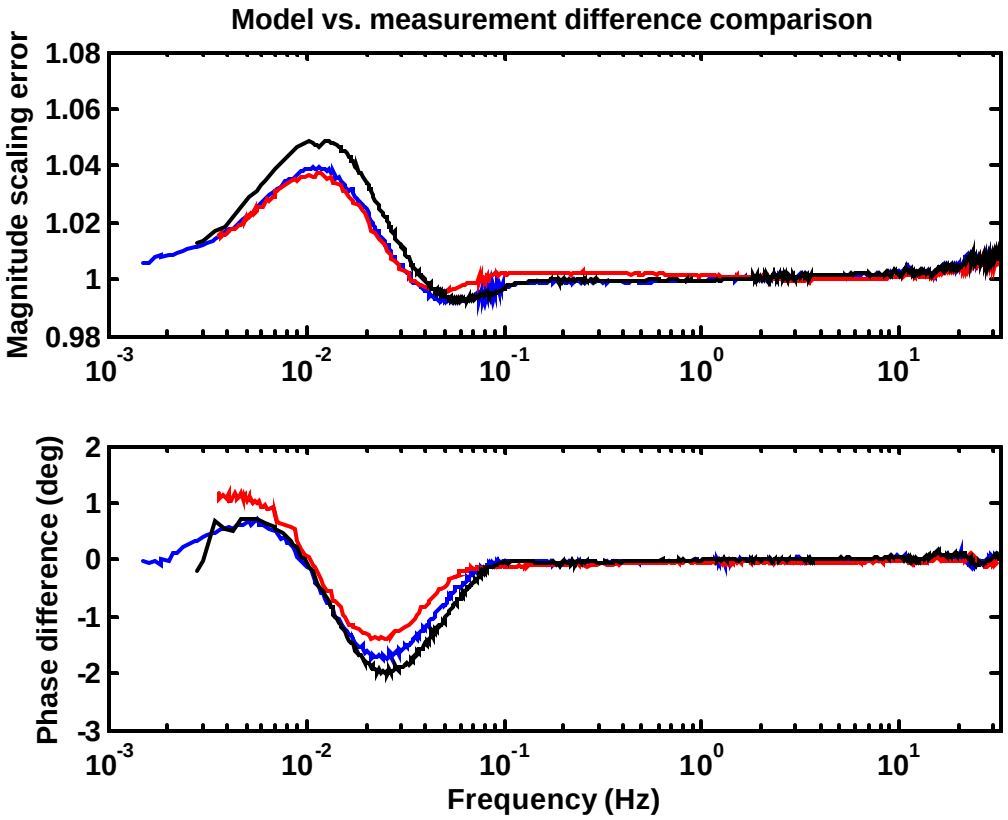

Figure **6-4**: Scaling and phase difference error for three pistonphone chamber pressure response measurements. The maximum magnitude error lies below 6% on all tests, and above 0.1 Hz the scaling error lies below 1%.

The model and the measurements appear to have some significant discrepancies. The discrepancies are significant although far smaller than would result if one neglects thermo-viscous effects.

Much effort was expended in attempting to isolate and eliminate this systematic error. In the process, it was discovered that the lumped element model predicts the pressure response inside the pistonphone chamber almost perfectly when helium gas is used. The prediction and the measurement for helium gas are shown in Figure **6-5** .

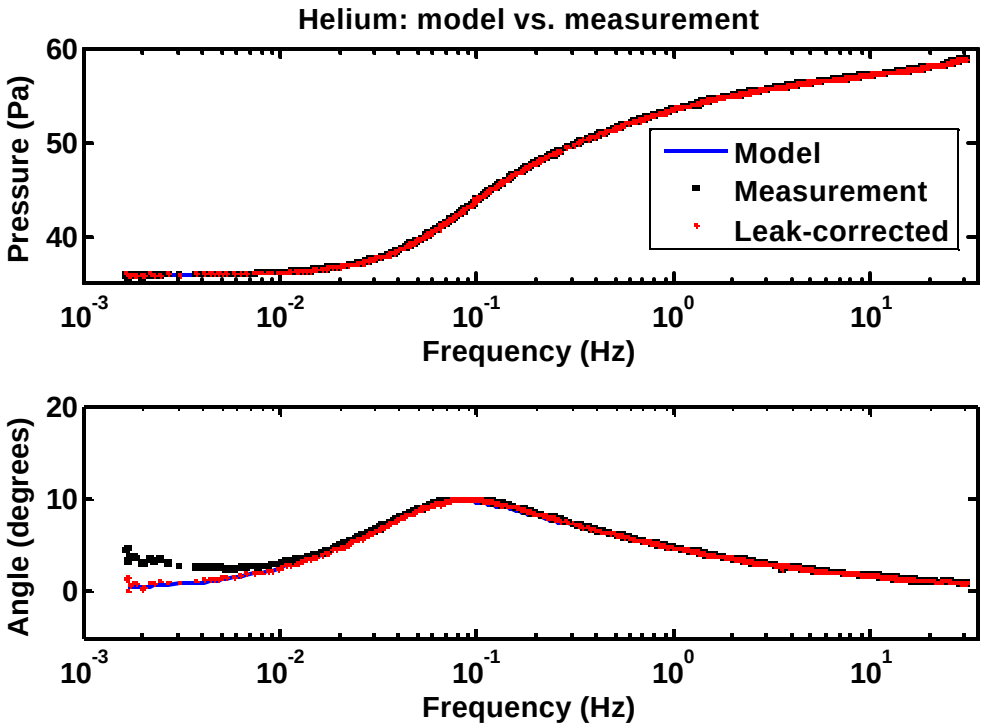

Figure **6-5**: Pressure predictions and measurements made inside the pistonphone chamber, when the chamber is filled with helium.

The helium experiment confirms that the model is most likely not the cause of the deviation and that the discrepancy is not likely to be directly associated with the adiabatic-to-isothermal transition. Various methods are used to attempt to isolate the error and many sources of error including: humidity, relaxation, signal processing techniques, LVDT circuitry error, pressure sensor response error, in-adequate modeling of the solid properties of the chamber, and end-cap losses, are eliminated as the primary source of the recurring measurement/model deviation. The cause is still undetermined.

Despite the persistence of the roughly 5% peak error (0.45dB) introduced into the calibration measurements, the peak error is still small compared to the error introduced by ignoring thermo-viscous effects.

An absolute calibration of a B&K 4193 microphone is shown, along with a relative calibration made for comparison. The reference transducer used for the relative

calibration is the same transducer used to measure the pressure response inside the tube. Figure **6-6** shows the results of the two calibration methods:

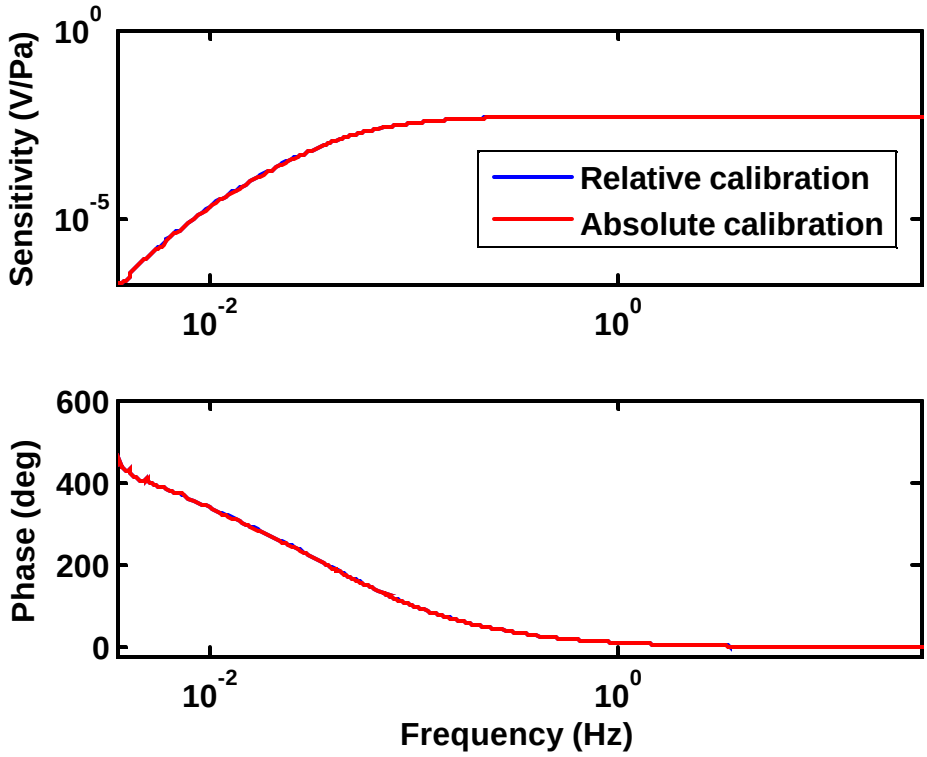

Figure **6-6**: Relative and absolute calibrations for *B&K* 4193 serial number 275624

A number of additional measurements were made:

- A measurement to isolate the low-frequency roll-off from the microphone pressure-equalization leak.
- An evaluation of the low-frequency bandwidth extension accessory
- An evaluation of the stability of mic response over several calibrations
- Measurements of a group of four mics of the same model to evaluate variations in response.

These measurements demonstrate the potential of the pistonphone to aid in making a wide variety of response and performance characterizations of acoustic transducers.

6.3 Research conclusions and future work

Historically, microphone calibrations focus on the response magnitude; however, the phase response is crucial in understanding the influence of the microphone on acoustic-pulse waveforms. The pistonphone described here was designed specifically for absolute calibration of both magnitude and phase. The magnitude and phase response of several transducers have been directly measured using the infrasonic pistonphone described in this thesis. Infrasonic pistonphone calibration is not free from difficulties or complications; however, this research has demonstrated that if construction, measurements, and post processing are done carefully, pistonphone calibration is a viable method for characterizing the low-frequency response of some important acoustic measurement transducers.

Despite the success of this demonstration, much work can still be done to improve the pistonphone design. The exact cause of the model vs. measurement discrepancy is still unknown, and calibrations could be greatly improved if the source of error could be located and either eliminated or properly modeled. Additionally, many other mechanical improvements could be made. The following paragraphs describe some mechanical improvements that could greatly aid transducer calibration.

The Airpot™ graphite and glass piston makes an extremely useful addition to the design; however, it would be advantageous to drive the shaft directly using a linear motor rather than a rotational motor and set of gears. Excess vibration could be reduced, and the wave-form improved with such an addition. Furthermore, different calibration sound pressure levels could be easily achieved.

Mechanical design could further be improved by making a better connection between the piston shaft and piston head, to eliminate any error that would be caused by independent motion of the piston head and shaft.

The transducer insertion hole at the end of the chamber is too narrow to accommodate transducers with diameters wider than one inch. Such transducers must be inserted by removing the cone at the front of the pipe. A better transducer insertion method would ease the calibration process of some transducers.

The precision rectifier circuit used has fairly low DC offset drift, but the effects of drift are still visible. Creating a design with less offset drift would increase the accuracy of displacement measurements over long periods of time.

Uncertainty in measurements of the volume of the chamber contributes significantly to calibration error. Calibration uncertainty could be reduced by finding a more exact figure for the volume – perhaps by weighing or measuring the amount of water require to completely fill the chamber.

PVC is a cheap, stiff, easily to machine material; however, its thermal properties are very poor for the present application. The walls would resemble ideal walls more closely if the chamber walls could be replaced with aluminum or some metal instead of PVC.

A chamber with an integrated, seamless taper on the front of the end instead of a series of joined disks would improve the seal of the chamber and similarity between the physical design and theoretical model.

The seals around the major sources of leakage – the transducer insertion plug and seal between the cone and main chamber – could be improved.

The pistonphone could be placed on a moveable cart so that it could be shipped or moved to different locations.

The method for measuring ambient pressure inside the control and main chambers could be improved.

As has been demonstrated in this thesis, the pistonphone as it is currently designed appears to work in a reasonably effective manner; however, these changes in design and many others could improve the ability of the pistonphone to make accurate calibrations. The author of this thesis wishes to express a sincere hope that some of this research may be useful to acousticians making measurements in the field of infrasonics, and any improvements upon this research are welcomed.

Bibliography

1. B. Alcoverro, "Device for calibrating a pressure detector." U. S. Patent No. 7,249,487 (2007)

2. B. Ben-Ary, and Uri Fehr, "Analytical Review of the Electromechanical Piston and the Modified Moore Variomeder used in infrasound studies." J. Acoust. Soc. Am. 41, pp. 1599 (1967)

3. F. Biagi, and R. K. Cook, "Acoustic impedance of a right circular cylindrical enclosure." J. Acoust. Soc. Am. 26, pp. 506 – 509 (1954)

4. H. E. Dahlke and J. J. Van Houten, "Pistonphone Calibration of Microphones at Infrasonic Frequencies." J. Acoust. Soc. Am. 37, pp. 1209 (1965)

5. Fred B. Daniels, "Acoustic impedance of enclosures." J. Acoust. Soc. Am. 19, pp. 569 – 571 (1947)

6. F.B. Daniels, "On the propagation of sound waves in a cylindrical conduit." J. Acoust. Soc. Am. 22, pp. 563, 564 (1950).

7. T. B. Gabrielson, *Compliant walls: lecture notes*, The Pennsylvania State University, 2006

8. T. B. Gabrielson, "Extraction of infrasonic waveforms from conventional condenser microphones," J. Acoust. Soc. Am. 122, pp. 2958-2959 (2007)

9. T. B. Gabrielson, *Low frequency response of B&K4193 microphones: unpublished measurements*, Penn State, 2008

10. S. I. Hayek, *Advanced Mathematical Methods in Science and Engineering*, CRC Press, 2001

11. W. Hill, P. Horowitz, *The Art of Electronics*, 2nd ed, Cambridge University Press, 1989

12. R. Horuichi, T. Fujimori, and S. Sato, "Development of a laser-pistonphone for an infrasonic measurement standard." J. Acoust. Soc. Am. 120, pp. 3233 (2006)

13. W. Howard, K. Dillon, and F. D. Shields, "Acoustic properties of porous hose wind-noise filters," J. Acoust. Soc. Am. 122, 2985 (2007)

14. I. E. Idelchik, *Handbook of hydraulic resistance*, 3rd edition, (Begell House), 1996

15. T. Marston, "Diffraction correction and low-frequency response extension for condenser microphones," [M.S. Thesis] *The Pennsylvania State University*, 2006

16. T. Marston, and T. B. Gabrielson, "Comparison of measurement and theory for the acoustic pressure field in an infrasonic calibrator through the isentropic-to-isothermal transition", J. Acoust. Soc. Am. 122 pp. 2984 (2007)

17. G. Rassmussen, "Infrasonic Instrumentation." J. Acoustic. Soc. Am. 122, pp. 2984 (2007)

18. N. Rott, "Thermoacoustics." Adv. Appl. Mech. 20, 135 (1980)

19. T. Starecki, "Loss improved electroacoustical modeling of small Helmholtz resonators." J. Acoust. Soc. Am. 122, pp. 2118-2123 (2007)

20. G.W. Swift, "Thermoacoustic engines." J. Acoust. Soc. Am. 84, pp. 1145 – 1180 (1988)

21. G.W. Swift, *Thermoacoustics*, (Acoustical Society of America), 2002

22. Stephen C. Thompson, and J. L. LoPresti, "Thermal boundary layer effects on the acoustical impedance of enclosures and consequences for acoustical sensing devices." J. Acoust. Soc. Am. 123, pp. 1364 – 1370 (2008)

23. L. Wilen, "Measurements of scaling properties for acoustic propagation in a single pore." J. Acoust. Soc. Am. 101, pp.1388 – 1397 (1996)

24. L. Wilen, "Measurements of thermoacoustic functions for single pores." J. Acoust. Soc. Am. 103, pp.1406 – 1412 (1997)

25. L. Wilen, "Dynamic measurements of the thermal dissipation function of reticulated vitreous carbon." J. Acoust. Soc. Am. 109, pp.179 – 184 (2001)

26. Allan J. Zuckerwar, J. E. Teter, and W.E. Robbins, "Infrasonic Pistonphone" J. Acoust. Soc. Am. 115, pp. 2527 (2004)

27. http://www.mikesflightdeck.com/lvdt_circuitry.htm

Appendix A

Calculating the internal pistonphone pressure field using *pfunc.m*

"pfunc.m" is the name of a Matlab function that has been written for the special purpose of calculating the pressure inside the pistonphone at the location of a transducer immersed in the chamber. This code, in various forms, was used for all pressure predictions plotted in this thesis. In this section of the appendix, the function and its sub-functions will be broken down, portion by portion.

A.1 *pfunc.m*

```
function [resp, pnorm] = Pfunc(F, calpres, swingin, plotting, sclr, Micloc);
```

The above line is the function call statement, showing the inputs and outputs of the function. The inputs are the following:

1) *F:* A one-dimensional column or row vector containing all the frequencies in Hz that the function will evaluate the pressure response at. It is advisable to keep this value below 50 Hz because of some numerical problems that occur when evaluating the F-function at higher frequencies for the pistonphone geometry.
2) *Calpres:* The calibration pressure in *millibars*. This will adjust the output pressure according to the ambient pressure inside the chamber at the time of calibration.
3) *Swingin:* This is the peak-to-peak swing of the piston, in inches, of the model piston. The standard value used in the code is 1 inch.
4) *Plotting:* If this value is set to 1, then the code will return a plot of the magnitude and phase of the generated pressures at the passed frequencies. If it is set to 0, nothing will be plotted.
5) *Sclr:* If this value is set to 1, the plot will be normalized by the adiabatic pressure response value. This kind of returned response is the type that can be divided from a measured microphone response, to compensate for the adiabatic-to-isothermal transition calibration error.
6) *Micloc:* This is the distance from the end-cap of the main chamber that the transducer is located in meters.. The differential transducer is permanently located 0.1 m from the end, and the *B&K* 4193 microphones are calibrated consistently near 0.83 m from the end.

The function returns the following:

1) *Resp:* This is a complex pressure vector that contains pressure magnitude and phase information. The phase is with respect to the piston displacement.
2) *Pnorm:* This is the adiabatic, purely compliant pressure response. It can be used as a normalization value to turn the *Resp* vector into a scaling correction vector.

```
% DEFINE THE CONSTANTS
% These will be the atmospheric and density conditions for the p-phone
rho = 1.21;             % Density: 1.2 kg/m3
gamma = 1.402;            % Ratio of specific heats
c = 341;                % Speed of sound, room temp.
Atcor = calpres/1013;


w = 2*pi*F;
f1 = min(F);
f2 = max(F);
```

The above lines of code define gas properties, and the atmospheric pressure correction factor. The passed frequencies in the *F* vector are converted to angular frequency in radians-per-second, and *f1* and *f2* are used for plotting, later.

```
prad = (0.942*2.54/2)/100;
pswing = swingin*0.0254/2;

vv = (w)*(pswing)*(pi*prad^2);    % Generated volume velocities
```

Prad is the piston radius in meters, based on a micrometer measurement. *Pswing* is the amplitude (pk-pk/2) of the piston swing in meters. From these two values and the angular frequency vector, *vv*, the vector containing all the volume velocities, is calculated. The values in *vv* are one of the boundary conditions for the pistophone chamber.

```
Tubemeas = [3.7800, 3.7832, 3.7719, 3.7722, 3.7660, 3.7779, 3.7803,
3.7762, 3.7780, 3.779];
TubeDiam = sum(Tubemeas)/length(Tubemeas);
mnrad = (TubeDiam*2.54)/100;
mnrad = mnrad/2;            % It's a radius

tblen = 58.4375*2.54/100;
cnlen = 9.656*2.54/100;
cylen = 1.49*2.54/100+0.01;
```

The previous lines of code are measured geometrical values for the pistonphone chamber. 10 micrometer-measured values for the inner radius of the main chamber are

given in *Tubemeas*. These values are averaged in *TubeDiam*, and converted to an average radius in meters, in *mnrad. Tblen* is the length of the main tube, measured in inches but converted to centimeters. *Cnlen* is the length of the cone at the front of the main chamber, and *Cylen* is the length of the cylinder, from mouth to center-point of piston swing.

```
a2 = [ prad      prad    mnrad           mnrad;
       prad     mnrad    mnrad           mnrad;
       cylen     cnlen    tblen-Micloc    Micloc;
       100       100      100             10;]

num2 = length(a2(1,:));
```

This is the “chamber definition matrix.” The top row of each column is the opening radius of the segment, the second row is the closing radius of each segment, the third row is the length of each segment, and the last row is the number of Tee-sections used to model each segment. Column 1 is the cylinder housing the piston. Column 2 is the cone, (the opening and closing radii are different), column 3 is the portion of the main chamber in front of the immersed transducer, and column 4 is the portion of the main chamber behind the immersed transducer. *Micloc* is the passed location parameter.

```
for n = 1:length(w)
    Tf = 1;
    for nn = 1:num2-1
        T = Tcalc(a2(:,nn), w(1,n));
        Tf = Tf*T;
    end
    Tf2 = Tcalc(a2(:,num2), w(1,n));
    clear T;
    T = [Tf(2,1), Tf(2,2); Tf2(2,1), -Tf2(2,2)];
    P = inv(T)*[vv(n); 0];
    P2(1,n) = P(1);
end
```

This loop carries out the calculations described in **3.3** for finding the pressure at the location of the transducer. The outer *for* loop is over all frequencies, because the values of the impedances in the Tee-sections will vary with frequency. The inner *for* loop calculates the conglomerate Tee-section describing the chamber between the piston cylinder and the transducer. The *Tcalc.m* function (described in the next section), calculates the transfer matrix for a passed column of the *a*-matrix. The conglomerate transfer matrices for each segment between the piston and transducer are multiplied together in *Tf*.

Tf2 is the transfer matrix for the last segment of the chamber, between the transducer and the end-cap. The last portion of the loop calculates the complex pressure at the location of the transducer using these transfer matrices.

```
mags = Atcor*abs((P2)/(sqrt(2)));
```

```
phas = angle(j*P2);
vl = avol(a2);
swvol = ((pswing/sqrt(2)))*(pi*prad^2)
pnorm = gamma*calpres*100*swvol/vl;
```

Mags and *Phas* are magnitude and phase vectors used for plotting if plotting is requested when the function is called. *Vl* is the volume of the chamber, as calculated by the *"avol"* function, described in [sec]. *Swvol* is the ? V value, caused by the swing of the piston. *Pnorm* is the adiabatic pressure response of the chamber, calculated using V and ?V. *Pnorm* is a returned value.

```
if sclr == 1
    mags = mags./pnorm;
end
```

This conditional makes the returned magnitudes and phases into a correction type vector if the *sclr* input is set to 1.

```
if plotting == 1 & sclr ~= 1
    figure;
    subplot(2,1,1)
    semilogx(F, mags, 'k');
    axis([f1, f2, 30, 60])
    xlabel('Frequency (Hz)');
    ylabel('Rms amplitude, Pa');
    title('Swept sine, 0.001 to 35 Hz')

    subplot(2,1,2)
    semilogx(F, R2D(phas), 'k');
    axis([f1, f2, 0, R2d(pi/16)]);
    xlabel('Frequency (Hz)');
    ylabel('Angle, (deg)')
elseif plotting == 1 & sclr == 1
    figure;
    subplot(2,1,1)
    semilogx(F, mags, 'k');
    axis([f1, f2, 0.5, 2])
    xlabel('Frequency (Hz)');
    ylabel('Rms amplitude, Pa');
    title('Swept sine, 0.001 to 35 Hz')

    subplot(2,1,2)
    semilogx(F, R2D(phas), 'k');
    axis([f1, f2, 0, R2D(pi/16)]);
    xlabel('Frequency (Hz)');
    ylabel('Angle, (deg)')
end
```

These are plotting commands, if the *plotting* input is set to 1.

```
resp = mags.*exp(j*phas);
```

The last line of code defines the returned complex pressure vector. It is reassembled from the magnitudes and phases using a complex exponential.

A.2 *Tcalc.m*

Tcalc.m is sub-function of *pfunc.m* which returns the transfer matrix for a passed angular frequency and column of the *a*-matrix defining the pistonphone geometry. It is where most of the modifications occur when gas and wall properties are altered.

```
function [T] = Tcalc(aa, w)
```

This is the function call statement for *Tcalc.m* The passed parameters are:

1) *aa:* This is a one dimensional, four element column vector describing a segment of tubing. Value 1 is the opening radius of a segment, value 2 is the closing radius, value 3 is the length, and value 4 is the number of differential slices the segment will be chopped into. The first three values are in meters.
2) *w:* This vector is the angular frequency at which the impedances in the segment will be evaluated at.

The returned parameters are:

1) *T:* This is the transfer matrix resulting from a multiplication of all the transfer matrixes describing each differential Tee-section slice, for the segment described by *aa*.

```
rho = 1.21;             % Density: 1.2 kg/m3
gamma = 1.4;            % Ratio of specific heats
c = 341;                % Speed of sound, room temp.
p0 = (rho*c^2)/gamma;   % Ambient Pressure
```

Properties for the gas inside the chamber.

```
%% FIRST SEGMENT: small segment length 10 cm connected to pistonphone
L = aa(3);
N = aa(4);                      % Number of elements in pipe model
dx = L/N;                      % The length of each model element
n = 1;
```

L is the length, as defined by *aa*. *N* is the number of differential segments, *dx* is the length of each tube slice as defined by the passed length and number of slices. *n = 1* is a remnant command from a previous version of the code.

```
if aa(1) == aa(2)
```

If the opening radius and closing radius are equal, the following calculations will be done…

```
a = aa(1);
A = pi*a.^2;
nn = 1;
du = sqrt(2*1.85e-5/(w(1,n)*1.21));     % Viscous
dk = sqrt(2*2.3e-5/(w(1,n)));           % Thermal

fu = (2*besselj(1, (j-1)*a(1,nn)/du))...
  /(((j-1)*a(1,nn)/du)*besselj(0,(j-1)*a(1,nn)/du));   % viscous
fk = (2*besselj(1, (j-1)*a(1,nn)/dk))...
  /(((j-1)*a(1,nn)/dk)*besselj(0,(j-1)*a(1,nn)/dk));   % thermal
```

a is defined as the radius of the tube, and *A* is the cross-sectional area. *nn = 1* is an assignment that varies if a cone is being evaluated but is held at 1 because this is a cylinder. It will be explained during the cone description. *du* and *dk* are the thermal and viscous penetration depths for room temperature air. *fu* and *fk* are the thermal and viscous *f*-functions, calculated with the penetration depths and slice geometry.

```
dm = (rho*dx/A(1,nn))*(1 - real(fu))/(abs(1 - fu))^2;
dC = (A(1,nn)*dx/(gamma*p0))*(1 + (gamma - 1)*real(fk));
dRu = ((w(1,n)*rho*dx)/(A(1,nn)))*imag(-fk)/(abs(1 - fu))^2;
Gk = (w(1,n)*A(1,nn)*dx/(gamma*p0))*(gamma - 1)*imag(-fk);
dRk = 1/Gk;

Zm = j*w(1,n)*dm;
ZC = 1/(j*w(1,n)*dC);

Z1 = (Zm/2 + dRu/2);
Z2 = (ZC*dRk/(ZC + dRk));
```

dm, dC, dRu, dRk are the differential acoustic mass, compliance, and thermal and viscous dissipation resistances that can be plugged into the Tee-sections for the slices of the segment. *Z1* is the series combination of the mass and viscous resistance impedances, (divided by two because of the Tee-section arrangement), and *Z2* is the parallel combination of the compliance impedance, and the thermal dissipation resistor.

```
T = [(1 + Z1/Z2), (2*Z1 + (Z1^2)/Z2); (1/Z2), (1 + Z1/Z2)];
T = T^N;
```

The transfer matrix is assembled from the calculated impedances, and raised to a power equal to the number of slices to represent the total transfer-matrix if each of the slices were multiplied together.

```
else
```

If the opening and closing radii are not equal, then the segment is a cone and the following code is run…

```
a = linspace(aa(1), aa(2), N);
A = pi*a.^2;
a1 = a;
TT = 1;
```

In this case *a*, the radius, is not constant and a vector varying linearly, with *N* elements, is constructed containing the radii for the Tee-sections to be assembled to form the cone. *TT* will be the vector containing the total transfer matrix for the whole cone, but is initialized to 1.

```
for nn = 1:N
    du = sqrt(2*1.85e-5/(w(1,n)*1.21));     % Viscous
    dk = sqrt(2*2.3e-5/(w(1,n)));           % Thermal

    fu = (2*besselj(1, (j-1)*a(1,nn)/du))/...
        (((j-1)*a(1,nn)/du)*besselj(0,(j-1)*a(1,nn)/du));
    fk = (2*besselj(1, (j-1)*a(1,nn)/dk))/…
        (((j-1)*a(1,nn)/dk)*besselj(0,(j-1)*a(1,nn)/dk));
```

The inner loop, begun here, evaluates each individual Tee-section. The *f*-functions are evaluated *a(1,nn)*, where *a* is the vector containing the radii along the cone, and *nn* is the element containing the local radius.

```
    dm = (rho*dx/A(1,nn))*(1 - real(fu))/(abs(1 - fu))^2;
    dC = (A(1,nn)*dx/(gamma*p0))*(1 + (gamma - 1)*real(fk));
    dRu = ((w(1,n)*rho*dx)/(A(1,nn)))*imag(-fk)/(abs(1 - fu))^2;
    Gk = (w(1,n)*A(1,nn)*dx/(gamma*p0))*(gamma - 1)*imag(-fk);
    dRk = 1/Gk;

    Zm = j*w(1,n)*dm;
    ZC = 1/(j*w(1,n)*dC);

    Z1 = (Zm/2 + dRu/2);
    Z2 = (ZC*dRk/(ZC + dRk));
```

```
        T = [(1 + Z1/Z2), (2*Z1 + (Z1^2)/Z2); (1/Z2), (1 + Z1/Z2)];
        TT = TT*T;
```

The impedance definitions are exactly like in the cone section, except that the impedances are defined for the local radius, *a(1,nn)*. The total matrix, *TT*, is assembled by multiplying the transfer matrix *T*, by the total *TT*, every time the loop is completed for each radius.

```
        end
        T = TT;
    end
```

The final two lines of the code, the output vector, *T*, is defined as the total matrix, and the function is ended. *T* is used twice in this code, once to represent a local Tee-section transfer matrix, and at the end of the code, storing the total matrix.

A.3 *avol.m*

avol.m is a function that returns the volume of a chamber defined by an *a*-matrix. It has the following call pattern:

```
function    [vol] = avol(a);
```

The passed parameter is an *a*-matrix for a chamber volume, and the returned value, *vol*, is the volume in meters cubed.

```
for n = 1:nseg
    if a(2,n) == a(1,n)
        vol(n) = pi*a(1,n)^2*a(3,n);
    else
        r1 = a(1,n);
        r2 = a(2,n);
        h1 = a(3,n);
        vol(n) = (pi/3)*(r1^3*h1/(r1-r2)-r1*r2^2*h1/(r1-r2)+r2^2*h1);
    end
end

vol = sum(vol);
```

This is the entire function. If the segment is a cylinder, the volume of the cylinder for the passed radius and length is calculated and stored in the *vol* vector. If it is a cone, the volume of the cone with the passed opening and closing radii is calculated. The *vol* vector is then summed and returned.

A.4 *aplot.m*

This function isn't specifically called in *pfunc.m*, however it is often used with the code, especially during the development, to plot the outline of the chamber, to enable the programmer to see what shape of tube is being evaluated. Figure **A-1** is an example of the kind of plot that can be generated using the code:

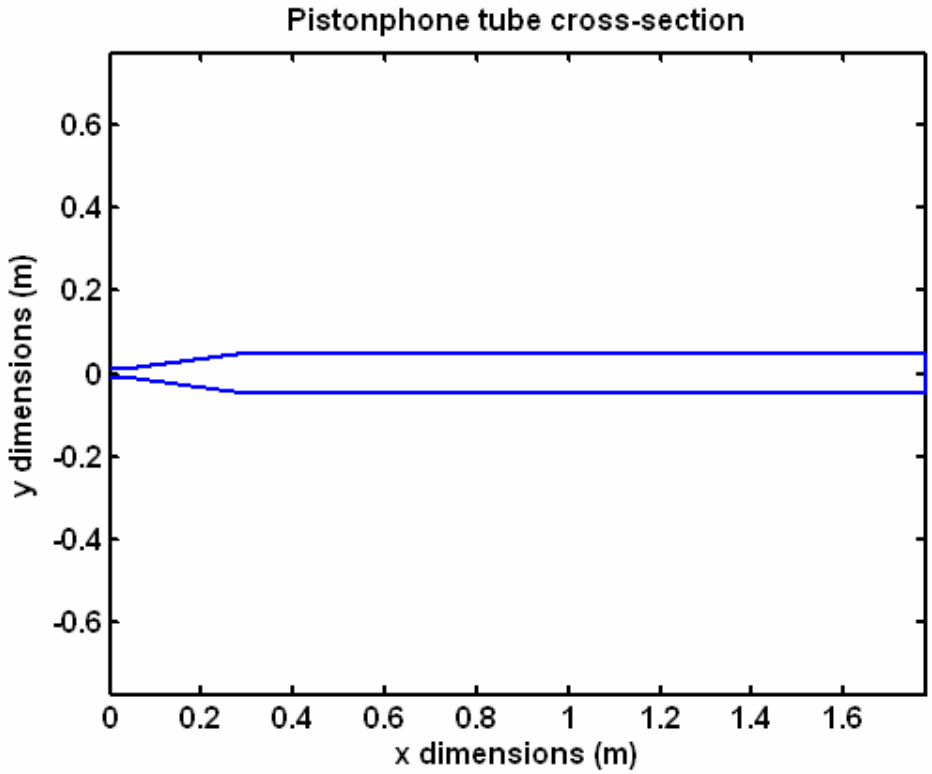

Figure **A-1**: The output of the *aplot.m* function when passed the *a*-matrix defining the pistonphone geometry.

The code has the following call pattern:

```
function [out] = aplot(a);
```

The input is an *a*-matrix for a chamber, and the output is meaningless, (out defined as 1, because at the time of coding the author was not proficient).

```
num = length(a(1,:));

plen = 0;
tlen = 0;
for n = 1:num
    seg = linspace(tlen, tlen+a(3,n), a(4,n));
    tlen = tlen + a(3,n);
    plen = [plen, seg];
end
len = plen(2:length(plen));
```

A vector is being assembled with all the x-values for all the points where the radius is defined.

```
trad = 0;
for n = 1:num
    r = linspace(a(1,n), a(2,n), a(4,n));
    trad = [trad, r];
end
rad = trad(2:length(trad));
rad2 = -fliplr(rad);
len2 = fliplr(len);
rad = [rad, rad2];
len = [len, len2];
```

A radius value is found for each x-value, and is mirrored over the x-axis. Another set of x-coordinates is made, in reverse, to correspond with the flipped x-values. It is reversed so that the plot will have a vertical line at the end-cap, and be open in the front.

```
plot(len, rad)
axis([0, max(len), -(30.1*max(rad) + 0.1)/2, (30.1*max(rad) + 0.1)/2])
xlabel('x dimensions (m)')
ylabel('y dimensions (m)')
title('Pistonphone tube cross-section')
out = 1;
```

The x-coordinates, and radii are plotted in a single graph, and the output, *out* is defined as 1.

Appendix B

Analyzing pistonphone signals with the HEBI code.

HEBI.m is a code specifically written for evaluating swept sine measurements made with the pistonphone. It essentially creates a spectrogram of two signals, the pressure signal and reference, displacement signal. The window-size of the spectrogram automatically adjusts to place the fundamental within a particular bin range. The ratio of the fundamentals is tracked as the spectrograms of the signals are assembled.

The code can be fairly easily altered to work with any swept sine signal that has a constant-amplitude reference signal. The accuracy verification of the code can be found in **4.7.2**. The code presented in this appendix evaluates the output of the differential pressure sensor mounted on the side of the pistonphone chamber. It is also the evaluation code used for measuring the response of immersed transducers, and the modifications made to the code to do this kind of data analysis are discussed in this appendix.

An overview of the functionality, and graphic illustrations of the signal processing are given in section **4.4.2**. For a reader unfamiliar with the HEBI code, it is highly advisable to read that section before or simultaneously with this section.

B.1 *HEBI.m* folder

To use the code as it is written, the HEBI.m file and supporting functions are placed in the same folder as the wave files generated from a pistonphone swept-sine measurement. There must not be other wav-files in the same folder or the code will return erroneous results. The code, as presented in this section, is optimized to work with four sets of wave files: 0.001 to 0.087 Hz data sets, 0.087 to 0.27 Hz data sets, 0.27 to 3.5 Hz data sets, and 1 to 30 Hz data sets. The ranges are defined by the most convenient gearing configurations. Each data set is a set of 4 wave files denoted by postscripts *a, b, c*, or *d.* So, for example, a file may have the following wave file names in it:

GX100301a.wav
GX100301b.wav
GX100301c.wav
GX100301d.wav
GX100302a.wav
…
GX100304d.wav

The total number of *.wav files in the folder would be 16, with this formatting. Files ending in *a* and *d* are generally unused, though they can be set up to work with the 15 PSI sensor, and ambient atmospheric sensors.

The following list of *m*-files must also be in the same folder as the HEBI function:

R2D.m	% Converts radians to degrees
phasedif.m	% Calculates phase difference between fundmentals
LVDTcoef.m	% Returns polynomial values for LVDT curve fit
PowG2.m	% Calculates single sided power spectrum
SKresponse.m	% Calculates Sallen Key response

The uses of these functions will be discussed in the relevant portion of the code breakdown.

B.2 HEBI.m

The code will be explained in chunks. The code is commented, however comments will mostly be eliminated so that the lines of code fit on the appendix page in an orderly manner.

```
clear all
close all

tic

files = dir('*.wav');
```

A structure is initialized that contains the names of all the wave-files in the current directory. This enables the code to access each wave file, so that the code does not have to be re-run sixteen times, and the final data set be assembled in a separate code. The *tic* command lets a timer be run, to get an idea of how long the code takes to function.

```
sts = [1, 2];
for m = sts
```

These lines begin the outer loop for the code. The *sts* variable contains the sets of wave-files that should be evaluated. In this example, only sets 1 and 2, (0.001 to 0.087 and 0.087 to 0.27 Hz) are being evaluated.

```
    n = m;
    PXsens = 0.00503;       %use w/PX sensor
```

The variable *PXsens* is equal to the measured sensitivity of the differential piezo-resistive sensor mounted in the side of the chamber. The value is in *V/Pa*, and was measured relatively by comparing the strength of a measured signal with a signal measured by a plane-wave relative calibrated 2 PSI Endevco PZR. The reference for the 2 PSI Endevco PZR was a ¼'' B&K measurement microphone calibrated by a B&K 4228 pistonphone. Unsurprisingly, there is probably several percent of error in PXsens.

```
%% Define overlap parameters etc. for the various files
if m == 1   % Normally, the 0.001 to 0.087 Hz data
    flip = 0;            % High - to - low, set to 1
    winlen = 3000;       % Length of window
    twin = winlen;       % length of hann (or whatever) window
    ovlp = 0.93;         % Percentage of overlap.
    lbin = 4;            % low bin
    hbin = 7;            % high bin
    sclf = 1;            % un-used scale factor for LVDT data
    slp = 1;             % Slope adjustment for TEAC input range
    tlen = 10000;        % Decimated vector length
elseif m == 2   % 0.087 to 0.27 Hz data
    flip = 0;
    winlen = 4000;
    twin = winlen;
    ovlp = 0.90;
    lbin = 6;
    hbin = 10;
    sclf = 1;
    slp = 1;
    tlen = 30000;
elseif m == 3   % 0.27 to 3.5 Hz data
    flip = 0;
    winlen = 2000;
    twin = winlen;
    ovlp = 0.9;
    lbin = 4;
    hbin = 8;
    sclf = 1;
    slp = 1;
    tlen = 10000;
else    % 1 to 30+ Hz data
    flip = 0;
    winlen = 5*2^10;
    twin = winlen;
    ovlp = 0.25;
    lbin = 6;
    hbin = 12;
    sclf = 1;
    slp = 1;
    tlen = 100000;
end
```

This is the initialization portion of the code, that allows the user to optimize the analysis for the sets of *.wav files to be evaluated. The variables perform the following functions:

flip.m:	This variable is set to 1 if the signal sweep goes from high frequencies to low requencies, instead of low frequencies to high frequencies.
Winlen.m:	This is the length of the initial cropped segment of signal that will be evaluated by the HEBI code. This value changes when the peak signal is not in the bin-range.
Twin:	This is the length of the hanning, hamming, or other window used with the initial cropped set of data.
ovlp:	This is the overlap specified for the segments. If it is specified as 0.9, then 90% of the window length will be overlapped.
lbin:	This is the value of the low-bin that the index of the peak may not be below. If the peak does lie below this value, the window will be elongated.
hbin:	This is the value of the high-bin that the index of the peak may not be above. If the peak does like above this value, the window will be truncated.
sclf:	This is a scale-factor that was introduced for some LVDT debugging and is not used in all recent variations of the code.
slp:	This is a slope-adjustment value for the transducer/PZR, that is adjusted according to the input range of the TEAC channel. The assumed slope is +/- 1V, and is multiplied by 2 if the range is +/- 2 volts, 0.5 if the range is +/- 0.5 volts, etc.
tlen:	This is the total length of the signal that the *.wav data will be decimated to. It ought to be set high enough that the decimation will not filter out the highest frequency portion of the swept-sine signal.

In the variable definition, 4 conditionals allow the variables to be modified for each set. So, the overlap factor for the 0.001 to 0.087 Hz sweep does not have to be the same value (and is not), for the 1 to 30 Hz sweep. More conditionals can be added if additional sets have been recorded. This version of the code has four conditionals to match the convenient ranges of sine sweeps.

```
[y, fs, nbits] = wavread(files(4*n-1).name); % This set is the LVDT
len1 = length(y);

if round(len1/tlen)>1
    y = decimate(y, round(len1/tlen), 'FIR');
    len2 = length(y);
else
    len2 = len1;
end
```

```
[y2, fs, nbits] = wavread(files(4*n-2).name); % Data from PZR
if round(len1/tlen)>1
    y2 = decimate(y2, round(len1/tlen), 'FIR');
    fs = fs*(len2/len1);
end

[y3, fs2, nbits] = wavread(files(4*n).name);  % unused
if round(len1/tlen)>1
    y3 = decimate(y3, round(len1/tlen), 'FIR');
end
```

This portion of code reads the data from the appropriate **.wav* files into the decimated variables *y, y2,* and *y3*. "*files(4*n-3).name*" is the name of the **.wav* file of the *a* subscripted **.wav* file in the *n*th set. *4*n-2* corresponds to the *b* subscript, *4*n-1* the *c* subscript, and *4*n* the *d* subscript. Only the *b* (transducer) and *c* (LVDT) data sets are used in this code. The *decimate* function reduces the size of a wave file approximately to *tlen*.

The '*FIR*' statement inside the *decimate* function changes the type of low-pass filtering that is used to eliminate anti-aliasing. The built in filter does not have a flat enough pass-band, and glitches between sets occurs if the '*FIR*' statement is not used.

```
if flip == 1;
    y = flipud(y);
    y2 = flipud(y2);
    y3 = flipud(y3);
end
```

This command flips the appropriate vectors, if the sine-sweep was reversed.

```
dat = y;
dat2 = y2;
dat3 = y3;

dt = 1/fs;
N = length(dat);
T = N*dt;
time = linspace(0, T-dt, N);

% Calibration of data
PhysVal = 2.6214/2;            % Scaling: waveunits to V
PhysValLVDT = 2*2.6214/2;      % *2 just for this set...
if PXsens > 0.00001     % detecting if I'm using a sensitive source
    PhysVal = PhysVal*5;       % use this value for +/-5v input
end
```

This section redefines the vector names, sets up some important signal processing parameters (*dt, N, T)*, and a time vector for the length of the entire sweep (*time)*. The units of the LVDT data are converted to volts, using the slope and range values defined by the TEAC header file. Some modifications have been installed to default the analysis so that +/-2 Volts is the standard input range in the TEAC for the LVDT input, and +/- 5 Volts is the input range for the PZR.

```
P = LVDTcoef;
y = y/sclf;                 % for the 17kHz bump (oops)
y = y*PhysValLVDT;          % Should be in V right now
```

LVDTcoef is a function that returns a polynomial modeling the calibration curve of the LVDT. The *LVDTcoef.m* script actually contains a series of LVDT measurements, and these measurements are fit with the returned polynomial. The *sclf* used to modify the amplitude of the LVDT when the signal generator setting was bumped in the middle of a test. It is unused in the present configuration. The last line converts the values from *.wav units to volts.

```
ycor = polyval(P, y);
y = ycor; clear ycor;
```

In these two lines of code, the LVDT polynomial is being used to convert the data from units volts to inches (where inches are used because of the units on the micrometer).

```
x = y;
x3 = dat3(:)*PhysValLVDT;
x2 = dat2(:)*slp;
clear y dat3 dat2;
```

This set of commands renames some variables, corrects units (though *x3* is no longer used), and adjusts the value of the transducer data according to the input *slp* variable. Memory is freed in the clear command.

```
% get rid of offset
x = x - sum(x)/length(x);       % LVDT
x2 = x2 - sum(x2)/length(x2);   % 2Psi
```

The DC term of the LVDT vector (*x*) and transducer vector (*x2*) are having the average subtracted out, eliminating the DC term that would show up in an FFT.

```
%%%%% ATMOSPHERIC CORRECTION STUFF %%%%%%%
ambav = sum(x3)./length(x3);
ambp(n) = -30.83*ambav + 976;
ambp(n) = 983;
```

```
acor(n) = ambp(1,n)/1013;
len = N;
```

The vector *x3* used to contain data from an electrical ambient pressure sensor. The atmospheric correction term would sweep, along with the signal evaluation, and update continuously. This idea was scrapped however, and *ambp*, the vector containing ambient pressure variables, was assigned a single measured value, 983 mBar in this case. *acor*, the variable used to correct for the ambient pressure at the end of the code, is calculated according to the value of *ampb*.

```
ovlppnts = floor(winlen - winlen*ovlp);        % Shifting points.
numloops = floor(N/ovlppnts - ceil(winlen/ovlppnts));
nn = 1;
up = winlen;
dwn = 1;
maxlen = length(x);
```

In this portion of code, *ovlppnts* is defined as the value in points that the initial evaluation window will actually be shifted. The value *numloops* is the number of loops that will be run by the code, as estimated from the total length of the signal (*N*), the size of the window *winlen*, and the shift size, *ovlppnts*. The other lines are initializations for variables that will used in the forth-coming analysis.

```
while up < maxlen
    if up < maxlen

        ind = 1;
        padfct = 10;
```

The *if* statement is unused, and is vestigial from a previous form of the code. The *while* loop keeps the data-evaluation running as long as the last point of the evaluation window lies below the maximum length of the total signal vector (*x* or *x2*).

```
        while (ind < lbin*padfct | ind > hbin*padfct) & (up < maxlen)
```

This *while* statement runs as long as the index of the peak lies outside of the bin range. Because the index of the peak is initialized to 1, it will always run at least once.

```
            if ind < lbin*padfct
```

The following portion of code is run if the index of the peak lies below the bin-range multiplied by the pad factor (when calculating the peak index, the data is zero-padded by *padfact*, 10 in this case).

```
win = hann(winlen);
Aw = length(win)/sum(win.*win);
```

The weighting window and compensation factor *Aw* are calculated for the segment.

```
seg1 = x(dwn:up);
seg2 = x2(dwn:up);

seg1 = seg1 - sum(seg1)/length(seg1);
seg2 = seg2 - sum(seg2)/length(seg2);

seg1 = seg1.*win;
seg2 = seg2.*win;

seg1 = seg1 - sum(seg1)/length(seg1);
seg2 = seg2 - sum(seg2)/length(seg2);

tmags = abs(fft(seg1, winlen*padfct));
frqzz = linspace(0, fs, winlen*padfct);
[mx, ind] = max(tmags);
```

Segments of data are trimmed from *x* and *x2*. The DC terms of these segments are subtracted, and the segments are windowed. The linear spectrum of the LVDT data is calculated, and a frequency for the spectrum is calculated (*frqzz*). The maximum of the magnitude spectrum, and the index of the maximum are found.

```
subplot(2,1,1)
plot(seg1);
ylim([-1.5, 1.5]);
xlim([0, floor(length(seg1)*1.2)])
drawnow
```

The segment currently being evaluated is plotted in subplot 2,1,1. The plot is updated at evaluation using the *drawnow* command.

```
if ind < lbin*padfct
    winlen = winlen + ovlppnts;
    up = dwn + winlen-1;
end
```

If the calculated index for the peak, stored in *ind*, is below the bin range, the length of the window is increased by *ovlppnts.*

```
    elseif ind > hbin*padfct
```

If the index of the peak is too high, the following lines of code will be run

```
        winlen = round(0.9*winlen);
        up = dwn + winlen-1;
        frag = 0;
        win = hann(winlen);
        Aw = length(win)/sum(win.*win);
        seg1 = x(dwn:up);
        seg2 = x2(dwn:up);

        seg1 = seg1 - sum(seg1)/length(seg1);
        seg2 = seg2 - sum(seg2)/length(seg2);

        seg1 = seg1.*win;
        seg2 = seg2.*win;

        seg1 = seg1 - sum(seg1)/winlen;
        seg2 = seg2 - sum(seg2)/winlen;

        tmags = abs(fft(seg1, winlen*padfct));
        frqzz = linspace(0, fs, winlen*padfct);
        [mx, ind] = max(tmags);

        subplot(2,1,1)
        plot(seg1);
        ylim([-1.5, 1.5]);
        xlim([0, floor(length(seg1)*1.2)])
        drawnow
        ovlppnts = floor(winlen - winlen*ovlp);
        twin = winlen;
    end
end
```

These lines of code do the exact same thing as in the case of the index being below the bin range, however the segment is always truncated approximately by 10%. Also, unlike the other case, this conditional will always alter the size of the vector, whereas the elongation in the previous conditional only occurs if the calculated spectrum puts the bin outside of the bin-range.

```
winlen = twin;      % Reset window length.
```

Setting the window length for the next loop based on the elongation or truncation.

```
% Calculate power spectra
[p1, f1] = powG2(seg1, fs);
[p2, f2] = powG2(seg2, fs);
```

```
[mx, ind2] = max(p1);
dff = f1(2) - f1(1);
```

This power spectra of the segments are calculated. The function *powG2* was previously written to return the single-sided power spectrum given a time signal and a sampling rate. The single-sided power spectrum, and a frequency vector for the spectrum are returned. The amplitude and index of the peak in the LVDT data are found using the *max* command, and the frequency resolution is found from the frequency vector.

```
if ind2 > 3
```

The conditional is to eliminate a special case error. The conditional is nearly always greater than three.

```
F(nn, m) = frqzz(ind);      % the accurate freq.
Lmag(nn, m) = sqrt(sum(Aw*p1(ind2 - 2:ind2 + 5))*dff);
PXmag(nn, m) = sqrt(sum(Aw*p2(ind2 - 2:ind2 + 5))*dff);
if flip == 1
    phas(nn, m) = phasedif(seg1, seg2, 10);
else
    phas(nn, m) = -phasedif(seg1, seg2, 10);
end
```

F contains the accurate frequency, measured using the zero-padded spectrum calculated earlier. *Lmag* contains the root-mean-square piston swing, calculated by integrating the power spectrum of the LVDT signal clip from 2 bins below the peak to 5 bins above the peak. *PXmag* is the same kind of value, however calculated for the output of the pressure transducer rather than the LVDT. The sign of the phase depends on the *flip* variable, as defined upon HEBI initialization. The function *phasedif.m* is called to calculate the phase difference between the fundamentals f the LVDT and pressure sensor data. A zero-padding factor is passed to the function, in addition to the segments, which is 10 in this case.

```
if nn > 2
    rwr = find(F ~= 0);
    Fplt = F(rwr);
    Mplt = PXmag(rwr)./Lmag(rwr);
    subplot(2,1,2)
    loglog(Fplt, Mplt, '+', 'MarkerSize', 2);
    xlim([0.001, 35])
end
drawnow
```

If more than two values have been found, the lower figure in the HEBI plot window is updated to show the ratio of the *PXmag* and *Lmag* values. This gives the user

an idea of how the program is progressing, if the data set is good or bad, and if the program has gotten stuck in a loop.

```
            end
        end
```

Inner loop and useless *if* conditional terminated.

```
    nn = nn + 1;            % increment counter
    up = dwn + ovlppnts+winlen-1;   % Set new segment vector endpoints
    dwn = dwn + ovlppnts;

    end                     % endwhile
end                         %endmain
toc
```

Segment beginning and end points are updated, *while* loop that keeps the program running while the end point is below the end of the entire vector is terminated, and the outer loop that is run for each **.wav* data set is terminated.

```
PXmag = (PhysVal/PXsens)*PXmag;
% PXmag = (PhysVal)*PXmag;
```

PXmag is converted to Volts, then to Pascals, using the value from the adjusted value from the header file for the data set, and the PZR calibration value (0.00503 V/Pa).

```
Lmag = Lmag*sqrt(2)*2;          % find the PK to PK voltage.
Lmag = Lmag/1;                  % Divide by Pk-Pk of simulation.
zs = find(Lmag == 0);
Lmag(zs) = 1e-10;
PXFinal = PXmag./Lmag;          % correcting the PZR for disp. Stuff
flen = length(F(1,:));
```

The peak-to-peak piston swing is calculated from the RMS, and normalized by the swing of the simulation (normally set to 1). This converts *Lmag* to a *scaling* vector. All the zeroes in the pistonphone swing magnitude vector are replaced with very small values to prevent NaN's from popping up later.

The pressure magnitudes in *PXmag* are normalized by *Lmag*, which has been converted to a vector of normalization values. This step cleans up the data a *huge* amount. The final, normalized values are placed in the vector *PXFinal.*

```
% Atmosph. correction and phase adjust
for m = 1:flen
    PXFinal(:,m) = PXFinal(:,m)/acor(m);
end
phas = phas + pi;
```

The atmosphere is corrected by the correction factor calculated using the ambient pressure measurement. The phase is adjusted by *pi* to account for the fact that the volume velocity produced by the piston and the displacement of the piston are 90 degrees out of phase.

```
% Organize everything into a nice set of vectors
inds = find(F ~= 0);
out(:,1) = F(inds);
out(:,2) = PXFinal(inds);         % CAREFUL
out(:,3) = phas(inds);
out(:,4) = Lmag(inds);
out = sortrows(out);
```

Final, nice vector called *out*, containing all the pertinent information for the data evaluation. Disturbingly, the author does not remember the reason for the all caps "CAREFUL" comment.

```
resp = SKresponse(out(:,1), 1500, 1.5);
```

It was found that the 2nd order Sallen-Key low pass filter used with the LVDT data was actually affecting the phase response of the LVDT data by about a degree at 30 Hz, even though the cutoff of the filter is about 1500 Hz. To compensate for the effects, function called *SKresponse* that calculates the magnitude and phase response of a 2nd order Sallen Key filter was written to allow the phase response of the filter to be subtracted from the data set. (The magnitude response is virtually unaffected).

```
% Do a theory comparison
Frad = F;
clear F
F = logspace(log10(min(out(:,1))), log10(max(out(:,1))), 100);
[resp2b, pnorm] = Pfunc2(F, 1013, 1, 0, 0, 0.1);
resp2 = interp1(F, resp2b, out(:,1)');
resp2 = resp2';
F = Frad;
```

In this section the theoretical response of the pistonphone is calculated for a set of 100 points between the lowest and highest frequencies of the data set. Using interpolation, the theoretical response is calculated for all the frequencies in the analyzed data set.

```
figure
subplot(2,1,1)
semilogx(out(:,1), abs(resp2), 'b', 'LineWidth', 2);
hold on;
semilogx(out(:,1), 1.0*out(:,2), 'r+', 'MarkerSize', 2);

axis([0.0015, 32, 33, 80])

xlabel('Frequency (Hz)');
ylabel('Rms amplitude, Pa');
title('Swept sine, 0.001 to 35 Hz')
legend('Prediction', 'Measurement');
```

In this section, the magnitude response of the data set and the prediction are plotted and compared.

```
subplot(2,1,2)

phss = ((out(:,3))-(angle(resp'))-(angle(resp2)))';
phzz = ((out(:,3))-(angle(resp')))';
phss = unwrap(phss);
phzz = unwrap(phzz);

semilogx(out(:,1), -R2D(angle(resp2)), 'b', 'LineWidth', 2);
hold on;
semilogx(out(:,1), R2D(phzz), 'r+', 'MarkerSize', 2);

title('Pistonphone phase response, Helium')
axis([0.0015, 32, -2, 20]);
xlabel('Frequency (Hz)');
ylabel('Angle, (deg)')
```

The phases are plotted, and the phase of the data set is corrected for the LVDT filter response. Some unwrapping is done, of the phase.

```
respmag = out(:,2);
respphs = R2D(phzz)-360;
Mphs = -R2D(angle(resp2));
Fqs = out(:,1);
Mmags = abs(resp2);

save Dataset1 respmag respphs Mphs Fqs Mmags
toc
```

In these last lines of code, tidy variables are being written for exportation into the file *Dataset1.mat.*

B.3 Support functions

Several support functions are required for HEBI to work. These must be placed in either the same directory as the HEBI.m file, or in another folder that Matlab will check for functions.

B.3.1 R2D.m

The name of the function stands for “Radians to degrees”

```
function    [deg] = R2D(rad)
deg = (rad/(2*pi))*360;
```

The above two lines are the entire function. It is passed an angle in radians, and returns an angle in degrees.

B.3.2 Phasedif.m

The name of the function stands for “phase difference.”

```
function [dif] = phasedif(sig1, sig2, pad);

sig1 = sig1 - sum(sig1)/length(sig1);
sig2 = sig2 - sum(sig2)/length(sig1);
N = length(sig1);

fmag1 = fft(sig1, N*pad);
fmag2 = fft(sig2, N*pad);
[mx, ind] = max(abs(fmag1));

%Now, find phase at ind;
ph1 = angle(fmag1(ind));
ph2 = angle(fmag2(ind));

dif = ph1 - ph2;
```

The function is passed three inputs, when it is called: *sig1*, *sig2*, and *pad*. *sig1* and *sig2* are both time vectors of the same length, having strong fundamentals each with a high signal-to-noise ratio. *pad* is a zero-padding factor. The length of the signal will be multiplied by *pad*.

Following the function call, the DC offset is subtracted from the signal, to eliminate errors caused if the DC term is the largest term in the spectrum.

The linear spectrum is calculated, and zero padded to reach *N***pad* in length, where *N* is the length of *sig1* and *sig2*. Following calculation of the linear spectrum, the index of the maximum of the magnitude spectrum of *sig1* is found and placed in the variable *ind*.

The phase difference between the peaks of *sig1* and *sig2* is found at the index stored in *ind.* The phase is the phase of *sig1* minus *sig2*.

B.3.3 LVDTcoef.m

LVDTcoef stands for "LVDT coefficients," and returns the coefficients of a fourth-order polynomial curve fit to a set of calibration data points measured for the LVDT.

```
function [P] = LVDTcoef();
```

The LVDTcoef.m function has no input parameters, as can be seen from the function definition line. The returned polynomial coefficient vector is stored in variable *P*.

```
d = 0:50:1100;
d = [d, 1125];
```

The *d* vector contains all the distances in mils that the voltage output of the LVDT was recorded. The zero-point was initialized to be somewhere near the LVDT's maximum insertion distance when connected to the axle wheel.

```
cal = [-202.2, -185.2, -167, -148, -128.6, -107.0, -86.8, -64.8,
        -42.2, -19.4, 4.4, 30.0, 55.2, 82.0, 107.0, 133.4, 158.8,
        184.2, 207.8, 231.0, 254.6, 277.4, 299.8, 309.6];
avg = cal/1000;
d = d/1000;
P = polyfit(avg, d, 4);
```

cal contains all the measured voltages (in mV) for the distances stored in *d*. *avg* and *d* store the values in inches and volts. The coefficients for a best fit curve are calculated using the *polyfit* command. The integer in the command determines the order, and the coefficients are stored in *P*.

B.3.4 powG2.m

This function returns the single-sided power spectrum for a given time series and sample rate. It also returns a frequency-vector that can be used in conjunction with the returned spectrum.

```
function [Gxx, freqs] = powG(mag, fs);
```

mags and *fs* are the passed time series and sample rate, an *Gxx* and *freqs* are the returned spectrum and frequency vector.

```
dt = 1/fs;
T = dt*length(mag);
len = ceil((length(mag))/2);
```

dt is the sample time, *T* is the total time of the signal, and *len* is the length of the power spectrum that will be created.

```
Xm = fft(mag)*dt;
Sxx = (1/T)*(Xm.*conj(Xm));
```

The fast-fourier transform is calculated and stored in *Xm*. From the linear spectrum, the double sided power spectrum is calculated and placed in *Sxx*.

```
Gxx = 2*Sxx(1:len);
Gxx(1) = Gxx(1)/2;
Gxx(length(Gxx)) = Gxx(length(Gxx))/2;
```

From the double sided power spectrum, *Gxx*, the single sided power spectrum is created by doubling *Sxx*, truncating at the *fs/2* point, and dividing the beginning and end points by 2.

```
freqs = linspace(0, fs/2, length(Gxx));
```

The last line of the code creates the frequency vector corresponding to the power spectrum.

B.3.5 SKresponse.m

SKresponse stands for "Sallen Key response" and returns the magnitude and phase response of a second order Sallen Key filter with the passed parameters.

```
function [resp] = SKresponse(F, fc, G);
```

The function call is passed three parameters, *F*, *fc*, and *G*. *F* is a vector of the frequencies over which the response of the filter will be evaluated, *fc* is the break-point of the filter, and *G* is the gain, which alters the quality factor in a Sallen-Key filter.

```
K = G;
R1 = 10000;
R2 = R1;
C1 = 1/(2*pi*R1*fc);
C2 = C1;
```

In these lines, the circuit parameters are being written. The resistors are assumed to be of equal value and equal to 10kOhm. The break-point is set by adjusting the capacitances. In the LVDT circuit, the resistances are roughly equal, and the capacitances are roughly equal.

```
for n = 1:length(F)
    s = j*2*pi*F(n);
    p1 = (R1*R2*C1*C2)*s^2;
    p2 = (R1*C1 + R2*C1 + R1*C2*(1-K))*s;
    p3 = 1;
    transf(n) = K/(p1 + p2 + p3);
end
resp = transf;
```

This loop evaluates the response of the filter over the specified frequencies, and assigns the output of the function.

B.4 Modifying HEBI.m to calibrate microphones

The HEBI code and the code for all its sub-functions have been explained. As it is introduced, the HEBI code is written to analyze the signal from a PZR with a known sensitivity, and compare the output to a model for the internal pressure field. This section will show the changes that are made to make the output of the code a sensitivity response for the immersed transducer. The modified code used in this example will be called "HEBI_T.m", *T* for transducer calibration. In this example, the HEBI_T code is modified to calibrate a *B&K* 4193 microphone.

B.4.1 Code modifications

The *sts* vector on line 15 is modified to contain numerals 1, 2, 3, 4, indicating that four data sets have been taken for the calibrated transducer, and all of them are to be processed by the code. The *PXsens* value is set to the nominal sensitivity value, or handheld pistonphone sensitivity value. In this example, the nominal sensitivity is roughly 0.05 V/Pa.

A *B&K* Nexus amplifier connected to the transducer is used to adjust the gain of the microphone output. Because of the low signal level in the 0.001 to 0.087 range, the signal was boosted by a factor of 3.16 times in that range. Furthermore, the input gain range has been altered to +/- 10 volts. In the variable declaration portion of the HEBI_T code, the slopes for each set are adjusted to be consistent, and to reflect the signal output in volts. A sample variable declaration for a particular set of HEBI_T looks like the following, for the first portion of code:

```
if m == 1   % Normally, the 0.001 to 0.087 Hz data
    flip = 0;            % High - to - low, set to 1
    winlen = 3000;       % Length of window
    twin = winlen;       % length of hann (or whatever) window
    ovlp = 0.9;         % Percentage of overlap.
    lbin = 5;            % low bin
    hbin = 7;            % high bin
    sclf = 1;            % un-used scale factor for LVDT data
    slp = 1/(10*3.16);   % Slope adjustment for TEAC input range
    tlen = 30000;        % Decimated vector length
```

In the calibration examples cited in this thesis, the differential pressure sensor is recording data at the same time that the immersed transducer is recording data. The differential pressure sensor is recording to channel 2, while the immersed transducer is recording to channel 4. The signal channel in HEBI_T needs to be switched from reading the channel 2 data to the channel 4 data. This is done by altering the following code, taken from HEBI.m (lines 72 through 76):

```
[y2, fs, nbits] = wavread(files(4*n-2).name); % Data from PZR
if round(len1/tlen)>1
    y2 = decimate(y2, round(len1/tlen), 'FIR');
    fs = fs*(len2/len1);
end
```

to…

```
[y2, fs, nbits] = wavread(files(4*n).name); % Data from PZR
if round(len1/tlen)>1
    y2 = decimate(y2, round(len1/tlen), 'FIR');
    fs = fs*(len2/len1);
end
```

The file opened by the *wavread* command is altered from *files(4*n-2).name* to *files(4*n).name*, indicating that the last file name in the set is opened. All the channel 4 data sets have been written with subscript *d* at the end of the file name, placing them at the end of each set.

The core of the program is un-altered, but when the unit changes are being made in the HEBI code (line 282):

```
PXmag = (PhysVal/PXsens)*PXmag;
```

The division by *PXsens*, the sensitivity of the transducer is eliminated, keeping the units in volts:

```
PXmag = (PhysVal)*PXmag;
```

When *pfunc.m* is called to predict the internal pressure of the pistonphone (line 314), the position entry is updated to match the position of the inserted transducer:

```
% Do a theory comparison
Frad = F;
clear F
F = logspace(log10(min(out(:,1))), log10(max(out(:,1))), 100);
[resp2b, pnorm] = Pfunc2(F, 1013, 1, 0, 0, 0.81);
resp2 = interp1(F, resp2b, out(:,1)');
resp2 = resp2';
F = Frad;
```

resp2 is a vector that contains the pressure in pascals at the location of the transducer inside the pistonphone main chamber for every frequency the response of the transducer is measured. The sensitivity of the transducer is found by dividing the voltage

response of the transducer by the pressure response calculated to occur at the position of the transducer inside the chamber.

Minor modifications are made to the graphing functionality, but generally speaking, the rest of the code, including the saving of the variables into a *.mat file is identical.

B.5 HEBI.m code

```
% HEBI
% Swept sine evaluation tool


clear all
close all

tic

files = dir('*.wav');

sts = [1, 2];
for m = sts
    n = m;
    PXsens = 0.00503;       %use w/PX sensor

    %% Define overlap parameters etc. for the various files
    if m == 1   % Normally, the 0.001 to 0.087 Hz data
        flip = 0;            % High - to - low, set to 1
        winlen = 3000;       % Length of window
        twin = winlen;       % length of hann (or whatever) window
        ovlp = 0.93;         % Percentage of overlap.
        lbin = 4;            % low bin
        hbin = 7;            % high bin
        sclf = 1;            % un-used scale factor for LVDT data
        slp = 1;             % Slope adjustment for TEAC input range
        tlen = 10000;        % Decimated vector length
    elseif m == 2   % 0.087 to 0.27 Hz data
        flip = 0;
        winlen = 4000;
        twin = winlen;
        ovlp = 0.90;
        lbin = 6;
        hbin = 10;
        sclf = 1;
        slp = 1;
        tlen = 30000;
    elseif m == 3   % 0.27 to 3.5 Hz data
        flip = 0;
        winlen = 2000;
        twin = winlen;
```

```
    ovlp = 0.9;
    lbin = 4;
    hbin = 8;
    sclf = 1;
    slp = 1;
    tlen = 10000;
else    % 1 to 30+ Hz data
    flip = 0;
    winlen = 5*2^10;
    twin = winlen;
    ovlp = 0.25;
    lbin = 6;
    hbin = 12;
    sclf = 1;
    slp = 1;
    tlen = 100000;
end

% Get the data
%%%%%%%%%%%%%%%%%%%%%%%%%%%%%%%%%%%%%%%%%%%%%%%%
[y, fs, nbits] = wavread(files(4*n-1).name); % This set is the LVDT
len1 = length(y);

if round(len1/tlen)>1
    y = decimate(y, round(len1/tlen), 'FIR');
    len2 = length(y);
else
    len2 = len1;
end

[y2, fs, nbits] = wavread(files(4*n-2).name); % Data from PZR
if round(len1/tlen)>1
    y2 = decimate(y2, round(len1/tlen), 'FIR');
    fs = fs*(len2/len1);
end

[y3, fs2, nbits] = wavread(files(4*n).name);  % unused
if round(len1/tlen)>1
    y3 = decimate(y3, round(len1/tlen), 'FIR');
end


%%%%%%%%%%%%%%%%%%%%%%%%%%%%%%%%%%%%%%%%%%%%%%%%

if flip == 1;
    y = flipud(y);
    y2 = flipud(y2);
    y3 = flipud(y3);
end
% Parameter setup, dt, N, etc. definition
dat = y;
dat2 = y2;
dat3 = y3;
```

```
    dt = 1/fs;
    N = length(dat);
    T = N*dt;
    time = linspace(0, T-dt, N);

    % Calibration of data
    PhysVal = 2.6214/2;             % Scaling: waveunits to V
    PhysValLVDT = 2*2.6214/2;       % *2 for teac input
    if PXsens > 0.00001             % sensitive source detect?
        PhysVal = PhysVal*5;        % use this value for +/-5v input
    end

    % LVDT correction shtuff
    P = LVDTcoef;
    y = y/sclf;                    % unused
    y = y*PhysValLVDT;             % Should be in V right now

    ycor = polyval(P, y);
    y = ycor; clear ycor;

    % I have no idea why I did this but whatev's
    x = y;
    x3 = dat3(:)*PhysValLVDT;           % Atmosph
    x2 = dat2(:)*slp;                   % Senser
    clear y dat3 dat2;


    % get rid of offset
    x = x - sum(x)/length(x);       % LVDT
    x2 = x2 - sum(x2)/length(x2);   % 2Psi

    %%%%% ATMOSPHERIC CORRECTION STUFF %%%%%%%
    ambav = sum(x3)./length(x3);
    ambp(n) = -30.83*ambav + 976;
    ambp(n) = 983;
    acor(n) = ambp(1,n)/1013;
    len = N;



    % Overlap stuff, initializing vector endpoints for sliding
    % power-spectrum window, etc.

    ovlppnts = floor(winlen - winlen*ovlp);        % Shifting points.
    numloops = floor(N/ovlppnts - ceil(winlen/ovlppnts));
    nn = 1;
    up = winlen;
    dwn = 1;
    maxlen = length(x);     % don't let the vectors go over length of
data
```

```
    % Begin loop. This loop takes a segment of the time data and
calculates
    % the power spectrum. If the index of the peak of the power-
spectrum is
    % greater than lbin, (if padded, then lbin*(pad factor)) and less
    % than hbin, then the ratio of the LVDT and the pressure
    % sensor output will be taken. Otherwise, the window will be
truncated
    % or elongated, to make the index fall in the bin range.
    % The bin's should not be put too close together, or the code will
get
    % stuck in a loop.

    while up < maxlen
        if up < maxlen   % The use of the if statement was a mistake,
                         % trim this up later
            ind = 1;
            padfct = 10;

         % Run this loop if the index is not in the correct bin.
         % It will always run the first time.
         while (ind < lbin*padfct | ind > hbin*padfct) & (up < maxlen)

               if ind < lbin*padfct        % Run if too short
                   win = hann(winlen);
                   Aw = length(win)/sum(win.*win);
                   seg1 = x(dwn:up);
                   seg2 = x2(dwn:up);

                   seg1 = seg1 - sum(seg1)/length(seg1);
                   seg2 = seg2 - sum(seg2)/length(seg2);

                   seg1 = seg1.*win;
                   seg2 = seg2.*win;

                   seg1 = seg1 - sum(seg1)/length(seg1);
                   seg2 = seg2 - sum(seg2)/length(seg2);

                   tmags = abs(fft(seg1, winlen*padfct));
                   frqzz = linspace(0, fs, winlen*padfct);
                   [mx, ind] = max(tmags);

                   subplot(2,1,1)
                   plot(seg1);
                   ylim([-1.5, 1.5]);
                   xlim([0, floor(length(seg1)*1.2)])
                   drawnow

                   % If ind is to small, update the window length
                   if ind < lbin*padfct
                       winlen = winlen + ovlppnts;
                       up = dwn + winlen-1;
```

```
                end

            % Run this loop if the window is too long.
            elseif ind > hbin*padfct

                winlen = round(0.9*winlen);
                up = dwn + winlen-1;
                frag = 0;
                win = hann(winlen);
                Aw = length(win)/sum(win.*win);
                seg1 = x(dwn:up);
                seg2 = x2(dwn:up);

                seg1 = seg1 - sum(seg1)/length(seg1);
                seg2 = seg2 - sum(seg2)/length(seg2);

                seg1 = seg1.*win;
                seg2 = seg2.*win;

                seg1 = seg1 - sum(seg1)/winlen;
                seg2 = seg2 - sum(seg2)/winlen;

                tmags = abs(fft(seg1, winlen*padfct));
                frqzz = linspace(0, fs, winlen*padfct);
                [mx, ind] = max(tmags);

                subplot(2,1,1)
                plot(seg1);
                ylim([-1.5, 1.5]);
                xlim([0, floor(length(seg1)*1.2)])
                drawnow
                ovlppnts = floor(winlen - winlen*ovlp);
                twin = winlen;
            end
        end

        winlen = twin; % Reset window length.
                       % If the window has ever been truncated,
                       % then the new twin value is the truncated
                       % length. (high-low sweeps don't work well
                       % with this code, in other words, only
                       % low-high sweeps).

        % Calculate power spectra
        [p1, f1] = powG2(seg1, fs);
        [p2, f2] = powG2(seg2, fs);
        [mx, ind2] = max(p1);
        dff = f1(2) - f1(1);

% The conditional is for a special case which can cause a crash
% of the program (occurs if ind is still < 3 near end of
% vector)
```

```
            if ind2 > 3
                % Record our values
                F(nn, m) = frqzz(ind);      % accurate freq.
                Lmag(nn, m) = sqrt(sum(Aw*p1(ind2 - 2:ind2 + 5))*dff);
                PXmag(nn, m) = sqrt(sum(Aw*p2(ind2 - 2:ind2 + 5))*dff);
                if flip == 1
                    phas(nn, m) = phasedif(seg1, seg2, 10);
                else
                    phas(nn, m) = -phasedif(seg1, seg2, 10);
                end
                numloops-nn;


                if nn > 2
                    rwr = find(F ~= 0);
                    Fplt = F(rwr);
                    Mplt = PXmag(rwr)./Lmag(rwr);
                    subplot(2,1,2)
                    loglog(Fplt, Mplt, '+', 'MarkerSize', 2);
                    xlim([0.001, 35])
                end
                drawnow
            end
        end                 % endif

    nn = nn + 1;            % increment counter
    up = dwn + ovlppnts+winlen-1;   % Set new segment vector endpoints
    dwn = dwn + ovlppnts;

    end                     % endwhile
end                         %endmain
%%

% correction for the amplitudes from GX scaling and sensitivity etc.
PXmag = (PhysVal/PXsens)*PXmag;
% PXmag = (PhysVal)*PXmag;

% normalize the pistonphone displacement as determined by the LVDT.
Lmag = Lmag*sqrt(2)*2;                  % find the PK to PK voltage.
Lmag = Lmag/1;                          % Divide by Pk-Pk of simulation.
zs = find(Lmag == 0);
Lmag(zs) = 1e-10;
PXFinal = PXmag./Lmag;                  % correcting the PZR for stuff
flen = length(F(1,:));

% Atmosph. correction and phase adjust
for m = 1:flen
    PXFinal(:,m) = PXFinal(:,m)/acor(m);
end
phas = phas + pi;

% Organize everything into a nice set of vectors
inds = find(F ~= 0);
```

```
out(:,1) = F(inds);
out(:,2) = PXFinal(inds);          % CAREFUL
out(:,3) = phas(inds);
out(:,4) = Lmag(inds);
out = sortrows(out);


resp = SKresponse(out(:,1), 1500, 1.5);

% Do a theory comparison
Frad = F;
clear F
F = logspace(log10(min(out(:,1))), log10(max(out(:,1))), 100);
[resp2b, pnorm] = Pfunc2(F, 1013, 1, 0, 0, 0.1);
resp2 = interp1(F, resp2b, out(:,1)');
resp2 = resp2';
F = Frad;


%%
figure
subplot(2,1,1)
semilogx(out(:,1), abs(resp2), 'b', 'LineWidth', 2);
hold on;
semilogx(out(:,1), 1.0*out(:,2), 'r+', 'MarkerSize', 2);

axis([0.0015, 32, 33, 80])

xlabel('Frequency (Hz)');
ylabel('Rms amplitude, Pa');
title('Swept sine, 0.001 to 35 Hz')
legend('Prediction', 'Measurement');

subplot(2,1,2)

phss = ((out(:,3))-(angle(resp'))-(angle(resp2)))';
phzz = ((out(:,3))-(angle(resp')))';
phss = unwrap(phss);
phzz = unwrap(phzz);

semilogx(out(:,1), -R2D(angle(resp2)), 'b', 'LineWidth', 2);
hold on;
semilogx(out(:,1), R2D(phzz), 'r+', 'MarkerSize', 2);

title('Pistonphone phase response, Helium')
axis([0.0015, 32, -2, 20]);
xlabel('Frequency (Hz)');
ylabel('Angle, (deg)')

% Let's save the data now...
respmag = out(:,2);
respphs = R2D(phzz)-360;
```

```
Mphs = -R2D(angle(resp2));
Fqs = out(:,1);
Mmags = abs(resp2);

save Dataset1 respmag respphs Mphs Fqs Mmags
toc
```

Appendix C

Tee-sections

Additional work has been done by the author to integrate Tee-sections into more complex one-dimensional acoustic systems. This appendix is a summary of the Tee-section work developed by the author for use with infrasonic arrays and modeling acoustic propagation through porous hoses.

The concepts used for construction of all models described in this appendix are exactly the same as the concepts applied to the pistonphone model. The ability of the model to predict the pressure response of pistonphone chamber, especially when filled with a gas like helium, lends a lot of credibility to the type of model used for the following examples. While not immediately pertinent to the rest of the content of this dissertation, it is hoped that, should a reader desire to use Tee-section theory in another application, the following illustrations of its implementation will be a helpful resource.

The first part of the original version of this appendix covers the exact same material as sections **3.2** through **3.3** in the dissertation. Some overlap exists between section **3.3** and the following sections; however, for the most part redundant portions have been edited out.

C.1 Modeling the acoustic properties of ducts

C.1.1 Calculating the pressures and velocities at the ends of ducts

This section will cover the basic matrix algebra for calculating the pressure at different locations in ducts for different boundary conditions. In some cases the velocities at the ends of the ducts are known, (velocity is zero if the end is capped, and defined if the end is a piston with a known displacement), and in some cases the pressure is known (zero if the end is open and no pressure source exists, defined if a pressure source exists). Methods for calculating the pressure at the ends and any point within the duct are outlined.

C.1.1.1 Velocity boundary conditions

In a pistonphone the boundary conditions of the problem are the velocities at the ends of the duct. At the piston face the velocity is determined by the displacement and diameter of the piston, and angular frequency of operation. The other end of the chamber may have a cap (at which the velocity is zero), or another piston. Methods for including leaks at both ends will be included.

The first step is to slice the piston into a large number of segments each of which are identical. The impedances of the Tee-section representing each slice are calculated, and the transfer-matrix for the Tee-section is assembled based on the impedance values.

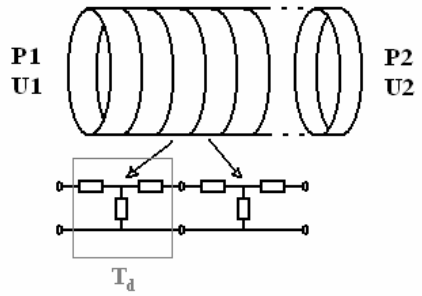

Figure **C-1**: The duct is composed of multiple Tee-sections, which can be converted to transfer matrices.

For a pipe having N-segments, a transfer-matrix representing the entire tube is calculated by raising the slice transfer-matrix to the *Nth* power:

$$T_d^N = T = \begin{bmatrix} A & B \\ C & D \end{bmatrix}$$

This matrix relates the pressure and velocity at one end of the tube to the other. Because the velocities are known at both ends, the strategy will be to re-arrange the variables so that all the known variables are on one side of the equation, and the unknowns are on the other. Then the solution can be found using simple matrix multiplication:

$$\begin{bmatrix} P_1 \\ U_1 \end{bmatrix} = T * \begin{bmatrix} P_2 \\ U_2 \end{bmatrix}$$

$$P_1 = AP_2 + BU_2$$
$$U_1 = CP_2 + DU_2$$

$$P_1 - AP_2 = BU_2$$
$$-CP_2 = -U_1 + DU_2$$

$$\begin{bmatrix} 1 & -A \\ 0 & -C \end{bmatrix} * \begin{bmatrix} P_1 \\ P_2 \end{bmatrix} = \begin{bmatrix} 0 & B \\ -1 & D \end{bmatrix} * \begin{bmatrix} U_1 \\ U_2 \end{bmatrix}$$

$$\begin{bmatrix} P_1 \\ P_2 \end{bmatrix} = \begin{bmatrix} 1 & -A \\ 0 & -C \end{bmatrix}^{-1} * \begin{bmatrix} 0 & B \\ -1 & D \end{bmatrix} * \begin{bmatrix} U_1 \\ U_2 \end{bmatrix}$$

$$"M" = \begin{bmatrix} 1 & -A \\ 0 & -C \end{bmatrix}^{-1} * \begin{bmatrix} 0 & B \\ -1 & D \end{bmatrix}$$

$$P_1 = M(1,1) * U_1 + M(1,2) * U_2$$
$$P_2 = M(2,1) * U_1 + M(2,2) * U_2$$

In this case, because both velocities are known, the transfer-matrices are used to form an impedance matrix ("M") that can be used to solve for the pressures.

C.1.1.2 Decreasing the impedance of the boundaries

In the case of a piston-phone, where the piston is made of solid and stiff piece of material and the end cap is also solid, the zero-velocity boundary condition at the end and the velocity = piston velocity condition at the front are good approximations. However, in some cases (*e.g.* when a leak is present), this might be inadequate, and the following method can be used to approximate a finite impedance at either end.

Figure **C-2** is an illustration of the method used for reducing the impedances to finite values. The impedances Z_{Lfront} and Z_{Lback} are added in parallel to the pipe model:

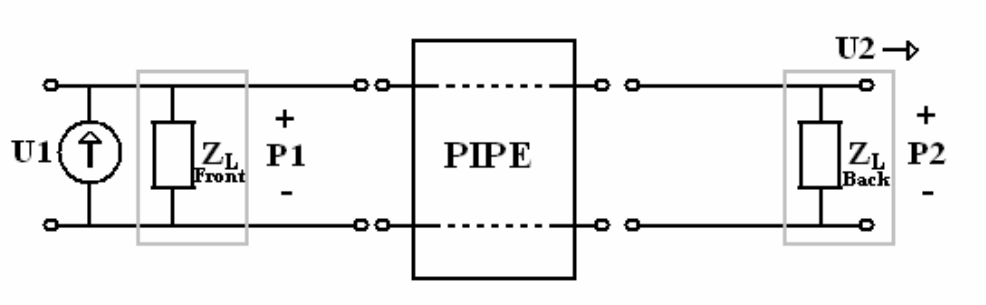

Figure **C-2**: Leak models at the piston and end-cap.

To include the leak resistances in the transfer matrix calculation, the transfer matrix for the leak elements are included in the calculations in the order they appear between the ends of the duct:

$$\begin{bmatrix} P_1 \\ U_1 \end{bmatrix} = \begin{bmatrix} 1 & 0 \\ \frac{1}{ZL_{Front}} & 1 \end{bmatrix} * T * \begin{bmatrix} 1 & 0 \\ \frac{1}{ZL_{Back}} & 1 \end{bmatrix} * \begin{bmatrix} P_2 \\ U_2 \end{bmatrix}$$

$$T_T = \begin{bmatrix} A_T & B_T \\ C_T & D_T \end{bmatrix} = \begin{bmatrix} 1 & 0 \\ \frac{1}{ZL_{Front}} & 1 \end{bmatrix} * T * \begin{bmatrix} 1 & 0 \\ \frac{1}{ZL_{Back}} & 1 \end{bmatrix}$$

$$\begin{bmatrix} P_1 \\ U_1 \end{bmatrix} = T_T * \begin{bmatrix} P_2 \\ U_2 \end{bmatrix}$$

In this case the variable T_T represents the new transfer matrix found by multiplying the transfer matrices for the leaks with the pipe transfer matrix. The order is important if the acoustic wavelength is smaller than the length of the tube. The transfer matrices must be ordered in the same way that they are ordered physically (i.e. the transfer matrix for the leak at the front must come first, followed by the pipe matrix, followed by the leak at the back of the pipe).

C.1.1.3 Pressure and velocity boundary conditions

The fixed-free pipe is a representation of a pipe with one end determined by a pressure source (fixed pressure), and one end terminated rigidly, so that it has a zero velocity condition and a free pressure condition. This condition is more similar to an infrasonic array, in the sense that the pressure at the open end of the pipe is determined

by the atmosphere. The actual infrasonic array pressure calculation is more similar to finding the pressure at the midpoint of a pipe which is open at both ends, but this example introduces the solution for pressure boundary conditions.

The strategy for solving the problem is to get all the known variables on one side of the equation and all the unknowns on the other side:

$$\begin{bmatrix} P_1 \\ U_1 \end{bmatrix} = T * \begin{bmatrix} P_2 \\ U_2 \end{bmatrix}$$

$$P_1 = AP_2 + BU_2$$
$$U_1 = CP_2 + DU_2$$

$$P_1 - BU_2 = AP_2$$
$$DU_2 = -U_1 + CP_2$$

$$\begin{bmatrix} 1 & -B \\ 0 & -D \end{bmatrix} * \begin{bmatrix} P_1 \\ U_2 \end{bmatrix} = \begin{bmatrix} A & 0 \\ C & -1 \end{bmatrix} * \begin{bmatrix} P_2 \\ U_1 \end{bmatrix}$$

$$\begin{bmatrix} P_2 \\ U_1 \end{bmatrix} = \begin{bmatrix} A & 0 \\ C & -1 \end{bmatrix}^{-1} * \begin{bmatrix} 1 & -B \\ 0 & -D \end{bmatrix} * \begin{bmatrix} P_1 \\ U_2 \end{bmatrix}$$

$$"M" = \begin{bmatrix} 1 & -B \\ 0 & -D \end{bmatrix}^{-1} * \begin{bmatrix} A & 0 \\ C & -1 \end{bmatrix}$$

$$P_2 = M(1,1) * P_1 + M(1,2) * U_2$$
$$U_1 = M(2,1) * P_1 + M(2,2) * U_2$$

In this case, the matrix is not populated completely by impedances, some of the terms, (*M(1,1)* and *M(2,2)*) are unit-less. If the pipe is radiating into the atmosphere a radiation impedance can be added:

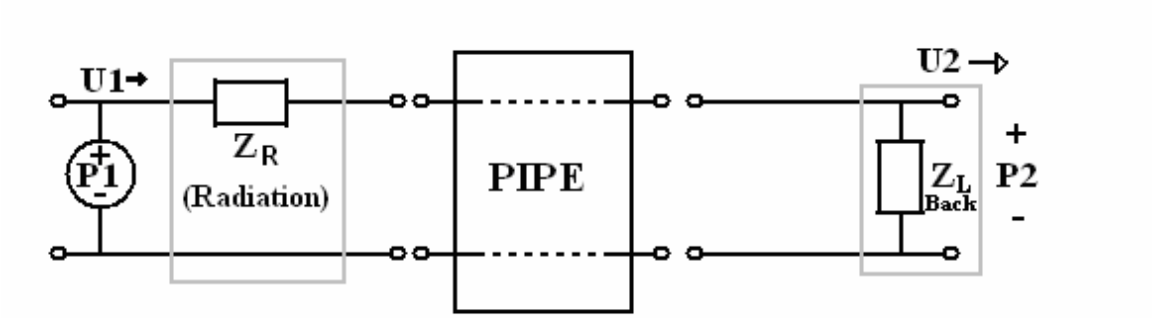

Figure **C-3**: Pipe with radiation impedance included in the model. U_2 is zero, because the end-cap is rigid.

To solve for the pressure at the termination of the pipe, the transfer matrix for the radiation load is multiplied by the transfer matrix for the rest of the duct, and this modified transfer matrix is operated on in the method defined above.

C.1.1.4 Pressure boundary conditions

When the pressures at both ends of the duct are given as the boundary conditions, the volume velocities at the end may be solved for using the exact same method that the pressures were solved for in the situation that the velocities at both ends were given as boundary conditions.

The pressure at an arbitrary point in the tube may also be calculated, as will be demonstrated in the following section.

C.1.2 Pressure and velocity calculations at arbitrary locations in ducts

The multiple-segment Tee-section model allows calculation of the pressure at any point along the length of a duct. This is useful for calculating the pressure at the location of an inserted transducer, or for making plots of how the pressure along the length of the duct varies with time. If many segments are used and the spatial variation of the field is slow, this pressure is estimated to be the pressure at the nearest Tee-section junction in the model.

The pressure at the desired location can be found using the boundary conditions of the duct and two transfer matrices, T_1 and T_2:

$$T_1 = \begin{bmatrix} a_1 & b_1 \\ c_1 & d_1 \end{bmatrix}$$
$$T_2 = \begin{bmatrix} a_2 & b_2 \\ c_2 & d_2 \end{bmatrix}$$

T_1 is the transfer matrix for the portion of the duct between the location and one end of the duct. T_2 is the transfer matrix for the portion between the location and the other end. The problem is pictured in Figure **C-4**:

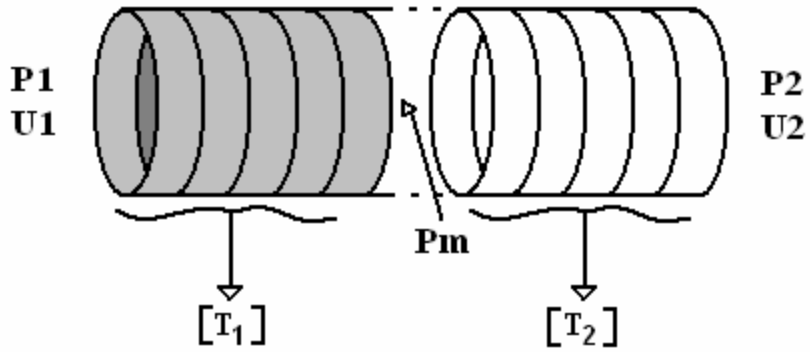

Figure **C-4**: This is an example of the division of a pipe into separate transfer matrices, to solve for the pressure P_m at a location between the ends.

Together, *T1* and *T2* relate the pressure and volume velocity at the required location to the boundary conditions at the ends. The two transfer matrices impose the following relationships,

$$\begin{bmatrix} P_1 \\ U_1 \end{bmatrix} = T_1 \begin{bmatrix} P_m \\ U_m \end{bmatrix}$$
$$\begin{bmatrix} P_2 \\ U_2 \end{bmatrix} = T_2 \begin{bmatrix} P_m \\ -U_m \end{bmatrix}$$

What occurs next depends on the given boundary conditions. The strategy for solving remains the same, however: matrices are multiplied through by P_m and U_m, and the equations relating P_m and U_m to the known boundary conditions are selected. This forms a set of 2 equations with 2 unknowns, which can be solved the same way as the previous sets were solved. For example, consider the situation of a pistonphone, which has a zero velocity boundary condition for U_2, and a known velocity boundary condition at U_1.

The equations relating the boundary velocities to P_m and U_m, are selected:

$$U_1 = c_1 P_m + d_1 U_m$$
$$0 = c_2 P_m - d_2 U_m$$

Using these, another matrix equation can be written:

$$\begin{bmatrix} U_1 \\ 0 \end{bmatrix} = \begin{bmatrix} c_1 & d_1 \\ c_2 & -d_2 \end{bmatrix} \begin{bmatrix} P_m \\ U_m \end{bmatrix}$$

This equation is defined as T_3, and inverting T_3, P_m and U_m are solved:

$$T_3 = \begin{bmatrix} c_1 & d_1 \\ c_2 & -d_2 \end{bmatrix}$$

$$\begin{bmatrix} P_m \\ U_m \end{bmatrix} = T_3^{-1} \begin{bmatrix} U_1 \\ 0 \end{bmatrix}$$

This matrix equation directly relates the pressure and volume velocity at the location in along the length of the duct to the boundary conditions at the end, in terms of the matrix, T_3, and the volume velocities at the end. Similar matrices are found for other boundary conditions.

C.1.2.1 Pipes of multiple radii

If a pipe has segments with differing radii, the process can get more complicated because the order of matrix operations becomes significant. Because of how T_1 and T_2 were defined above, the order of the matrix multiplication is reversed for one of the matrices. The order of matrix operation always occurs *from the outside in*, when T_1 and T_2 are defined as they were above.[14] This is because the boundary conditions were on the left-hand side of both equations. In some cases, each differential Tee-element will have a different radius. This would occur if a cone is being modeled. In other cases, a duct may be composed of several longer cylinders, each having a unique radius. Each cylinder may be divided into hundreds of smaller differential segments. In both cases, the matrices are ordered in exactly the same way as they come in the duct, but working from the outside inwards, with respect to the location at which the pressure and volume velocities are being solved for.

It is important to note that sign of the velocity must be consistent throughout the model, or it will not function properly. Secondly, solving for the pressure along a duct having cones is far more time-consuming than for cones of constant radius, because the computation of T_1 and T_2 is no longer as simple as calculating the transfer matrix for a single slice and raising it to the *Nth* power. Instead, transfer matrix values have to be calculated for each element in a cone.

---

[14] Many possibilities are available, for sign convention and matrix definition, this happens to be the one chosen by the author.

C.1.3 Time domain propagation

The impedances of the pipes used to calculate the Tee-sections are functions of $j?$, and solutions thus far have been frequency domain solutions. A time domain solution for the pressure response of a tube subjected to some input signal at either end of the duct can be found by calculating the Fourier spectrum of the input signal and evaluating the response of the duct to the signal. The resulting frequency domain solution that is calculated is reverted to the time domain using an inverse Fourier transform. The results correspond to the time-domain pressure response at the evaluated point. If the time-domain response is calculated for multiple points along the pipe, a plot that varies with respect to time can be used to plot the pulse as it travels down the tube. Examples are shown in Figure **C-5** and Figure **C-6**:

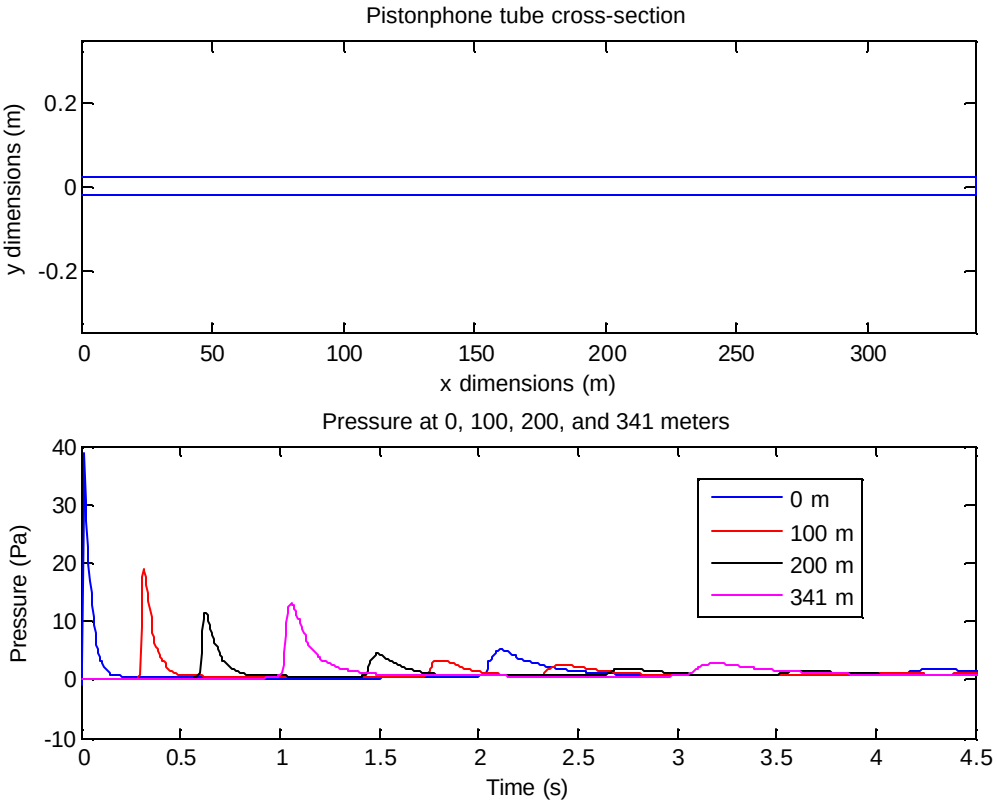

Figure **C-5**: Time domain response of a 341 meter pistonphone subjected to a pulsed velocity input. The time-domain response is recovered by calculating the spectrum of the input, evaluating the response of the tube at 5 locations (0, 100, 200, and 341 meters), applying the response to the input spectrum, and reverting to the time domain. The differential Tee-sections function like a transmission line and appropriately model the time-delay associated with acoustic propagation.

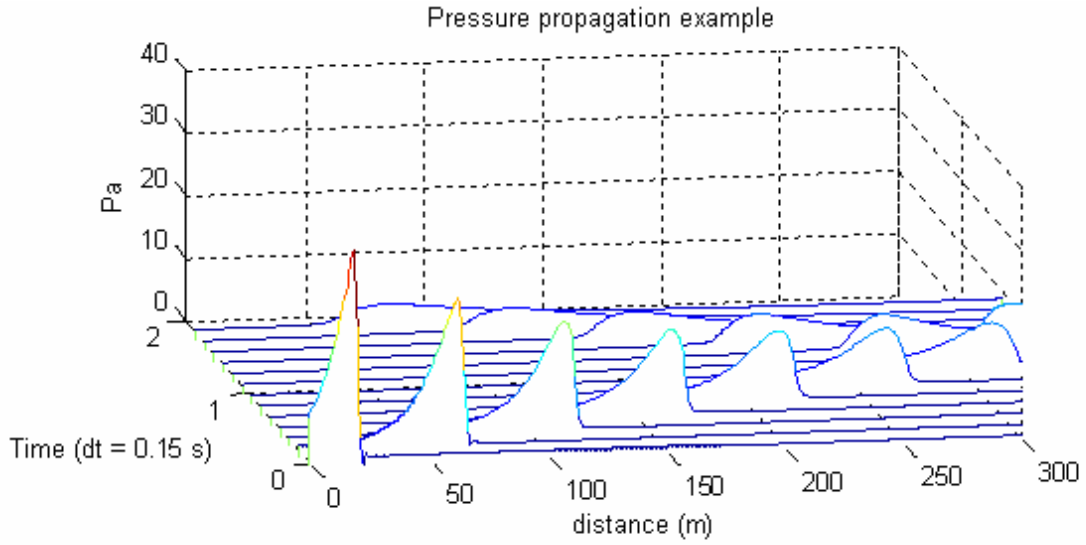

Figure **C-6**: Plot of the impulse traveling through the length of the tube. In this example a large number of points have been calculated along the length of the pipe.

Time domain plots are extremely useful for debugging models. Often times, if a computational error has occurred, (e.g. incorrectly ordering the matrices for cones, or inconsistency with velocity signs), the error isn't obvious when looking at the spectrum. When looking at a time domain plot, however, it is usually immediately apparent if the model has been assembled incorrectly.

C.1.3.1 Time domain cautions

In addition to making sure the model is computed correctly, several additional considerations need to be made when setting up a model that will evaluate the time-domain response of a duct to an input signal.

C.1.3.1.1 Low-pass filtering

If the input signal has significant spectral information near the Nyquist rate the time domain output will look like the following figure, in which the exact same input is being applied as in the previous figures but the data is not being low-pass filtered:

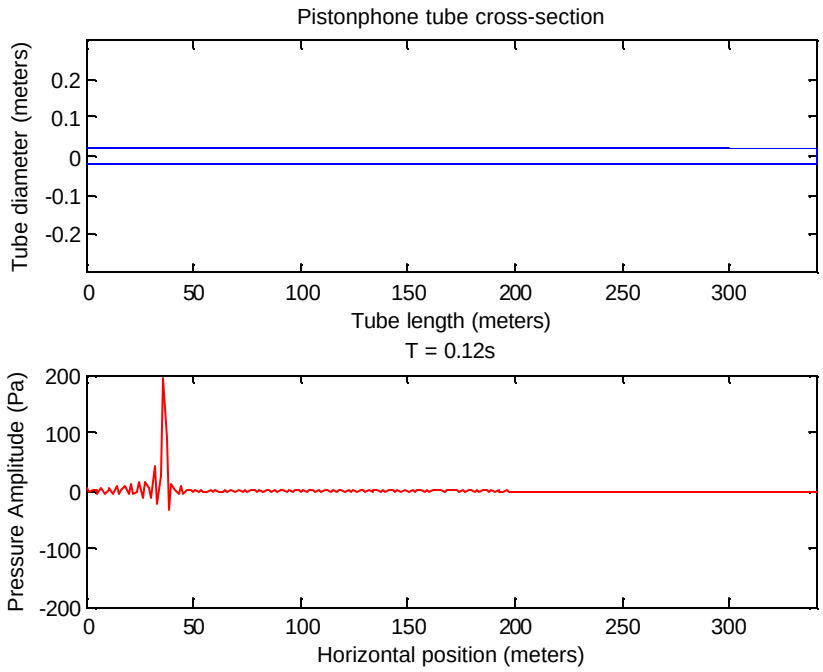

Figure **C-7**: Effects of neglecting to low-pass filter a time-domain signal

Significant amplitude disturbances seem to be propagating ahead of the leading edge of the pulse. Examining the pressure with respect to time, it can be seen that the high-frequency noise precedes the trailing edge of the signal in time.

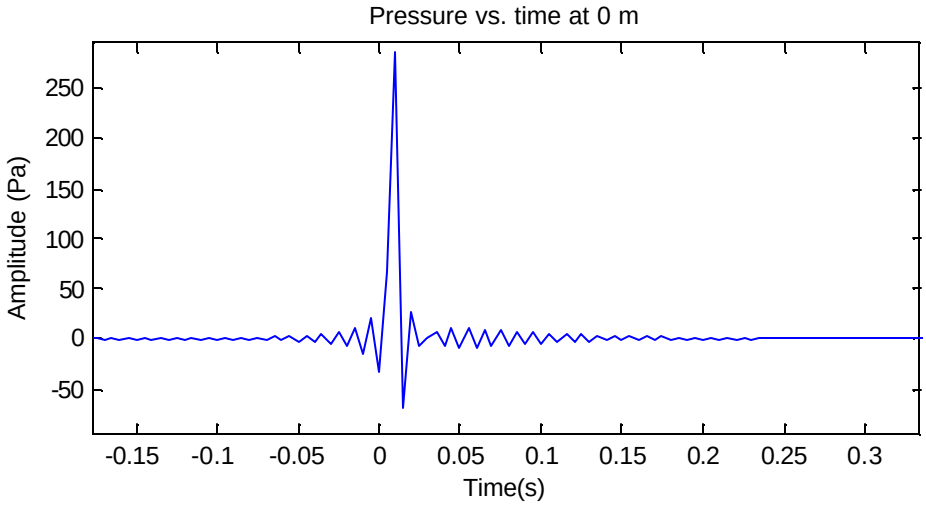

Figure **C-8**: Effects of neglecting to low-pass filter a time-domain signal. The *x*-axis is time, in this plot. Ripples lead and follow the main pulse propagating down the duct.

This problem is fixed by applying a low-pass filter to the signal with a steep enough cutoff to reduce the unwanted high-frequencies causing the ripples. If it is essential to retain high frequencies in the simulation the best option is to increase the sampling rate of the data so that a low-pass filter can be applied without affecting the desired frequency band.

C.1.3.1.2 Numerical dispersion

If the differential slices of the pipe are too few, the waves appear to propagate dispersively, as in the following illustration, (again using the same pipe and input pulse as in the first example):

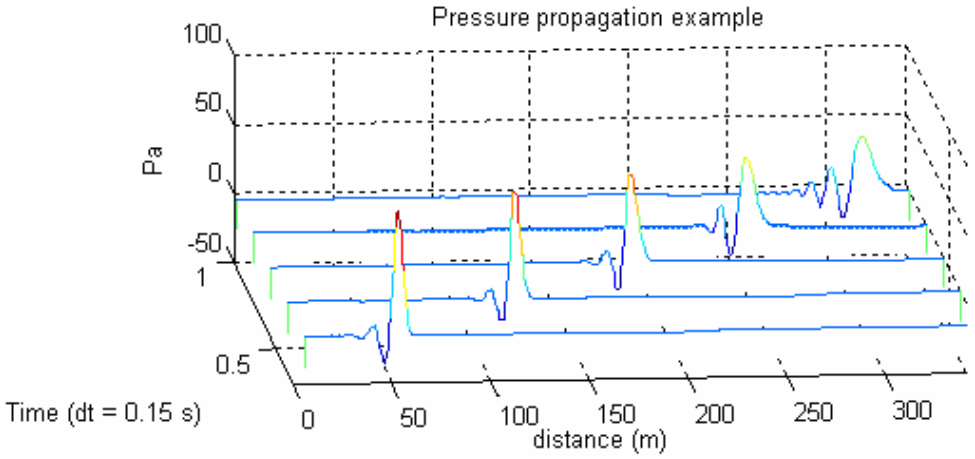

Figure **C-9**: Dispersion of a signal propagating through a duct modeled by an insufficient number of Tee-sections.

As the wave propagates down the pipe it accumulates a trail of ripples that propagate at a slightly slower speed than the leading pulse. This problem disappears if the density of Tee-sections is increased.

C.2 Three-port networks

The Tee-sections utilized in the previous examples are useful for describing a duct with two ends. Many applications require modeling duct networks in which pipes are joined, and the network may have three or more openings. In such a case Tee-sections with more than two-ports are useful for modeling the system. The three-port network will be examined because it forms a pattern for the construction of networks with more than

three ports, and the three-port network is also used predominately in the calculation of the acoustic response of porous hoses.

C.2.1 Y-model and experimental verification

An experiment is conducted in which the acoustic transfer function between two points in a network is measured. Two pressure sensors are mounted on the end-cap of a pipe connected to a 12 inch speaker cone as illustrated in Figure **C-10**:

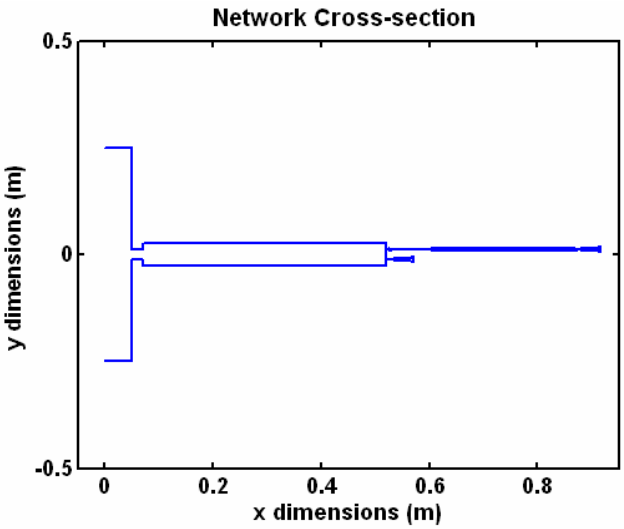

Figure **C-10**: Cross section of speaker/pipe/pressure sensor duct network. The 12'' speaker cone is placed at the large opening on the left side of the duct network.

The pressure sensors are connected to the end-cap of the pipe via capillaries with varying diameters. One of the pressure sensors is attached via a capillary that is approximately 40 cm, the other is only 5 cm long. Figure **C-11** is a zoomed in view of the cross section of the capillaries attached to the pipe.

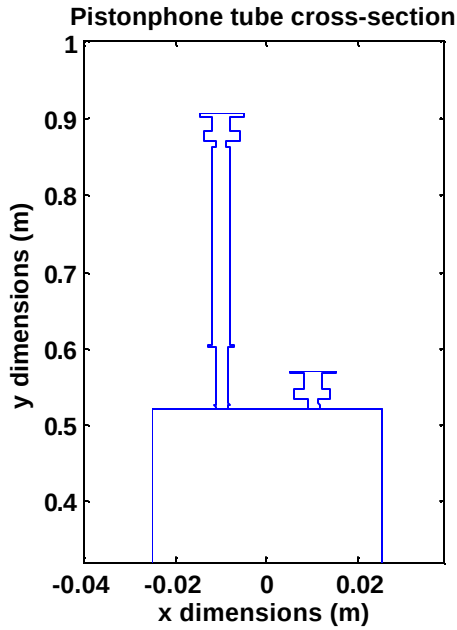

Figure **C-11**: Cross section of capillary tubes attached to the end-cap of the pipe.

The technique of interchange is used to determine the acoustic transfer function between the two mounting points for the pressure sensors.

It is initially assumed that the existence of one capillary will not affect the response at the other, because their acoustic impedances are large compared to the rest of the duct network. Using only two-port Tee-sections, a model is constructed for each pressure sensor neglecting the presence of other. The cross sections of the two models are plotted in Figure **C-12**, below:

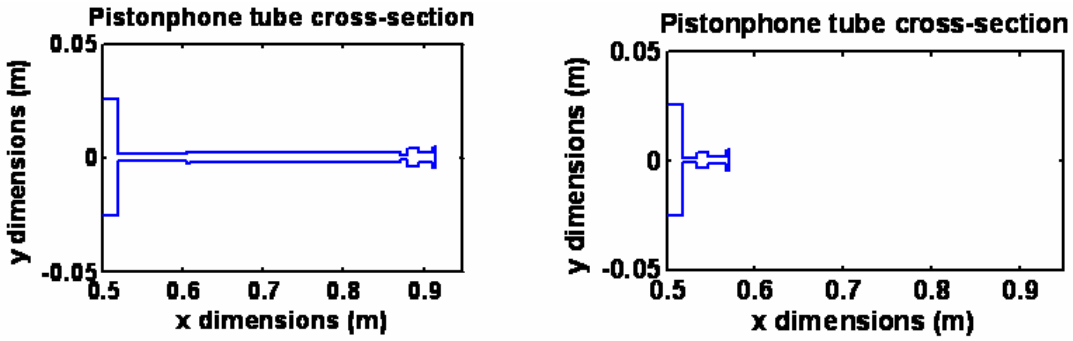

Figure **C-12**: Cross sections of the end-caps of the two models used to calculate the acoustic transfer function between the pressure sensor schematic illustrated in Figure **C11**.

The transfer function relating the two sensor locations is measured using interchange. A comparison of the measured transfer function response with the transfer function predicted using the models is shown in Figure **C-13**:

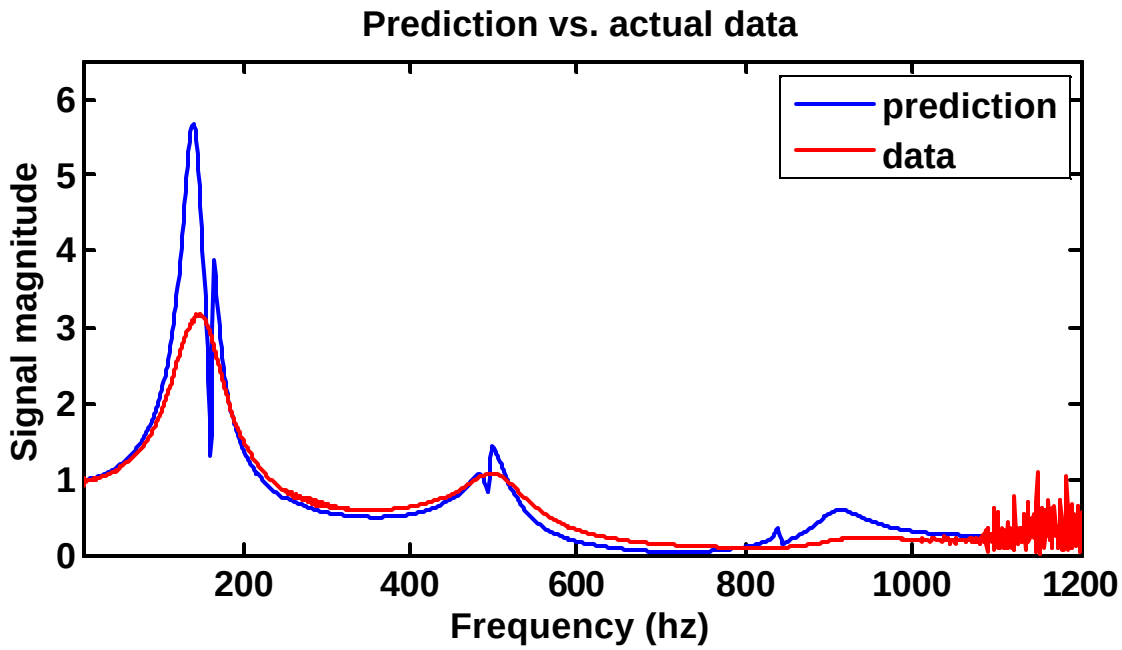

Figure **C-13**: Measured transfer function vs. prediction based on two Tee-section models that have been constructed using only two-port networks. Plot shows the linear spectrum, and the y-axis is linear in magnitude.

Several deficiencies in the model become apparent with this comparison. The predicted quality factors for the resonances differ from the measured quality factors. There are several reasons for this. Extra loss occurred in the capillaries due to insufficient sealing between segments of different diameter. There are also significant losses in acoustic systems similar to these due to flow separation and turbulence around abrupt diameter changes. A discussion of these losses and how they affect the prediction of quality factors for resonant systems can be found in references [**19**] and [**14**].

Just as obvious of a deficiency is the presence of glitches at the peaks of each resonance. These glitches are very prominent in the response predictions but are entirely absent from the measured response. To fix this problem a single model is constructed in which a three-port network is placed at the location of the end-cap of the main pipe, where the capillaries join with the main pipe. The Tee-section model for the main tube and speaker chamber are fixed to one branch of the three-port network, and the Tee-section models for the capillaries are fixed to the other two branches.

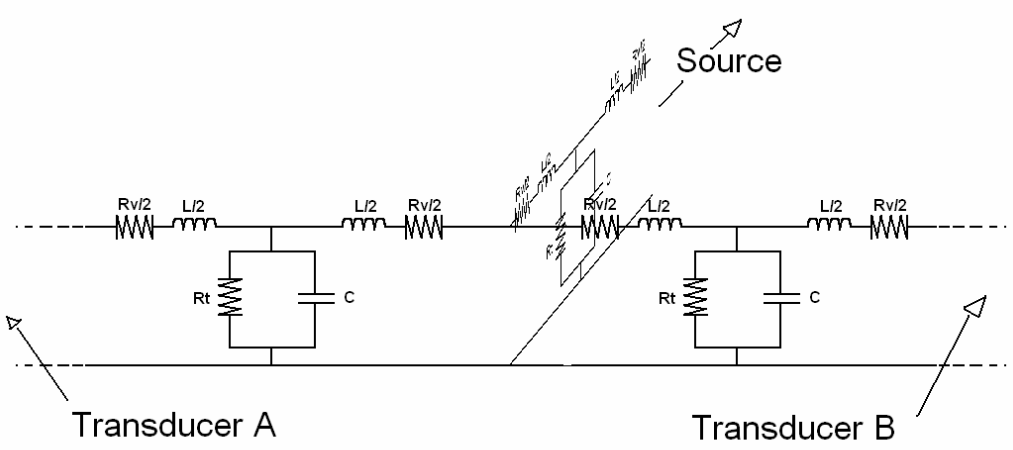

Figure **C-14**: Three-port network model illustration.

The solution is found using the following method. First, the model is broken up into three separate T-matrices connected in a three-port network:

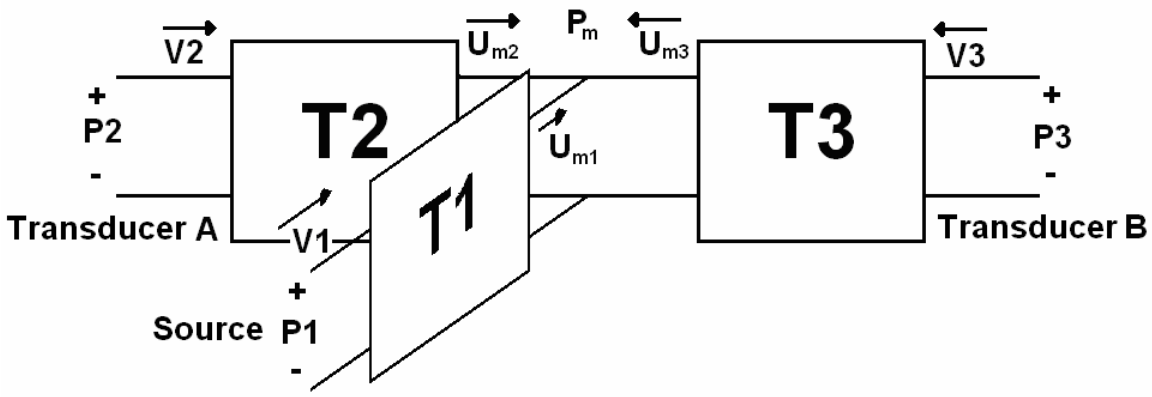

Figure **C-15**: Transfer matrix representation of Figure **C-14**.

Matrix *T1* represents the transfer matrix for the speaker chamber and large pipe, *T2* represents one of the capillaries, and *T3* represents the transfer matrix for the other capillary. The following equation can be written to describe the above matrix:

$$\begin{bmatrix} P_1 \\ U_1 \end{bmatrix} = \begin{bmatrix} a_1 & b_1 \\ c_1 & d_1 \end{bmatrix} \begin{bmatrix} P_m \\ U_{m1} \end{bmatrix}$$
$$\begin{bmatrix} P_2 \\ U_2 \end{bmatrix} = \begin{bmatrix} a_2 & b_2 \\ c_2 & d_2 \end{bmatrix} \begin{bmatrix} P_m \\ U_{m2} \end{bmatrix}$$
$$\begin{bmatrix} P_3 \\ U_3 \end{bmatrix} = \begin{bmatrix} a_3 & b_3 \\ c_3 & d_3 \end{bmatrix} \begin{bmatrix} P_m \\ U_{m3} \end{bmatrix}$$

It is important to keep track of the signs. In this case, from the perspective of the pressure at the junction *Pm*, all currents are flowing towards it and are positive. In this case, the boundary conditions are that U_1 and U_2 are zero, and P_3 is a constant pressure source. From this set of equations the following matrix can be generated:

$$\begin{bmatrix} P_1 \\ U_2 \\ U_3 \end{bmatrix} = \begin{bmatrix} a_1 & b_1 & 0 & 0 \\ c_2 & 0 & d_2 & 0 \\ c_3 & 0 & 0 & d_3 \end{bmatrix} \begin{bmatrix} P_m \\ U_{m1} \\ U_{m2} \\ U_{m3} \end{bmatrix}$$

The pressures and velocities at the junction can not be solved for yet, because the matrix is not square, and non-invertible. To make the matrix square, continuity is applied. The center of the junction is assumed to be non-compliant (it is simple to add a compliance, however, in situations where this becomes important), and mass must be conserved. The flow into the node must equal the flow out of the node, and therefore an additional row may be added to the matrix:

$$\begin{bmatrix} P_1 \\ U_2 \\ U_3 \\ 0 \end{bmatrix} = \begin{bmatrix} a_1 & b_1 & 0 & 0 \\ c_2 & 0 & d_2 & 0 \\ c_3 & 0 & 0 & d_3 \\ 0 & 1 & 1 & 1 \end{bmatrix} \begin{bmatrix} P_m \\ U_{m1} \\ U_{m2} \\ U_{m3} \end{bmatrix}$$

If compliance is required at the junction, the ones are replaced with the impedance, and the zero in the column on the left-hand side of the equation is replaced with the P_m.

The inverse of the matrix (call an "*M*" matrix in this appendix) is taken and multiplied by both sides of the equation.

$$\left[M^{-1}\right]\begin{bmatrix} P_1 \\ U_2 \\ U_3 \\ 0 \end{bmatrix} = \begin{bmatrix} P_m \\ U_{m1} \\ U_{m2} \\ U_{m3} \end{bmatrix}$$

$$\begin{bmatrix} M_{11}^{-1} & M_{12}^{-1} & M_{13}^{-1} & M_{14}^{-1} \\ M_{21}^{-1} & M_{22}^{-1} & M_{23}^{-1} & M_{24}^{-1} \\ M_{31}^{-1} & M_{32}^{-1} & M_{33}^{-1} & M_{34}^{-1} \\ M_{41}^{-1} & M_{42}^{-1} & M_{43}^{-1} & M_{44}^{-1} \end{bmatrix}\begin{bmatrix} P_1 \\ U_2 \\ U_3 \\ 0 \end{bmatrix} = \begin{bmatrix} P_m \\ U_{m1} \\ U_{m2} \\ U_{m3} \end{bmatrix}$$

U_1 and U_2 are both zero, however, so the above matrix equation reduces to:

$$\begin{bmatrix} P_m \\ U_{m1} \\ U_{m2} \\ U_{m3} \end{bmatrix} = \begin{bmatrix} M_{11}^{-1} \\ M_{21}^{-1} \\ M_{31}^{-1} \\ M_{41}^{-1} \end{bmatrix} P_1$$

Using the previously mentioned methods for solving pressures at the ends of tubes when the boundary conditions are known, the pressures at the locations of the transducers can be calculated:

$$\begin{bmatrix} P_2 \\ U_2 \end{bmatrix} = \begin{bmatrix} a_2 & b_2 \\ c_2 & d_2 \end{bmatrix}\begin{bmatrix} M_{11}^{-1}P_1 \\ M_{31}^{-1}P_1 \end{bmatrix}$$

$$\begin{bmatrix} P_3 \\ U_3 \end{bmatrix} = \begin{bmatrix} a_3 & b_3 \\ c_3 & d_3 \end{bmatrix}\begin{bmatrix} M_{11}^{-1}P_1 \\ M_{41}^{-1}P_1 \end{bmatrix}$$

$$P_2 = P_1\left(a_2 M_{11}^{-1} + b_2 M_{31}^{-1}\right)$$

$$P_3 = P_1\left(a_3 M_{11}^{-1} + b_3 M_{41}^{-1}\right)$$

The transfer function between the pressure sensors at P_2 and P_3 is found by dividing the calculated pressures. The amplitude of the pressure source falls out, and the following results is obtained:

$$\frac{P_2}{P_3} = H = \frac{\left(a_2 m_{11}^{-1} + b_2 m_{31}^{-1}\right)}{\left(a_3 m_{11}^{-1} + b_3 m_{41}^{-1}\right)}$$

This method is used to calculate the transfer function relating the acoustic pressure at one pressure sensor to the other in the experimental setup, and the prediction is compared to the actual measurement in Figure **C-16**:

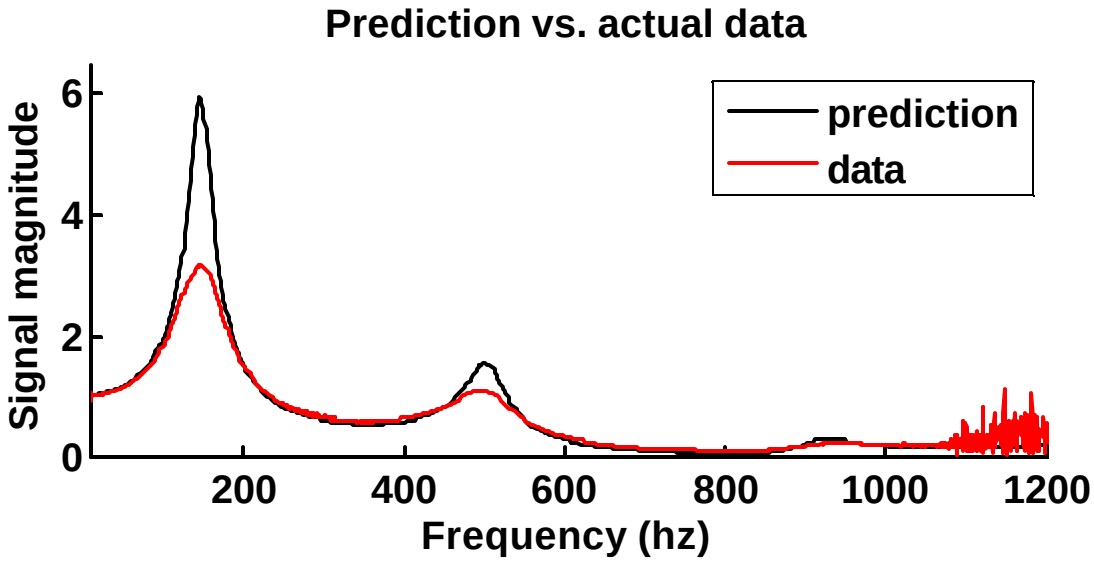

Figure **C-16**: Comparison of the measured response with the response calculated by a model incorporating a three-port network at the end-cap connected to the capillaries. The quality factor can be adjusted in the model by adding extra leak and flow resistance terms. The y-axis is linear in magnitude, units VS

The glitches completely disappear from the response, indicating that the capillaries affect the pressure response at the adjacent sensors, and this effect needs to be included in the model. This experiment demonstrates that three-port networks can effectively model acoustic duct networks having multiple branches that converge at a particular location.

C.2.2 Modeling porous ducts

The three-port network described above is the major component of the porous hose model that has been developed. The model is initially set up exactly the same as a regular duct. The duct is partitioned into *n* slices, where the acoustic properties of each slice are described by a Tee-section. In the non-porous model all the transfer matrices corresponding to the Tee-sections are multiplied together to form one large T-matrix. In the case of the porous model, each slice is divided in half,* forming two equally sized T-matrices T_{d1} and T_{d2} that if multiplied together equal the transfer matrix representing one full slice.

* The reason for not initially slicing the pipe into twice as many segments is that it is necessary that T_{d1} and T_{d2} are equal to each other, to make calculations simpler. This will not be the case if the pipe is conical and the pipe is partitioned by dividing it into 2**n* segments.

To represent the pore, a port of a third two-port network is connected to the junction of T_{d1} and T_{d2}. The components of this third network are entirely up to the model designer. It could be a single resistance, a very thin hose, or it could also have a zero-velocity boundary condition at the opposing side, forming a resonator as in the Y-model example. There are a lot of possibilities.

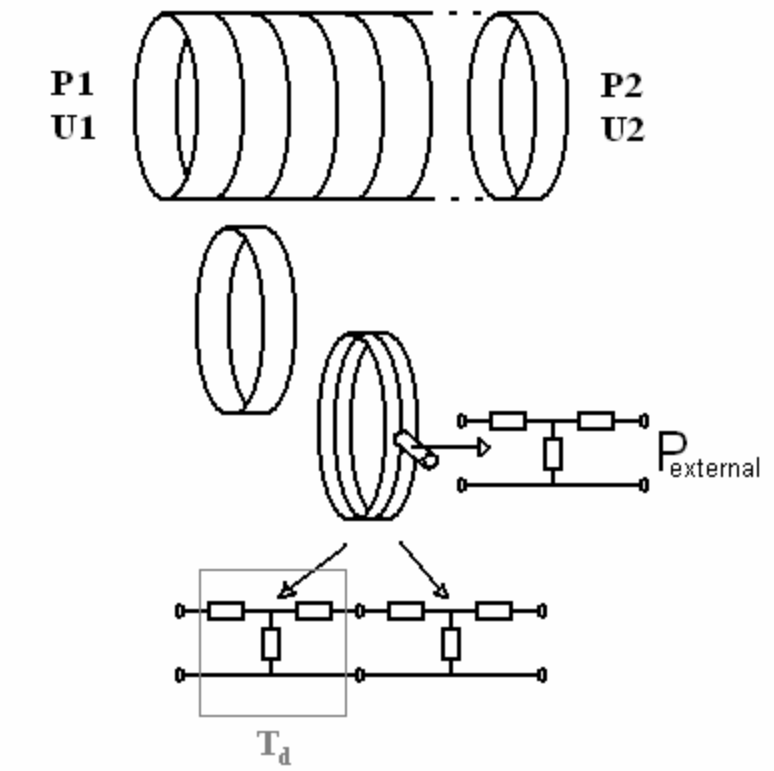

Figure **C-17**: Illustration of the process in which the differential segments are divided and each half, along with the leak (represented by a small tube), are represented by Tee-sections.

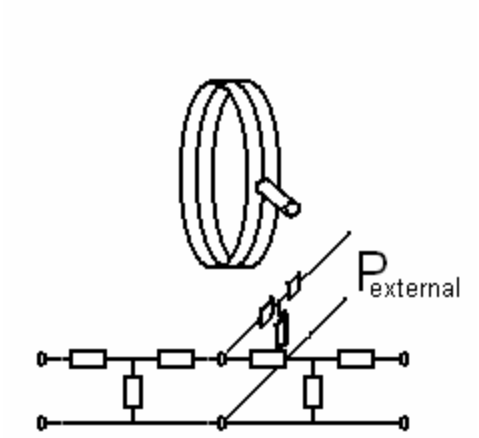

Figure **C-18**: Illustration of the connection of the transmission line model in which the third Tee-section (representing the pore), has been connected to the junction of the other Tee-sections representing the halves of the segment. $P_{external}$ is the local pressure at the location of the pore.

The inputs for the porous hose model are the boundary conditions on either end of the hose and the local acoustic pressure seen by each pore along the length of the hose. If the hose is open at both ends then all the boundary conditions for the porous hose solution are pressures. Representing the transfer matrices formed by multiplying adjacent halves of adjacent slices as T_{ddn} and the transfer matrices of the pores as T_{pn}, the following illustration for the porous hose is constructed:

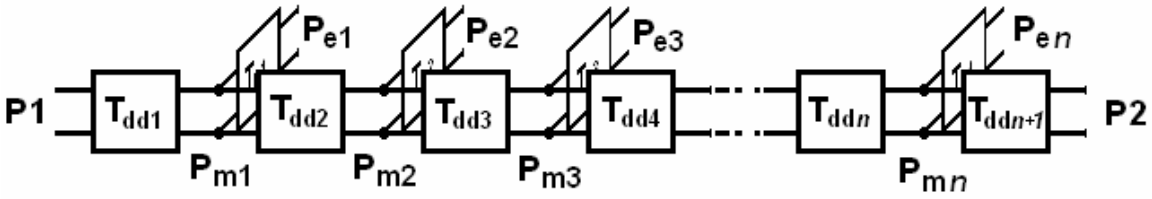

Figure **C-19**: Porous hose model showing transfer matrices between key locations along the length of the hose. P_1 and P_2 are the pressures at the mouths of the hose, P_{e1} through P_{en} are the local pressures at the pores along the hose, and $P_{m1}…P_{mn}$ are the local pressures inside the hose along the length of the hose.

The pressures inside the hose $P_{m(1-n)}$ are useful to calculate for visualization of propagation through the hose and debugging purposes.

Assuming that all boundary conditions are known, the pressure inside the pipe may be calculated as follows. Assume that the current flows as shown in Figure **C-20**:

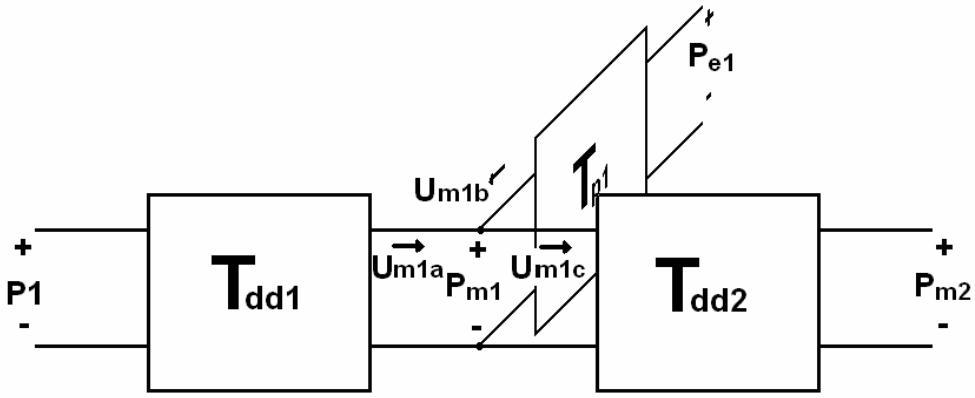

Figure **C-20**: Figure showing the current flow for the first section of Figure **C-19**.

Defining positive as towards the node, the following matrix-equation can be used to define this portion of the hose:

$$\begin{bmatrix} P_1 \\ P_{e1} \\ P_{m2} \\ 0 \end{bmatrix} = \begin{bmatrix} a_1 & b_1 & 0 & 0 \\ a_2 & 0 & b_2 & 0 \\ a_3 & 0 & 0 & -b_3 \\ 0 & 1 & 1 & -1 \end{bmatrix} \begin{bmatrix} P_{m1} \\ U_{m1a} \\ U_{m1b} \\ U_{m1c} \end{bmatrix}$$

In a similar way, the next node can be described by:

$$\begin{bmatrix} P_{m1} \\ P_{e2} \\ P_{m3} \\ 0 \end{bmatrix} = \begin{bmatrix} a_1 & b_1 & 0 & 0 \\ a_2 & 0 & b_2 & 0 \\ a_3 & 0 & 0 & -b_3 \\ 0 & 1 & 1 & -1 \end{bmatrix} \begin{bmatrix} P_{m2} \\ U_{m2a} \\ U_{m2b} \\ U_{m2c} \end{bmatrix}$$

Assuming the porous hose is of constant diameter, and the leaks have uniform impedance, the pressures inside the hose can be related to each other using:

$$\begin{bmatrix} P_{m(n-1)} \\ P_{emn} \\ P_{m(n+1)} \\ 0 \end{bmatrix} = M * \begin{bmatrix} P_{mn} \\ U_{mna} \\ U_{mnb} \\ U_{mnc} \end{bmatrix}$$

$$M = \begin{bmatrix} a_1 & b_1 & 0 & 0 \\ a_2 & 0 & b_2 & 0 \\ a_1 & 0 & 0 & -b_1 \\ 0 & 1 & 1 & -1 \end{bmatrix}$$

$$T_{dd} = \begin{bmatrix} a_1 & b_1 \\ c_1 & d_1 \end{bmatrix}$$

$$T_p = \begin{bmatrix} a_2 & b_2 \\ c_2 & d_2 \end{bmatrix}$$

Using these values, P_{mn} can be calculated in terms of the adjacent pressures:

$$\left[M^{-1}\right] \begin{bmatrix} P_{m(n-1)} \\ P_{emn} \\ P_{m(n+1)} \\ 0 \end{bmatrix} = \begin{bmatrix} P_{mn} \\ U_{mna} \\ U_{mnb} \\ U_{mnc} \end{bmatrix}$$

$$M^{-1} = \begin{bmatrix} M_{11}^{-1} & M_{12}^{-1} & M_{13}^{-1} & M_{14}^{-1} \\ M_{21}^{-1} & M_{22}^{-1} & M_{23}^{-1} & M_{24}^{-1} \\ M_{31}^{-1} & M_{32}^{-1} & M_{33}^{-1} & M_{34}^{-1} \\ M_{41}^{-1} & M_{42}^{-1} & M_{43}^{-1} & M_{44}^{-1} \end{bmatrix}$$

$$P_{mn} = M_{11}^{-1} P_{m(n-1)} + M_{12}^{-1} P_{emn} + M_{13}^{-1} P_{m(n+1)}$$

Using this relationship, a matrix relating all the boundary pressures to the pressures inside the hose can be constructed:

$$d = M_{11}^{-1}$$

$$e = M_{12}^{-1}$$

$$f = M_{13}^{-1}$$

$$\begin{bmatrix} dP_1 + eP_{e1} \\ eP_{e2} \\ eP_{e3} \\ eP_{e4} \\ \vdots \\ eP_{en} + fP_2 \end{bmatrix} = \begin{bmatrix} 1 & f & 0 & 0 & \cdots & 0 \\ d & 1 & f & 0 & & 0 \\ 0 & d & 1 & f & & 0 \\ 0 & 0 & d & 1 & & 0 \\ \vdots & & & & \ddots & 0 \\ 0 & 0 & 0 & 0 & d & 1 \end{bmatrix} \begin{bmatrix} P_{m1} \\ P_{m2} \\ P_{m3} \\ P_{m4} \\ \vdots \\ P_{mn} \end{bmatrix}$$

where *n* represents the total number of points being solved for inside the pipe. At this point, the pressures may be solved for:

$$G = \begin{bmatrix} 1 & f & 0 & 0 & \cdots & 0 \\ d & 1 & f & 0 & & 0 \\ 0 & d & 1 & f & & 0 \\ 0 & 0 & d & 1 & & 0 \\ \vdots & & & & \ddots & 0 \\ 0 & 0 & 0 & 0 & d & 1 \end{bmatrix}$$

$$G^{-1}\begin{bmatrix} dP_1 + eP_{e1} \\ eP_{e2} \\ eP_{e3} \\ eP_{e4} \\ \vdots \\ eP_{en} + fP_2 \end{bmatrix} = \begin{bmatrix} P_{m1} \\ P_{m2} \\ P_{m3} \\ P_{m4} \\ \vdots \\ P_{mn} \end{bmatrix}$$

$$P_{m1} = G_{11}^{-1}\left(dP_1 + eP_{e1}\right) + G_{12}^{-1}\left(eP_{e2}\right) + \ldots + G_{1n}^{-1}\left(eP_{en} + fP_2\right)$$

$$P_{m2} = G_{21}^{-1}\left(dP_1 + eP_{e1}\right) + G_{22}^{-1}\left(eP_{e2}\right) + \ldots + G_{2n}^{-1}\left(eP_{en} + fP_2\right)$$

$$\vdots$$

This is an example of the solution for a single porous hose with open ends, but very few modifications need to be made to the example above to change the boundary conditions, or to add additional hose characteristics, such as radiation impedance from the ends or pores.

The fact that calculating the pressure response of a porous hose requires solving for the pressure at numerous points along the length of the hose means that porous hose pressure calculations are readily adaptable to time-domain plots illustrating the pressure along the length of the hose as a function of time.

C.2.2.1 Zero pressure external ducts

The porous hose model that has been calculated assumes that the magnitude of the acoustic pressure outside the hose at the mouth of the tube is large enough to significantly affect the pressure inside the tube. If the acoustic pressure at the openings of the pores can be considered zero (useful for predicting the attenuation of signals from one end of a porous hose to the other), then the model can be simplified considerably. This can be done in two ways. The simplest way, given the formula above, is to assume that all the $e*P_e$ coefficients are zero, and solve for all the pressures.

If the acoustic pressure outside the pore can be approximated as zero, Figure **C-19** can be re-drawn such that the pore-pressures are replaced with wires shorted to ground, as is drawn in Figure **C-21**:

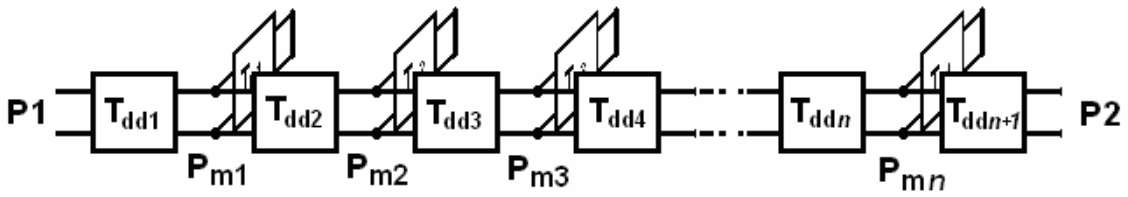

Figure **C-21**: Modifying the network in Figure **C-19**, so that the acoustic pressure at the pores (on the outside of the hose) is zero.

Short circuiting the input to ground allows the pore impedance network to be modeled as a single impedance to ground, (*"Zpore"* in the figure below). The Tee-section can be re-worked so that instead of having the pore impedance located between separate Tee-sections, the pore impedance is placed in parallel with the compliance of the portion of tube.

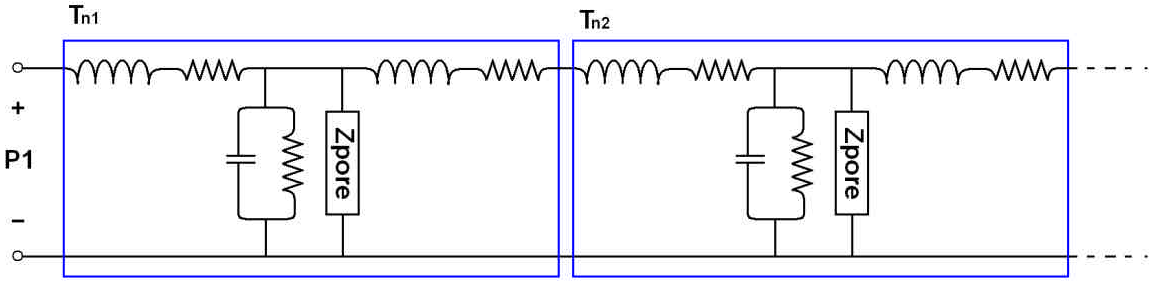

Figure **C-22**: Illustration of a Tee-section hose model, modified to include pores subjected to no external acoustic signal.

At this point the Tee-sections assemble to form a duct in exactly the same way as described in the non-porous section, and acoustic propagation through complicated models composed of porous cones, cylinders of different radius and porosity, and multiple branches can be evaluated.

C.2.3 Experimental verification

It would be impractical to model each pore in a porous hose. The pores in the constructed model represent a "lumped pore impedance" for a length of hose, (the

impedance is dominated by resistance, however, and may occasionally be referred to as "lumped pore *resistance*" in this appendix). For example, a 5 meter soaker hose may be partitioned into 500 segments, so that each Tee-section models one centimeter of hose. The lumped pore impedance would represent the total impedance formed by the parallel combination of all the small pores that exist in that segment of hose. The question then becomes one of finding a way to measure the lumped pore impedance for a segment of hose, so that an actual experimentally determined value may be plugged into the model. This section describes two methods for experimentally determining the lumped porous *resistance* of a segment of tubing. The methods assume that the impedance is dominated by an acoustic resistance. A model is constructed, and the pressure response of the model is compared to experimentally measured values for acoustic resistance.

C.2.3.1 Measuring lumped pore resistance (method 1)

The hose used in this measurement is a standard black soaker hose purchased from Lowe's. The hose varies in many ways from an ideal porous tube. Its normal application does not require a precisely uniform porosity, nor does it require a huge amount of a quality control. This means that the lumped pore resistance at one part of the hose may vary significantly from the lumped pore resistance at another part. The porosity may also vary significantly from one hose to another. In this experiment, a two meter section of hose is analyzed. No work has yet been done to evaluate the consistency between different hoses. Lastly, it is unknown what effects such as temperature, age, humidity, dampness or dirt may have on the lumped pore impedance of a porous hose.

The first method used to determine the lumped pore resistance is to attach a segment of porous hose to a variable-frequency infrasonic pistonphone, and clamp the end of the hose at a particular length. A 0.1 to 3 Hz swept-sine signal is produced by the piston, and the low-frequency roll-off resulting from the resistance of the hose and compliance of the pistonphone chamber is directly measured. Once the curve is measured for a particular length of hose, it is clamped at a different length and the roll-off is measured again. An illustration of the experimental apparatus is shown in Figure **C-23**.

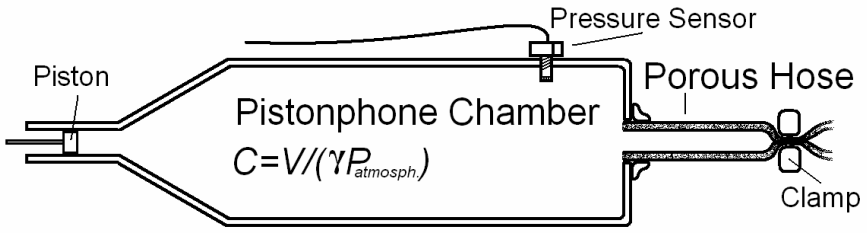

Figure **C-23**: Experimental apparatus used to measure the lumped pore impedance of a length of porous hose.

This process is repeated for lengths of hose ranging from 0.05 to 1.6 meters. The lumped element impedances that result in the best curve fit for each length is found. Using a conductance conversion, these measured resistances are then converted to an equivalent lumped resistance for 1 meter of tubing (i.e. if the hose was extended or truncated to 1 meter, it would have the following resistances). The following list is a table of values measured for different lengths of porous hose.

Table **C-1**: Measured lumped pore resistances (equivalent for 1 meter of hose) that resulted in the best curve fits for the listed lengths of porous hose.

Porous hose length (m)	Best fit resistance kg/(s m^5)
0.1	1.20e6
0.2	1.50e6
0.4	1.52e6
0.6	1.50e6
0.8	1.48e6
1.0	1.50e6
1.2	1.50e6
1.4	1.48e6
1.6	1.54e6

The measured values are fairly consistent, the average is 1.47e6 kg/(s m^5), and the standard deviation is 7%. Figure **C-24** is a plot of several of the measured response curves overlaid on predictions employing Tee-section models for the pistonphone, and the porous hose segment incorporating the best-fit resistances:

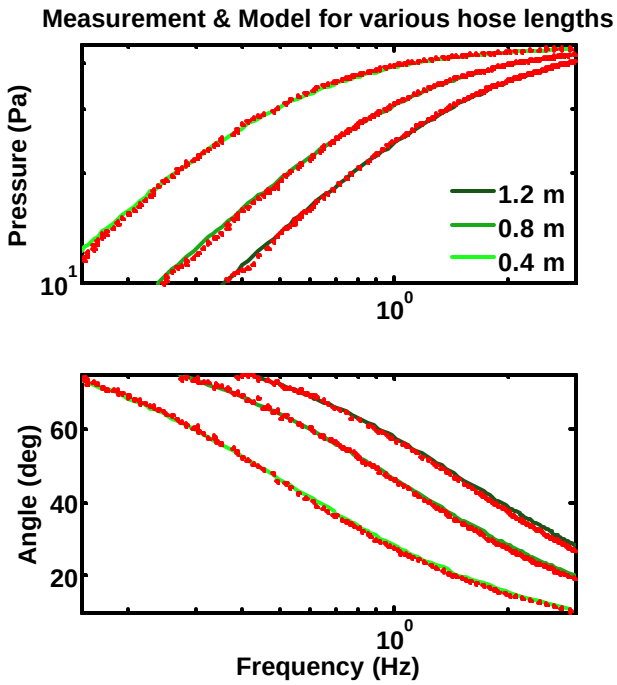

Figure **C-24**: Illustration of the method by which the lumped pore resistance is measured. A model for the pistonphone/porous hose apparatus is constructed, and the lumped pore resistance is varied until the roll-off of the model matches the measured roll-off. This lumped-pore-resistance can be used to characterize the porosity of the hose.

Figure **C-24** shows that the model and the measurements line up extremely well, using the previously defined porous-hose model and correctly tuned resistances. These curves lend credibility to the previously described porous hose model, at low frequencies.

C.2.3.2 Measured lumped pore resistance (method 2)

The data spread and measurement consistency is good in the previous example, but the measurement requires an infrasonic pistonphone. This section presents a very cheap and quick method for measuring the lumped acoustic resistance of a length of hose. If a volume of air is known, the acoustic compliance can be calculated. Using the equation **t** = RC, the resistance of a portion of hose can be found by over-pressurizing the volume of air and measuring the time constant resulting from equilibrating the pressure through a length of porous hose. The experimental setup is diagramed in Figure **C-25**.

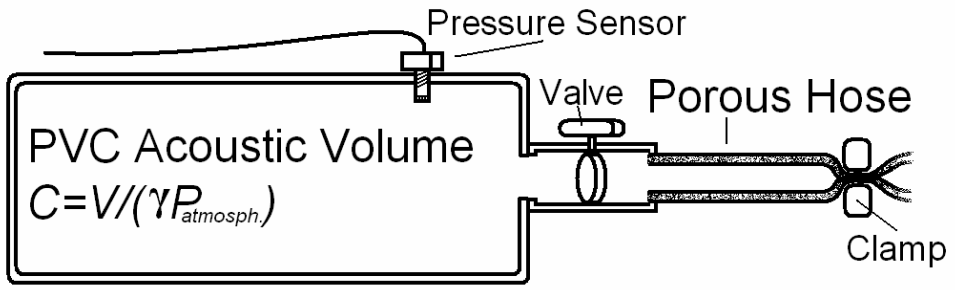

Figure **C-25**: Apparatus used to determine the acoustic resistance of a length of hose. The volume is pressurized, and the valve is quickly opened. Using the pressure sensor, the decay time of the internal pressure is measured. The resistance can be calculated from the equation **t** = RC.

An interesting phenomenon is observed when actual measurements are made. The decay time is highly dependant on the pressure inside the volume. When the volume is pressurized to several PSI, the decay time is shorter than when the volume is pressurized to a value on the order of the pressure generated by the pistonphone. This is relatively important because it means that the lumped pore impedance may be non-linear with pressure amplitude, and the frequency response of the hose could be dependent on the amplitude of the acoustic signal it is subject to. It has bee suggested to the author that at higher pressures the hose bulges and the average pore size increases. Because the resistance is proportional to r^4, a small change in pore radius *r* can create a large change in flow resistance.

Table **C-2** is a list of values measured using the time constant method:

Table **C-2**: Lumped-pore resistance values (1 meter equivalent) for the same porous hose, measured using the time constant method.

Porous hose length (m)	Best fit resistance kg/(s m^5)
0.8	1.34e6
1.0	1.28e6
1.2	1.37e6
1.4	1.40e6
1.6	1.42e6

The standard deviation is 4%, and the average value is 1.36e6 kg/(s m^5). The values are consistently lower than the values measured by the other method; however, the averages vary by only 8%. Given that the hose being measured is a $5 soaker hose, and

the total parts cost for this method of resistance-measurement is about $30 (aside from the data acquisition system), this isn't a bad method for estimating the lumped-pore-resistance of a length of porous hose.

C.2.3.3 Measurement vs. model

The high degree of correspondence between the model and the measurement shown in Figure **C-24** provides ample experimental verification for the porous hose model. In addition, however, several conclusions were drawn from prior experiments with porous hoses made by D. Shields [**13**]. The conclusions from his experiments are that 1) the termination of a porous hose used for infrasonic array deployment (> 10 meters) makes no measurable difference on the acoustic response of the hose, and 2) the hose exhibits no resonances. Both of these conclusions are supported by porous hose simulations.

Figure **C-26** is a time-domain plot of the pressure response of a 10 meter porous hose, excited on one end by a 20 Hz signal. The model incorporates a measured value for lumped acoustic impedance (plugging in the value from either method results in nearly identical graphs).

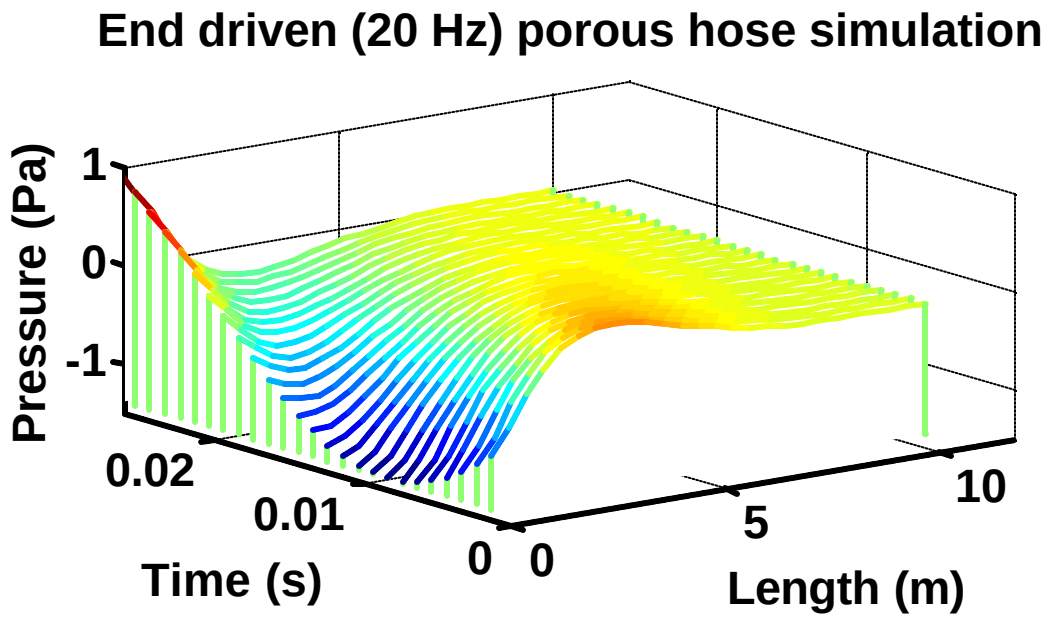

Figure **C-26**: Time domain response of a 10 meter porous hose incorporating measured resistance values.

The important thing to note about this graph is that the signal has attenuated at 10 meters to such an extent that reflections off the end are negligibly small. This would

imply both conclusions made in the D. Shields presentation: 1) no resonances are present, and 2) the termination of the end of the pipe makes little difference. These conclusions are further supported by an infrasonic array simulation, in which a typical array setup is modeled and the response from 1 to 100 Hz is evaluated. Figure **C-27** is a plot of the array model, and Figure C-28 is the plot of the modeled response, along with the response for the same system if no pores are added into the system.

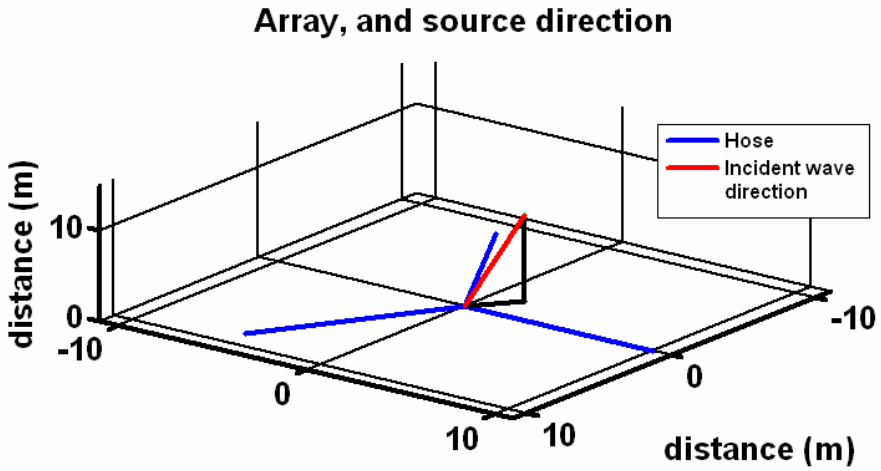

Figure **C27**: Infrasonic array model. Blue lines show the spatial location of the porous hoses and the red line indicates the direction normal to the direction of the propagation of the plane wave used to excite the response.

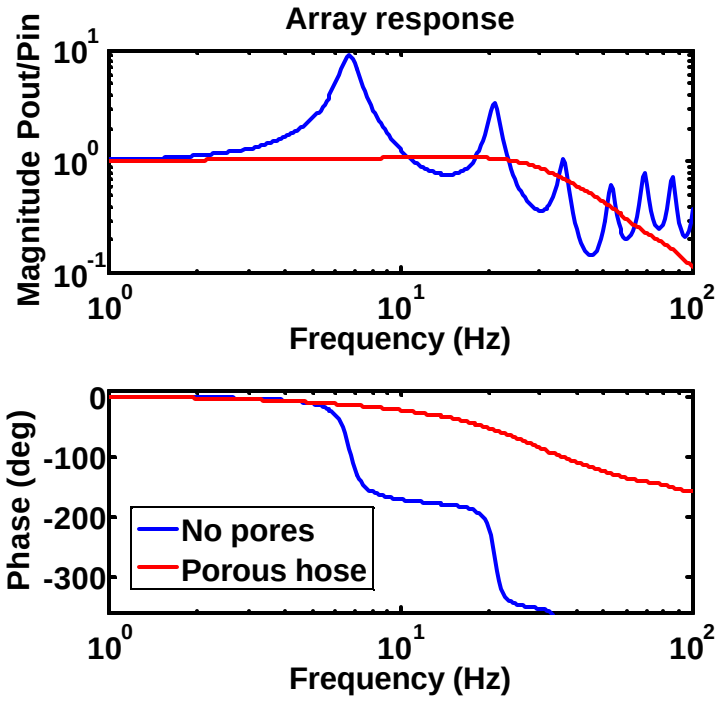

Figure **C-28**: Acoustic response of a porous-hose array, compared to the acoustic response of a solid infrasonic array having the same pipe layout. The infrasonic array exhibits no resonance.

Methods used for evaluating the response of externally-excited porous hoses joined in multiple branches are more complicated than the modeling methods yet demonstrated, and some of the math will be worked out in the next section. The important thing to note from the above figures is that the porous hose infrasonic array response exhibits no resonance peak, which is consistent with the conclusions in reference [**13**].

All experimentation thus far appears to be consistent with the model, and actual measured responses correspond extremely well with predicted responses. Aside from problems that could be introduced by a non-linear pore resistance, (acoustic signals with a high enough amplitude for the resistance to become non-linear is difficult to produce), the model appears to work well for modeling the plane wave response of acoustic signals in porous ducts.

C.3 Modeling more complicated networks

This section will describe the matrix algebra used to model infrasonic arrays and porous duct networks that have multiple branches. The models in this section are

explicitly designed to model infrasonic arrays, however it is hoped that the re-occurring patterns in the solutions will be useful for a reader who wishes to apply tee-sections to a broader variety of applications.

Several array designs are constructed. Non-porous infrasonic arrays normally have a single primary summer and multiple secondary summers, such as the example in Figure **C-29**.

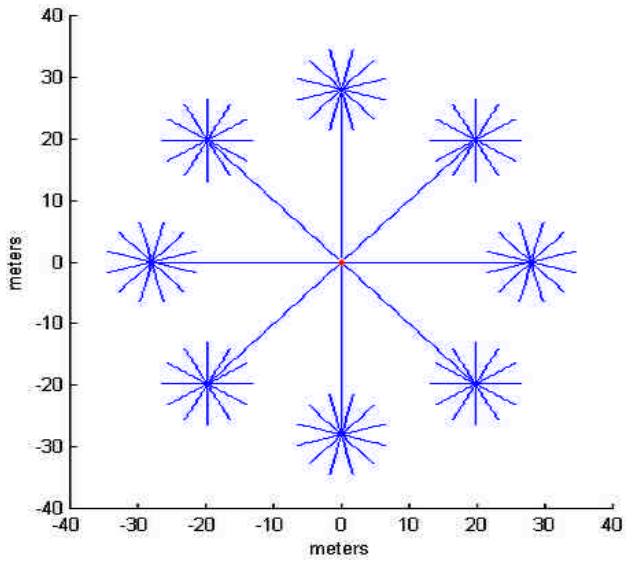

Figure **C-29**: Model of an actual infrasonic array deployed in France. The pipes used in construction are non-porous.

This model is a useful example for implementation of *n*-port networks where *n* can be arbitrarily sized. Arrays that use porous hoses typically have a primary summer and no secondary summers, however some arrays employ hoses that are solid between the secondary summers and primary summer, but use porous hoses for the pipes extending from the secondary summers. For this reason, a model is also developed for a porous hose version having primary and secondary summers, and the solution will also be described.

C.3.1 Solid pipe arrays

The solution for a network of three joined pipes has already been given in section **C.2.1**. The present goal is to find a formula for the pressure at any point in a solid-pipe network having an arbitrary number of secondary summers and air inlets per summer. The boundary conditions for the network are the pressures at the inlets. To develop such a model, it is often useful to start with the simplest case and work up in complexity.

Figure **C-30** depicts the simplest case for an infrasonic array having both primary and secondary summers.

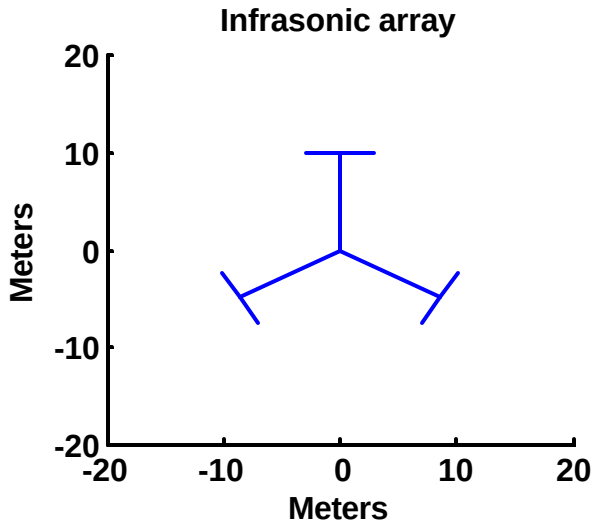

Figure **C-30**: Simplest case infrasonic array with primary and secondary summers

In this example, three pipes extend from each summer and there are six inlets into the network. Figure **C-31** shows the relevant pressures for the problem:

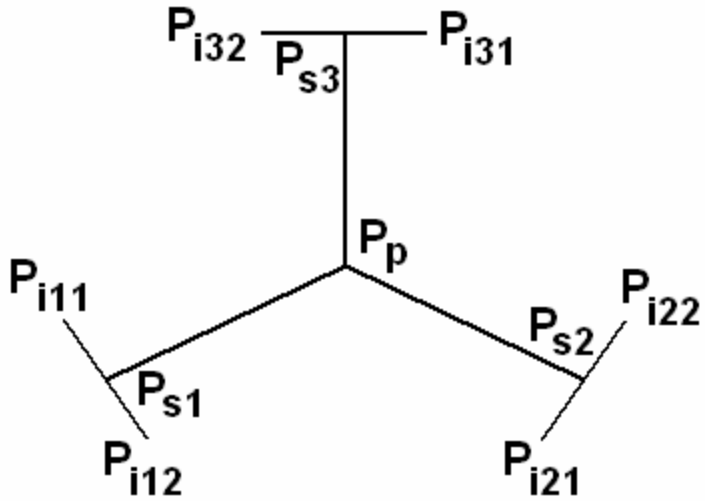

Figure **C-31**: Relevant pressures inside the infrasonic array.

P_p is the pressure at the primary summer, and is the pressure that would be detected by a micro-barometer inside the array. P_s is a pressure at a secondary summer,

and which summer is denoted by the subscript. P_i is a pressure at an air inlet, and is a "known" in the problem. The volume velocities at each point are denoted U, where a, b, and c corresponds to pipe 1, 2, or the primary pipe respectively.

The first goal is to find the pressure at the primary summer, where the micro-barometer is located. The matrix equations at the primary and secondary summers are written:

$$\begin{bmatrix} P_{s1} \\ U_{s1c} \end{bmatrix} = \begin{bmatrix} a_1 & b_1 \\ c_1 & d_1 \end{bmatrix} \begin{bmatrix} P_p \\ U_{pa} \end{bmatrix}$$

$$\begin{bmatrix} P_{s2} \\ U_{s2c} \end{bmatrix} = \begin{bmatrix} a_1 & b_1 \\ c_1 & d_1 \end{bmatrix} \begin{bmatrix} P_p \\ U_{pb} \end{bmatrix}$$

$$\begin{bmatrix} P_{s3} \\ U_{s3c} \end{bmatrix} = \begin{bmatrix} a_1 & b_1 \\ c_1 & d_1 \end{bmatrix} \begin{bmatrix} P_p \\ U_{pc} \end{bmatrix}$$

$$\begin{bmatrix} P_{s1} \\ P_{s2} \\ P_{s3} \\ 0 \end{bmatrix} = \begin{bmatrix} a_1 & b_1 & 0 & 0 \\ a_1 & 0 & b_1 & 0 \\ a_1 & 0 & 0 & b_1 \\ 0 & 1 & 1 & 1 \end{bmatrix} \begin{bmatrix} P_p \\ U_{pa} \\ U_{pb} \\ U_{pc} \end{bmatrix}$$

Above is the matrix equation relating the pressure at the secondary summers to the primary summer. It is assumed that all the pipes have the same radius, and are divided into the same number of slices. The equations for the secondary summers are also written:

$$\begin{bmatrix} P_{i11} \\ P_{i12} \\ P_p \\ 0 \end{bmatrix} = \begin{bmatrix} a_2 & b_2 & 0 & 0 \\ a_2 & 0 & b_2 & 0 \\ a_1 & 0 & 0 & -b_1 \\ 0 & 1 & 1 & -1 \end{bmatrix} \begin{bmatrix} P_{s1} \\ U_{s1a} \\ U_{s1b} \\ U_{s1c} \end{bmatrix}$$

$$\begin{bmatrix} P_{i21} \\ P_{i22} \\ P_p \\ 0 \end{bmatrix} = \begin{bmatrix} a_2 & b_2 & 0 & 0 \\ a_2 & 0 & b_2 & 0 \\ a_1 & 0 & 0 & -b_1 \\ 0 & 1 & 1 & -1 \end{bmatrix} \begin{bmatrix} P_{s2} \\ U_{s2a} \\ U_{s2b} \\ U_{s2c} \end{bmatrix}$$

$$\begin{bmatrix} P_{i11} \\ P_{i12} \\ P_p \\ 0 \end{bmatrix} = \begin{bmatrix} a_2 & b_2 & 0 & 0 \\ a_2 & 0 & b_2 & 0 \\ a_1 & 0 & 0 & -b_1 \\ 0 & 1 & 1 & -1 \end{bmatrix} \begin{bmatrix} P_{s3} \\ U_{s3a} \\ U_{s3b} \\ U_{s3c} \end{bmatrix}$$

For this model, the sign convention is that positive flow is towards the evaluated node, and that all volume velocities are pointed towards the primary node. For this reason the sign on the (3, 4) and (4, 4) elements are reversed. The sign convention can be different, but must be consistent. The inverses of the matrices can be taken, and a system of equations is formed:

$$M_p = \begin{bmatrix} a_1 & b_1 & 0 & 0 \\ a_1 & 0 & b_1 & 0 \\ a_1 & 0 & 0 & b_1 \\ 0 & 1 & 1 & 1 \end{bmatrix}$$

$$M_s = \begin{bmatrix} a_2 & b_2 & 0 & 0 \\ a_2 & 0 & b_2 & 0 \\ a_1 & 0 & 0 & -b_1 \\ 0 & 1 & 1 & -1 \end{bmatrix}$$

$$P_p = M_{p11}^{-1} P_{s1} + M_{p12}^{-1} P_{s2} + M_{p13}^{-1} P_{s3}$$

$$P_{s1} = M_{s11}^{-1} P_{i11} + M_{s12}^{-1} P_{i12} + M_{s13}^{-1} P_p$$

$$P_{s2} = M_{s11}^{-1} P_{i21} + M_{s12}^{-1} P_{i22} + M_{s13}^{-1} P_p$$

$$P_{s3} = M_{s11}^{-1} P_{i31} + M_{s12}^{-1} P_{i32} + M_{s13}^{-1} P_p$$

By separating the known and unknown variables, this system of equations can be re-written in matrix form, and the pressures at the primary and secondary summers can be calculated using a matrix inversion:

$$0 = M_{p11}^{-1} P_{s1} + M_{p12}^{-1} P_{s2} + M_{p13}^{-1} P_{s3} - P_p$$

$$M_{s11}^{-1} P_{i11} + M_{s12}^{-1} P_{i12} = P_{s1} - M_{s13}^{-1} P_p$$

$$M_{s11}^{-1} P_{i21} + M_{s12}^{-1} P_{i22} = P_{s2} - M_{s13}^{-1} P_p$$

$$M_{s11}^{-1} P_{i31} + M_{s12}^{-1} P_{i32} = P_{s3} - M_{s13}^{-1} P_p$$

$$\begin{bmatrix} 0 \\ M_{s11}^{-1} P_{i11} + M_{s12}^{-1} P_{i12} \\ M_{s11}^{-1} P_{i21} + M_{s12}^{-1} P_{i22} \\ M_{s11}^{-1} P_{i31} + M_{s12}^{-1} P_{i32} \end{bmatrix} = \begin{bmatrix} M_{p11}^{-1} & M_{p12}^{-1} & M_{p13}^{-1} & -1 \\ 1 & 0 & 0 & -M_{s13}^{-1} \\ 0 & 1 & 0 & -M_{s13}^{-1} \\ 0 & 0 & 1 & -M_{s13}^{-1} \end{bmatrix} \begin{bmatrix} P_{s1} \\ P_{s2} \\ P_{s3} \\ P_p \end{bmatrix}$$

$$G = \begin{bmatrix} M_{p11}^{-1} & M_{p12}^{-1} & M_{p13}^{-1} & -1 \\ 1 & 0 & 0 & -M_{s13}^{-1} \\ 0 & 1 & 0 & -M_{s13}^{-1} \\ 0 & 0 & 1 & -M_{s13}^{-1} \end{bmatrix}$$

At this point, matrix G may be inverted, and pressures P_p, $P_{s1\text{-}3}$ may be solved for in terms of the known pressures, and the elements of the inverted M_s, M_p, and G matrices, which are all determined from the geometry of the ducts used in the array.

Changing the number of inlets or the number of secondary summers alters the size of the M_p and M_s matrices. For a network with n inlets per secondary summer, and m secondary summers, the equations are modified:

$$M_p = \begin{bmatrix} a_1 & b1 & 0 & 0 & \cdots & 0 \\ a_1 & 0 & b1 & 0 & & 0 \\ a_1 & 0 & 0 & b1 & & 0 \\ \vdots & & & & \ddots & \vdots \\ a_1 & & & & & b1 \\ 0 & 1 & 1 & 1 & \cdots & 1 \end{bmatrix}$$

$$M_s = \begin{bmatrix} a2 & b2 & 0 & 0 & \cdots & 0 \\ a2 & 0 & b2 & 0 & & 0 \\ a_2 & 0 & 0 & b2 & & 0 \\ \vdots & 0 & 0 & 0 & \ddots & \vdots \\ a_1 & & & & & -b1 \\ 0 & 1 & 1 & 1 & \cdots & -1 \end{bmatrix}$$

$$P_p = M_{p11}^{-1} P_{s1} + M_{p12}^{-1} P_{s2} + \ldots + M_{p1m}^{-1} P_{sm}$$

$$P_{s1} = M_{s11}^{-1} P_{i11} + M_{s12}^{-1} P_{i12} + \ldots + M_{s1n}^{-1} P_p$$

$$P_{s2} = M_{s11}^{-1} P_{i21} + M_{s12}^{-1} P_{i22} + \ldots + M_{s1n}^{-1} P_p$$

$$\vdots$$

$$P_{sm} = M_{s11}^{-1} P_{im1} + M_{s12}^{-1} P_{im2} + \ldots + M_{s1(n-1)}^{-1} P_{im(n-1)} + M_{s1n}^{-1} P_p$$

Visible from these calculations is that the final G matrix remains square, despite the fact that there are a different number of pipes connected to the primary summer than there are connected to the secondary summers. The solution for the pressure at the secondary and primary summers for a solid pipe array can be found using the matrix inverse of G:

$$0 = M_{p11}^{-1}P_{s1} + M_{p12}^{-1}P_{s2} + \ldots + M_{p1m}^{-1}P_{sm} - P_p$$

$$M_{s11}^{-1}P_{i11} + M_{s12}^{-1}P_{i12} + \ldots + M_{s1(n-1)}^{-1}P_{i1(n-1)} = P_{s1} - M_{s1n}^{-1}P_p$$

$$M_{s11}^{-1}P_{i21} + M_{s12}^{-1}P_{i22} + \ldots + M_{s1(n-1)}^{-1}P_{i2(n-1)} = P_{s2} - M_{s1n}^{-1}P_p$$

$$\vdots$$

$$M_{s11}^{-1}P_{im1} + M_{s12}^{-1}P_{im2} + \ldots + M_{s1(n-1)}^{-1}P_{im(n-1)} = P_{sm} - M_{s1n}^{-1}P_p$$

$$\begin{bmatrix} 0 \\ M_{s11}^{-1}P_{i11} + M_{s12}^{-1}P_{i12} + \ldots + M_{s1(n-1)}^{-1}P_{i1(n-1)} \\ M_{s11}^{-1}P_{i21} + M_{s12}^{-1}P_{i22} + \ldots + M_{s1(n-1)}^{-1}P_{i2(n-1)} \\ \vdots \\ M_{s11}^{-1}P_{im1} + M_{s12}^{-1}P_{im2} + \ldots + M_{s1(n-1)}^{-1}P_{im(n-1)} \end{bmatrix} = \begin{bmatrix} M_{p11}^{-1} & M_{p12}^{-1} & \cdots & M_{p1m}^{-1} & -1 \\ 1 & 0 & \cdots & 0 & -M_{s1n}^{-1} \\ 0 & 1 & & 0 & -M_{s1n}^{-1} \\ \vdots & & \ddots & \vdots & -M_{s1n}^{-1} \\ 0 & 0 & \cdots & 1 & -M_{s1n}^{-1} \end{bmatrix} \begin{bmatrix} P_{s1} \\ P_{s2} \\ \vdots \\ P_{sm} \\ P_p \end{bmatrix}$$

$$G = \begin{bmatrix} M_{p11}^{-1} & M_{p12}^{-1} & \cdots & M_{p1m}^{-1} & -1 \\ 1 & 0 & \cdots & 0 & -M_{s1n}^{-1} \\ 0 & 1 & & 0 & -M_{s1n}^{-1} \\ \vdots & & \ddots & \vdots & -M_{s1n}^{-1} \\ 0 & 0 & \cdots & 1 & -M_{s1n}^{-1} \end{bmatrix}$$

$$\begin{bmatrix} P_{s1} \\ P_{s2} \\ \vdots \\ P_{sm} \\ P_p \end{bmatrix} = G^{-1} \begin{bmatrix} 0 \\ M_{s11}^{-1}P_{i11} + M_{s12}^{-1}P_{i12} + \ldots + M_{s1(n-1)}^{-1}P_{i1(n-1)} \\ M_{s11}^{-1}P_{i21} + M_{s12}^{-1}P_{i22} + \ldots + M_{s1(n-1)}^{-1}P_{i2(n-1)} \\ \vdots \\ M_{s11}^{-1}P_{im1} + M_{s12}^{-1}P_{im2} + \ldots + M_{s1(n-1)}^{-1}P_{im(n-1)} \end{bmatrix}$$

$$P_{s1} = G_{1,2}^{-1}\left(M_{s11}^{-1}P_{i11} + M_{s12}^{-1}P_{i12} + \ldots + M_{s1(n-1)}^{-1}P_{i1(n-1)}\right) + G_{1,3}^{-1}\left(M_{s11}^{-1}P_{i21} + M_{s12}^{-1}P_{i22} + \ldots + M_{s1(n-1)}^{-1}P_{i2(n-1)}\right)\ldots$$
$$+ G_{1,m+1}^{-1}\left(M_{s11}^{-1}P_{im1} + M_{s12}^{-1}P_{im2} + \ldots + M_{s1(n-1)}^{-1}P_{im(n-1)}\right)$$

$$\vdots$$

$$P_p = G_{m+1,2}^{-1}\left(M_{s11}^{-1}P_{i11} + M_{s12}^{-1}P_{i12} + \ldots + M_{s1(n-1)}^{-1}P_{i1(n-1)}\right) + G_{m+1,3}^{-1}\left(M_{s11}^{-1}P_{i21} + M_{s12}^{-1}P_{i22} + \ldots + M_{s1(n-1)}^{-1}P_{i2(n-1)}\right)\ldots$$
$$+ G_{m+1,m+1}^{-1}\left(M_{s11}^{-1}P_{im1} + M_{s12}^{-1}P_{im2} + \ldots + M_{s1(n-1)}^{-1}P_{im(n-1)}\right)$$

The above solution is for a solid tube array with *m* secondary summers, and *n* inlets per secondary summer. For this calculation, the summers were assumed to have no compliance. The summers actually have finite, significant compliance. To modify the solution to include the summing compliance, the rows of ones on the bottom of the M_s and M_p matrices are replaced with the appropriate summer compliance, and the zero on the left-hand-side of the equation is replaced with the pressure at that summer. The equations are slightly modified as a result, but the algebra is not difficult.

This solution is useful for predicting the response of the network as seen by a pressure sensor located at the primary or one of the secondary summers. It may be useful, however, to find the pressure at an arbitrary point along any of the pipes in the network. This calculation would allow the propagation of the sound-wave through the network to

become visible. Such a plot is useful both to gain an intuitive understanding of what is occurring in an infrasonic array, but also because it can be used for error checking. It is the experience of the author that if any of the signs are incorrect, the time-domain plots nearly invariably returns garbage. The next section will outline the process for finding the pressure at a point along a solid-tube infrasonic array having an arbitrary number of inlets and secondary summers.

C.3.1.1 Solid-pipe arrays – arbitrary locations

To calculate the pressure at any arbitrary point along any of the tubes, several techniques can be used. The pressures at all nodes have been calculated, and using techniques outlined in Chapter 1, the pressure at an arbitrary point along each tube can be calculated using these pressures. The pressure at an individual point can also be calculated directly, though the solutions look a little different depending on whether the point being solved for is along one of the secondary or primary pipes or one of the inner branches (connecting the secondary summers to the primary summer). To calculate the pressure P_m along an outer branch, transfer matrices for the sections of pipe above and below the point are calculated. These two matrices will be called "T_{sL}" and "T_{sU}", L standing for "Lower", U standing for "Upper", and the subscript *s* referring to the fact that the pipe has the diameter of the secondary (outer) pipes, not the primary (inner) pipes. Figure **C-32** illustrates the setup:

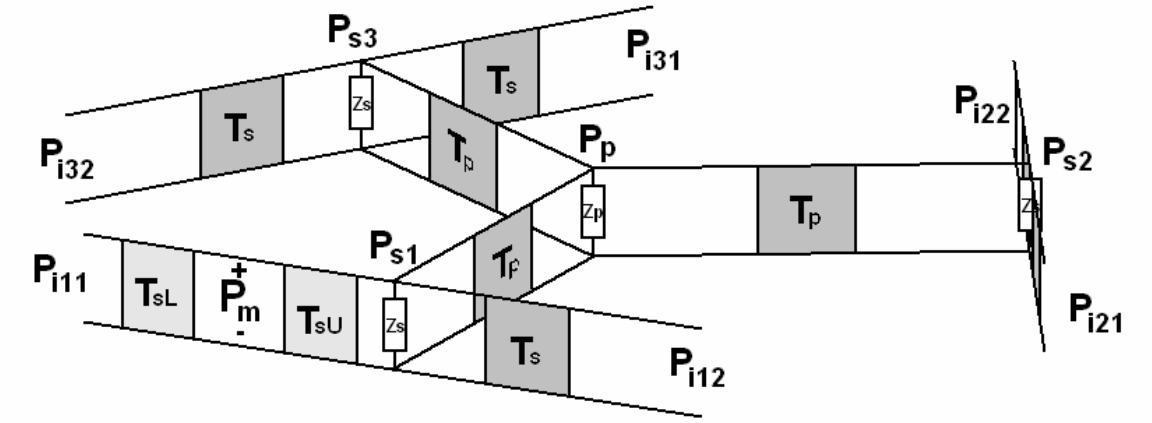

Figure **C-32**: Figure illustrating the transfer-matrix set up used to solve for the pressure at a point along an outer branch.

$$T_{sU} = \begin{bmatrix} a_{2U} & b_{2U} \\ c_{2U} & d_{2U} \end{bmatrix}$$
$$T_{sL} = \begin{bmatrix} a_{2L} & -b_{2L} \\ c_{2L} & -d_{2L} \end{bmatrix}$$

The values for the upper and lower matrices are defined above. The signs on T_{sL} are swapped because the positive direction for current is towards P_m, but the direction of flow is towards the summer. The equations relating P_m to P_{i11} and P_{s1} (in this example) are the following:

$$\begin{bmatrix} P_{i11} \\ U_{i11} \end{bmatrix} = \begin{bmatrix} a_{2L} & b_{2L} \\ c_{2L} & d_{2L} \end{bmatrix} \begin{bmatrix} P_m \\ U_m \end{bmatrix}$$
$$\begin{bmatrix} P_{s1} \\ -U_{s1} \end{bmatrix} = \begin{bmatrix} a_{2U} & -b_{2U} \\ c_{2U} & -d_{2U} \end{bmatrix} \begin{bmatrix} P_m \\ U_m \end{bmatrix}$$

From these equations a relationship can be written about P_{i11} in terms of P_{s1} and P_m:

$$\begin{bmatrix} P_{i11} \\ P_{s1} \end{bmatrix} = \begin{bmatrix} a_{2L} & b_{2L} \\ a_{2U} & -b_{2U} \end{bmatrix} \begin{bmatrix} P_m \\ U_m \end{bmatrix}$$
$$N = \begin{bmatrix} a_{2L} & b_{2L} \\ a_{2U} & -b_{2U} \end{bmatrix}$$
$$P_m = N_{11}^{-1} P_{i11} + N_{12}^{-1} P_{s1}$$
$$P_{i11} = \frac{P_m}{N_{11}^{-1}} - \frac{N_{12}^{-1}}{N_{11}^{-1}} P_{s1}$$

The node equation at P_{s1} can be written in terms of P_m (in this instance we are assuming the summing chambers have compliance):

$$\begin{bmatrix} P_m \\ P_{i12} \\ P_p \\ P_{s1} \end{bmatrix} = \begin{bmatrix} a_{2u} & b_{2u} & 0 & 0 \\ a_2 & 0 & b_2 & 0 \\ a_1 & 0 & 0 & -b_1 \\ 0 & Z_s & Z_s & -Z_s \end{bmatrix} \begin{bmatrix} P_{s1} \\ U_{s1a} \\ U_{s1b} \\ U_{s1c} \end{bmatrix}$$
$$M_{sN} = \begin{bmatrix} a_{2u} & b_{2u} & 0 & 0 \\ a_2 & 0 & b_2 & 0 \\ a_1 & 0 & 0 & -b_1 \\ 0 & Z_s & Z_s & -Z_s \end{bmatrix}$$

The node equations can then be re-written in terms of the inverses of M_s, M_p, and M_{sN}:

$$P_p = M_{p11}^{-1}P_{s1} + M_{p12}^{-1}P_{s2} + M_{p13}^{-1}P_{s3} + M_{p14}^{-1}P_p$$
$$P_{s1} = M_{sN11}^{-1}P_m + M_{sN12}^{-1}P_{i12} + M_{sN13}^{-1}P_p + M_{sN14}^{-1}P_{s1}$$
$$P_{s2} = M_{s11}^{-1}P_{i21} + M_{s12}^{-1}P_{i22} + M_{s13}^{-1}P_p + M_{s14}^{-1}P_{s2}$$
$$P_{s3} = M_{s11}^{-1}P_{i31} + M_{s12}^{-1}P_{i32} + M_{s13}^{-1}P_p + M_{s14}^{-1}P_{s3}$$
$$P_{i11} = \frac{P_m}{N_{11}^{-1}} - \frac{N_{11}^{-1}}{N_{12}^{-1}}P_{s1}$$

Rewriting the unknowns on one side and the constants on the other, a square matrix can be assembled, and all the relevant pressure locations, including P_m can be solved:

$$0 = M_{p11}^{-1}P_{s1} + M_{p12}^{-1}P_{s2} + M_{p13}^{-1}P_{s3} + \left(M_{p14}^{-1} - 1\right)P_p$$
$$M_{sN12}^{-1}P_{i12} = M_{sN11}^{-1}P_m + M_{sN13}^{-1}P_p + \left(M_{sN14}^{-1} - 1\right)P_{s1}$$
$$M_{s11}^{-1}P_{i21} + M_{s12}^{-1}P_{i22} = M_{s13}^{-1}P_p + \left(M_{s14}^{-1} - 1\right)P_{s2}$$
$$M_{s11}^{-1}P_{i31} + M_{s12}^{-1}P_{i32} = M_{s13}^{-1}P_p + \left(M_{s14}^{-1} - 1\right)P_{s3}$$
$$P_{i11} = \frac{P_m}{N_{11}^{-1}} - \frac{N_{11}^{-1}}{N_{12}^{-1}}P_{s1}$$

$$\begin{bmatrix} 0 \\ M_{sN12}^{-1}P_{i12} \\ M_{s11}^{-1}P_{i21} + M_{s12}^{-1}P_{i22} \\ M_{s11}^{-1}P_{i21} + M_{s12}^{-1}P_{i22} \\ P_{i11} \end{bmatrix} = \begin{bmatrix} 0 & M_{p11}^{-1} & M_{p12}^{-1} & M_{p13}^{-1} & \left(M_{p14}^{-1} - 1\right) \\ M_{sN11}^{-1} & \left(M_{sN14}^{-1} - 1\right) & 0 & 0 & M_{sN13}^{-1} \\ 0 & 0 & \left(M_{s14}^{-1} - 1\right) & 0 & M_{s13}^{-1} \\ 0 & 0 & 0 & \left(M_{s14}^{-1} - 1\right) & M_{s13}^{-1} \\ \frac{1}{N_{11}^{-1}} & -\frac{N_{11}^{-1}}{N_{12}^{-1}} & 0 & 0 & 0 \end{bmatrix} \begin{bmatrix} P_m \\ P_{s1} \\ P_{s2} \\ P_{s3} \\ P_p \end{bmatrix}$$

$$G_N = \begin{bmatrix} 0 & M_{p11}^{-1} & M_{p12}^{-1} & M_{p13}^{-1} & \left(M_{p14}^{-1} - 1\right) \\ M_{sN11}^{-1} & \left(M_{sN14}^{-1} - 1\right) & 0 & 0 & M_{sN13}^{-1} \\ 0 & 0 & \left(M_{s14}^{-1} - 1\right) & 0 & M_{s13}^{-1} \\ 0 & 0 & 0 & \left(M_{s14}^{-1} - 1\right) & M_{s13}^{-1} \\ \frac{1}{N_{11}^{-1}} & -\frac{N_{11}^{-1}}{N_{12}^{-1}} & 0 & 0 & 0 \end{bmatrix}$$

$$P_m = G_{N12}^{-1}\left(M_{sN12}^{-1}P_{i12}\right) + G_{N13}^{-1}\left(M_{s11}^{-1}P_{i21} + M_{s12}^{-1}P_{i22}\right) + G_{N13}^{-1}\left(M_{s11}^{-1}P_{i21} + M_{s12}^{-1}P_{i22}\right) + G_{N14}^{-1}\left(P_{i11}\right)$$
$$P_{s1} = G_{N22}^{-1}\left(M_{sN12}^{-1}P_{i12}\right) + G_{N23}^{-1}\left(M_{s11}^{-1}P_{i21} + M_{s12}^{-1}P_{i22}\right)\ldots$$
$$\vdots$$

This is the solution for the pressure at all the nodes, including P_m, and including finite summing impedances. The solution can be generalized to work for a network with an arbitrary number of secondary summers and inlets per summer, as well.

The method for solving the pressure for a point located between a primary and secondary summer is different. To begin, the node equations for the primary and the secondary summers located on both sides of the point are re-written as follows (for the purpose of example we will assume that the point is located between summer S_1 and the primary summer):

$$\begin{bmatrix} P_{i11} \\ P_{i12} \\ P_m \\ P_{s1} \end{bmatrix} = \begin{bmatrix} a_2 & b_2 & 0 & 0 \\ a_2 & 0 & b_2 & 0 \\ a_{1L} & 0 & 0 & -b_{1L} \\ 0 & Z_s & Z_s & -Z_s \end{bmatrix} \begin{bmatrix} P_{s1} \\ U_{s1a} \\ U_{s1b} \\ U_{s1c} \end{bmatrix}$$

$$\begin{bmatrix} P_m \\ P_{s2} \\ P_{s3} \\ P_p \end{bmatrix} = \begin{bmatrix} a_{1H} & b_{1H} & 0 & 0 \\ a_1 & 0 & b_1 & 0 \\ a_1 & 0 & 0 & b_1 \\ 0 & Z_s & Z_s & Z_s \end{bmatrix} \begin{bmatrix} P_p \\ U_{pa} \\ U_{ab} \\ U_{ac} \end{bmatrix}$$

$$M_{sN} = \begin{bmatrix} a_2 & b_2 & 0 & 0 \\ a_2 & 0 & b_2 & 0 \\ a_{1L} & 0 & 0 & -b_{1L} \\ 0 & Z_s & Z_s & -Z_s \end{bmatrix}$$

$$M_{pN} = \begin{bmatrix} a_{1H} & b_{1H} & 0 & 0 \\ a_1 & 0 & b_1 & 0 \\ a_1 & 0 & 0 & b_1 \\ 0 & Z_s & Z_s & Z_s \end{bmatrix}$$

P_m can be related to P_{s1} and P_p by the following equation:

$$\begin{bmatrix} P_{s1} \\ P_m \end{bmatrix} = \begin{bmatrix} a_{1L} & b_{1L} \\ a_{1U} & -b_{1U} \end{bmatrix} \begin{bmatrix} P_m \\ U_m \end{bmatrix}$$

$$N = \begin{bmatrix} a_{1L} & b_{1L} \\ a_{1U} & -b_{1U} \end{bmatrix}$$

$$P_m = N_{11}^{-1} P_{s1} + N_{12}^{-1} P_p$$

$$0 = -\frac{P_m}{N_{11}^{-1}} + P_{s1} + \frac{N_{12}^{-1}}{N_{11}^{-1}} P_p$$

Writing out the node equations and separating the knowns from the unknowns, a square matrix can be made and the pressures solved for:

$$P_p = M_{p11}^{-1}P_m + M_{p12}^{-1}P_{s2} + M_{p13}^{-1}P_{s3} + M_{p14}^{-1}P_p$$
$$P_{s1} = M_{sN11}^{-1}P_{i11} + M_{sN12}^{-1}P_{i12} + M_{sN13}^{-1}P_m + M_{sN14}^{-1}P_{s1}$$
$$P_{s2} = M_{s11}^{-1}P_{i21} + M_{s12}^{-1}P_{i22} + M_{s13}^{-1}P_p + M_{s14}^{-1}P_{s2}$$
$$P_{s3} = M_{s11}^{-1}P_{i31} + M_{s12}^{-1}P_{i32} + M_{s13}^{-1}P_p + M_{s14}^{-1}P_{s3}$$
$$P_m = N_{11}^{-1}P_{s1} + N_{12}^{-1}P_p$$
$$\downarrow$$
$$0 = M_{p11}^{-1}P_m + M_{p12}^{-1}P_{s2} + M_{p13}^{-1}P_{s3} + \left(M_{p14}^{-1} - 1\right)P_p$$
$$M_{sN11}^{-1}P_{i11} + M_{sN12}^{-1}P_{i12} = M_{sN13}^{-1}P_m + \left(M_{sN14}^{-1} - 1\right)P_{s1}$$
$$M_{s11}^{-1}P_{i21} + M_{s12}^{-1}P_{i22} = M_{s13}^{-1}P_p + \left(M_{s14}^{-1} - 1\right)P_{s2}$$
$$M_{s11}^{-1}P_{i31} + M_{s12}^{-1}P_{i32} = M_{s13}^{-1}P_p + \left(M_{s14}^{-1} - 1\right)P_{s3}$$
$$0 = -P_m + N_{11}^{-1}P_{s1} + N_{12}^{-1}P_p$$
$$\downarrow$$
$$\begin{bmatrix} 0 \\ M_{sN11}^{-1}P_{i11} + M_{sN12}^{-1}P_{i12} \\ M_{s11}^{-1}P_{i21} + M_{s12}^{-1}P_{i22} \\ M_{s11}^{-1}P_{i31} + M_{s12}^{-1}P_{i32} \\ 0 \end{bmatrix} = \begin{bmatrix} M_{p11}^{-1} & 0 & M_{p12}^{-1} & M_{p13}^{-1} & \left(M_{p14}^{-1} - 1\right) \\ M_{sN13}^{-1} & \left(M_{sN14}^{-1} - 1\right) & 0 & 0 & 0 \\ 0 & 0 & \left(M_{s14}^{-1} - 1\right) & 0 & M_{s13}^{-1}P_p \\ 0 & 0 & 0 & \left(M_{s14}^{-1} - 1\right) & M_{s13}^{-1} \\ -1 & N_{11}^{-1} & 0 & 0 & N_{12}^{-1} \end{bmatrix} \begin{bmatrix} P_m \\ P_{s1} \\ P_{s2} \\ P_{s3} \\ P_p \end{bmatrix}$$
$$\downarrow$$
$$G_N = \begin{bmatrix} M_{p11}^{-1} & 0 & M_{p12}^{-1} & M_{p13}^{-1} & \left(M_{p14}^{-1} - 1\right) \\ M_{sN13}^{-1} & \left(M_{sN14}^{-1} - 1\right) & 0 & 0 & 0 \\ 0 & 0 & \left(M_{s14}^{-1} - 1\right) & 0 & M_{s13}^{-1}P_p \\ 0 & 0 & 0 & \left(M_{s14}^{-1} - 1\right) & M_{s13}^{-1} \\ -1 & N_{11}^{-1} & 0 & 0 & N_{12}^{-1} \end{bmatrix}$$
$$\downarrow$$
$$P_m = G_{N12}^{-1}\left(M_{sN11}^{-1}P_{i11} + M_{sN12}^{-1}P_{i12}\right) + G_{N13}^{-1}\left(M_{s11}^{-1}P_{i21} + M_{s12}^{-1}P_{i22}\right) + G_{N14}^{-1}\left(M_{s11}^{-1}P_{i31} + M_{s12}^{-1}P_{i32}\right)$$
$$P_{s1} = G_{N22}^{-1}\left(M_{sN11}^{-1}P_{i11} + M_{sN12}^{-1}P_{i12}\right) + \ldots$$
$$\vdots$$

The pressures have been solved for. This set can also be readily generalized to work with arrays having an arbitrary number of secondary summers and inlets per summer.

At this point the solutions for the pressure at any point in an array having secondary summers have been solved. Signs are important to keep straight, when writing down the node equations; however, sign errors are fixable in coding because the errors

affect propagation through the pipes in obvious ways (the solution will look horribly wrong if the signs in the matrix calculations are entered incorrectly).

C.3.2 Porous hose arrays

C.3.2.1 Porous hose arrays with no secondary summers

Various arrays make use of porous hoses instead of solid tubes. Some arrays use solid tubes between the primary and secondary summers, and porous hoses between the secondary summers and inlets. This section will outline the process for finding the pressures inside porous hose arrays that have no secondary summers.

Recall from the calculation of the pressure inside a porous hose that the relationship between the pressures inside the hose to the ends, P_1 and P_2, can be related as follows:

$$d = M_{11}^{-1}$$
$$e = M_{12}^{-1}$$
$$f = M_{13}^{-1}$$
$$\begin{bmatrix} dP_1 + eP_{e1} \\ eP_{e2} \\ eP_{e3} \\ eP_{e4} \\ \vdots \\ eP_{en} + fP_2 \end{bmatrix} = \begin{bmatrix} 1 & f & 0 & 0 & \cdots & 0 \\ d & 1 & f & 0 & & 0 \\ 0 & d & 1 & f & & 0 \\ 0 & 0 & d & 1 & & 0 \\ \vdots & & & & \ddots & 0 \\ 0 & 0 & 0 & 0 & d & 1 \end{bmatrix} \begin{bmatrix} P_{m1} \\ P_{m2} \\ P_{m3} \\ P_{m4} \\ \vdots \\ P_{mn} \end{bmatrix}$$

In the array example P_2 represents the pressure inside the primary summer, and is an unknown. Furthermore, several other branches extending out of the summer exist. To solve this problem, the matrix equation above is solved like normal, only P_2 is left as a variable in the solution. The problem will assume 3 branches, a b, and c, (denoted by a subscript after the P_m), with n pores each.

$$M_{pr} = \begin{bmatrix} 1 & f & 0 & 0 & \cdots & 0 \\ d & 1 & f & 0 & & 0 \\ 0 & d & 1 & f & & 0 \\ 0 & 0 & d & 1 & & 0 \\ \vdots & & & & \ddots & 0 \\ 0 & 0 & 0 & 0 & d & 1 \end{bmatrix}$$

$$P_{mAn} = M_{prn1}^{-1}\left(dP_{a1} + eP_{ae1}\right) + M_{prn2}^{-1}\left(eP_{ae2}\right) + \ldots + M_{prnn}^{-1}\left(eP_{aen} + fP_2\right)$$

$$P_{mBn} = M_{prn1}^{-1}\left(dP_{b1} + eP_{be1}\right) + M_{prn2}^{-1}\left(eP_{be2}\right) + \ldots + M_{prnn}^{-1}\left(eP_{ben} + fP_2\right)$$

$$P_{mCn} = M_{prn1}^{-1}\left(dP_{c1} + eP_{ce1}\right) + M_{prn2}^{-1}\left(eP_{ce2}\right) + \ldots + M_{prnn}^{-1}\left(eP_{cen} + fP_2\right)$$

$$\downarrow$$

$$P_{mAn} = A_{cnst} + M_{prnn}^{-1} fP_2$$

$$P_{mBn} = B_{cnst} + M_{prnn}^{-1} fP_2$$

$$P_{mCn} = C_{cnst} + M_{prnn}^{-1} fP_2$$

A_{cnst}, B_{cnst}, and C_{cnst} are the summed portions of the solutions that can be found by plugging in pore and inlet pressures. At this point, the pressures at the points nearest to the summer have been solved for in terms of the pressure at the summer and constants determined by the summation of the inverted matrix values and the pressure inputs. There is one more unknown than there are equations. The last equation is provided by the node equation for the summer:

$$\begin{bmatrix} P_{mAn} \\ P_{mBn} \\ P_{mCn} \\ P_2 \end{bmatrix} = \begin{bmatrix} a_1 & b_1 & 0 & 0 \\ a_1 & 0 & b_1 & 0 \\ a_1 & 0 & 0 & b_1 \\ 0 & Z_s & Z_s & Z_s \end{bmatrix} \begin{bmatrix} P_2 \\ U_{2a} \\ U_{2b} \\ U_{2c} \end{bmatrix}$$

$$M_p = \begin{bmatrix} a_1 & b_1 & 0 & 0 \\ a_1 & 0 & b_1 & 0 \\ a_1 & 0 & 0 & b_1 \\ 0 & Z_s & Z_s & Z_s \end{bmatrix}$$

$$P_2 = M_{p11}^{-1} P_{mAn} + M_{p12}^{-1} P_{mBn} + M_{p13}^{-1} P_{mCn} + M_{p14}^{-1} P_2$$

$$0 = M_{p11}^{-1} P_{mAn} + M_{p12}^{-1} P_{mBn} + M_{p13}^{-1} P_{mCn} + \left(M_{p14}^{-1} - 1\right) P_2$$

This can be combined with the other three to form a matrix-solvable set of equations:

$$P_{mAn} = A_{cnst} + M_{prnn}^{-1} f P_2$$
$$P_{mBn} = B_{cnst} + M_{prnn}^{-1} f P_2$$
$$P_{mCn} = C_{cnst} + M_{prnn}^{-1} f P_2$$
$$0 = M_{11}^{-1} P_{mAn} + M_{12}^{-1} P_{mBn} + M_{13}^{-1} P_{mCn} + \left(M_{14}^{-1} - 1\right) P_2$$
$$\downarrow$$
$$A_{cnst} = P_{mAn} - M_{prnn}^{-1} f P_2$$
$$B_{cnst} = P_{mBn} - M_{prnn}^{-1} f P_2$$
$$C_{cnst} = P_{mCn} - M_{prnn}^{-1} f P_2$$
$$0 = M_{p11}^{-1} P_{mAn} + M_{p12}^{-1} P_{mBn} + M_{p13}^{-1} P_{mCn} + \left(M_{p14}^{-1} - 1\right) P_2$$
$$\downarrow$$
$$\begin{bmatrix} A_{cnst} \\ B_{cnst} \\ C_{cnst} \\ 0 \end{bmatrix} = \begin{bmatrix} 1 & 0 & 0 & -M_{prnn}^{-1} f \\ 0 & 1 & 0 & -M_{prnn}^{-1} f \\ 0 & 0 & 1 & -M_{prnn}^{-1} f \\ M_{p11}^{-1} & M_{p12}^{-1} & M_{p13}^{-1} & \left(M_{p14}^{-1} - 1\right) \end{bmatrix} \begin{bmatrix} P_{mAn} \\ P_{mBn} \\ P_{mCn} \\ P_2 \end{bmatrix}$$

The constants are known and the summer pressure, as well as the adjacent pressures may be calculated:

$$G = \begin{bmatrix} 1 & 0 & 0 & -M_{prnn}^{-1} f \\ 0 & 1 & 0 & -M_{prnn}^{-1} f \\ 0 & 0 & 1 & -M_{prnn}^{-1} f \\ M_{p11}^{-1} & M_{p12}^{-1} & M_{p13}^{-1} & \left(M_{p14}^{-1} - 1\right) \end{bmatrix}$$
$$P_2 = G_{41}^{-1} A_{cnst} + G_{42}^{-1} B_{cnst} + G_{43}^{-1} C_{cnst}$$

The other pressures were characterized in terms of P_2 and A_{cnst}, B_{cnst}, and C_{cnst}, and may be solved for by plugging in values at this point. The only modification that needs to be done to make the solution work for more branches is that the M_p matrix needs to sized to match the number of hoses extending from the primary summer.

C.3.2.2 Porous hose arrays with secondary summers

Adding secondary summers into the model increases the complexity of the solution slightly. In this example the array will have three secondary summers, denoted $S_{1\text{-}3}$. The tubes extending from the summer will be denoted *a*, *b*, and *c*. Each secondary

summer will have two inlets, denoted S_{na} and S_{nb}, where n is the number of the secondary summer the inlet leads to.

To begin the solution, the equations for the outer branches and inner branches are written (these are branches S_{1a} and P_a):

$$\begin{bmatrix} dP_{s1a} + eP_{s1ae1} \\ eP_{s1ae2} \\ eP_{s1ae3} \\ eP_{s1ae4} \\ \vdots \\ eP_{s1aen} + fP_{s1} \end{bmatrix} = \begin{bmatrix} 1 & f & 0 & 0 & \cdots & 0 \\ d & 1 & f & 0 & & 0 \\ 0 & d & 1 & f & & 0 \\ 0 & 0 & d & 1 & & 0 \\ \vdots & & & & \ddots & 0 \\ 0 & 0 & 0 & 0 & d & 1 \end{bmatrix} \begin{bmatrix} P_{s1am1} \\ P_{s1am2} \\ P_{s1am3} \\ P_{s1am4} \\ \vdots \\ P_{s1amn} \end{bmatrix}$$

$$\begin{bmatrix} dP_{s1} + eP_{pae1} \\ eP_{pae2} \\ eP_{pae3} \\ eP_{pae4} \\ \vdots \\ eP_{paen} + fP_{p} \end{bmatrix} = \begin{bmatrix} 1 & f & 0 & 0 & \cdots & 0 \\ d & 1 & f & 0 & & 0 \\ 0 & d & 1 & f & & 0 \\ 0 & 0 & d & 1 & & 0 \\ \vdots & & & & \ddots & 0 \\ 0 & 0 & 0 & 0 & d & 1 \end{bmatrix} \begin{bmatrix} P_{pam1} \\ P_{pam2} \\ P_{pam3} \\ P_{pam4} \\ \vdots \\ P_{pamn} \end{bmatrix}$$

$$M_{prs} = \begin{bmatrix} 1 & f & 0 & 0 & \cdots & 0 \\ d & 1 & f & 0 & & 0 \\ 0 & d & 1 & f & & 0 \\ 0 & 0 & d & 1 & & 0 \\ \vdots & & & & \ddots & 0 \\ 0 & 0 & 0 & 0 & d & 1 \end{bmatrix}$$

$$M_{prp} = \begin{bmatrix} 1 & f & 0 & 0 & \cdots & 0 \\ d & 1 & f & 0 & & 0 \\ 0 & d & 1 & f & & 0 \\ 0 & 0 & d & 1 & & 0 \\ \vdots & & & & \ddots & 0 \\ 0 & 0 & 0 & 0 & d & 1 \end{bmatrix}$$

The solutions for the pressures at the points adjacent to each node are solved for. The number of pores n, as well as values d, e, and f are assumed to be equal to simplify the algebra, but this does not have to be assumed. Solving for the adjacent pressures:

$$P_{s1amn} = A_{s1} + M^{-1}_{prsnn} fP_{s1}$$
$$P_{s1bmn} = B_{s1} + M^{-1}_{prsnn} fP_{s1}$$
$$P_{pam1} = A_{pa} + M^{-1}_{prp11} dP_{s1} + M^{-1}_{prp1n} fP_p$$

$$P_{s2amn} = A_{s2} + M^{-1}_{prsnn} fP_{s2}$$
$$P_{s2bmn} = B_{s2} + M^{-1}_{prsnn} fP_{s2}$$
$$P_{pbm1} = B_{pb} + M^{-1}_{prp11} dP_{s2} + M^{-1}_{prp1n} fP_p$$

$$P_{s3amn} = A_{s3} + M^{-1}_{prsnn} fP_{s3}$$
$$P_{s3bmn} = B_{s3} + M^{-1}_{prsnn} fP_{s3}$$
$$P_{pcm1} = C_{pb} + M^{-1}_{prp11} dP_{s3} + M^{-1}_{prp1n} fP_p$$

$$P_{pamn} = A_{pa} + M^{-1}_{prpn1} dP_{s1} + M^{-1}_{prpnn} fP_p$$
$$P_{pbmn} = B_{pb} + M^{-1}_{prpn1} dP_{s1} + M^{-1}_{prpnn} fP_p$$
$$P_{pcmn} = C_{pc} + M^{-1}_{prpn1} dP_{s1} + M^{-1}_{prpnn} fP_p$$

There are not enough equations to solve for pressures yet. The final equations are provided by the node equations at the summers:

$$0 = M^{-1}_{p11} P_{pamn} + M^{-1}_{p12} P_{pbmn} + M^{-1}_{p13} P_{pcmn} + \left(M^{-1}_{p14} - 1\right) P_p$$
$$0 = M^{-1}_{sp11} P_{s1amn} + M^{-1}_{sp12} P_{s1bmn} + M^{-1}_{sp13} P_{s1cmn} + \left(M^{-1}_{sp14} - 1\right) P_{s1}$$
$$0 = M^{-1}_{sp11} P_{s2amn} + M^{-1}_{sp12} P_{s2bmn} + M^{-1}_{sp13} P_{s2cmn} + \left(M^{-1}_{sp14} - 1\right) P_{s2}$$
$$0 = M^{-1}_{sp11} P_{s3amn} + M^{-1}_{sp12} P_{s3bmn} + M^{-1}_{sp13} P_{s3cmn} + \left(M^{-1}_{sp14} - 1\right) P_{s3}$$

These equations can be assembled into a square matrix that may be solved by finding the matrix inverse:

$$
\begin{bmatrix} A_{s1} \\ B_{s1} \\ A_{pa} \\ 0 \\ A_{s2} \\ B_{s2} \\ B_{pb} \\ 0 \\ A_{s3} \\ B_{s3} \\ C_{pb} \\ 0 \\ A_{pa} \\ B_{pb} \\ C_{pc} \\ 0 \end{bmatrix} =
\begin{bmatrix}
1 & & & -M_{prsnnf}^{-1} & & & & & & & & & & & & \\
 & 1 & & -M_{prsnnf}^{-1} & & & & & & & & & & & & \\
 & & 1 & -M_{prp11^d}^{-1} & & & & & & & & & & & & \\
M_{sp11}^{-1} & M_{sp12}^{-1} & M_{sp13}^{-1} & \left(M_{sp14}^{-1}\right) & & & & & & & & & & & & \\
 & & & & 1 & & & & & & & & & & & \\
 & & & & & 1 & & -M_{prsnnf}^{-1} & & & & & & & & \\
 & & & & & & 1 & -M_{prsnnf}^{-1} & & & & & & & & \\
 & & & & & & & -M_{prp11^d}^{-1} & & & & & & & & \\
 & & & & M_{sp11}^{-1} & M_{sp12}^{-1} & M_{sp13}^{-1} & \left(M_{sp14}^{-1}\right) & & & & & & & & \\
 & & & & & & & & 1 & & & & & & & \\
 & & & & & & & & & 1 & & -M_{prsnnf}^{-1} & & & & \\
 & & & & & & & & & & 1 & -M_{prsnnf}^{-1} & & & & \\
 & & & & & & & & & & & -M_{prp11^d}^{-1} & & & & \\
 & & & & M_{sp11}^{-1} & M_{sp12}^{-1} & M_{sp13}^{-1} & \left(M_{sp14}^{-1}\right) & & & & & & & & \\
 & & & -M_{prpn1}^{-1} & & & & & & & & & & & & \\
 & & & -M_{prpn1}^{-1} & & & & & & & & & & & & \\
 & & & & & & & -M_{prpn1}^{-1} & & & & & & & & \\
 & & & & M_{sp11}^{-1} & M_{sp12}^{-1} & M_{sp13}^{-1} & \left(M_{sp14}^{-1}\right) & & & & & & & & \\
 & & & & & & & & 1 & & & & & & & \\
 & & & & & & & & & 1 & & & & & & \\
 & & & & & & & & & & 1 & & & & & \\
 & & & & & & & & & & & -M_{prpnnf}^{-1} & & & & \\
 & & & & & & & & & & & -M_{prpnnf}^{-1} & & & & \\
 & & & & & & & & & & & -M_{prpnnf}^{-1} & & & & \\
 & & & & & & & & & & & \left(M_{p14}^{-1}\right) & & & &
\end{bmatrix}
\begin{bmatrix} P_{s1amn} \\ P_{s1bmn} \\ P_{pam1} \\ P_{s1} \\ P_{s2amn} \\ P_{s2bmn} \\ P_{pbm1} \\ P_{s2} \\ P_{s3amn} \\ P_{s3bmn} \\ P_{pcm1} \\ P_{s3} \\ P_{pamn} \\ P_{pbmn} \\ P_{pcmn} \\ P_{p} \end{bmatrix}
$$

At this point, the pressures at the summers and the adjacent points may be solved by multiplying both sides by the inverse of the matrix. After this has been completed, the rest of the points may be solved by substituting the solved values into the branch equations. This matrix may look large, however it is fairly easy to generalize to an arbitrary number of secondary summers and inlets. The size of each L-shaped section in the above matrix depends on the number of inlets, and the number of L-shaped sections depends on the number of summers.

As a last point about this solution process, it is important to note that though the matrix above appears large, it is still much smaller than the branch matrices when a large number of pores are being evaluated. The size of the matrix above will, for any number of secondary summers and inlets per summer, always be: *[nm + 3m + 1] * [nm + 3m + 1]*, where *n* is the number of inlets, and *m* is the number of secondary summers. If this matrix is too large and slowing computation time down, it is possible to break it into smaller matrices, and solve through more operations. However, for the author's modestly powered 1.6 GHz laptop, the inversion for a 181 x 181 matrix (12 summers and 12 inlets per summer – impractically large for a real infrasonic array) takes only 0.026 seconds to evaluate.

C.3.3 Final notes about evaluating array responses

Once the array model has been constructed, the final step is to subject it to an external signal for response evaluation. For a solid tube array the pressure at each inlet is an input, however for a porous hose the pressure at each pore is also an inlet. To cut down on memory and hard-drive space, it is often easier to pass the array one single excitation signal and then apply a linear phase delay to the excitation signal in the frequency domain, according to the location of the pore being evaluated relative to some reference plane (or point, if the source is spherically spreading).

Getting the volume-velocity signs correct in the Tee-section networks is critical to getting the code work properly. The sign convention presented in this appendix is that the "positive" direction is *towards* the point being evaluated, but the flow is always towards the primary summer. Neither of these two assumptions have to be made, however the signs and flow directions must remain consistent throughout the construction of the model.

For porous hoses, it ought to be remembered that the model will be significantly idealized, when compared to an actual porous hose. The porosity of a real porous hose is not uniform down the length of the hose, and neither is the porosity of one hose going to perfectly match that of another. Furthermore, there is no guarantee that the porosity of a hose will remain consistent with age, and in varying environmental conditions.

Radiation impedance from inlets has been neglected in this model. It is a fairly simple matter to include it though, as the only modification needed to include it is to include an extra transfer matrix representing the radiation impedance between the inlet and the first Tee-section representing a pipe segment's impedance.

C.4 Array simulation results

The porosity of tubes, as measured by the methods listed in section **C.2.3**, is implemented into an actual model for a porous hose array and response characteristics are made for many variables, some of which include incident wave azimuth and elevation, primary summer volume, and hose length. The effects of different end terminations are also plotted. The phase response color bar units are degrees, and the magnitude color bar is amplitude with respect to the low-frequency limit.

C.4.1 Array specifications:

Number of hoses: 3
Hose length: 10
Hose resistance (1m): 1.5e6 kg/(s m^4)
Hose diameter: 0.02 m
Primary summer volume: 2 liters

C.4.2 Swept parameters

Hose resistance
Azimuth and elevation of incoming wave
Primary summer volume
Length of porous hose

C.4.3 Porosity sweep

Incident angle (deg):	0 degrees
Incident elevation (deg):	90 degrees

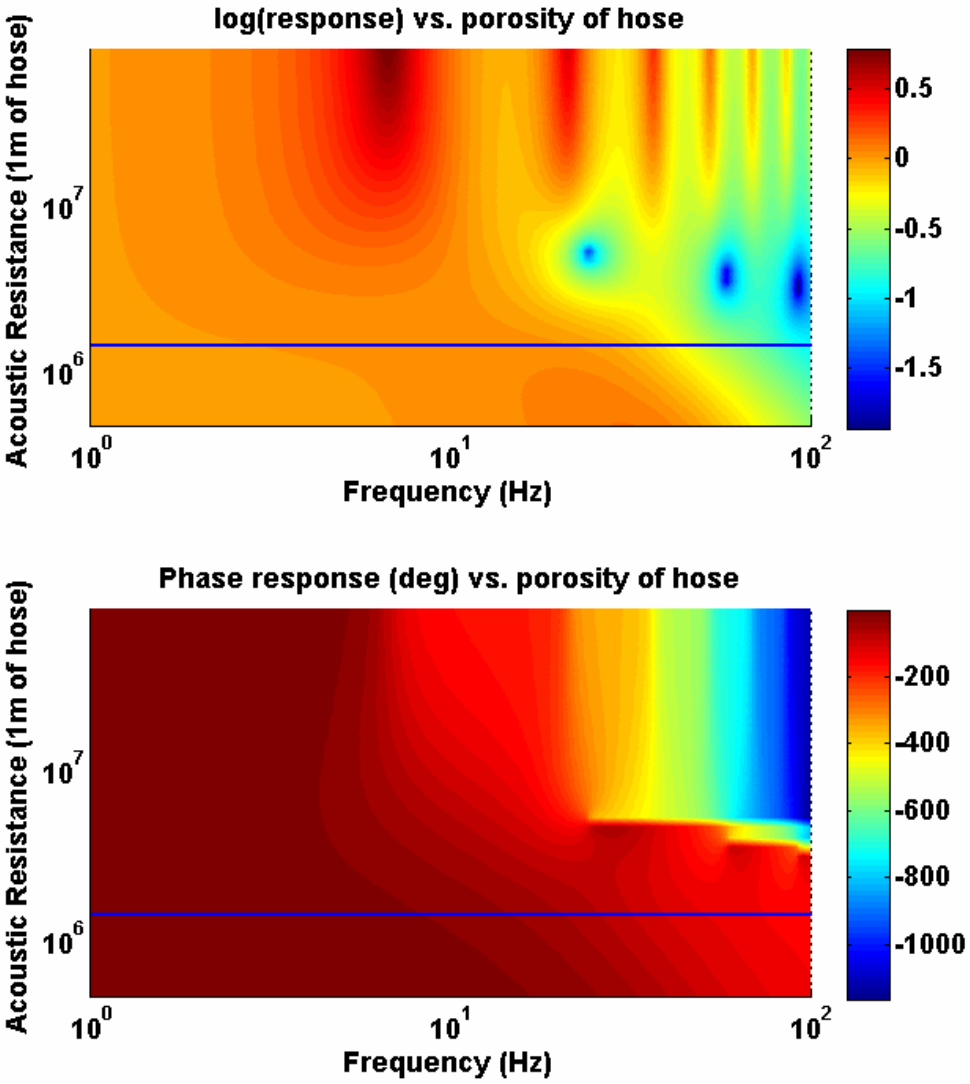

Figure **C-33**: Porosity sweep. The blue line indicates the experimentally measured value. The color bar on the magnitude graph is the magnitude normalized by the low-frequency value. The units of the phase color bar are degrees.

C.4.4 Incident angle sweep, (0 to 120 degrees, porous hose)

Incident angle (deg): 0 : 120
Incident elevation (deg): 0
Porosity: 1.5e6 kg/(s m^4) [measured]

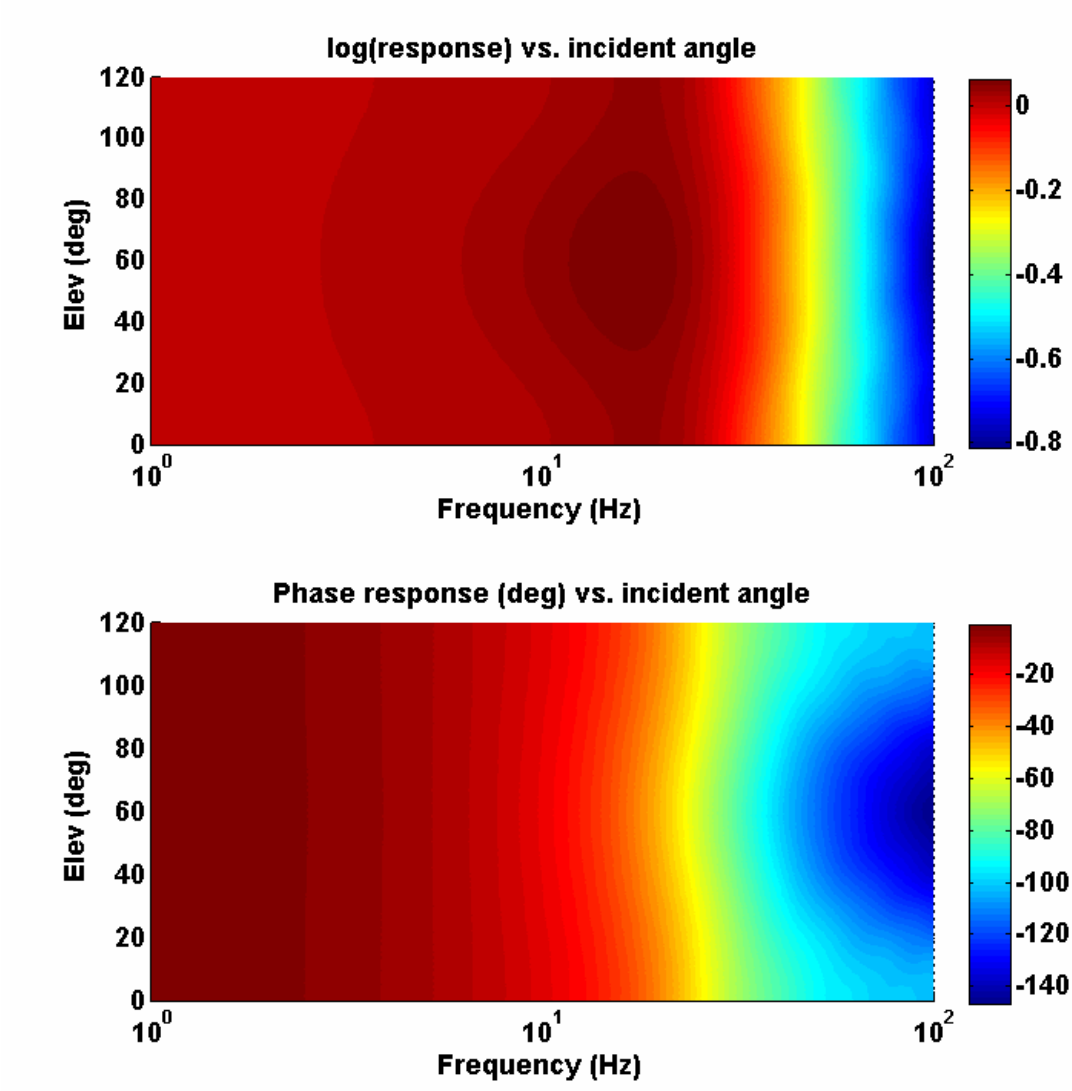

Figure **C-34**: Magnitude response as a function of incident angle.

C.4.5 Incident angle sweep, (0 to 120 degrees), *non*-porous array

Incident angle (deg): 0 to 120
Incident elevation (deg): 0
Porosity: Non-porous

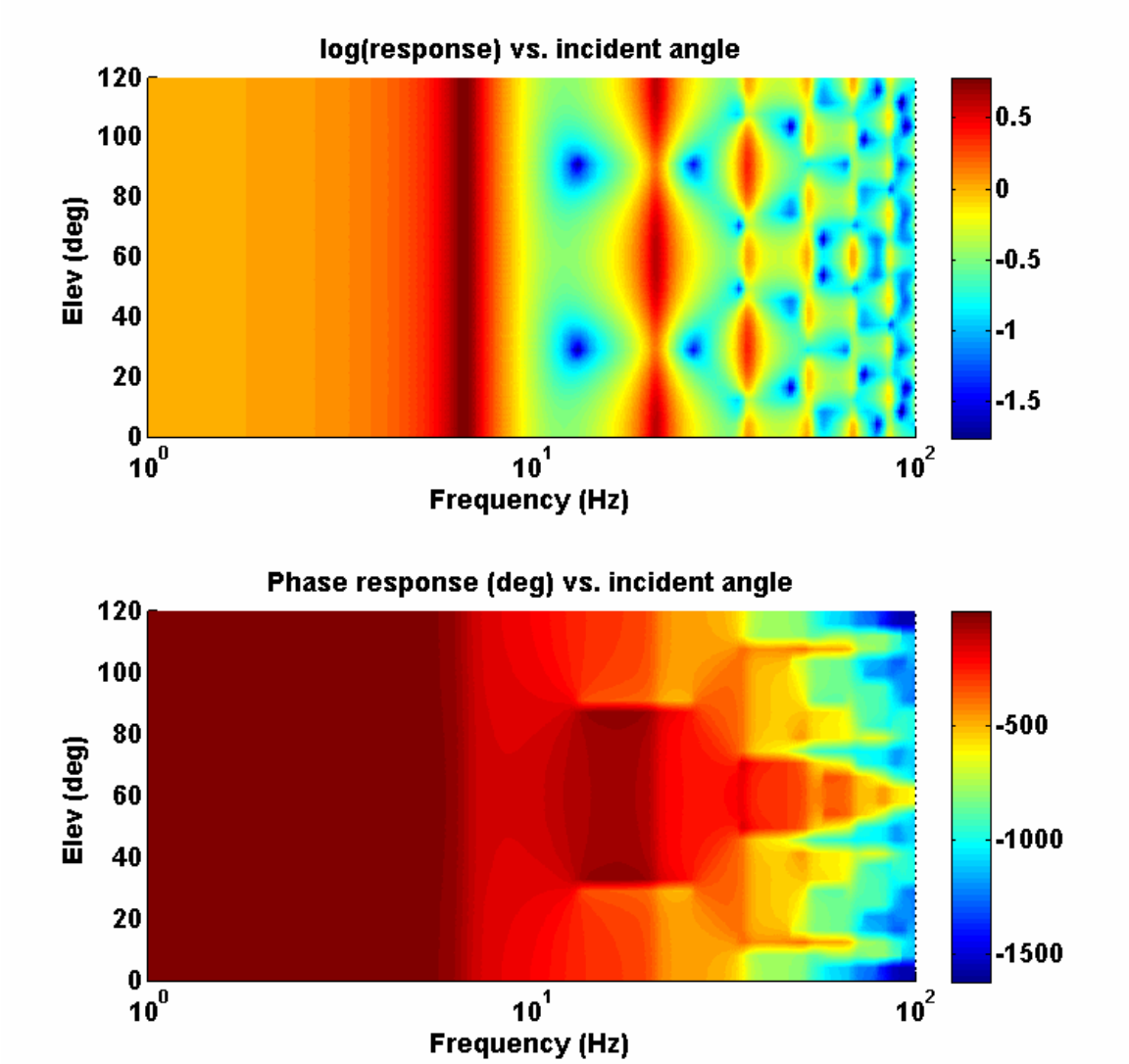

Figure **C-35**: Incident angle sweep for a non-porous array. Past the first resonance, the response is highly dependent on the angle of incidence.

C.4.6 Incident elevation sweep (0 to 180 degrees, *non*-porous)

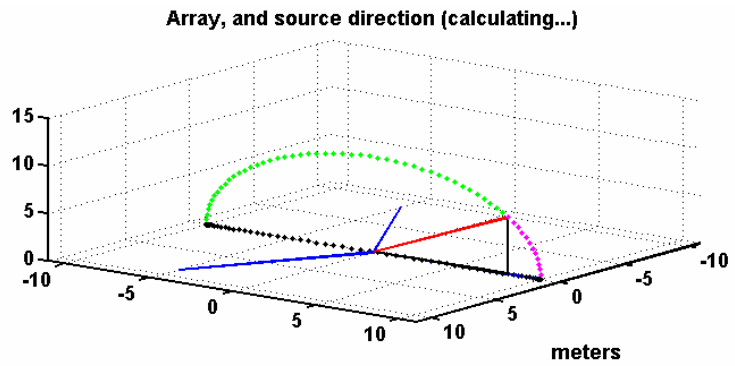

Figure **C-36**: Illustration of the angles over which the array is evaluated in this simulation. The blue lines are the array tubes. The green dots are the angles not yet evaluated by the code (this figure is a screen shot of the evaluation code used by the author while calculations are proceeding), and the purple dots are the evaluated angles. The red line is orthogonal to the propagation of the incident wave.

Incident angle (deg):	0
Incident elevation (deg):	0 : 180
Porosity:	Non-porous

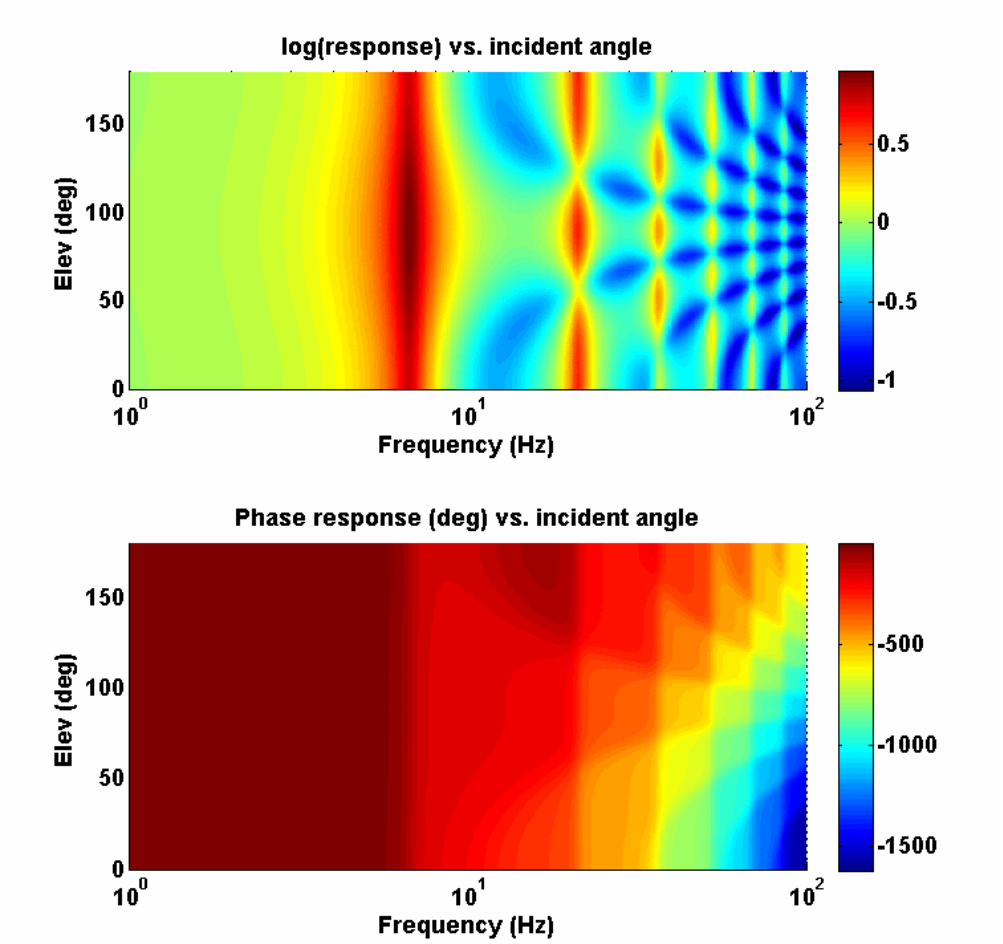

Figure **C-37**: Response elevation dependence, in the non-porous case, for frequencies above the first resonance.

C.4.7 Incident angle sweep, (0 to 180 degrees, porous)

Incident angle (deg):	0
Incident elevation (deg):	0 : 180
Porosity:	1.5e6 kg/(s m^4)

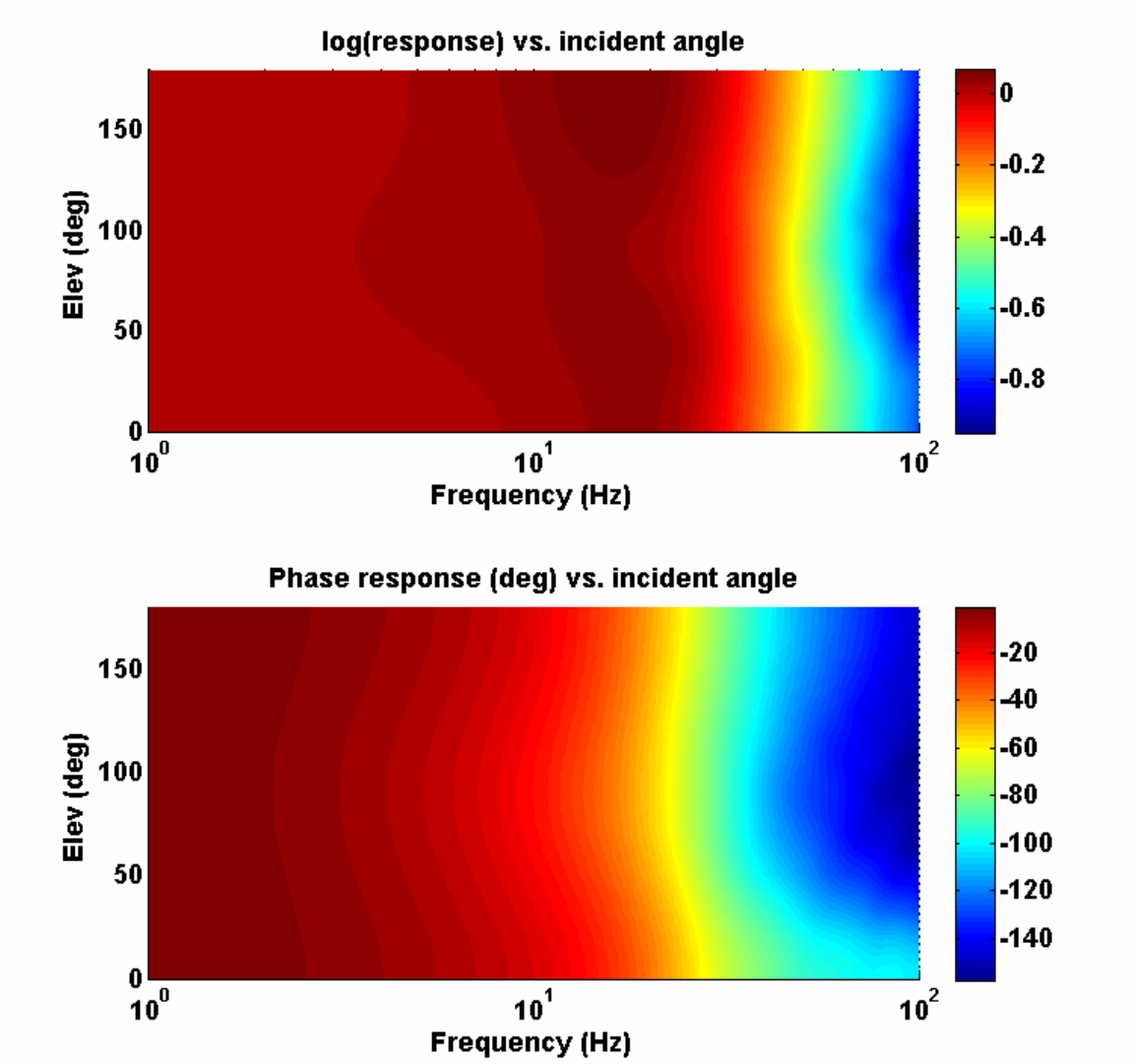

Figure **C-38**: Porous hose elevation response.

C.4.8 Summer volume sweep

Incident angle (deg): 0
Incident elevation (deg): 90
Porosity: 1.5e6 kg/(s m^4)

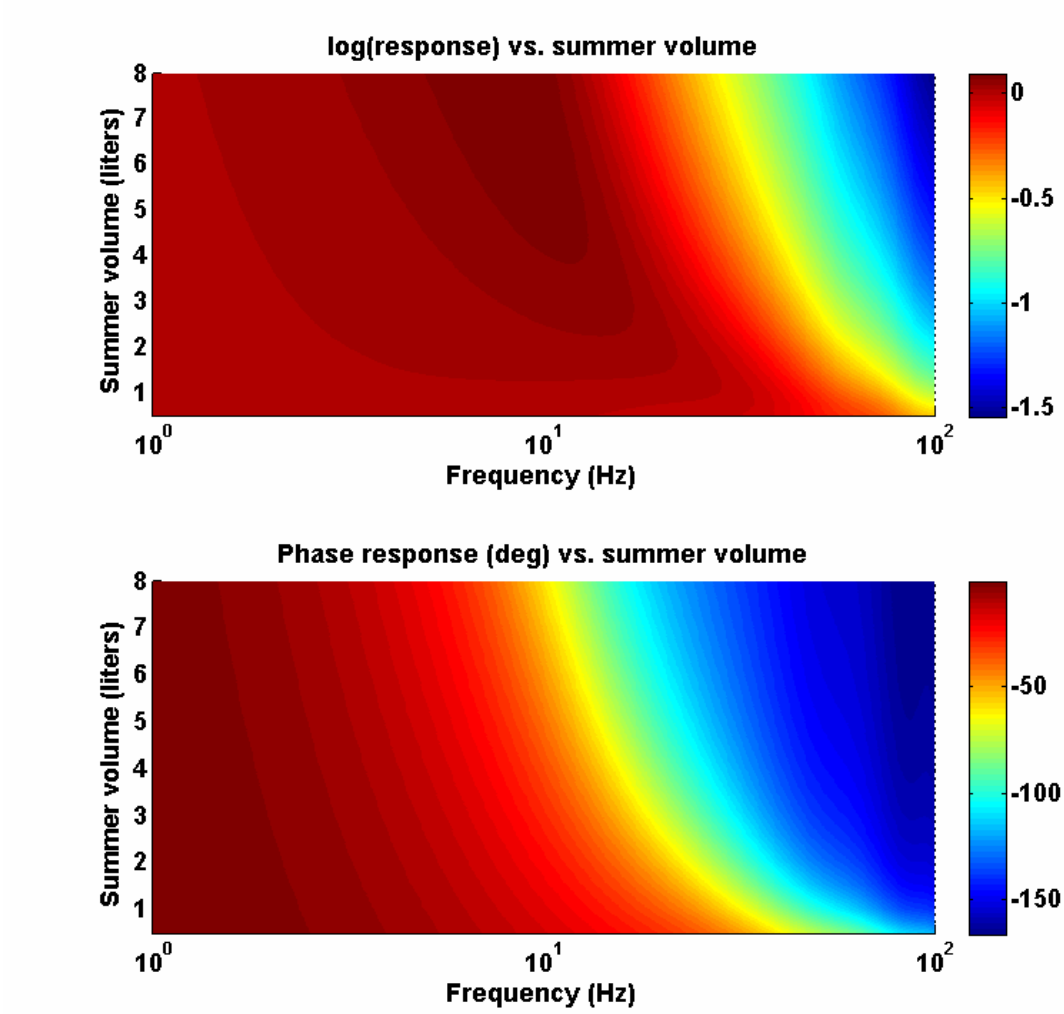

Figure **C-39**: Response as summer volume is changed

C.4.9 Porous hose length sweep (0.5 m to 100 m)

Incident angle (deg):	0
Incident elevation (deg):	90
Porosity:	1.5e6 kg/(s m^4)
Hose termination:	OPEN

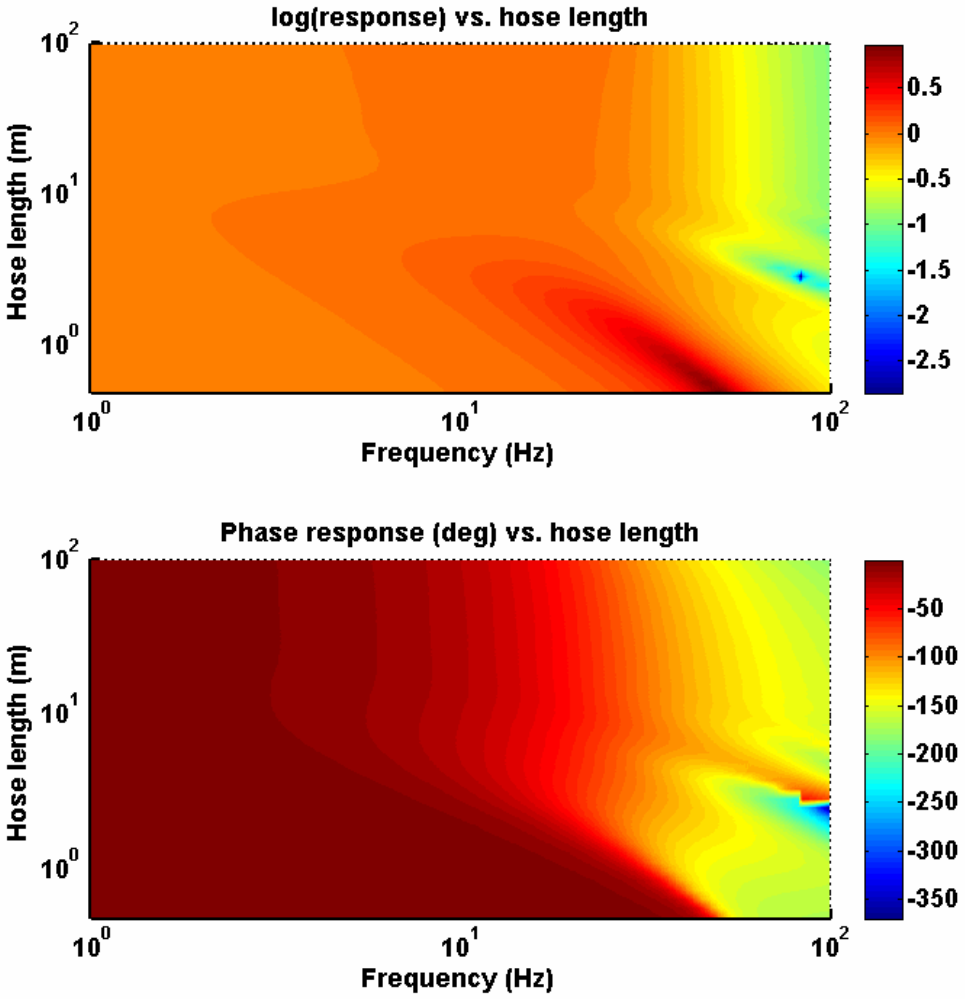

Figure **C-40**: Array response for varying hose lengths.

C.4.10 Porous hose length sweep (0.5 m to 100 m, *capped*)

Incident angle (deg):	0
Incident elevation (deg):	90
Porosity:	1.5e6 kg/(s m^4)
Hose termination:	CLOSED

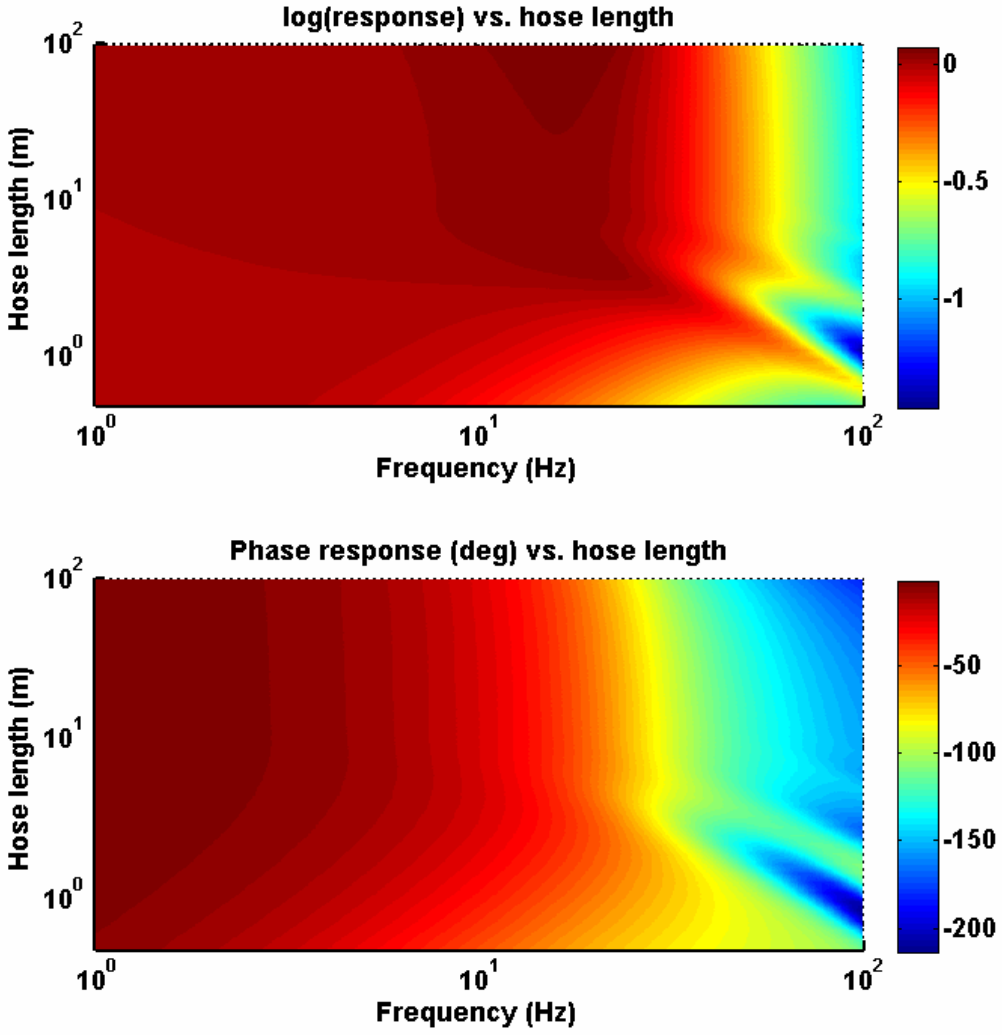

Figure **3-41**: Response as array hose lengths with capped ends are varied.

C.4.11 Closed vs. open termination, 1, 25, and 100 meter lengths

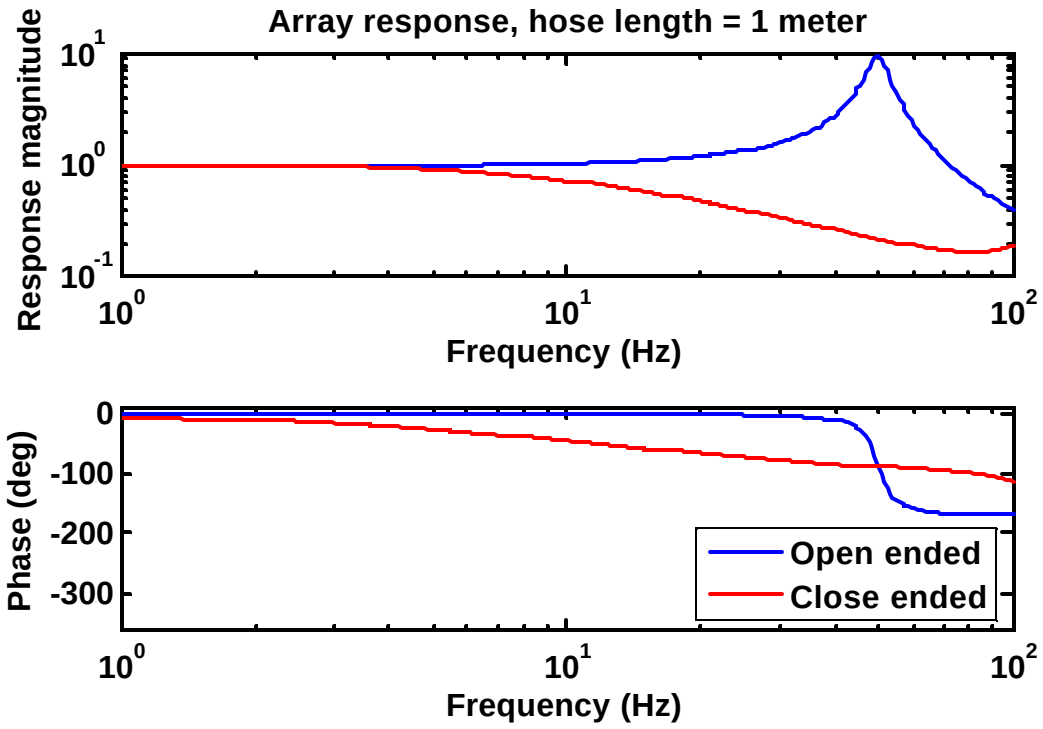

Figure **C-42**: Open vs. closed end 1 meter porous hose array response.

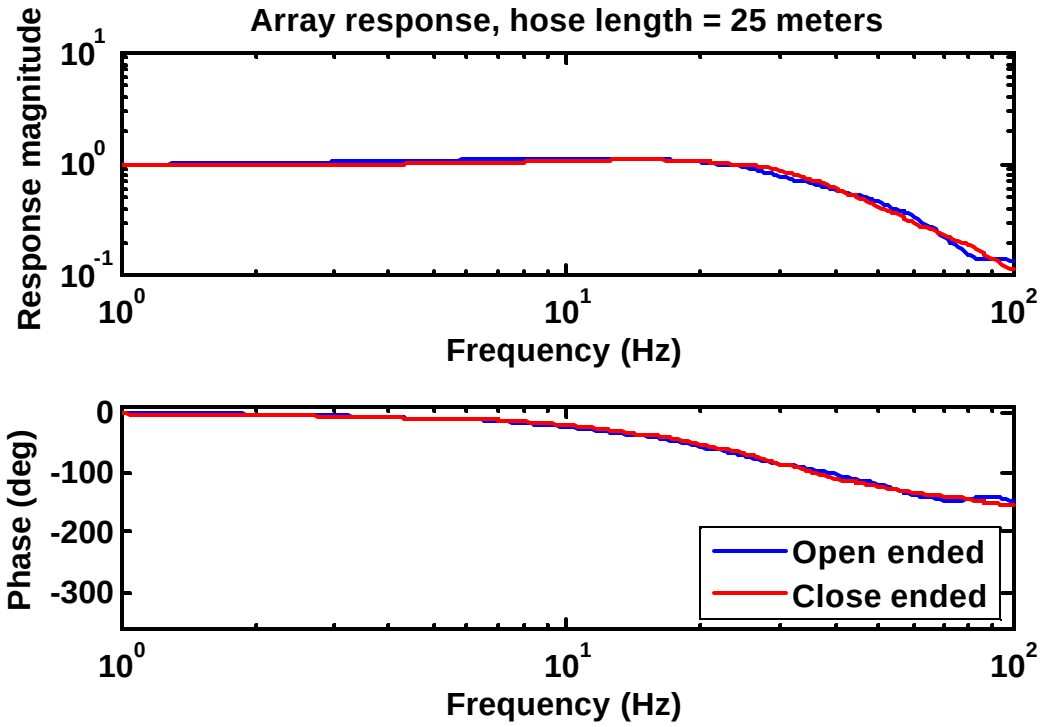

Figure **C-43**: Open vs. closed end 25 meter porous hose array response.

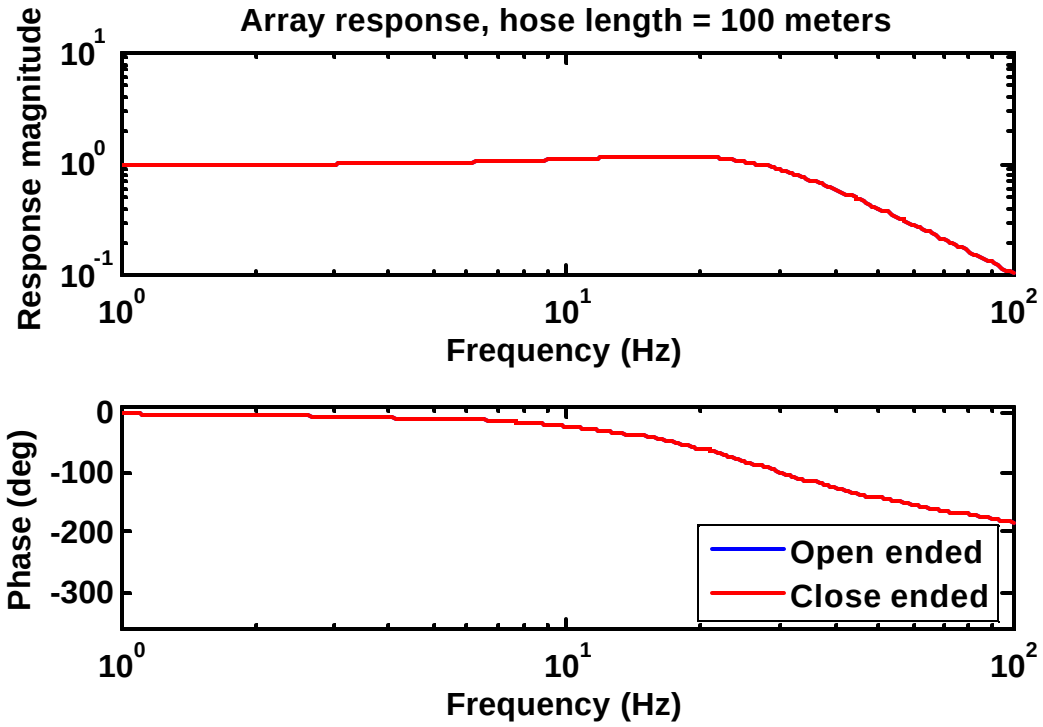

Figure **C-44**: Open vs. closed end 100 meter porous hose array response.

C.4.12 Simulation conclusions

1) The response of a porous array is less dependent on the wave elevation and angle of incidence than an equivalent array made of non-porous tubing.

2) The location of the high-frequency roll-off is highly dependent on the volume of the summing chamber. The location of the high-frequency roll-off and the quality factor of any resonances are also dependent on the porosity of the hose.

3) For a given porosity of tubing, an effective length exists such that:

a) The termination of the pipe does not significantly effect the response of the array when the pipe is sufficiently long.

b) Past a particular length that depends on the porosity, the addition of more pipe has negligible effect on the response of the array.

Appendix D

Microphone calibrations

Several transducer calibrations have been completed using the present pistonphone design. This appendix is a catalogue of the calibrations that have been completed with the infrasonic pistonphone.

Section **D.1** contains the pages of the calibration report for the calibrations referred to and used as examples in **5.2**. Several points are necessary to understand, to interpret the calibration charts correctly. First, each microphone was shipped with its own removable attenuator. The attenuators added a small amount of capacitance between the signal from the microphone capsule and ground, with the purpose of extending the low-frequency response. For each microphone, sensitivities in both attenuated and un-attenuated configurations were measured at 250 Hz using a *Brüel & Kjaer* type 4228 pistonphone, and from 0.01 to 30 Hz using the infrasonic pistonphone.

Secondly, the 250 Hz sensitivities found using the *Brüel & Kjaer* pistonphone were recorded for each microphone in volts-per-pascal. The other sensitivity measurements (found using the infrasonic pistonphone) were *normalized* by the 250 Hz value, and are recorded as sensitivity *ratios* having the units volts-per-volt. As an example, the 30 Hz sensitivity of serial #2571624 is 1.01 V/V, meaning that the sensitivity at 30 Hz was found to be 1.01 times greater than the 250 Hz sensitivity.

The preamplifier gains were all set to 31.6 mV/Pa. As demonstrated by the 250 Hz calibrations, these gain specifications are good but only approximate. The sensitivity of serial # 2571624 at 250 Hz, for example, was 31.8 mV/Pa. The voltage reference used for all calibrations in section **D.1** is in the header file of the data recorded by the data acquisition system, (a TEAC™ GX). The GX is internally calibrated using a reference voltage source at startup, and the volts-per-bit are returned as a slope in the header file for each recording.

Section **D.2** contains the calibration data measured for a G.R.A.S. 40AN microphone, lent by G.R.A.S. measurement microphone company.

D.1 BK4193 calibrations

Low-Frequency Response of B&K 4193 Microphones

The following is a summary of very-low-frequency calibration results for the following microphones:

B&K 4193 Serial Number 2571624
B&K 4193 Serial Number 2571625
B&K 4193 Serial Number 2571626

The responses were measured both with and without the matching UC0211 Low-Frequency Adapters. These measurements were made during the period 12 – 16 July 2008.

All responses are reported with respect to the response at 250 Hz determined with a B&K Model 4228 pistonphone (S/N 2350128) corrected for local barometric pressure. The microphones were powered and conditioned by a B&K NEXUS (S/N 2368212) set to 31.6 mV/Pa and a low-frequency roll-off of 0.1 Hz.

The calibration data is provided in the form of MatLab .mat files. The number of the mat-file corresponds to the serial number of the microphone. File names with an "i" are interpolated to a logarithmically spaced set of 300 frequencies from 5 mHz to 30 Hz. A file name with an "a" refers to a microphone with the UC0211 attenuator in place.

Two measurements were made of the response of SN2571625, in the unattenuated configuration, to test repeatibility. The serial number of the second measurement is followed by a "b."

Each mat-file contains three variables

mag:	Relative magnitude response (relative to 250 Hz pistonphone response)
phase:	Phase response in degrees
hz:	Frequencies

All reported calibration values are made with respect to a 250 Hz pistonphone calibration of the same microphone in un-attenuated configuration:

(Low-frequency calibrator sensitivity measurement)/(250 Hz pistonphone calibration sensitivity measurement)

In all plots, the blue curve is the microphone without the UC0211; the red curve is the microphone with the UC0211.

Calibration and data analysis by: Timothy M. Marston, quinault@gmail.com

Contact: T. Gabrielson (814) 865-1370, tbg3@psu.edu

Serial Number 2571624

***

250 Hz sensitivity:	0.0318 V/Pa	+/- 1%	with NEXUS set to 0.0316 V/Pa
Atm pressure:	966 mbar		
Temperature:	21 C		

***

30 Hz sens. ratio:	1.01 V/V	+/- 2%
Atm pressure:	966 mbar	+/- 0.5 mbar
Temperature:	21 C	+/- 0.2 C

***

-3dB frequency 0.51 Hz +/- 0.01 Hz
[Using 30 Hz sensitivity as the 0dB reference]

Serial Number 2571624 – with UC0211

***

250 Hz sens. ratio:	0.159 V/V	relative to unattenuated 250 Hz resp.
Atm pressure:	976 mbar	
Temperature:	20.5 C	

***

30 Hz sens. ratio:	0.159 V/V
Atm pressure:	976 mbar
Temperature:	20.5 C

***

-3dB frequency 0.10 Hz
[Using 30 Hz sensitivity as the 0dB reference]

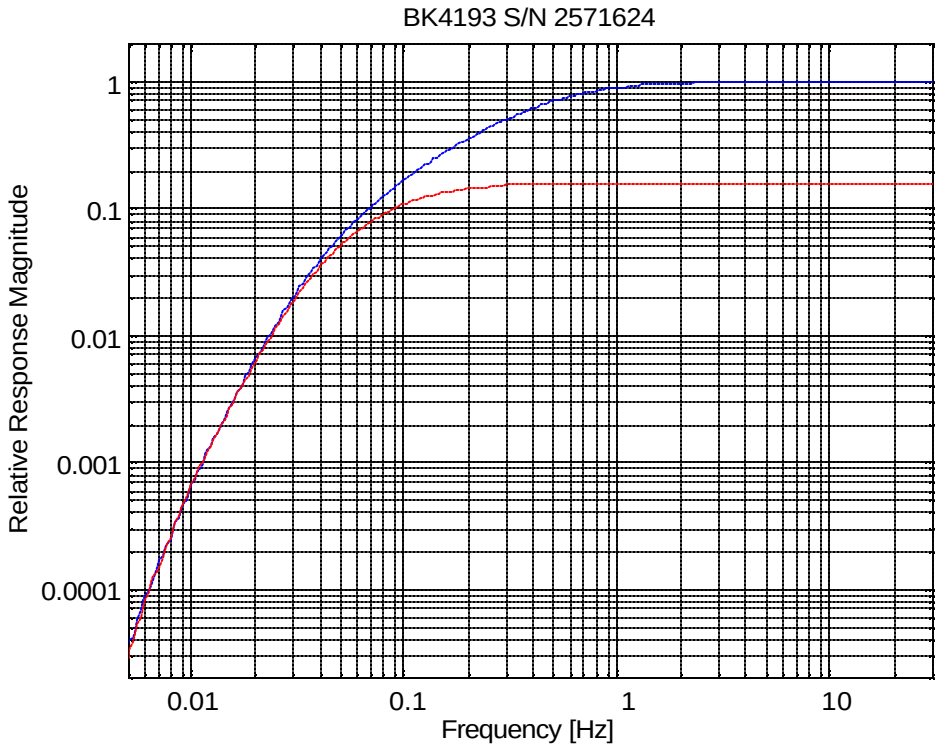
BK4193 S/N 2571624
Relative Response Magnitude
1
0.1
0.01
0.001
0.0001
0.01
0.1
1
10
Frequency [Hz]

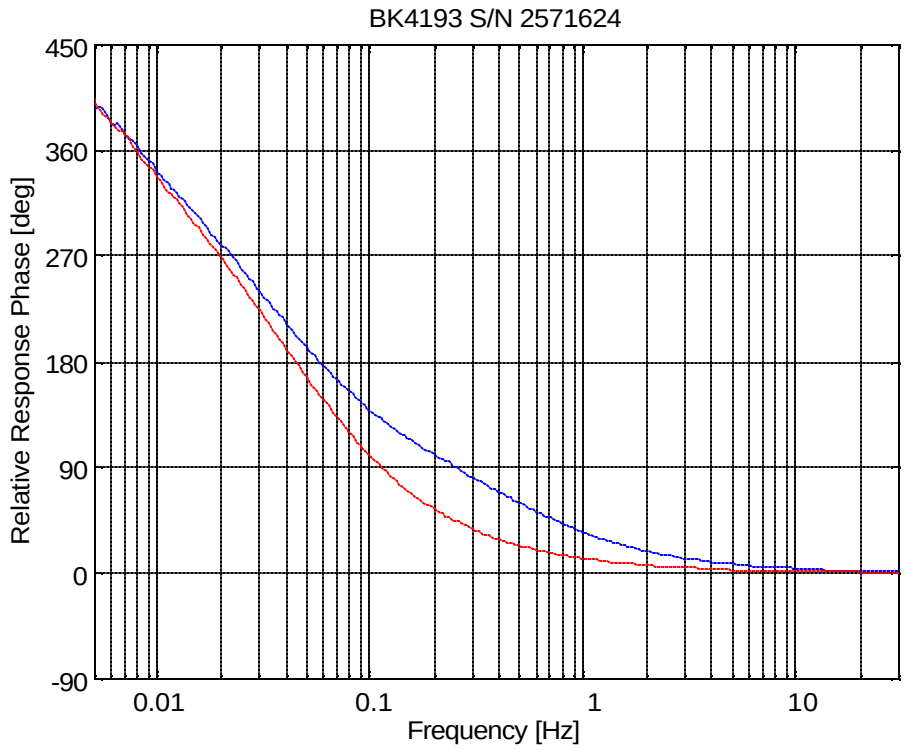
BK4193 S/N 2571624
Relative Response Phase [deg]
450
360
270
180
90
0
-90
0.01
0.1
1
10
Frequency [Hz]

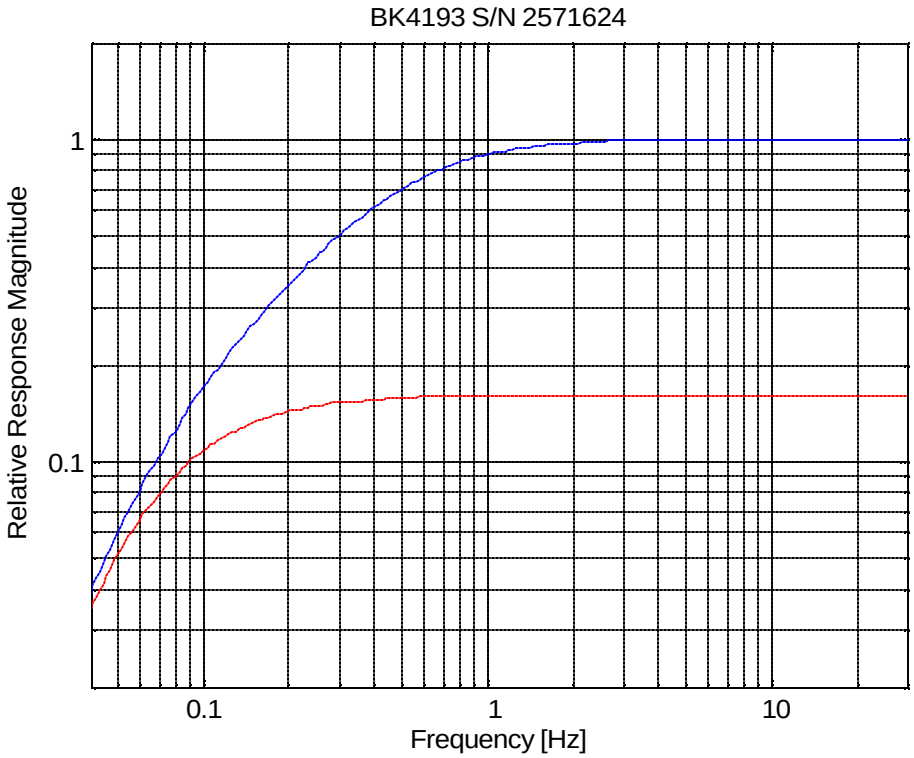
BK4193 S/N 2571624
Relative Response Magnitude
1
0.1
0.1
1
10
Frequency [Hz]

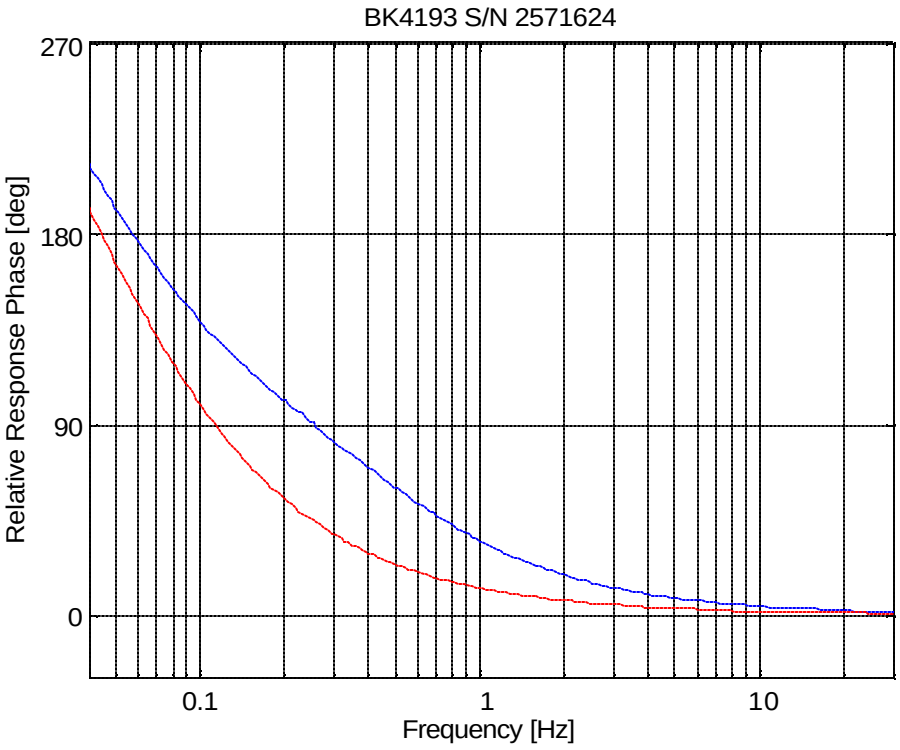
BK4193 S/N 2571624
Relative Response Phase [deg]
270
180
90
0
0.1
1
10
Frequency [Hz]

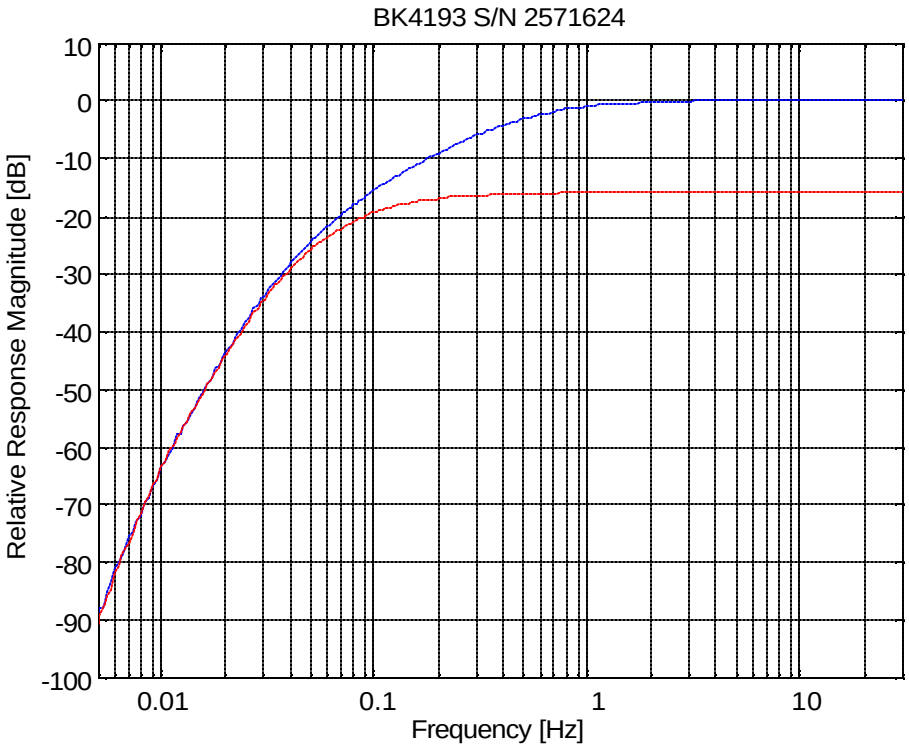
BK4193 S/N 2571624
Relative Response Magnitude [dB]
10
0
-10
-20
-30
-40
-50
-60
-70
-80
-90
-100
0.01
0.1
1
10
Frequency [Hz]

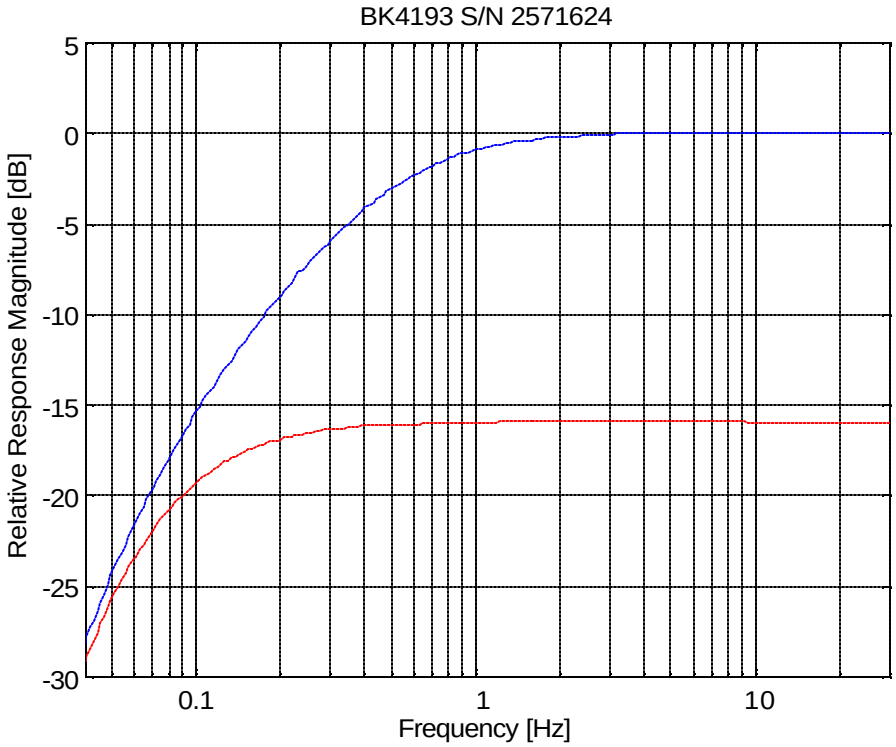
BK4193 S/N 2571624
Relative Response Magnitude [dB]
5
0
-5
-10
-15
-20
-25
-30
0.1
1
10
Frequency [Hz]

Serial Number 2571625

***

250 Hz sensitivity: 0.0318 V/Pa with NEXUS set to 0.0316 V/Pa
Atm pressure: 978 mbar
Temperature: 21 C

***

30 Hz sens. ratio: 1.00 V/V
Atm pressure: 978 mbar
Temperature: 21 C

***

-3dB frequency 0.49 Hz
[Using 30 Hz sensitivity as the 0dB reference]

Serial Number 2571625 - With UC0211

***

250 Hz sens. ratio: 0.163 V/V
Atm pressure: 973 mbar
Temperature: 21 C

***

30 Hz sens. ratio: 0.164 V/V
Atm pressure: 973 mbar
Temperature: 21 C

***

-3dB frequency 0.10 Hz
[Using 30 Hz sensitivity as the 0dB reference]

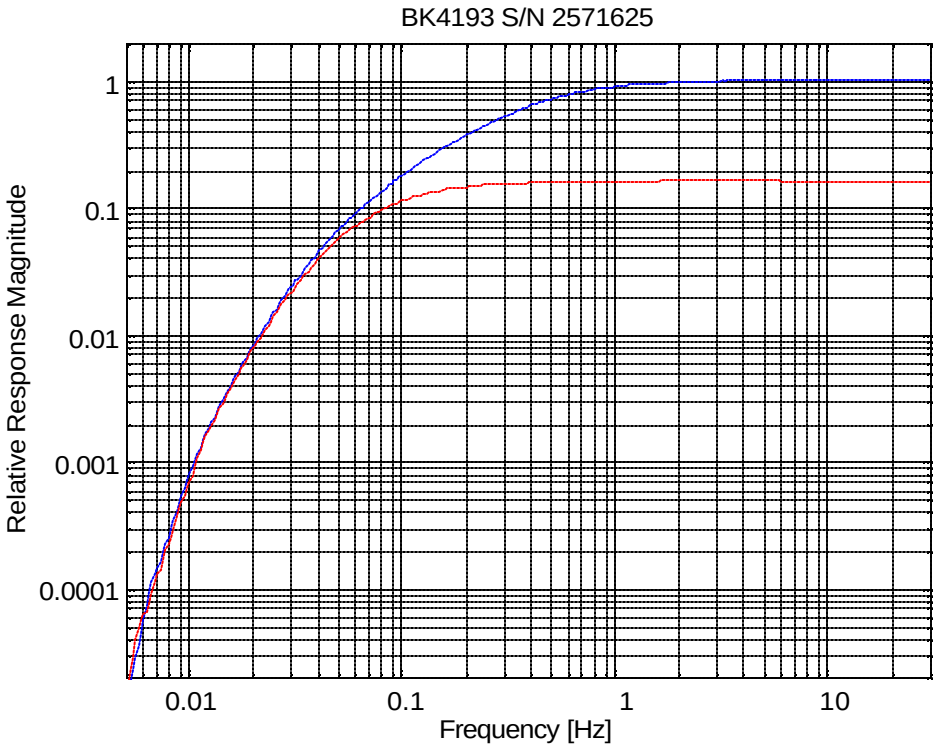
BK4193 S/N 2571625
Relative Response Magnitude
1
0.1
0.01
0.001
0.0001
0.01
0.1
1
10
Frequency [Hz]

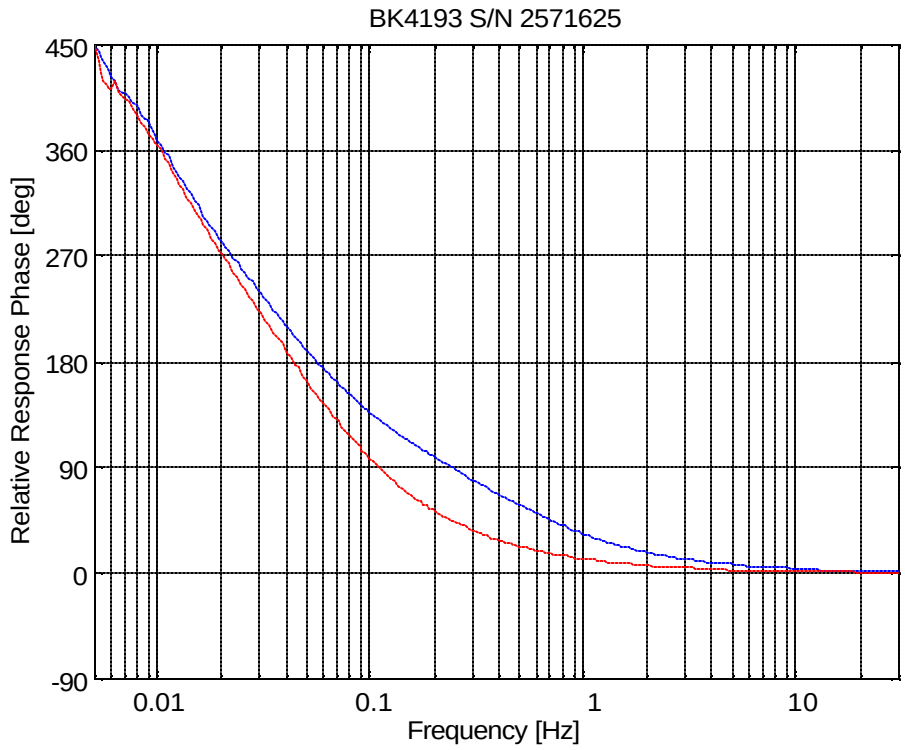
BK4193 S/N 2571625
Relative Response Phase [deg]
450
360
270
180
90
0
-90
0.01
0.1
1
10
Frequency [Hz]

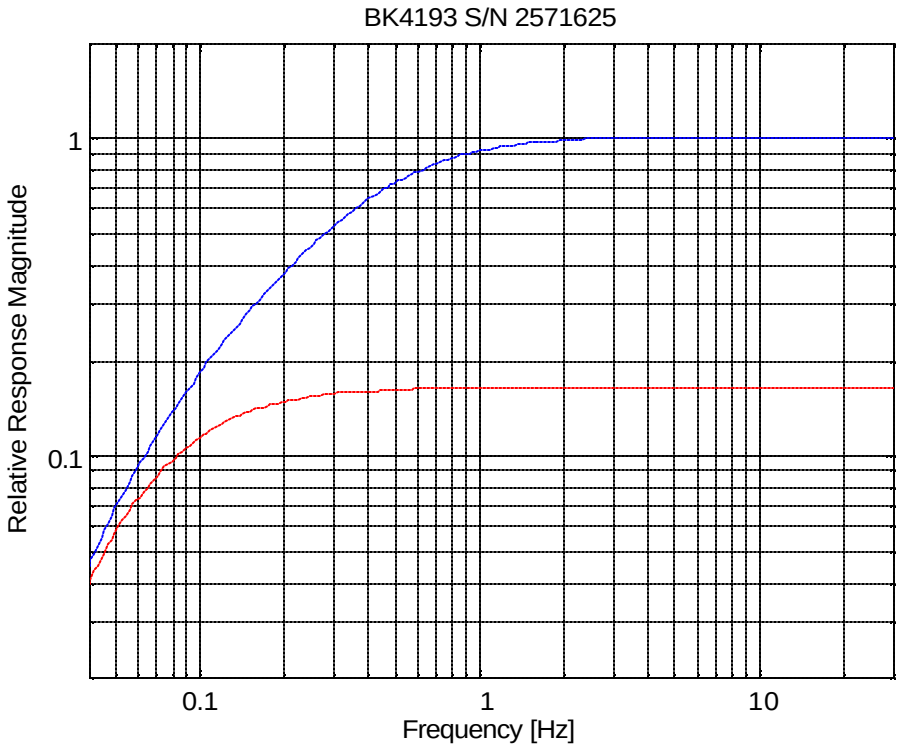
BK4193 S/N 2571625
Relative Response Magnitude
1
0.1
0.1
1
10
Frequency [Hz]

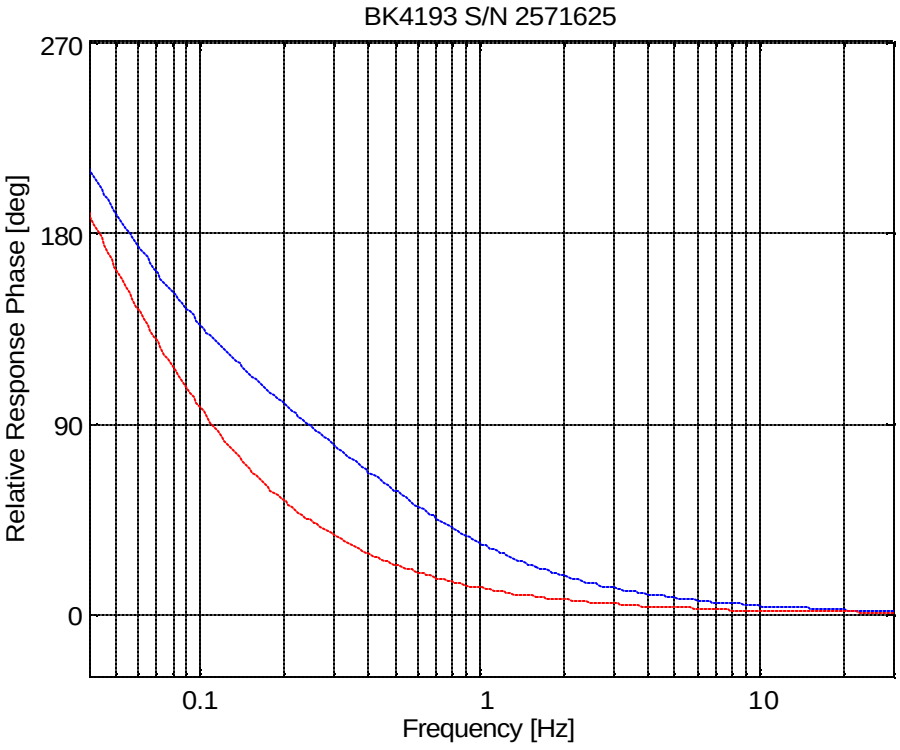
BK4193 S/N 2571625
Relative Response Phase [deg]
270
180
90
0
0.1
1
10
Frequency [Hz]

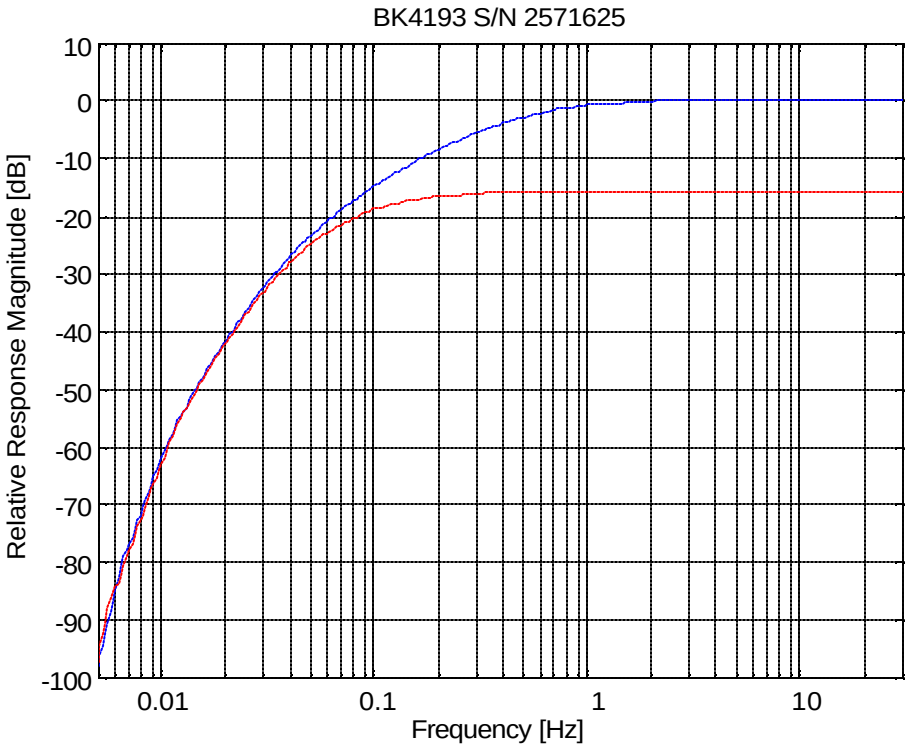
BK4193 S/N 2571625
Relative Response Magnitude [dB]
10
0
-10
-20
-30
-40
-50
-60
-70
-80
-90
-100
0.01
0.1
1
10
Frequency [Hz]

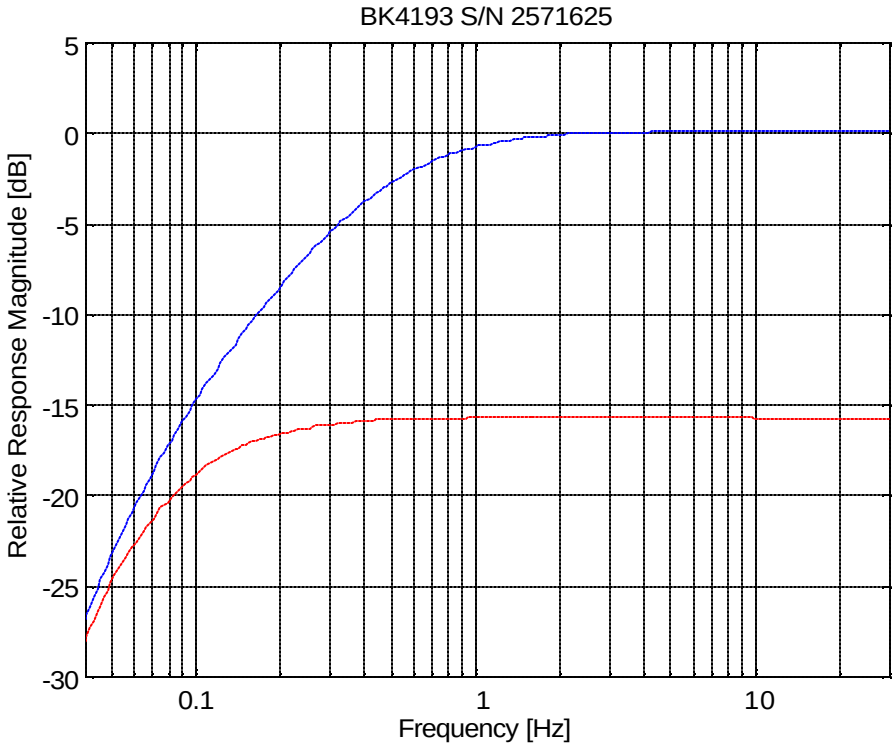
BK4193 S/N 2571625
Relative Response Magnitude [dB]
5
0
-5
-10
-15
-20
-25
-30
0.1
1
10
Frequency [Hz]

Serial Number 2571626

***

250 Hz sensitivity: 0.0293 V/Pa with NEXUS set to 0.0316 V/Pa
Atm pressure: 968 mbar
Temperature: 20.2 C

***

30 Hz sens. ratio: 1.00 V/V
Atm pressure: 968 mbar
Temperature: 20.2 C

***

-3dB frequency 0.46 Hz
[Using 30 Hz sensitivity as the 0dB reference]

Serial Number 2571626 - With UC0211

***

250 Hz sens. ratio: 0.163 V/V
Atm pressure: 971 mbar
Temperature: 21 C

***

30 Hz sens. ratio: 0.163 V/V
Atm pressure: 971 mbar
Temperature: 21 C

***

-3dB frequency 0.10 Hz
[Using 30 Hz sensitivity as the 0dB reference]

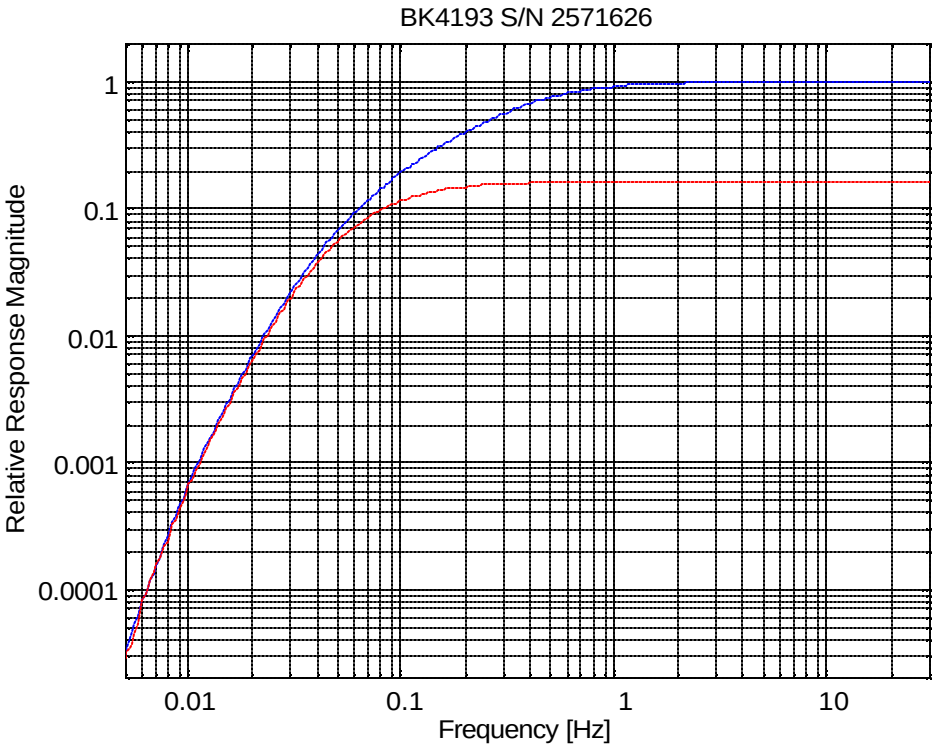
BK4193 S/N 2571626
Relative Response Magnitude
1
0.1
0.01
0.001
0.0001
0.01
0.1
1
10
Frequency [Hz]

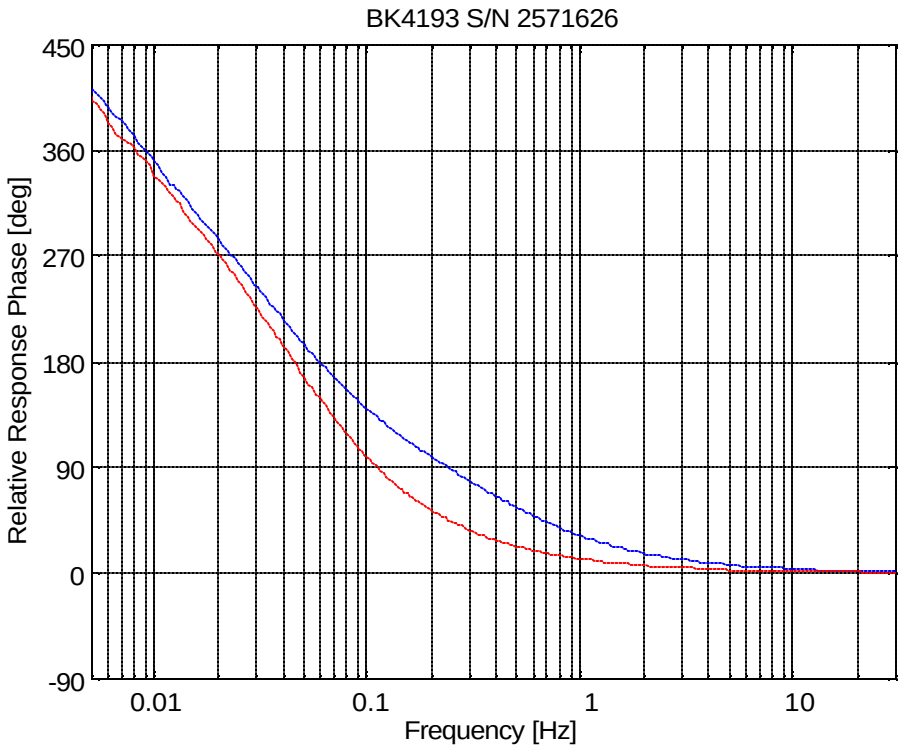
BK4193 S/N 2571626
Relative Response Phase [deg]
450
360
270
180
90
0
-90
0.01
0.1
1
10
Frequency [Hz]

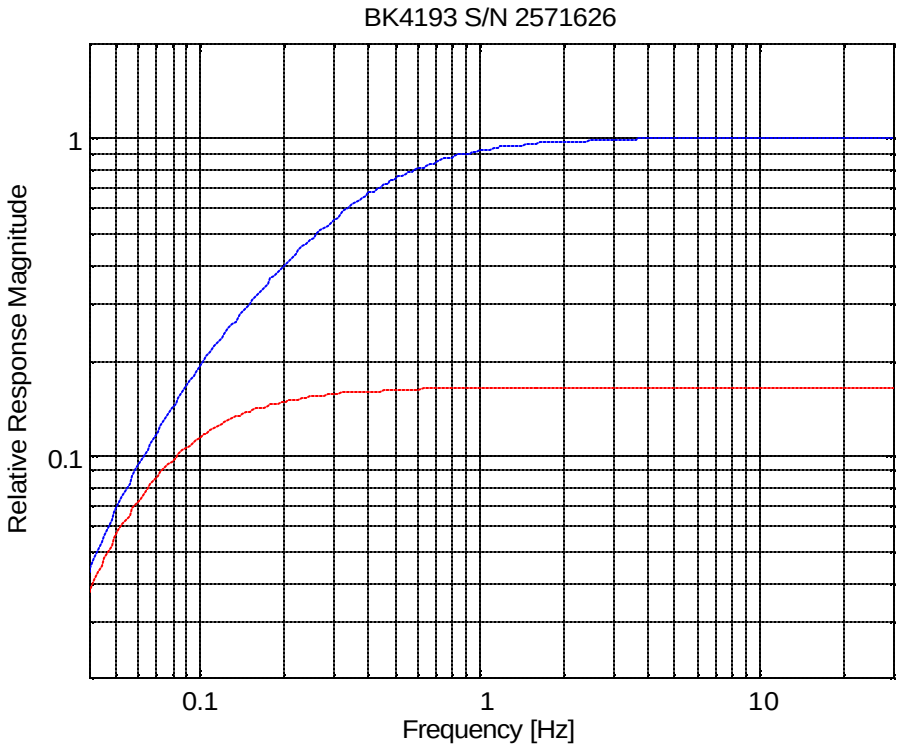
BK4193 S/N 2571626
Relative Response Magnitude
1
0.1
0.1
1
10
Frequency [Hz]

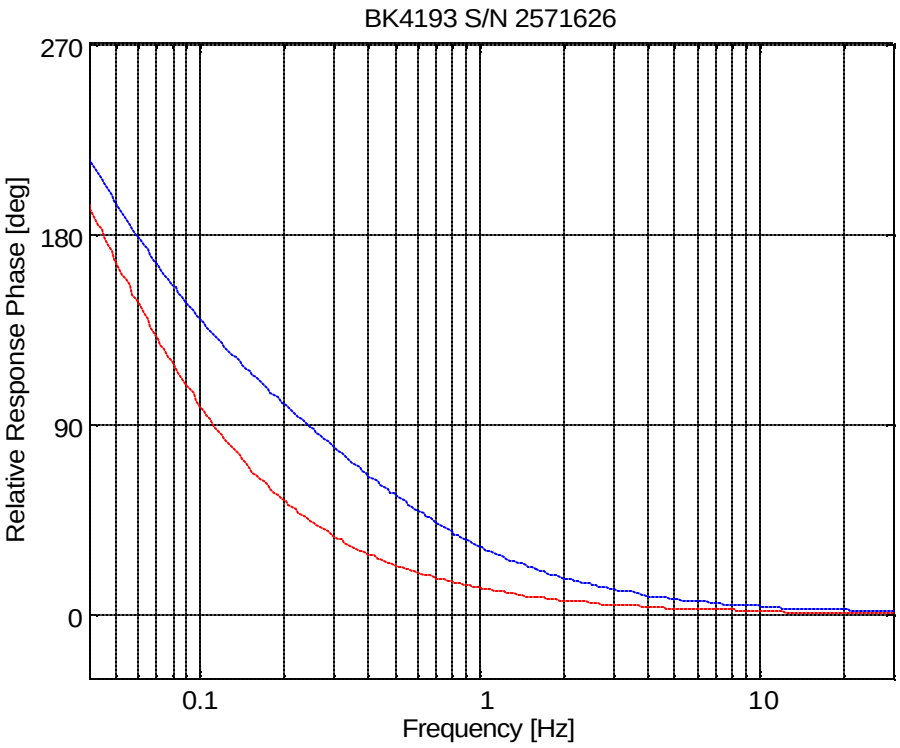
BK4193 S/N 2571626
Relative Response Phase [deg]
270
180
90
0
0.1
1
10
Frequency [Hz]

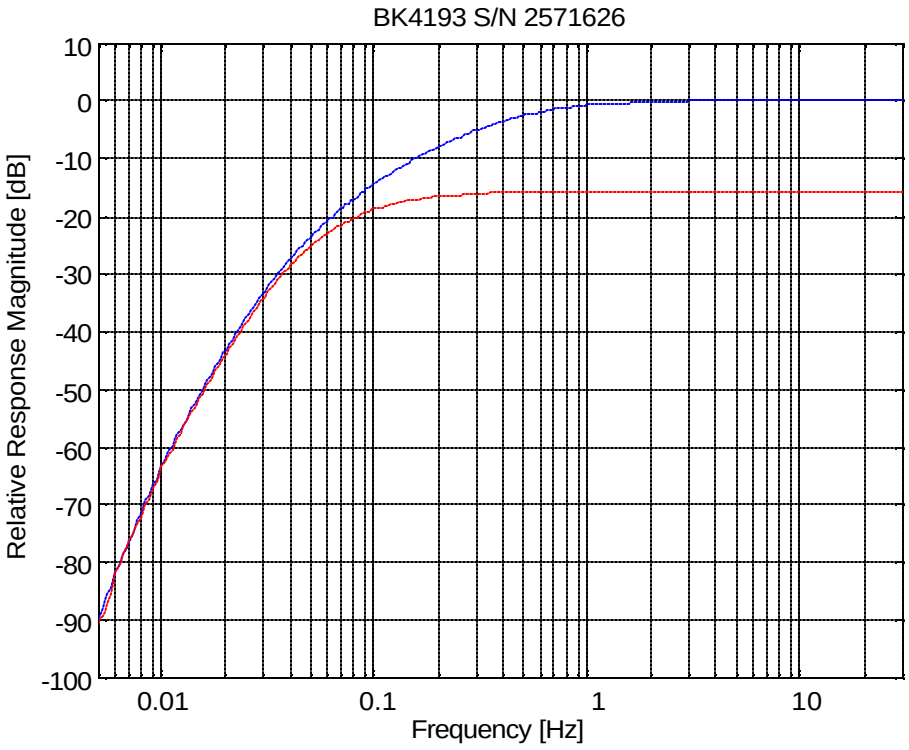
BK4193 S/N 2571626
Relative Response Magnitude [dB]
10
0
-10
-20
-30
-40
-50
-60
-70
-80
-90
-100
0.01
0.1
1
10
Frequency [Hz]

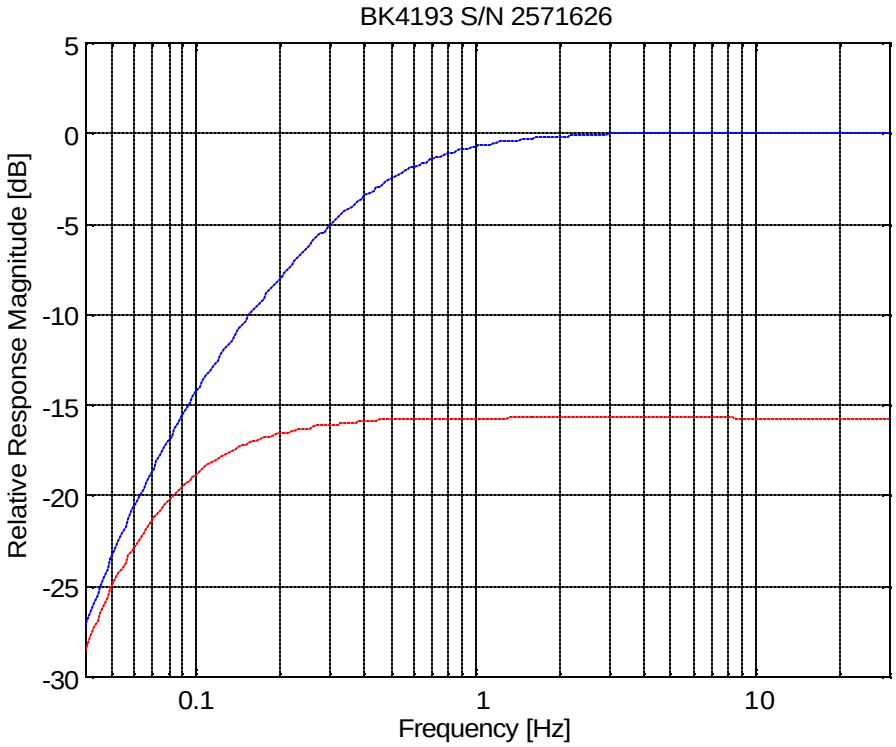
BK4193 S/N 2571626
Relative Response Magnitude [dB]
5
0
-5
-10
-15
-20
-25
-30
0.1
1
10
Frequency [Hz]

D.2 G.R.A.S. 40AN low frequency calibration

Summer of 2008, as an educational research opportunity, G.R.A.S. microphone company lent a 40AN condenser microphone capsule, preamplifier and amplifier to the Penn State acoustics department for an infrasonic pistonphone calibration test. The following 250 Hz sensitivities were recorded on three separate occasions using a type 4228 B&K pistonphone. The 30 Hz sensitivities found using the infrasonic pistonphone.

G.R.A.S. 40AN, serial # 73462
¼'' preamp 12AR, serial # 55726

***

250 Hz sensitivity
Cal 1: 0.0459 V/Pa
Cal 2: 0.0458 V/Pa
Cal 3: 0.0457 V/Pa

30 Hz sensitivity
Cal1: 0.0457 V/Pa
Cal2: 0.0460 V/Pa
Cal3: 0.0459 V/Pa

The following calibration charts shows the sensitivity in V/Pa, recorded for the same microphone on three separate occasions. Figure **D-1**

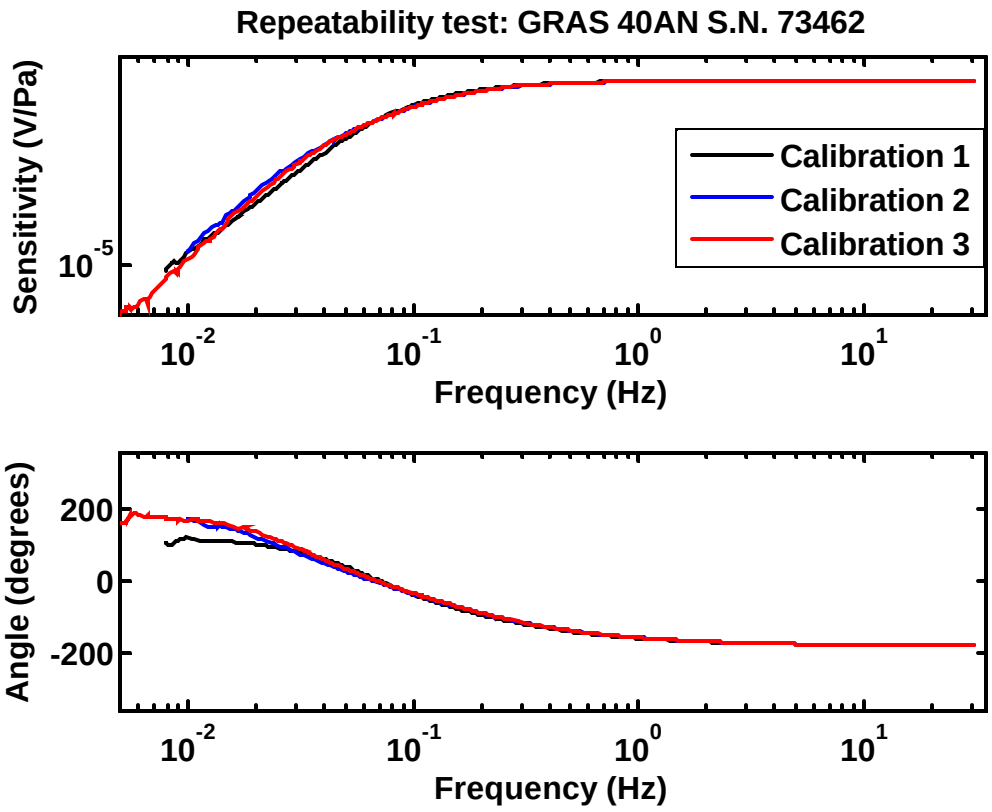

Figure **D-1**: 0.005 to 30 Hz response of a G.R.A.S. 40AN microphone measured on three separate occasions.

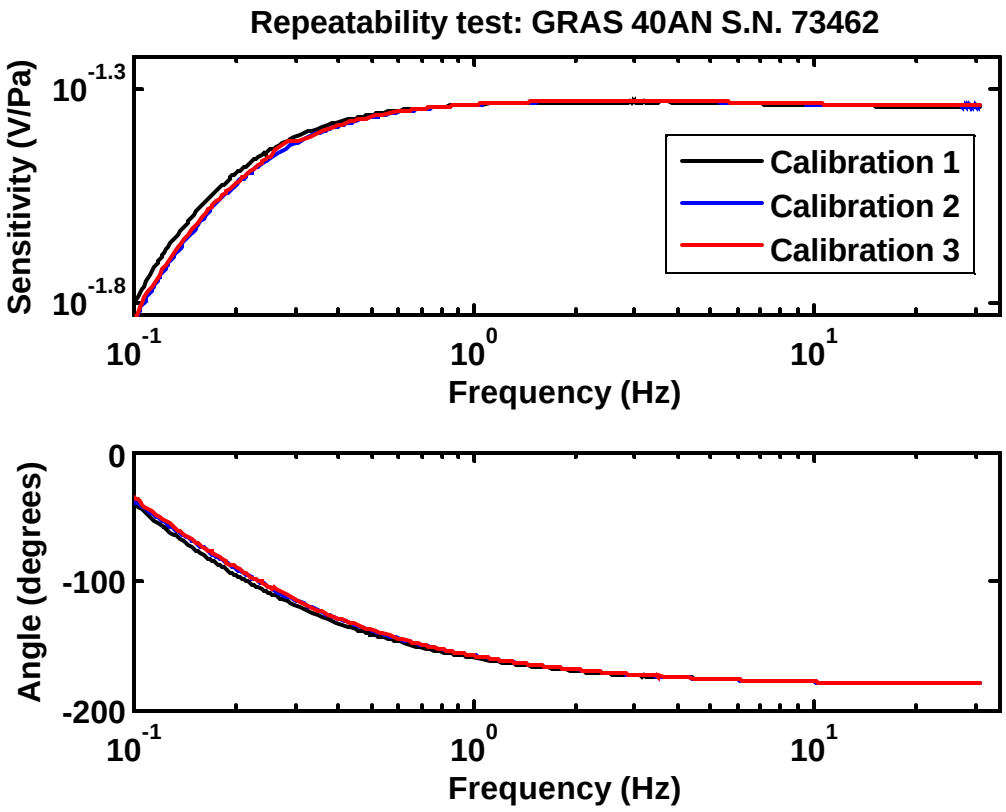

Figure **D-2**: 0.1 to 30 Hz response of a G.R.A.S. 40AN microphone measured on three separate occasions.

Appendix E

Infrasonic condenser microphone

An infrasonic microphone was constructed and partially calibrated using the infrasonic pistonphone. There are several motivations behind the construction of the microphone. It has been built to emulate the performance of a micro-barometer but require roughly $1/100^{th}$ the cost in parts, evaluate the State College area as a potential site for infrasonic array deployment, and demonstrate the infrasonic calibration capability of the pistonphone.

A full calibration of the microphone was never completed because of several other projects and design changes to the pistonphone that were occurring simultaneously during its development. This appendix is a mechanical and electrical description of the microphone. The one calibration that has been done for the microphone is rough and incomplete, and no noise-floor measurements have been made yet because the circuitry needs to be overhauled. Many problems exist with the microphone in its present design, however, the author believes the design has great potential in situations where an inexpensive very low-frequency microphone is required.

E.1 Microphone overview

The infrasonic microphone described in this section has been manufactured from a six-inch length of 2.5'' inner-diameter aluminum pipe that is half-inch thick. The condenser microphone does not work by the standard condenser microphone operating principle. Most condenser microphones place a stable charge differential between a diaphragm and conductive back-plate, then sense the ensuing voltage swings resulting from diaphragm displacement changes.

The problem with this technique, when it is applied to an infrasonic microphone, is that the microphone attenuates low frequencies because of the finite capsule capacitance and preamplifier input impedance. The capacitance of the capsule in the infrasonic condenser microphone is roughly 350 pF. If a cutoff at 0.001 Hz is desired, the input impedance of the microphone preamplifier must be roughly 400GOhms.

This is an impractically large resistance value. Even if a circuit could be constructed with a preamplifier having this high of an input resistance, the $1/f$ characteristics of the preamplifier would be extremely poor. For this reason, this method of achieving wide bandwidth is abandoned.

A technique that has been used in low-temperature physics for many years, and was brought to the attention of the author by Dr. Robert Keolian, is to modulate the amplitude of a carrier frequency using the change in capacitance of the diaphragm, and

demodulate the carrier. This technique avoids the problem of making the input impedance of the preamplifier ridiculously large, and side steps the high 1/f noise accompanying preamplifiers with high input resistance. It is actually possible to measure static offsets using the carrier frequency technique.

This carrier frequency technique is the same technique used by the company *Sennheiser* in all their condenser microphones. It might be possible to modify a *Sennheiser* microphone capsule to create a very good infrasonic microphone, but no work has been undertaken by the author to make such a modification.

E.2 Mechanical construction

Figure **E-1** is a picture of the chassis and diaphragm of the infrasonic microphone.

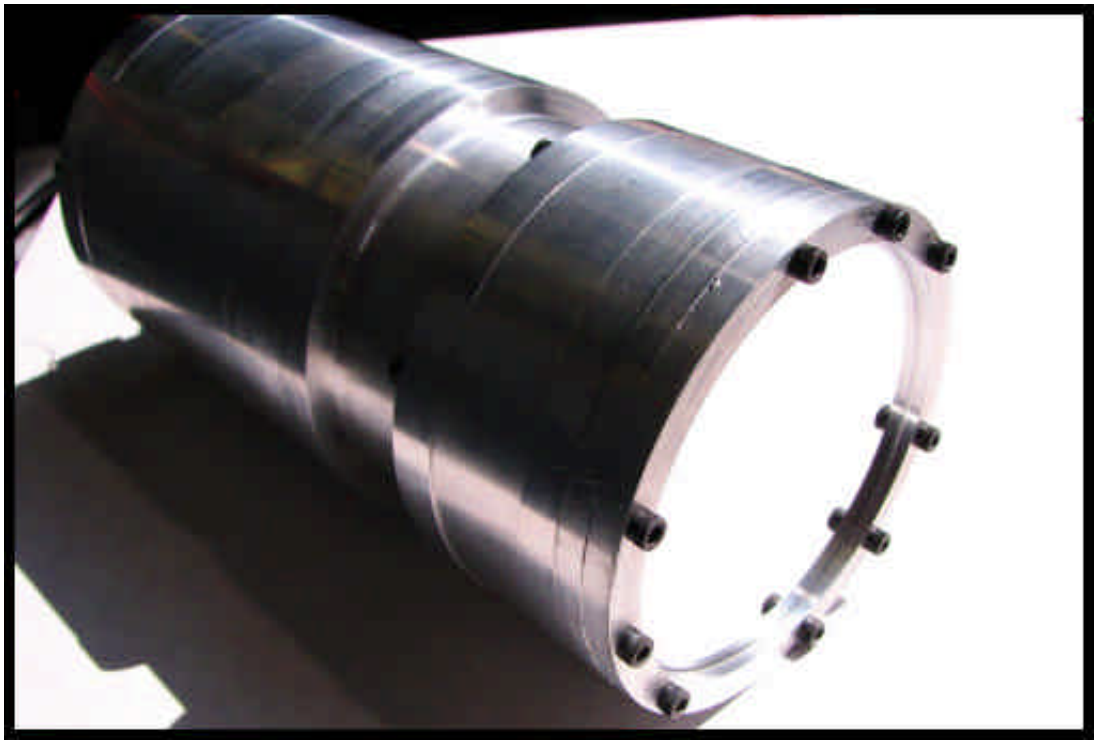

Figure **E-1**: Photo of the infrasonic condenser microphone chassis showing the aluminized mylar diaphragm.

The infrasonic condenser microphone is machined out of an aluminum tube with a 3.5'' outer diameter, and 2.5'' inner diameter. The microphone has a 2.6'' diameter diaphragm of aluminized mylar spaced roughly 2 mil in front of a back-plate. The capsule has a 400 mL volume located behind the diaphragm, which is vented by an air-

leak formed by a wound Teflon capillary. Figure **E-2** is a cutaway of the microphone, showing the mechanical components.

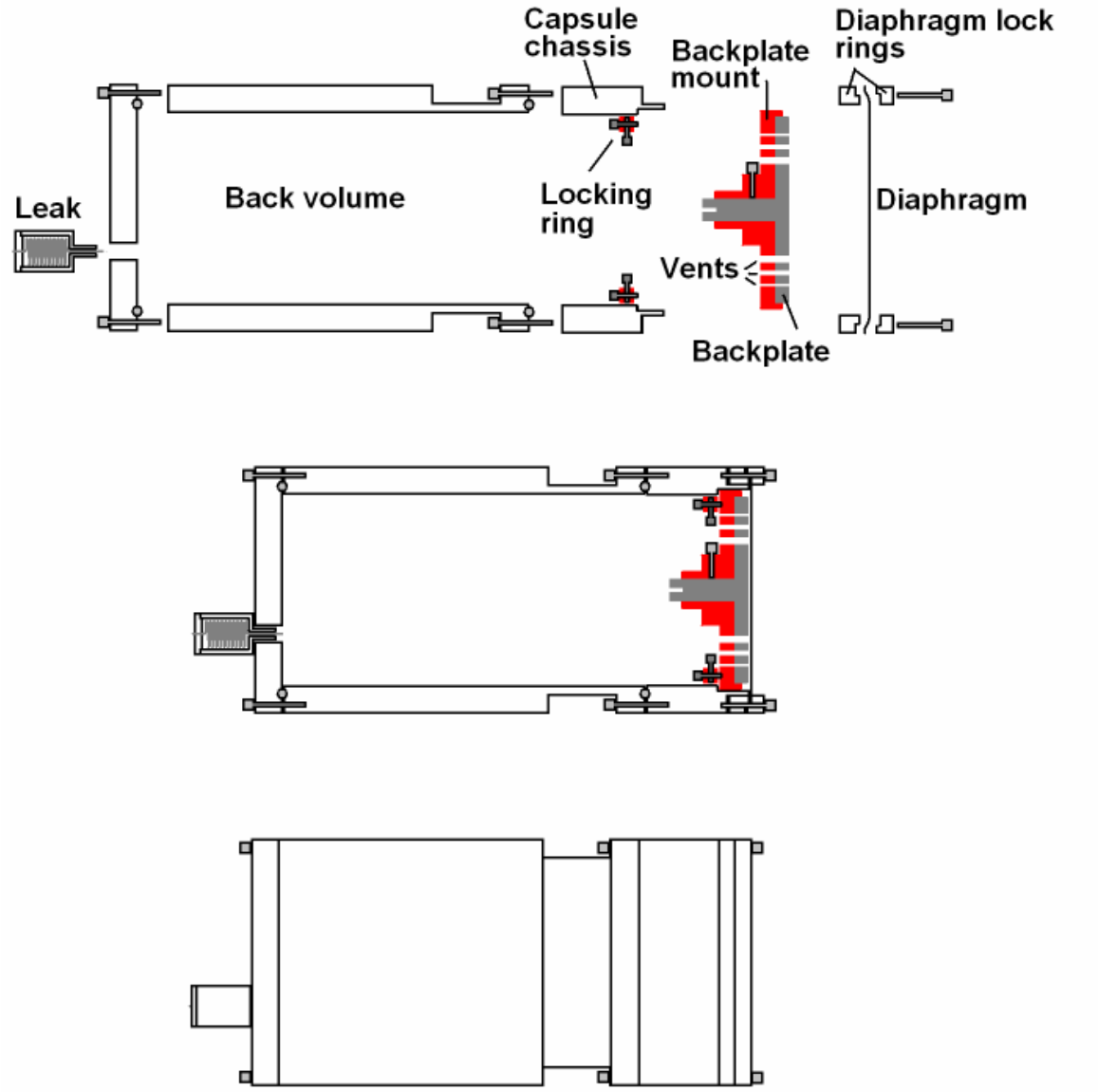

Figure **E-2**: Cutaway of the infrasonic microphone. The top illustration is an exploded view showing all the mechanical pieces in the microphone, in a disassembled state. The middle illustration shows the assembled microphone, and the bottom plot is an external view. Circuit components have been omitted from the diagrams.

The microphone has no inherent low-frequency attenuation mechanism. Because the atmosphere experiences gradual pressure changes that push the microphone into the non-linear region and make it clip, it is necessary to incorporate a mechanical leak into

the microphone to maintain linear operation. This is accomplished by venting the back volume to the atmosphere via a capillary tube. Using a capillary tube 1 meter long results in a -3dB cutoff at approximately 0.004 Hz. The capillary is wound around a spool and placed inside a small chamber which screws into the back of the microphone. The back-leak can be easily adjusted by altering the length of the capillary tube. Figure **E-3** and Figure **E-4** are photos of the capillary tubing chamber, and its attachment to the back of the infrasonic microphone.

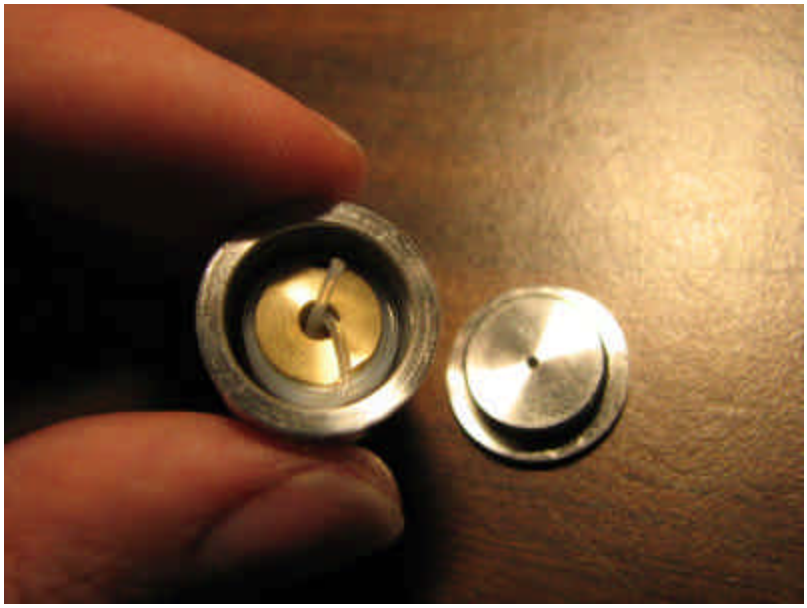

Figure **E-3**: Capillary tubing chamber and capillary tube wound around a spool. Approximately 1 meter of the capillary tubing is contained in this chamber, which screws into the back of the microphone.

Figure **E-4**: Capillary chamber screwed into the back of the microphone casing.

The back plate has a hole machined in the section that pokes out of the mount, pointing towards the back of the microphone. The hole is sized to snugly fit the banana plug mounted on the end of the preamplifier circuit board.

The back-plate is constructed from aluminum, and the back-plate mount is constructed from acrylic. Acrylic is not an optimum back-plate material because it expands and contracts with temperature; however, temperature fluctuations in the air mass behind the diaphragm probably contribute a great deal more noise from temperature fluctuations than the expansion and contraction of the back plate mount. A locking ring machined from acrylic prevents the back plate and mount from falling out of the chamber when the diaphragm is not installed.

E.3 Circuitry

The preamplifier circuitry for the microphone is placed inside the back volume, and is surrounded porous foam and insulation to force all pressure oscillations inside the volume to be isothermal. Figure **E-5** shows the circuit diagram of the microphone preamplifier.

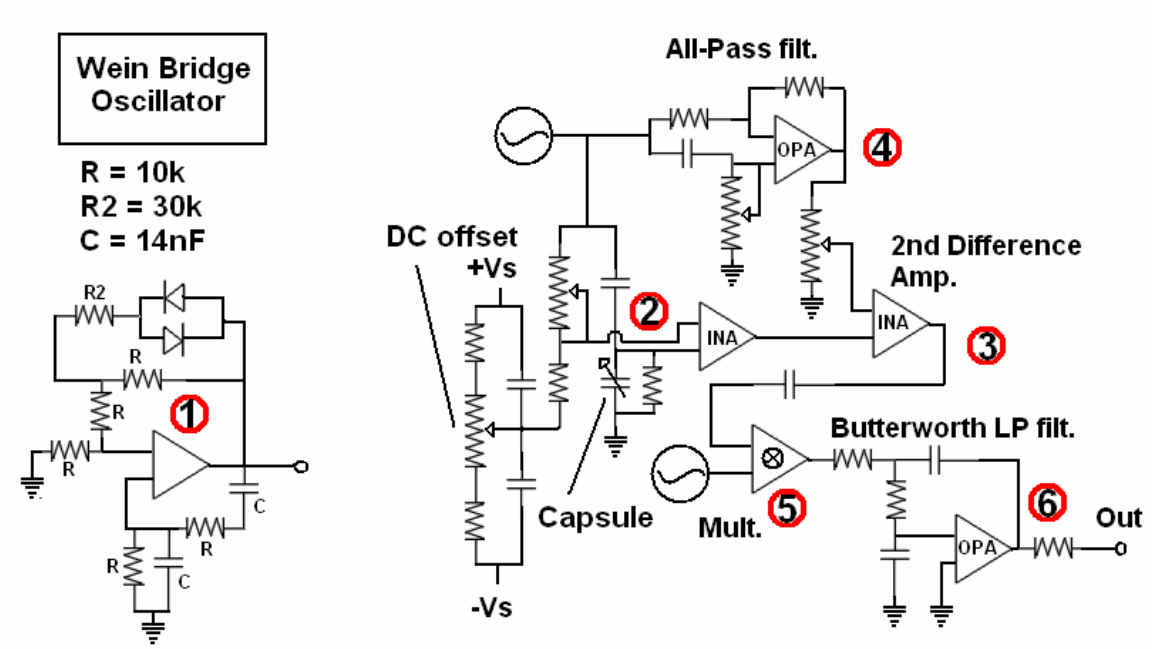

Figure **E-5**: Simplified circuit diagram for the preamplifier and oscillator mounted inside the microphone chassis. Several buffer and conditioning amplifiers, as well as power-supply circuitry and some component values have been omitted for illustration clarity.

The circuitry inside the microphone generates a 15 kHz carrier signal using a Wein-Bridge oscillator (shown at location *1* in Figure **E-5**). This signal then passes through two voltage dividers, one formed by a trim potentiometer and a resistor, and the other formed by a pair of series capacitances, one of which is the actual condenser microphone diaphragm. The trim potentiometer is adjusted so that the amplitudes of the two signals in the middle of the voltage dividers are as nearly equal as possible when the capacitance of the diaphragm is at its equilibrium location. These two signals are then fed through a difference amplifier, at location *2* in Figure **E-5**.

When the voltage dividers are balanced, the output of the difference amplifier is very small.[15] When the capacitance of diaphragm changes because of deflection due to a pressure source, the voltage divider becomes unbalanced. The difference between the two input signals is no longer small, the amplitude of the output of difference amplifier increases. A gain of 100 is present at the first differential amplifier stage.

Even when the diaphragm is at its equilibrium location, a signal is still present at the output of the first differential stage. To enable further amplification of the signal

[15] The output is non-zero, however, and above the common-mode rejection ratio of the difference amplifier because the two input signals are slightly out of phase.

before demodulation, the output of the oscillator is subtracted from the output of the first differential stage. This operation is done at location *3*. The phase and amplitude of the signal is different than the phase and amplitude of the oscillator, however, and the oscillator signal is passed through an all-pass filter with a tunable gain (at location *4*), to make the signals match before the difference is taken again. The second difference amplifier has a gain of 10.

The output of the second difference amplifier is multiplied by the carrier signal from the Wein bridge oscillator at *5*. This does several things to the signal. Because the oscillator has a steady amplitude, a component near DC proportional to the amplitude of the modulation is output. A large 30 kHz component is also present at the output as a result of the multiplication. The high frequency components of the signal are filtered out using a second-order Butterworth filter, before passing the signal out of the microphone.

The microphone preamplifier contains a power regulator, however the power to the preamplifier must be supplied externally. A small signal conditioner/power supply has been built to work in conjunction with the infrasonic condenser microphone.

E.4 Response measurement

Figure **E-6** plots the response of the microphone from 0.001 Hz to 30 Hz, as measured in the infrasonic calibrator chamber. The sensitivity is roughly 50 mV/Pa, and the plot is a plot of the response normalized by the pass-band sensitivity, and converted to decibels. The -3dB down point is at 0.004 Hz. The high frequency cutoff is near 30 Hz, and is determined by a low-pass filter on the external signal amplifier.

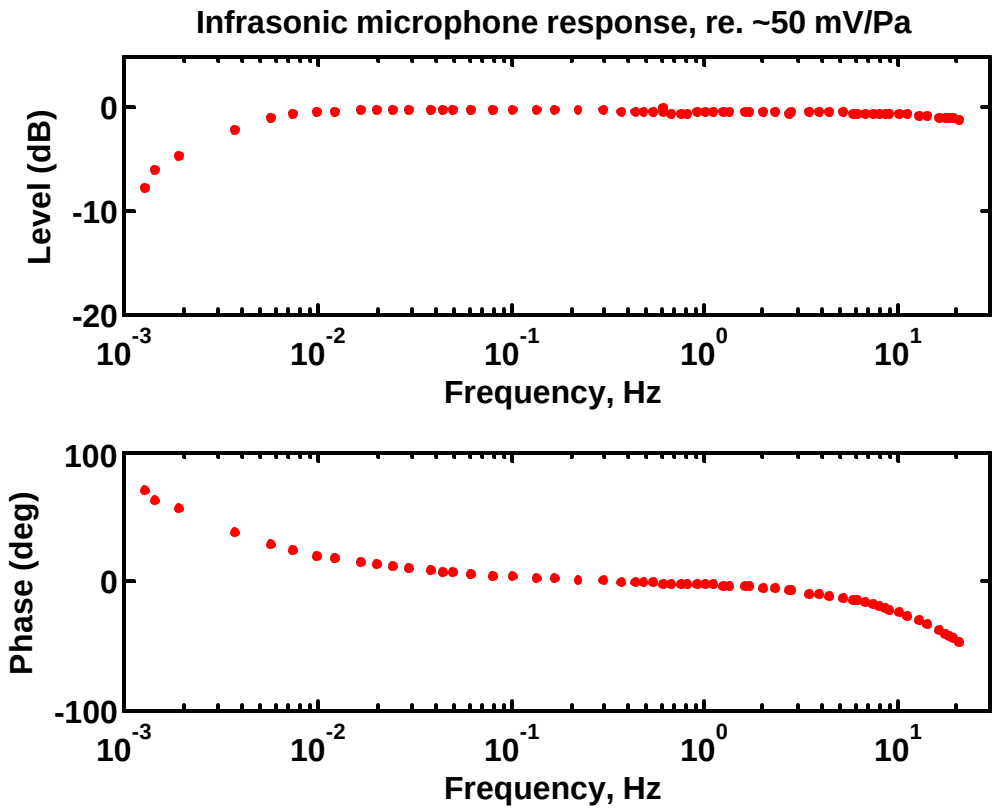

Figure **E-6**: Infrasonic condenser microphone response, as measured by the infrasonic pistonphone.

The response plot shows that the microphone has a relatively poor phase response. The phase is already at 20 degrees at 0.01 Hz, and -45 degrees at 20 Hz. The high frequency phase can be improved by increasing the frequency of the filter roll off, however the low-frequency phase is difficult to improve. The phase can be improved by decreasing the size of the back leak. To decrease the leak by a factor of 5, however, would require a capillary roughly 5 meters long, which would be difficult to house. If the leak is decreased using a smaller capillary, the dynamic range will still be affected, because the signal output will show larger atmospheric pressure fluctuations. It would probably be easier to digitally correct the phase using the response measured by the pistonphone.

E.5 Functionality and design problems

As it stands, the microphone is functional and more sensitive than the piezo-resistive pressure sensors used in this lab, while maintaining (in general) a lower noise

floor. There are several problems with the microphone, especially with the circuitry, that could be significantly improved, and these will be discussed in this section.

After being turned on the microphone appears to sense a rising pressure for approximately 45 minutes before reaching equilibrium. During this time the chamber must be vented or the signal will clip. Because the problem disappears when a large leak is introduced into the back volume, it is hypothesized that this is a result of the circuit board heating the air in the volume behind the diaphragm. The simple solution would be to move the circuitry outside of the back-volume, and external to the microphone. This would slightly increase the capacitance of the capsule. Given that the capacitance is already so large, this modification would not decrease performance. It would, however, eliminate a large source of user irritation and noise from temperature changes.

The circuit also appears to have more 1/f noise than should be present, given that the signal is being modulated. The characteristics of the onboard oscillator and the hair-triggered potentiometers may both be contributing to this problem. Many trim potentiometers exist on the actual circuit board, and are precisely set for signal cancellations. Slight changes in the resistances will have a large effect on the amplitude of the signal. This problem could be fixed by using a steadier oscillator, and circuit components that are fixed.

Multipliers are inherently noisy circuit components and have dynamic ranges limited to approximately 90 dB. A de-modulating circuit that has a higher dynamic range than 90 dB could be beneficial for an infrasonic microphone to have, because of the high dynamic range requirements of these instruments. Another way of circumventing the problem could be to feed the output of the multiplier directly to the front end of a digital acquisition system do the multiplication digitally. A high carrier frequency would require high data rates, however, which may not be practical for long periods of data recording.

A final design flaw is that the leak, in its present form, is made from plastic capillary tubing. The frequency of the mechanical cutoff will vary with temperature as the capillary changes radius.

It is the author's opinion that the microphone could be vastly improved by making the supporting circuitry external. This would relieve the space requirements and allow a better circuit to be built. A battery could also be housed in an external amplifier stage so that the microphone could operate independent of a wall-supplied power source. If the circuitry is improved, the infrasonic condenser microphone could be an inexpensive, simple way to make infrasound measurements.

Appendix F

Pistonphone design evolution

F.1 Overview

Many design stages preceded the pistonphone presently used for making calibration measurements. This appendix will provide an overview of the design stages leading up to the design described in Chapter **2**. For simplification, the development of the pistonphone is divided into four stages:

1. Initial prototype (model 1)
2. Enlarged chamber prototype (model 2)
3. Schedule 80 prototype (model 3)
4. Final prototype (model 4)

Testing during each stage revealed important design considerations crucial to the development of the final prototype. The first two design stages are discussed in detail in the appendix of reference [**15**] and will be covered more briefly than models 3 and 4.

F.2 Initial prototype (model 1)

The initial pistonphone prototype consists of a two foot section of 1 ¾ inch PVC pipe mated with a graphite and glass 1 ¾ inch[16] piston and cylinder at one end. The other end is sealed by a PVC pipe end-cap. The shaft of the piston is connected to a wheel with an axle mounted in an aluminum block. The axle is driven directly by a motor for achieving high calibration frequencies. The axle is connected to the motor via a 40:1 worm gear reducer to for lower frequency calibration signals. The total peak-to-peak piston swing is approximately 2.54 centimeters (1 in), but can be increased to 3.81 cm (1.5 in) using a different shaft mounting point on the wheel.

The pressure inside the chamber is measured by a 15 PSI piezo-resistive sensor ("PZR") manufactured by Endevco. The PZR is mounted near the end-cap of the pistonphone chamber. A plug in the end-cap allows a PZR sensor to be immersed inside the chamber, fully exposing the sensing element and the back-leak to the calibration

---

[16] SI units are standard units for dimension measurements in this thesis. English units will be used when objects that are commonly referred to by English unit sizes, such as pipes or microphones, are discussed.

signal pressure field for a complete measurement of the mechanical and electrical low-frequency response.

Figure **F-1** is a diagram of the initial prototype, illustrating the major parts of the design. The first motor used to drive the pistonphone was a drill powered through a Variac. The Variac was used to vary the rotations per minute. The drill was abandoned because of excessive noise during operation, and difficulty mounting the drill in a stable manner. People also needed to use the drill. In the place of the drill, a motor, provided by Dr. Atchley, is used. Running silently and predictably, the motor is a significant advancement over the drill and is used for all subsequent pistonphone design modifications.

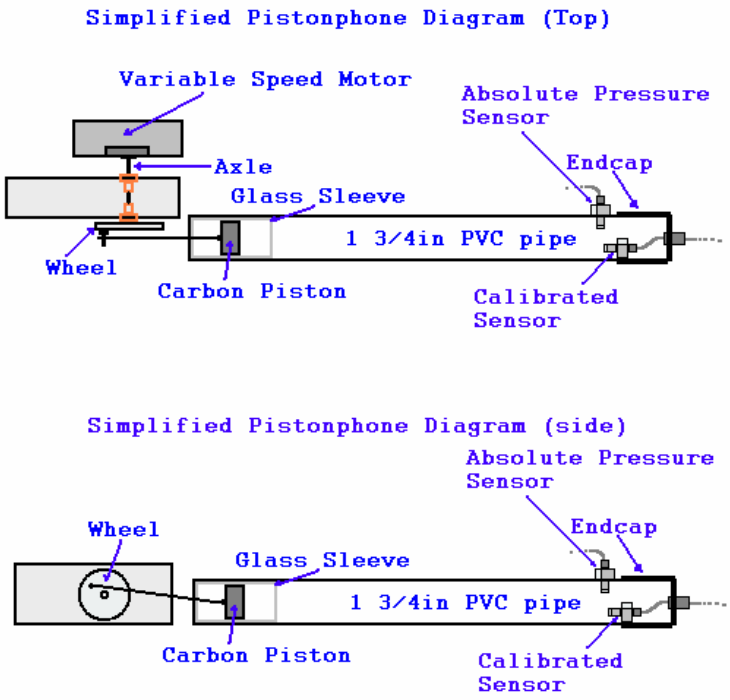

Figure **F-1**: Initial prototype illustration, showing the high-frequency operation configuration and major apparatus components. Not shown: 40:1 gear reducer and small connection pieces.

For the sake of illustration clarity, several features are omitted from Figure **F-1**. The main cog of the 40:1 gear reducer is mounted on the axle, on the side of the axle block opposite the wheel. The worm gear is fixed to the cog by means of an aluminum stand mounted on top of the axle block, as shown in Figure **F-2**.

Figure **F-2**: A picture showing the worm gear, worm gear mount, and cog.

Figure **F-3** is a top-view photo of the pistonphone geared for low frequency calibration. The worm gear is mounted and engaged with the cog fixed to the axle.

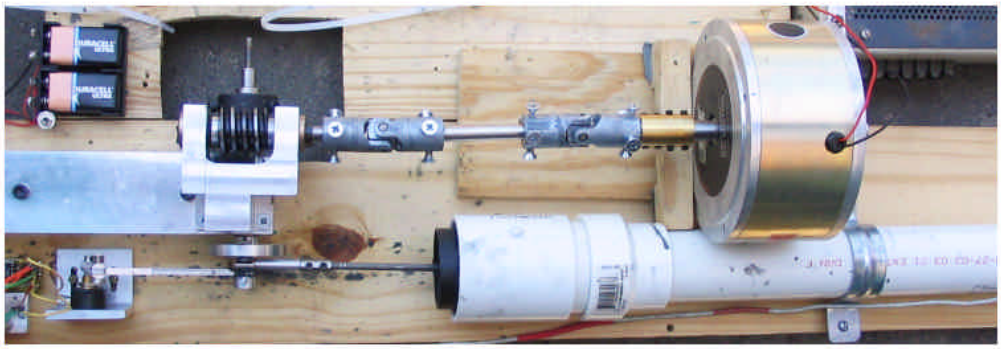

Figure **F-3**: Top view of the entire pistonphone assembly (model 1), with the 40:1 worm gear reducer engaged.

When gear reduction is not required the worm gear is removed from the mount, and the motor shaft is connected directly to the cog, as shown in Figure **F-4**.

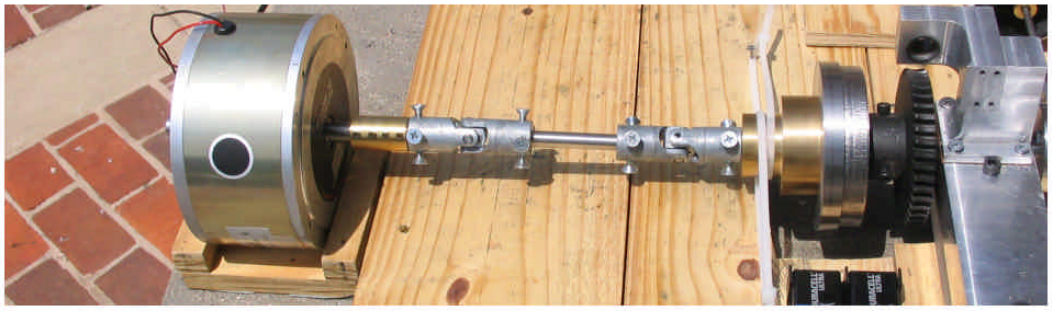

Figure **F-4**: A picture showing the direct connection of the motor shaft to the axle of the pistonphone. Two universal joints allow the motor shaft and axle axes to be independent. Weights and zip-ties are fixed to the axle to increase the steadiness of the load seen by the motor.

For making good relative calibrations down to 0.03 Hz, few changes to the design are needed. In the relative calibration process the measured transducer response changes introduced by variations in calibration signal amplitude are common to both the transducer and the reference, and cancel out in the response division process. Figure **F-5** is a sensitivity plot produced by dividing the response of a totally immersed 15 PSI PZR by the response of a side-mounted 15 PSI PZR being used as the reference.

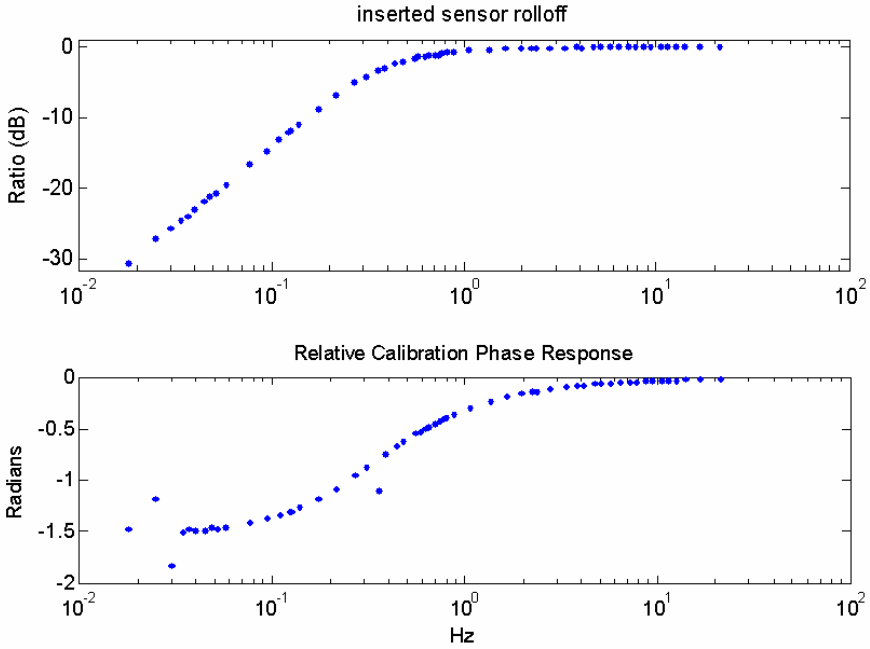

Figure **F-5**: Relative calibration of a totally immersed 15 PSI piezo-resistive pressure sensor, using an externally vented 15 PSI piezo-resistive pressure sensor as a reference. The calibration error due to thermo-viscous and other effects are common to both transducers and cancel out in the response calculation process.

Major problems exist with the initial prototype, however, for other types of calibrations. Absolute calibration of sensors is poor due to calibration signal amplitude inconsistency, and it is difficult to calibrate condenser microphones because of the high sound pressure level. The pressure generated in the chamber of the initial prototype is >170 dB re. 20 µPa. This sound pressure level surpasses the region of non-linear operation in most measurement microphones, making calibration inaccurate and possibly even damaging for very sensitive microphones.

Additionally, the inability to measure the displacement of the piston makes measurement of the phase response of transducers at low frequency impossible during absolute calibration. Certain frequencies are also un-measurable with the initial prototype design, because there is no overlap in frequency range of the reduced and direct connection motor configurations. The gear reduced region of operation spans 0.03 to 0.77 Hz, while the direct connection configuration spans 1 Hz to 30 Hz. From approximately 1 to 5 Hz, the torque of the motor is low enough that severely distorted waveforms are produced, reducing calibration accuracy.

Axis alignment problems caused by mounting the motor to the axle or shaft of the worm-gear are solved by using two series-mated universal joints. These solve the alignment problem, however mechanical vibration is introduced into the system by the universal joints, and the calibrator is very noisy when operating at high speeds. When measurements are taken of the free-field pressure generated inside the pistonphone chamber, the adiabatic-to-isothermal transition occurs at a higher frequency than predicted for the measured chamber radius, indicating that a source of loss is present in the system that is not accounted for by the thermo-viscous model used to describe the system.

Most of these problems are only solved adequately in much later design stages, but modifications are made to the initial prototype to reduce the error introduced by most of these problems. To reduce jitter from the universal joints and improve the performance of the motor at low frequencies a set of weights is added to the axle to add rotational inertia and zip ties are used to put the axle under a constant resistive load. It is found that by putting the axle under a constant resistive load the motor becomes less sensitive to the loading of the piston. Furthermore the jitter in the universal joints is reduced and the distortion in the 1-5 Hz range decreases. The addition of the weights further reduces the jitter introduced by the universal joints and the sensitivity of the motor to the loading of the piston.

The first major improvement to the initial prototype is to add a displacement sensor to the piston. The displacement measurement of the pistonphone provides a phase reference for the absolute calibration measurements, as well as a signal with a high signal-to-noise ratio for the calculation of the fundamental frequency of the calibration signal. Figure **F-6** illustrates the operation of the displacement sensor:

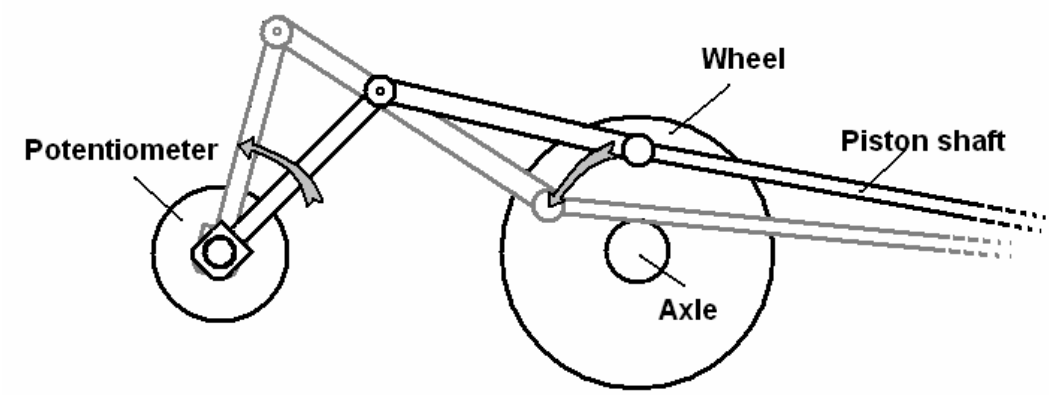

Figure **F-6**: Potentiometer based displacement sensor. As the wheel turns, pumping the piston in and out of the cylinder, the shaft of the potentiometer swings through an arc. A steady voltage is placed across the potentiometer, and the voltage at the center-tap corresponding to the angle of the potentiometer shaft rotation is measured.

The rotational motion of the wheel pumping the piston in and out of the shaft is translated to a roughly sinusoidal voltage signal from the potentiometer center-tap. The length of the connection rods between the wheel and the potentiometer determine the angle through which the potentiometer shaft swings. For the configuration in model 1, the potentiometer swings back and forth through an arc of about 45 degrees. To measure the angle of rotation and power an output signal, a 5V potential is placed across the upper and lower taps of the potentiometer. The center tap produces a voltage signal proportional to the angle of the shaft.

In this configuration, the potentiometer signal is out-of-phase with the piston displacement, and will also distort differently when the motor has insufficient driving capability to produce a clean sine-wave. The phase offset is uniform across frequencies, and is measured in comparison with the reference calibrator. This phase offset is subtracted from the phase measurements used in absolute calibration. When the motor is operating at a low-torque frequency and the waveform distorts, the displacement sensor and pressure signal distort differently. This particular displacement sensor therefore does not clean up the measurements a great deal in the 1 – 5 Hz region, when used for synchronization. Another problem with this displacement sensor is that there is a small amount of mechanical play and jitter between the potentiometer and the motion of the piston.

The addition of a device to measure displacement allows for model vs. measurement comparisons to be made. Figure **F-7** is an early model vs. measurement comparison made using pistonphone model 1, with the potentiometer displacement-sensor being used for a phase reference:

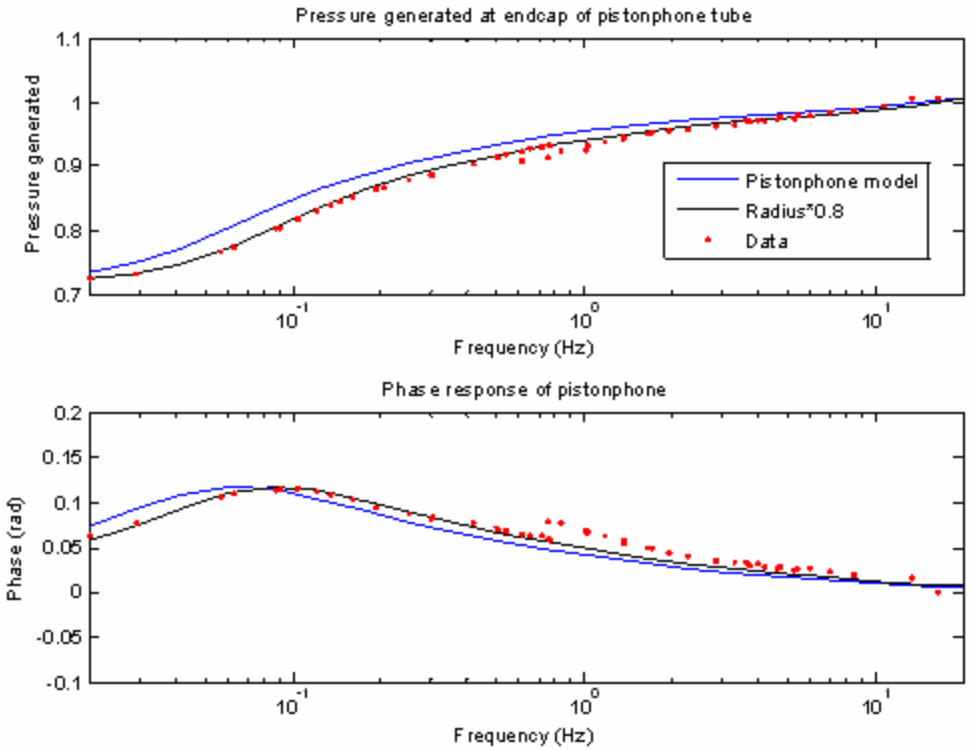

Figure **F-7**: Measurement of the pressure generated in the pistonphone for frequencies between 0.01 Hz, and 20 Hz. The pressure has been normalized by the adiabatic pressure response. The model is a prediction for the generated pressure accounting for thermo-viscous effects.

The measured values fall on a curve similar to that predicted by the pressure prediction model (developed in the next chapter); however, a much better curve fit is obtained by reducing the radius of the theoretical model by twenty percent. Reasons for this are not fully understood, however it is thought that discontinuities in the radius of the chamber may add more loss to the system than is being simulated by the theoretical model.

F.3 Enlarged chamber prototype (model 2)

During the summer of 2006, a request was made to calibrate four one-inch Larson-Davis measurement microphones below 30 Hz. The generated SPL of model 1 is far too high for the microphones, so model 2, the "Enlarged chamber prototype," was created by expanding the volume of the chamber. This is accomplished by fixing a coupler to the end of the main chamber of model 1, then adding a large four-inch

diameter chamber approximately five feet long to the end. A short length of 1 ¾ inch tubing is fixed to the end of this expansion chamber. This end tube is the location where microphones are immersed into the calibration sound field. Figure **F-8** is a top-view sketch of the expanded chamber version of the pistonphone, and Figure **F-9** is the cross section of the theoretical model used to calculate the response of the pistonphone tube.

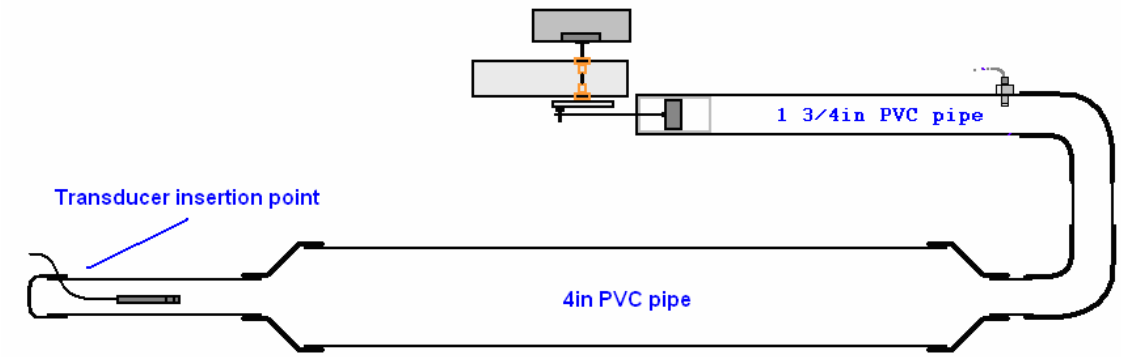

Figure **F-8**: Top view, expanded chamber prototype (model 2).

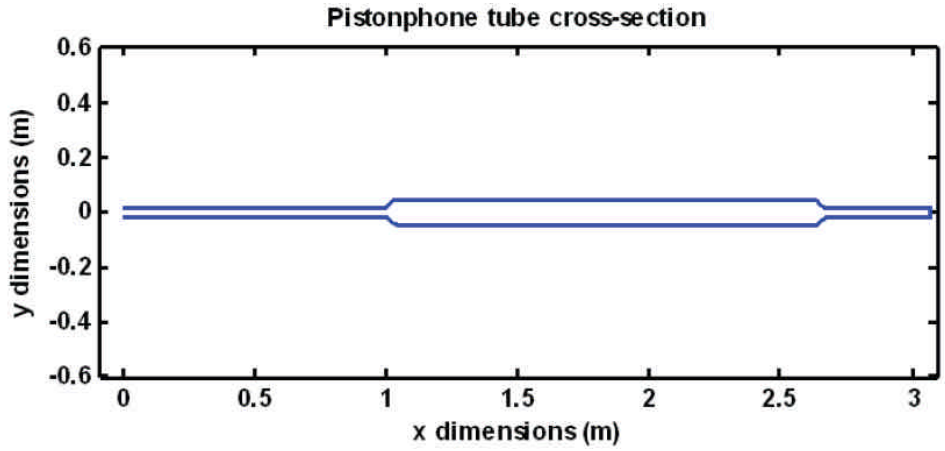

Figure **F-9**: Matlab generated cross section of theoretical model for the expanded chamber version of the pistonphone.

In the expanded chamber version of the pistonphone, all the PVC tubes extending past the model 1 chamber are sealed by vacuum grease. A large number of PVC pieces are joined together to make the chamber of this pistonphone prototype, and as a result a very large amount of vacuum grease is used to make it airtight. A major drawback of this design is the affinity for acquiring hard to locate leaks, and also that it is possible to get vacuum grease on an immersed transducer, potentially damaging the transducer.

This version of the pistonphone has the most convenient method for maintaining an air-tight seal around the cable of an inserted transducer. The end-cap has a notch cut in it, slightly smaller than the normal diameter of the transducer cable. A matched notch is cut into the end of the 1 ¾ inch PVC pipe mounted on the end of the chamber. The cable is fit into the notch in the PVC pipe. The end-cap is installed on the end of the pipe, sliding the cable into the notch on the end-cap, forming a complete seal, as shown in Figure **F-10**. The major problem with this method of sealing the cable is that it gets a small amount of vacuum grease on the cable. It is also possible to damage the cable by pressing the end-cap onto the pipe with too much force.

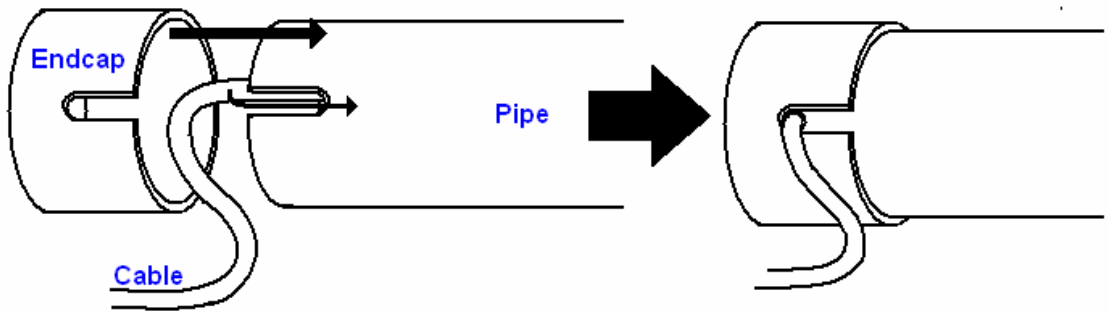

Figure **F-10**: Cable seal method used in the expanded chamber prototype of the pistonphone. The cable fits into notches cut into the end-cap and pipe. These notches close together, forming a complete seal around the cable.

The expansion of the chamber lowered the sound pressure level of the calibration signal to approximately 135 dB. The expanded chamber version of the pistonphone was used only briefly, for the sake of calibrating the Larson Davis microphones, and research was not focused on comparing the pressure response inside the pistonphone to the model for the pistonphone, because relative calibrations were being made. Figure **F-11** is a comparison of the pressure response inside the tube made at various frequencies, compared to the root-mean-square pressure predicted by the theoretical model:

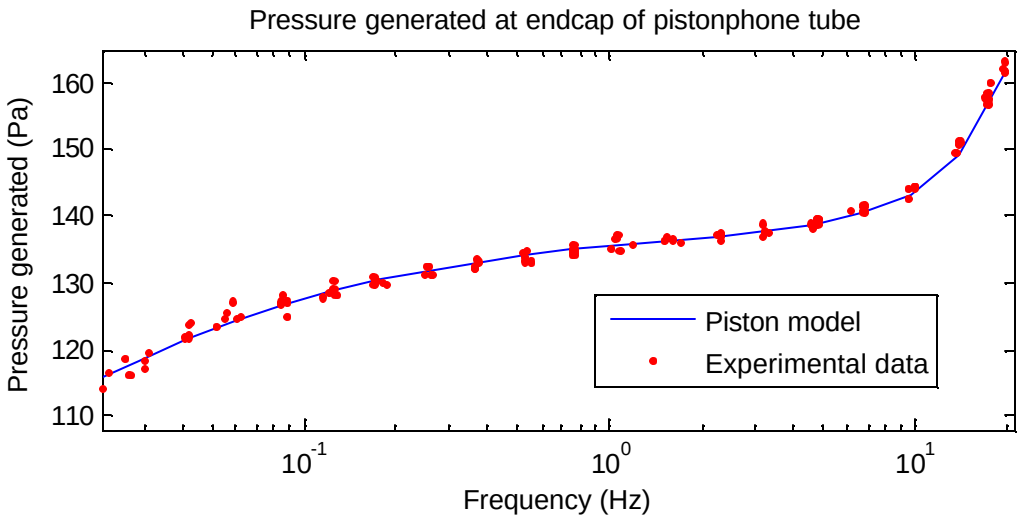

Figure **F-11**: Expanded chamber model pressure predictions vs. measurements.

A side-effect of lowering the pressure generated by the piston is that the loading on the motor is reduced. Reducing loading correspondingly decreases calibration signal distortion in regions where the motor has a low amount of torque. The absence of a discontinuity in the measured response near 1 Hz is a result of the lower distortion. Figure **F-12** is an example of a relative microphone calibration carried out with this pistonphone model.

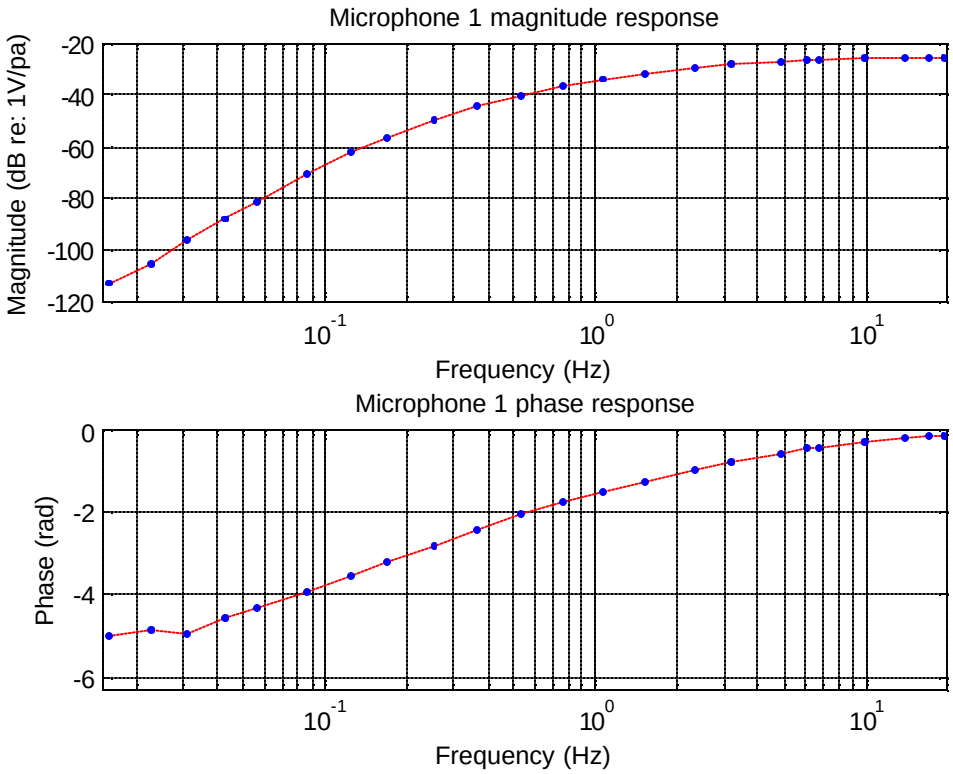

Figure **F-12**: Larson Davis microphone calibration example.

More details of the pistonphone, and further calibration examples are available in Appendix C of reference [**15**].

F.4 Schedule 80 prototype (mode 3)

Various problems with the initial and expanded chamber designs warrant a complete redesign of the pistonphone chamber. Keeping the pistonphone sealed and keeping the transducers free from vacuum grease are difficulties with model 2. Furthermore, various literature sources have indicated that unwanted loss can occur in pipe resonators when the pipe diameter changes too rapidly [**19**] [**14**]. The two cones used in the expanded chamber prototype are close to 60 degrees. The inconsistencies in the diameters of the schedule 40 pipe used to make the chambers prevented accurate volume estimations for the model used to predict the pressure response of the tube. A pistonphone with a more ideal chamber is desired.

The first major change in model 3 is that all the PVC tubing used in the previous models is replaced with a single 5 foot long segment of schedule 80 PVC pipe. Schedule

80 PVC is chosen for its more consistent inner diameter. Schedule 80 PVC has the added benefit of thicker side-walls and lower chamber wall compliance. Another change is that the large 1 ¾ inch piston and cylinder is replaced with a ¼ inch piston and cylinder, decreasing the calibration signal sound pressure level to approximately 112 dB. The calibration signal retains a high sound pressure level but remains below the 3% distortion limit of most measurement microphones. The driving method (motor, worm gear, axle) remains the same, but the total displacement of the piston is increased to 3.81 cm (1.5 inches) by changing the location where the piston shaft attaches to the rotating wheel.

To reduce the affect of losses associated with abrupt diameter changes in the pistonphone chamber, the piston cylinder is mounted to the chamber by means of a cone tapered at an 8 degree angle. The piston cylinder itself is flush mounted to the mouth of the cone via a PVC mount that is easily removable. A specialized plug at the opposite end of the chamber seals around cables for the insertion of transducers into the calibration signal pressure field. A drawback of the transducer insertion method used in this design, however, is that the hole for insertion is too small for transducers wider than one inch to fit through. Figure **F-13** is a cutaway showing the major features of the model 3 pistonphone design.

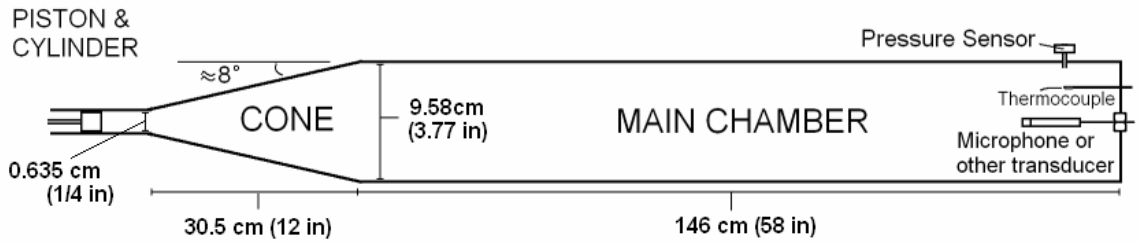

Figure **F-13**: Cross section of model 3 pistonphone. The main chamber is constructed from schedule 80 PVC.

Figure **F-14** and Figure **F-15** are photos of the cylinder mount at the front of the main-chamber, and the cable seal at the back of the main chamber.

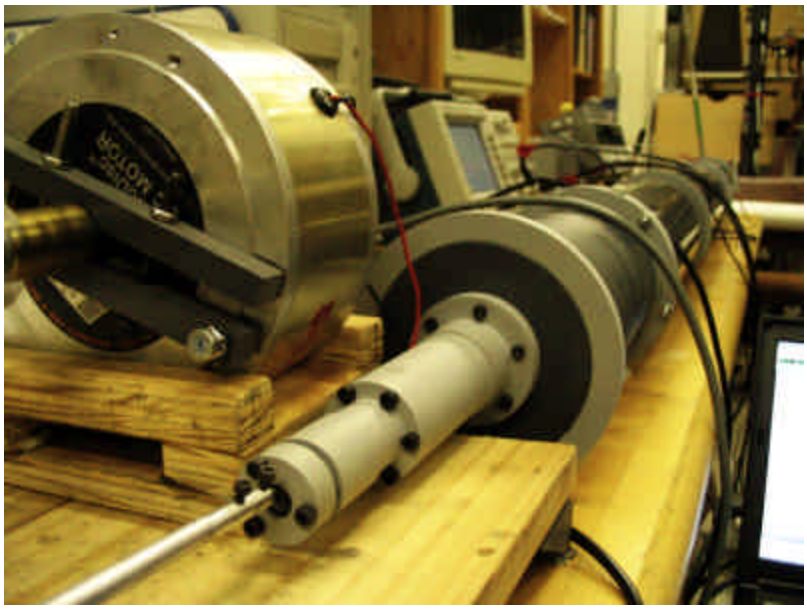

Figure **F-14**: The cylinder mount for the piston. Air-tightness is maintained by o-rings. The entire fixture is held together by screws and o-rings, and can be easily disassembled to replace the piston cylinder.

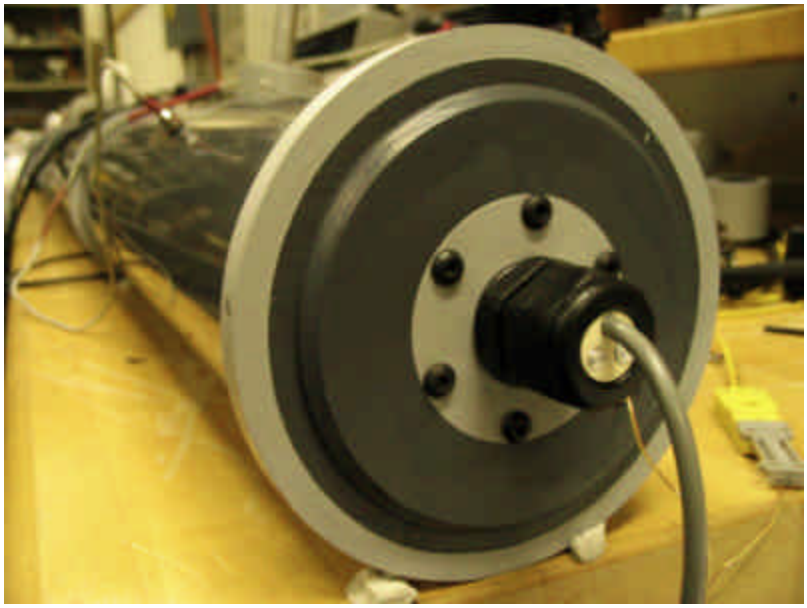

Figure **F-15**: Cable seal at the end of the pistonphone chamber. The plug can be removed and a microphone fit through a hole in the end-cap.

A major reason for redesigning the pistonphone chamber is to verify the thermoacoustic loss model used to predict calibration pressures inside the tube. The schedule 80 chamber has fewer discontinuities and minute deviations from the theoretical model used to calculate the pressure inside the main chamber due to motion of the piston.

Despite the upgraded chamber, good model verification measurements are still difficult to make, because the pressure transducers used to measure the calibration signal are externally vented to the laboratory. It is found using this pistonphone model that the ambient infrasonic noise in the laboratory is high enough to significantly increase measurement error. By taking enough measurements, however, a trend becomes visible, which can be used for comparison with the pistonphone model. Figure **F-16** is a plot of the pressure magnitudes produced in the tubes for a large number of frequencies between 0.02 and 20 Hz.

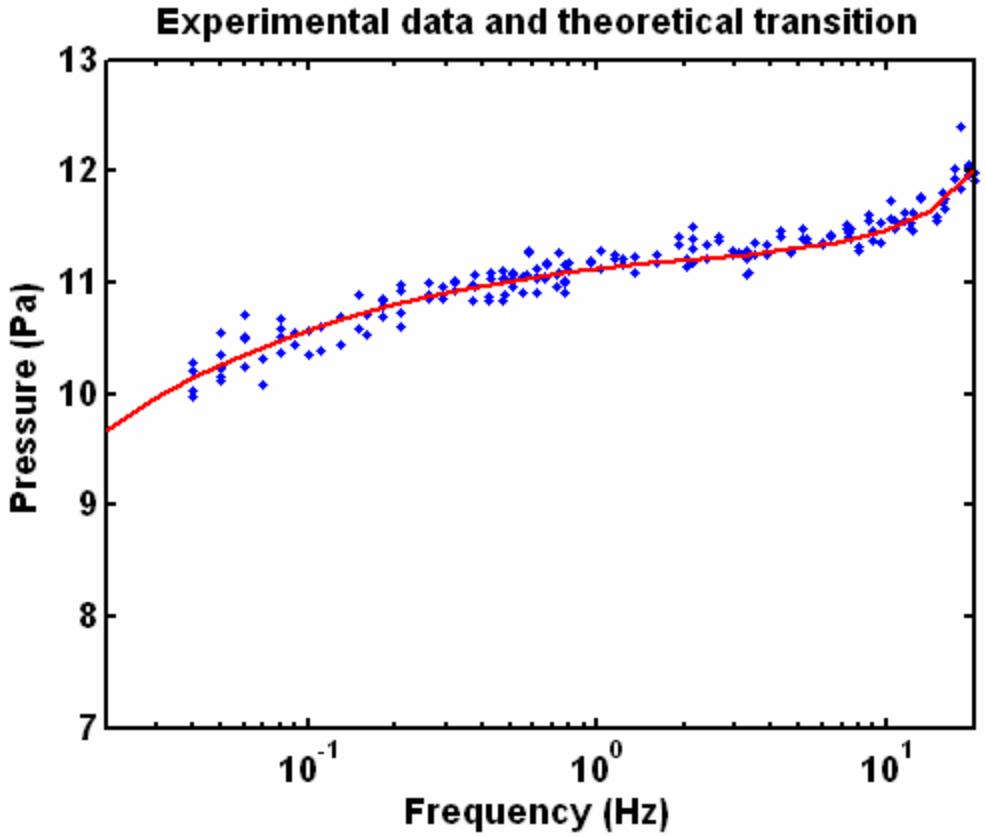

Figure **F-16**: Measured pressures vs. prediction curve, for the calibration signal generated inside the chamber of model 3.

All measurements in Figure **F-16** are recorded using a digital oscilloscope with a maximum recording length of 100 seconds. Increasing the record length of the signal decreases signal spread and improves the fit of the measurement to the curve. Figure **F-17** is an example of a measurement made using a Teac GX data acquisition system

instead of the oscilloscope. The longest recording taken with the GX for the measurements made in Figure **F-17** is 82 minutes.

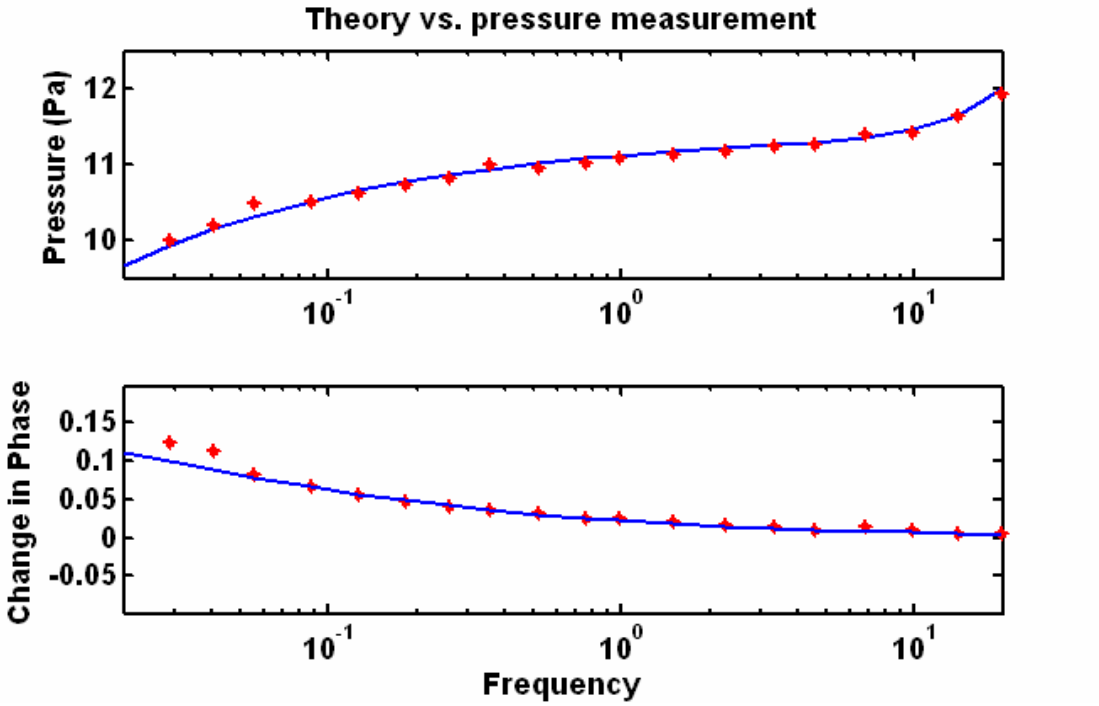

Figure **F-17**: Data points from 0.03 to 20 Hz, measured using a Teac Gx data acquisition system.

Model 3 is the first model that can be used to make a totally absolute, (i.e. free from the use of any reference pressure transducers) calibration of a transducer in the infrasonic frequency range. A ¼ inch B&K 4938 measurement microphone is placed in the calibration chamber and calibration values are measured for frequencies between 0.1 and 20 Hz. The sensitivities are calculated by comparing the voltage response of the microphone to the pressure generated by the pistonphone as predicted by the model based on thermoacoustic effects and precise measurements of the volume of the chamber. Figure **F-18** is a plot of the calibration:

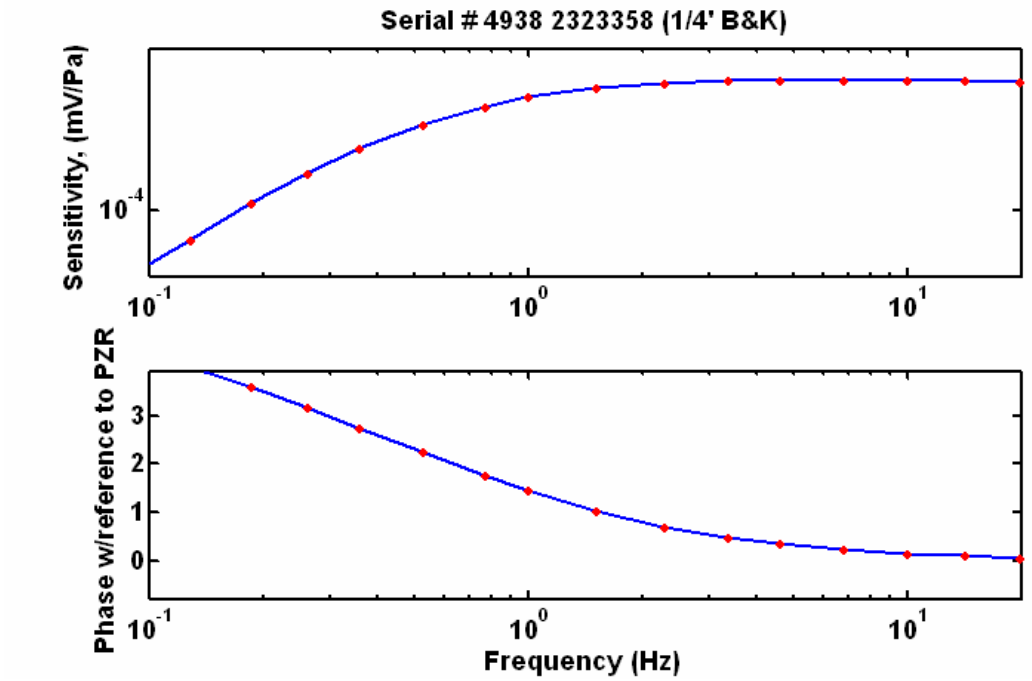

Figure **F-18**: Calibration chart for a ¼'' B&K microphone made using the model 3 pistonphone design and no reference (phase is with respect to piston displacement as measured by a cranked potentiometer).

The sensitivity at 20 Hz, based on the signal strength of the microphone and the calculated pressure inside the tube, is 2.24 mV/Pa. The sensitivity at 250 Hz as measured by a B&K type 4228 pistonphone is 2.29 mV/Pa. The 250 Hz B&K 4228 pistonphone sensitivity value and the 20 Hz low frequency pistonphone sensitivity value agree reasonably well. Numerous problems with the pistonphone still exist, however. The low signal level and high ambient noise make model verification measurements difficult. Furthermore, all the problems associated with the cranked potentiometer version of the displacement sensor still exist. The motor and gearing still add a huge amount of noise and wear on the system because of the mechanical vibration associated with the universal joints. It is nearly impossible to get speeds below 0.01 Hz with the 40:1 reducer, because the torque of the motor bottoms out. Finally, the SPL is too low, and does not take advantage of the full dynamic range of many measurement microphones. A large number of key additional upgrades are made in the final version of the pistonphone, described in Chapter **2**.

Appendix G

Pistonphone operation: step-by-step

G.1 Operation outline

An overview of the process used to measure the absolute pressure inside the pistonphone chamber is given in this section. The following is a step-by-step method for the measurement of pressures inside the pistonphone chamber.

1) Chamber and seal check.
2) Data-acquisition setup.
3) *Low – low* frequency gear assembly and check.
4) Environment measurements.
5) Lowest frequency sweep (0.001 to 0.087 Hz).
6) *Low – medium* gear assembly and check.
7) Environment measurements.
8) *Low – medium* frequency sweep (0.087 to 0.257 Hz).
9) Disassemble worm-gear, install *low – direct* connections.
10) *Low – direct* frequency sweep (0.257 to 3.5 Hz).
11) *Direct connection* assembly and check.
12) *Direct connection* frequency sweep (3.5 Hz to 30 Hz).

Each of these steps will be described in this section.

G.1.1 Chamber and seal check

This step ensures that the pistonphone looks as similar to the theoretical model as possible, by checking for leaks and eliminating foreign objects in the pistonphone chamber.

The first step in a pressure measurement is to inspect the chamber for any objects or transducers which may have been left in the chamber from recent calibrations. Most transducers are small enough that they would have an insignificant affect on the volume of the chamber; however, some can have a measurable affect on the pressure response. An infrasonic microphone such as the one described in Appendix **E** is an example of a

transducer that is large enough to affect the pressure response. If it is known that there is no such object in the chamber, then this step may be omitted.

A seal check is also completed. The screws holding the transducer insertion plug are checked for tightness, as are the screws mounting the LVDT to the cone. The screws holding the cone to the main-chamber are checked if the cone has been removed recently. If an Endevco pressure sensor is mounted on the side of the chamber, the tightness of this pressure sensor's installation into the side of the chamber is checked as well.

G.1.2 Data acquisition setup

The data-acquisition system used to gather all the data in this thesis is a TEAC GX 16-channel 16-bit recorder. Using the steps appropriate for the GX recorder, the GX and the computer used for storing the data are turned on, the appropriate channels are powered, and the recording parameters are set.

In the currently used setup, three transducers are used in the recording process: a 15 PSI Endevco sensor, (channel 1), a ~1 PSI omega PX differential transducer vented to the control chamber (channel 2), and the LVDT (channel 3). The output of the amplifiers powering each of the transducers are fed to both a Tektronix oscilloscope (for monitoring the signal), and Channels 1-3 on the TEAC GX recorder. The standard sample rate used for all the following pistonphone measurements is 200 Hz, with an incorporated 80 Hz 8^{th} order Butterworth filter at the front end serving as the anti-aliasing filter. The voltage range of the Endevco channel (channel 1) is +/- 0.5 volts, for the PX it is +/- 5 volts, and for the LVDT it is +/- 2 volts. Occasionally an external barometric pressure sensor made from a 5 PSI piezo-resistive sensor with no vent is used to measure ambient pressure. In such cases, the 4^{th} channel is used and the voltage range is set to +/- 0.5 volts.

G.1.3 Low-low gear assembly and check

The lowest frequency range (0.001 to 0.087 Hz) is swept by using the lowest possible gearing configuration. The lowest gearing configuration is set up by engaging the worm gear and using the highest reduction ratio with the cog/timing gear reducer. The worm-gear is engaged or removed using the 4 screws on the aluminum post mounted to the axle block. It is advisable to never disengage the worm gear by removing the worm-gear from the u-shaped aluminum fixture it is mounted in, because of inconsistent performance when re-assembled. When the worm gear and the cog mounted to the axle are appropriately meshed, the four screw-holes on the u-shaped worm-gear mount and the four screw holes on the post mounted to the axle block will line up. Figure **G-1** and Figure **G-2** illustrate the removal and installation process of the worm-gear.

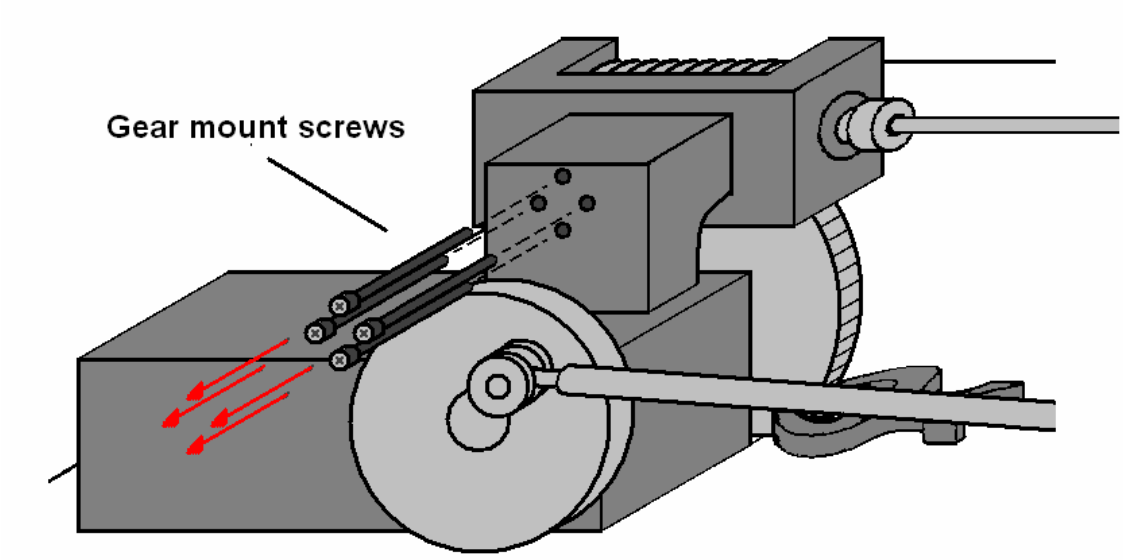

Figure **G-1**: Illustration of gear setup and screws used to fix the worm gear in place.

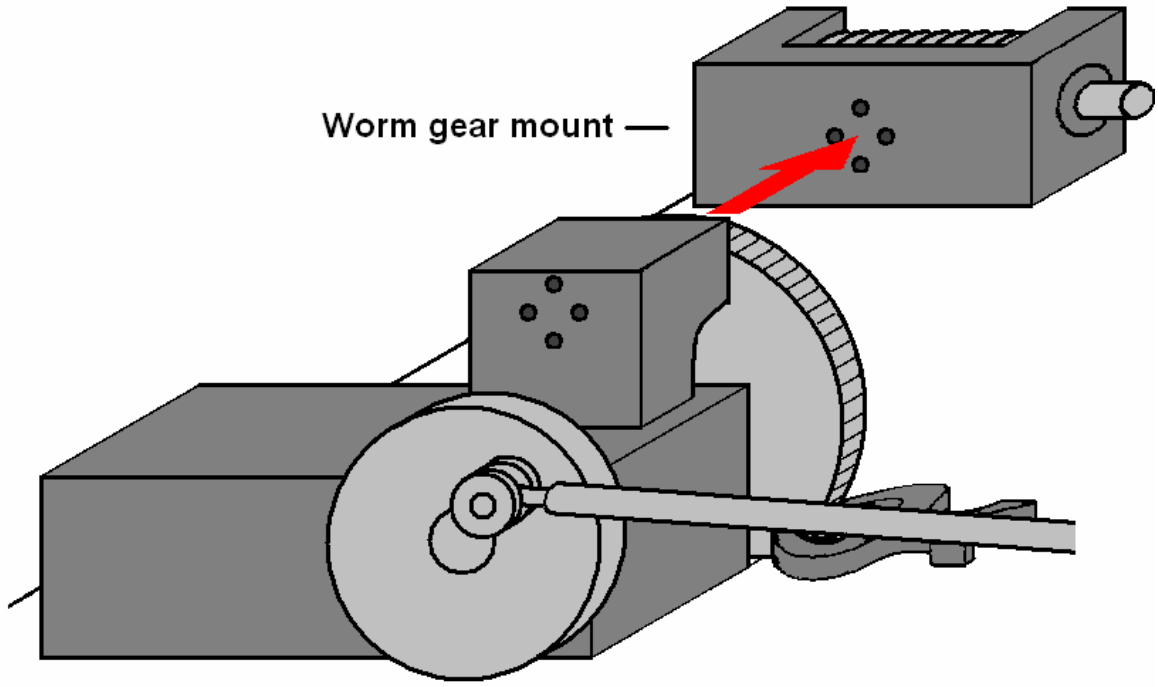

Figure **G-2**: Removing the worm-gear mount, after the screws have been removed.

The shaft of the worm-gear is attached to the timing belt reducer via a six-inch segment of vacuum hose and two hose clamps. The vacuum hose is used because precise alignment of the hose and reducer shaft axis and worm-gear shaft axis is not necessary. A small amount of vibration isolation is also achieved using this configuration. The vacuum hose has enough curvature that some unnecessary vibration is added to the system when the hose spins, and this represents a potential area of improvement.

The reducer has three shafts, and two cog-reduction wheels. The highest reduction ratio achievable is approximately 1:10 if both cogs are used. The worm-gear is attached via the vacuum hose to the shaft giving the highest reduction. The motor is connected to the input of the reducer via a six inch segment of stiff wire. The wire is stiff to a torque but limp to flexural forces and similar to the vacuum hose provides a degree of isolation between the motor and the gear reducer. Using a wire instead of two universal joints significantly reduces the mount of vibration noise at high rotations-per-minute. The wire has a copper core, and has a finite life span. When the wire eventually snaps, a new segment of wire may be trimmed and placed into the shaft-wire couplers at either end of the wire. A final measure used to lower excess vibration is the placement of a large bronze weight on the base of the reducer. Figure **G-3** shows the reducer:

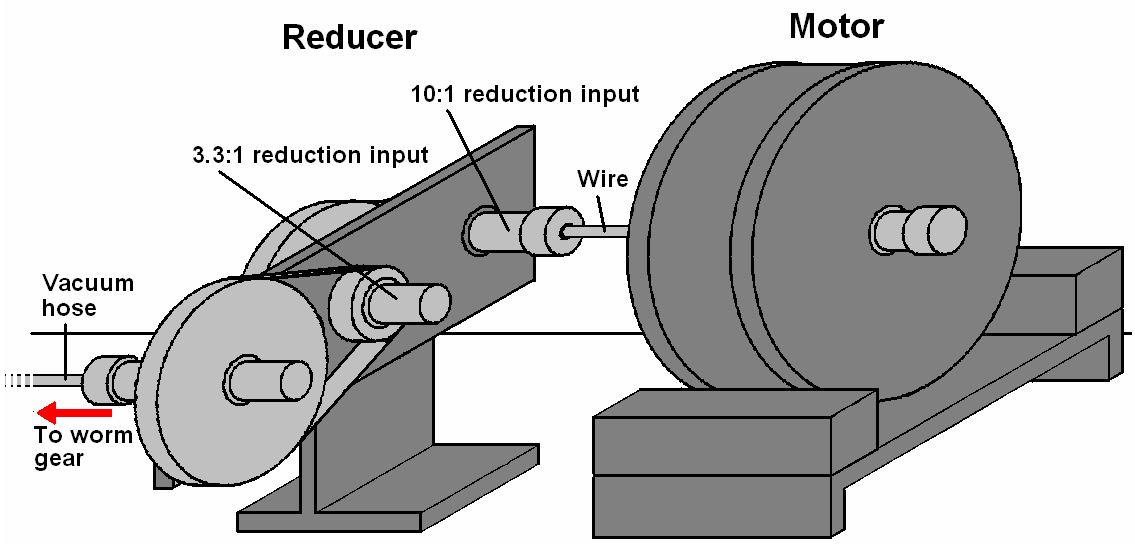

Figure **G-3**: Illustration of the motor and reducer, with the two reduction ratio inputs labeled. The bronze weight is omitted from the illustration.

When the low-low gearing has been assembled, the motor is connected to the DC power-supply. Two DC power-supplies are available for use with the motor: a manual 0-36 volt DC source, and a LabVIEW™ controlled DC source that automatically inputs a pre-set voltage sweep. To test the gearing configuration for problems, the manual 0-36 volt source is used. The motor is swept to its highest frequency, and the output of the oscilloscope screen and data-acquisition software are examined, to check the operation of all the transducers.

The direction of rotation of the motor is important to the operation of the pistonphone. The axis of the wheel that drives the piston shaft, and the piston shaft are not on the same elevation plane. The wheel must always turn counter-clockwise, so that at the low-point of the cycle the piston is experiencing an in-stroke rather than an outstroke. If the wheel is turning clockwise, the in-stroke occurs when the shaft connected to the wheel and the piston shaft are farthest from parallel, resulting in an unwanted force on the LVDT fixture. This problem is most significant at high frequencies, but consistency throughout the measurement is desirable. To have the correct polarity when operating the pistonphone, the red lead from the motor should be connected to the positive terminal of the DC source, and the black lead should be connected to the negative terminal. When the motor is directly connected to the wheel axle and the worm gear is disengaged, the black lead should be connected to the positive terminal and the red should be connected to the negative, reversing the polarity.

Once the polarity has been checked, the leads are connected to the LabVIEW™ controlled voltage supply rather than the manual supply. This allows for hands-free operation during the measurement. The equation governing the voltage sweep may be modified using the LabVIEW™ controller constructed for this operation. In the measurements made in this thesis the frequency is swept from low to high.

The final step is to adjust the screw on the resistance-clamp on the cog attached to the worm gear. A nut and bolt keep the clamp from tightening on the sides of the cog under normal circumstances, but when the worm-gear is engaged the nut may be loosened, allowing the clamp to tighten on the sides of the cog like a disk-brake. This provides a constant resistance for the motor to work against, which reduces unwanted vibration noise, and prevents the worm gear from shifting in its mount. Figure **G-4** shows the brake in its clamped and unclamped configurations.

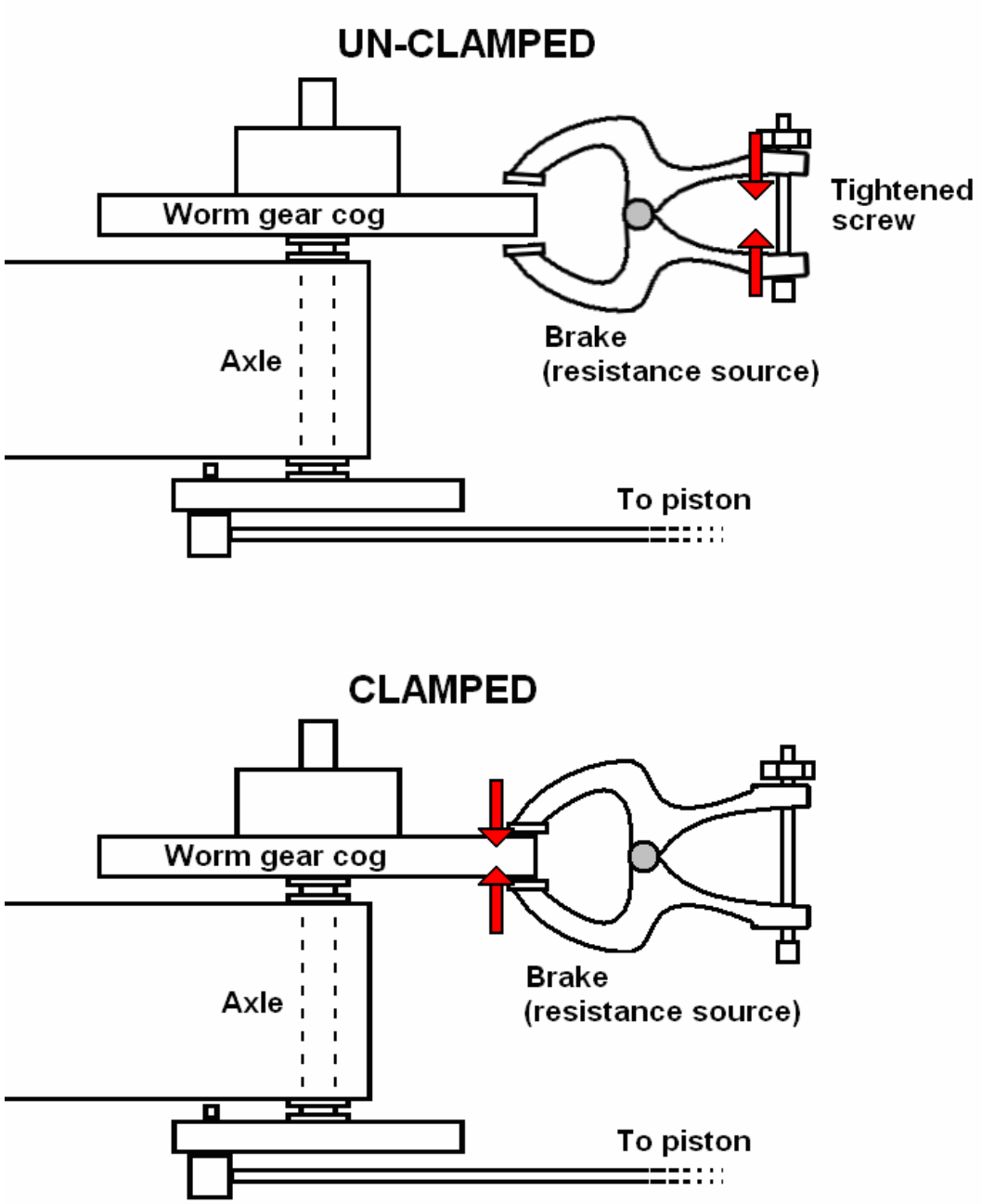

Figure **G-4**: Top view of the constant resistance source in clamped and unclamped configuration. When the screw is tightened, the pads are held away from the worm-gear cog. When the screw is loosened, a spring tightens the pads onto the sides of the cog.

Important: As shown in Figure **G-5**, a collar is mounted on the shaft of the piston, so that when the piston is placed under vacuum for purposes of replacing the gas, the piston does not get sucked through the cylinder and into the chamber. When hooking

up the piston shaft to the axle, it is imperative that the collar be spaced far enough away from the LVDT mount that it never touches the mount during an entire cycle of piston rotation. If this is not the case, the LVDT and glass piston cylinder may be destroyed by the collar.

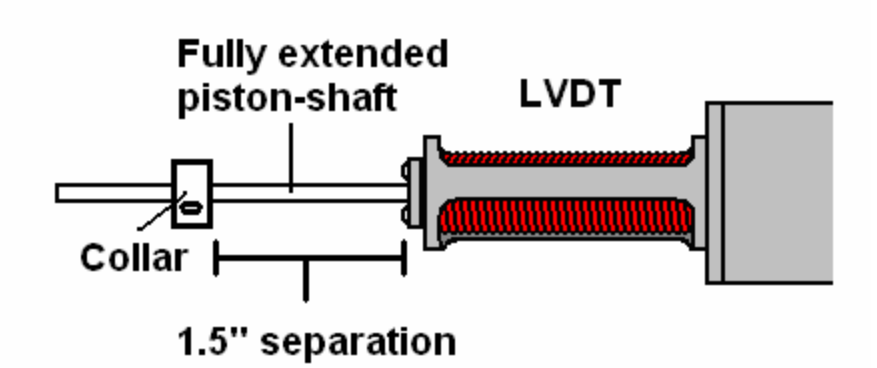

Figure **G-5**: The collar fixed to the piston shaft prevents the piston from being pulled out of the cylinder under vacuum. The collar must be farther from the front of the LVDT than the swing of the piston, but close enough that the piston head is still inside the cylinder when the collar is forced against the face of the LVDT.

G.1.4 Environmental measurements

Immediately prior to pistonphone operation the ambient pressure, temperature, and humidity are measured. Temperature is important because it can change gas parameters and in conjunction with a relative humidity measurement allows for the calculation of absolute humidity. Humidity has an unknown affect on the adiabatic-isothermal transition, and is recorded to allow for compensation in the event that an effect is discovered. Ambient pressure is measured, because it is directly proportional to the pressure generated inside the pistonphone chamber by the change in volume. The ambient pressure in the State College region is generally around 975 mBar, and has been observed by the author, to vary by +/-15 mBar. Not correcting for the ambient pressure can result in nearly 2% additional error in the calibration process, and is the most important environmental parameter to measure before making pressure measurements.

G.1.5 Lowest frequency sweep

Once the environmental conditions have been measured, a labVIEW™ controller is used to start the frequency sweep, and the TEAC™ data-acquisition recording function is started. The LabVIEW™ software allows for a frequency sweep that is quadratic, linear, or exponential. It is found that at very low frequencies the function $V = 0.97 + 0.1\exp(0.0006*t)$, where t equals 0 to 10,000 seconds, returns very good results. This equation may be adjusted, however, for any time-constraints placed on the measurement. In general, the longer the sweep time the better the results at very low frequencies. A long sweep time, however, can also result in changing barometric pressure, which is another source of measurement error. If the sweep-times are long enough, it is necessary to include the barometric-pressure sensor output in the data-acquisition system in channel 4. This allows for continual atmospheric correction during the final data processing.

G.1.6 Environment measurements

Temperature, humidity, and barometric pressure are recorded, again.

G.1.7 *Low-medium* gear assembly and sweep

After the low frequency sweep has finished, the TEAC recording software must be stopped and the data saved. The same recording settings are used for the next sweep. The vacuum hose is disconnected from the 10:1 reducer output, and reconnected to 3.3:1 reducer output. An 11 Volt signal across the leads of the motor will result in a starting frequency roughly equivalent to the maximum frequency achieved in the lowest gearing configuration. It is found that the following equation, implemented via the labVIEW™ controller, resulted in a successful sweep for the *low – medium* gearing configuration: $11 + 0.1*\exp(0.0057*t)$ for $t = 0$ to 1000 seconds. In this frequency sweep, the pressure response between 0.08 and 0.26 Hz is measured.

G.1.8 Disassembling the worm gear, and configuring the *low-direct* connection

The worm-gear assembly must be detached, as shown in Figure **G-2**, to sweep across the next frequency range. The reducer is disconnected from the worm-gear by unfastening the hose-clamps and removing the six-inch segment of vacuum hose. The motor is not detached from the timing-gear reducer, however. The four screws used to hold the worm-gear mount to the post on the axle block are unfastened, and the worm-

gear mount and worm-gear are removed. The motor and axis are re-located so that the 1:10 output of the reducer is on-axis with the axle in the aluminum axle block. A foot long piece of vacuum hose is used to connect the output of the reducer directly to the axel, in this configuration. An aluminum rod has been placed inside the vacuum hose to reduce curvature and unwanted vibrations. Figure **G-6** shows the *low-direct* gearing configuration from a top view.

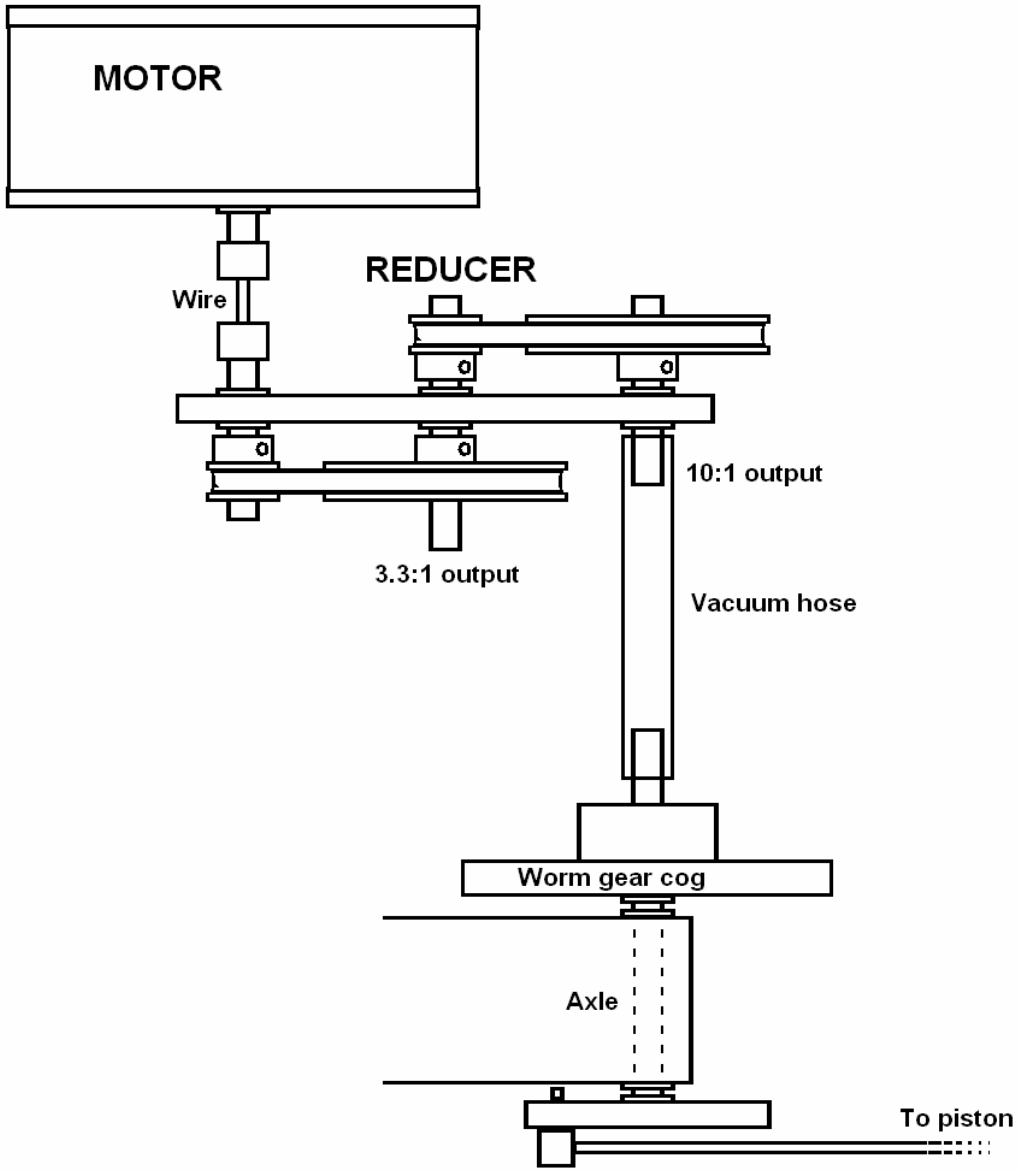

Figure **G-6**: Top view of *low-direct* gearing configuration. The worm-gear has been removed, and the output of the reducer is connected via a vacuum hose directly to the axle. The hose is fixed to the shafts by un-pictured hose clamps. In this configuration, the resistance-clamp is opened so that no resistance is placed on the worm-gear cog.

The resistance clamp that was tightened on the cog must be loosened, or the vacuum hose will be damaged. Lastly, the polarity of the motor leads must be switched, so that the wheel turns counter-clockwise.

G.1.9 *Low-direct* frequency sweep

The TEAC software is started using the same recording parameters as before. The environmental conditions do not have to be recorded before this measurement because the time between when this measurement is taken and the last environmental measurement recording is short enough that no significant change normally occurs. The range of frequencies over which this gearing configuration can sweep is 0.25 to 3.5 Hz. The manual power-supply is used instead of the labVIEW™ software in this case because the sweep time is small (generally on the order of 3 minutes). The sweep is completed by slowly turning the knob of the manual power supply. The LabVIEW™ software can be used instead, if desired.

G.1.10 Direct connect assembly and sweep

The final configuration is to connect the motor directly to the axle, with no gear reduction. This is done by attaching the vacuum hose directly to the shaft on the reducer to which the motor is connected, as shown Figure **G-7**:

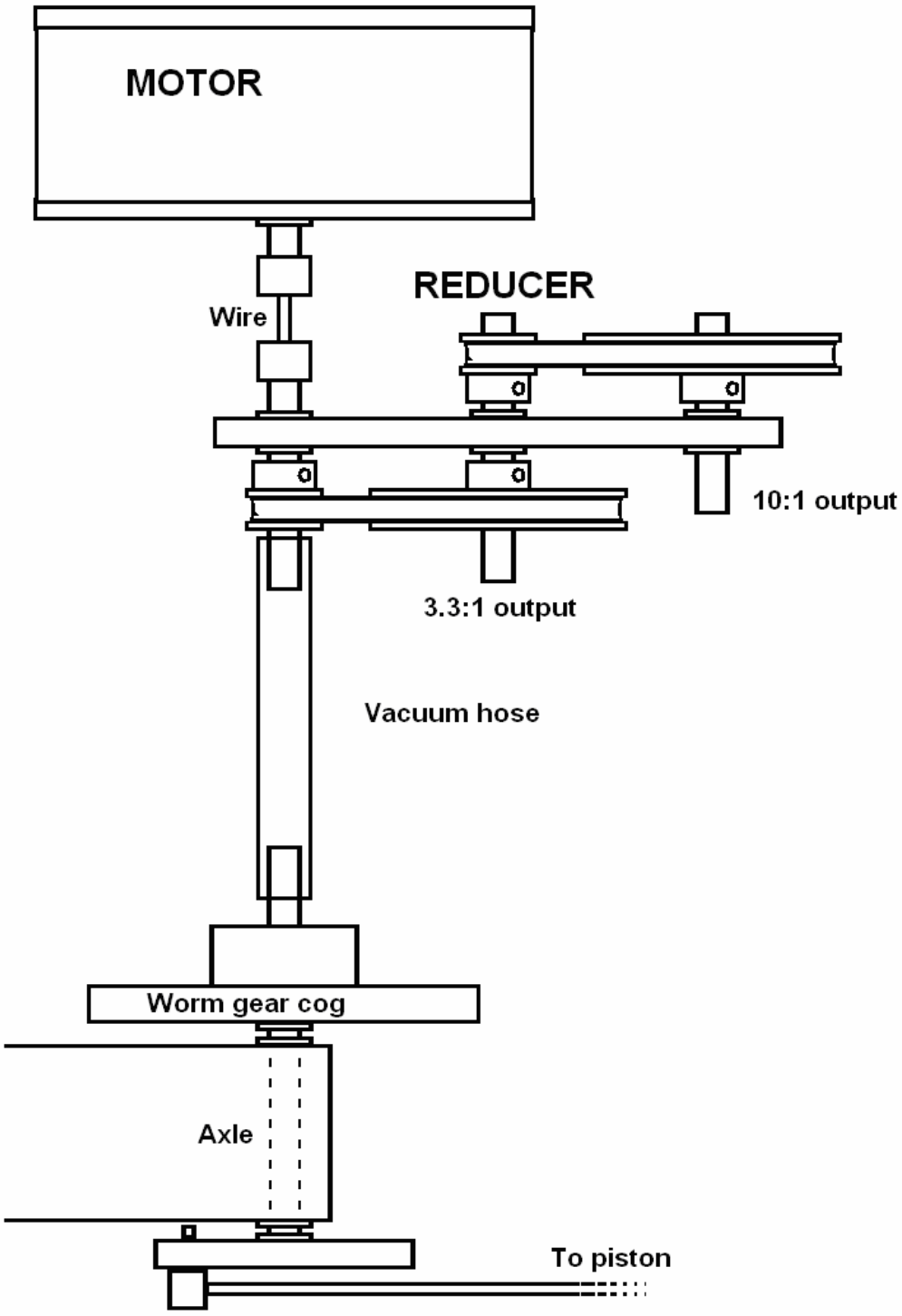

Figure **G-7**: Direct connection configuration, top view

This configuration can be used to measure 3.5 Hz to 30 Hz. At 30 Hz the mechanical pieces are being strained, and damage to the pistonphone may occur if a piece fails. For this reason, it is best not to leave the pistonphone operating at high frequencies for more than a couple seconds. Many upper-harmonics are visible on the oscilloscope screen, indicating that the piston motion has an excess of unwanted vibrations. This is an area for potential improvement, however, the measurement remains fairly clean because of the simultaneous displacement measurement.

Appendix H

Temperature profile derivation for a gas filled cylinder of finite thickness

The calculation of the thermal profile begins by assuming a pipe with the cross section shown in Figure **H-1**:

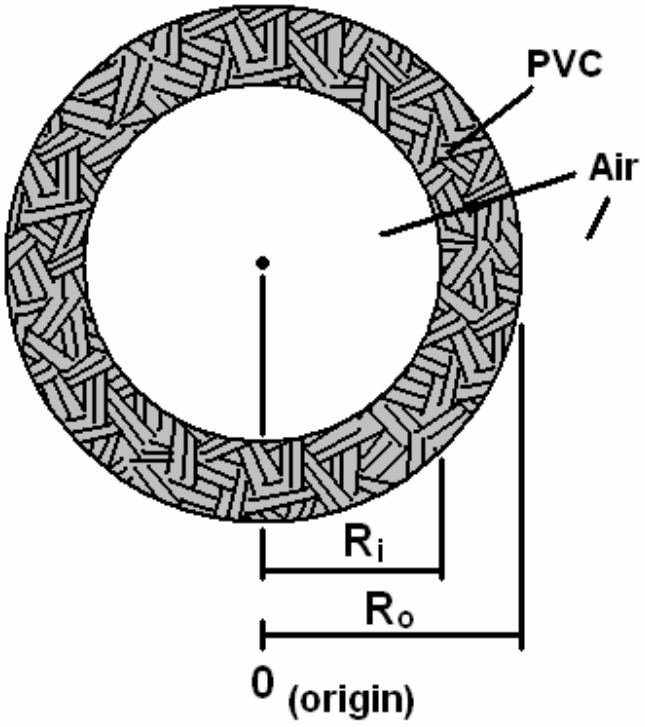

Figure **H-1**: Finite thickness PVC cylinder cross section with inner radius *Ri* and outer radius *Ro.* The outer boundary is considered to be insulated.

The heat equation for the pipe is: Eq. **H.1**

$$\frac{dT_s}{dt} = k_s \nabla^2 T_s \qquad \textbf{H.1}$$

T_s is the temperature in the solid, k_s is thermal diffusivity, and the Laplacian in cylindrical coordinates is:

$$\nabla^2_{cyl} T = \frac{d^2T}{dr^2} + \frac{1}{r}\frac{dT}{dr} + \frac{1}{r^2}\frac{d^2T}{dq} + \frac{d^2T}{dz^2}$$

In this scenario the temperature has no *z* or *?* dependence, and the equation reduces to:

$$\nabla^2_{cyl} T = \frac{d^2T}{dr^2} + \frac{1}{r}\frac{dT}{dr}$$

The temperature oscillations in Eq. **H.1** are time harmonic, and the time derivative may be replaced with *j?* :

$$k_s\left(T'' + \frac{1}{r}T'\right) = jwT$$

$$\downarrow$$

$$T'' + \frac{1}{r}T' - \frac{jwT}{k_s} = 0$$

The equation can be written in terms of the penetration depth, $d_k = \sqrt{2k/w}$:

$$\frac{jw}{k_s} = \frac{1}{\frac{k_s}{jw}} = \frac{1}{\left(\sqrt{\frac{k_s}{jw}}\right)\left(\sqrt{\frac{k_s}{jw}}\right)}$$

$$\frac{1}{\left(\sqrt{\frac{k_s}{jw}}\right)\left(\sqrt{\frac{k_s}{jw}}\right)} = \frac{1}{\left(\frac{1}{(1+i)^2}\right)\left(\sqrt{\frac{2k_s}{w}}\right)\left(\sqrt{\frac{2k_s}{w}}\right)}$$

$$= \frac{(1+i)^2}{d_{ks}^2} = M^2$$

$$T'' + \frac{1}{r}T' - M^2T = 0$$

$$\downarrow$$

$$r^2T'' + rT' - M^2r^2T = 0 \qquad \textbf{H.2}$$

Eq. **H.2** above is similar to the differential equation for a Bessel function, except that the sign in front of M^2 is negative instead of positive. The solution to the equation

takes the form of "modified" Bessel functions, denoted *I* and *K* for types one and two. A general solution for equation **H.2** is:

$$T_s = AI_o(Mr) + BK_o(Mr)$$

To solve for the unknown coefficients, boundary conditions are needed. The air surrounding the pistonphone on the outside acts as an insulator. From Hayek [**10**], the boundary condition for an insulating interface is that the spatial derivative of the temperature at the surface of the boundary is zero:

$$\text{B.C. \#1} = \left.\frac{dT}{dr}\right|_{r_0} = 0$$

Useful for calculating the derivatives of modified Bessel functions are their recursion formulae:

$$I'_P = I_{P+1} + \frac{P}{x} I_P$$

$$K'_p = -K_{P+1} + \frac{P}{x} K_P$$

Applying B.C. #1 to the solution…

$$\left.\frac{dT}{dr}\right|_{r_0} = AMI_1(Mr_o) - BMK_1(Mr_0) = 0$$

The second boundary condition is that the temperature on the inside surface of the tube is T_{b1}, which will be left as a variable at present.

$$\text{B.C. \#2} = T\big|_{r_i} = AI_0(Mr_i) - BK_o(Mr_i) = T_{b1}$$

Using B.C. #1, constant *A* can be solved for in terms of *B*:

$$A = \frac{K_1(Mr_0)}{I_1(Mr_o)} B$$

This can be substituted back into B.C. #2, and the two constants *A* and *B* can be calculated in terms of T_{b1} :

$$B\frac{K_1(Mr_0)}{I_1(Mr_o)}I_0(Mr_i)+BK_o(Mr_i)=T_{b1}$$

$$B\left(\frac{K_1(Mr_0)}{I_1(Mr_o)}I_0(Mr_i)+K_o(Mr_i)\right)=T_{b1}$$

$$B=\frac{T_{b1}}{\left(\frac{K_1(Mr_0)}{I_1(Mr_o)}I_0(Mr_i)+K_o(Mr_i)\right)}$$

$$B=\frac{T_{b1}I_1(Mr_o)}{(K_1(Mr_0)I_0(Mr_i)+K_o(Mr_i)I_1(Mr_o))}$$

$$A=\left(\frac{K_1(Mr_0)}{I_1(Mr_o)}\right)*B$$

$$A=\frac{T_{b1}K_1(Mr_o)}{(K_1(Mr_0)I_0(Mr_i)+K_o(Mr_i)I_1(Mr_o))}$$

At this point, the temperature in the solid can be found as a function of r and the oscillatory boundary temperature T_{b1}, by substituting the values found for A and B into the general solution:

$$T_s=\frac{T_{b1}K_1(Mr_o)I_o(Mr)}{(K_1(Mr_0)I_0(Mr_i)+K_o(Mr_i)I_1(Mr_o))}+\frac{T_{b1}I_1(Mr_o)K_o(Mr)}{(K_1(Mr_0)I_0(Mr_i)+K_o(Mr_i)I_1(Mr_o))}$$

$$T_s=T_{b1}\frac{K_1(Mr_o)I_0(Mr)+I_1(Mr_o)K_0(Mr)}{K_1(Mr_o)I_0(Mr_i)+I_1(Mr_o)K_0(Mr_i)} \qquad \textbf{H.3}$$

Eq. **H.3** is not yet solvable because T_{b1} remains unknown. This equation can, however, be used to plot the temperature profile through the cylinder wall with respect to T_{b1}. Figure **H-2** is a plot of the temperature profile of the cylinder with a thickness of 0.37 inches, assuming that the cylinder is insulated on the outside:

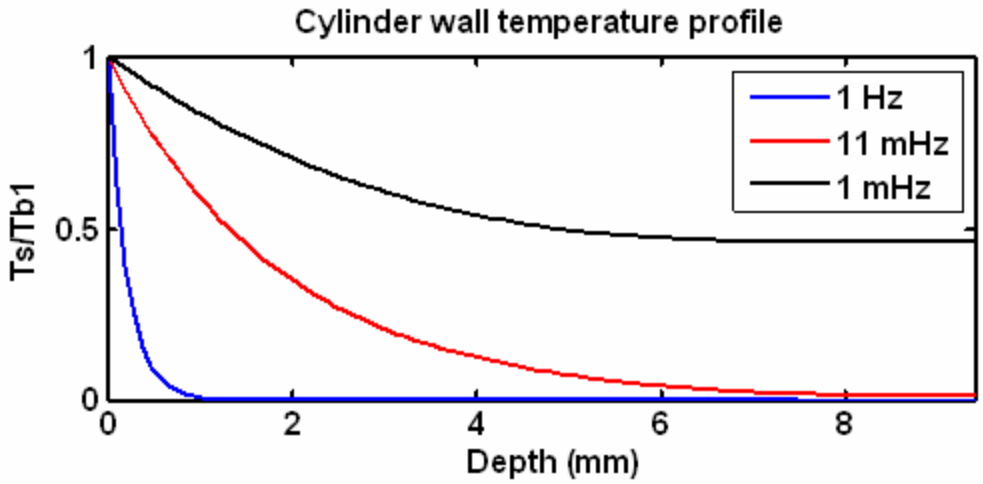

Figure **H-2**: This graph shows the temperature profile of the cylinder from the inner surface to the outer surface for three frequencies. The maximum discrepancy in the model and measurement comparisons in the pistonphone occurs around 10 mHz, but at this point the temperature at the outer boundary is roughly 1.5% the temperature of the inner boundary.

Notice that, while the thermal-penetration depth is less than the thickness of the PVC tube at 0.001 Hz the temperature fluctuations at the outside of the wall are almost half the value of the temperature fluctuations at the inner surface.

T_{b1} remains unknown, and to solve for this quantity the heat equation is applied to the air in the center of the tube. Eq. **H.4** can be found in the appendix of Swift [**20**]:

$$r T_m \left(\frac{\partial s}{\partial t} + V \bullet \nabla S \right) = k \nabla^2 T_s \qquad \textbf{H.4}$$

Variable k in Eq. **H.4** is thermal conductivity. In the region of interest the volume velocity at all locations in the pistonphone is small enough that the velocity term can be neglected. Substituting $ds = \left(\frac{C_p}{T_m} \right) dT - \left(\frac{b}{r} \right) dp$ the equation becomes:

$$r T_m \left(\frac{C_p}{T_m} \frac{\partial T}{\partial t} - \frac{b}{r} \frac{\partial p}{\partial t} \right) = k \nabla^2 T_s$$

$$r C_p (iw) T - T_m b (iw) p = k \nabla^2 T_s$$

Writing out the cylindrical Laplacian assuming no variations in the ? and z directions:

$$kT'' + \frac{k}{r}T' - rC_p(iw)T = -T_m b(iw)p$$

$$\downarrow$$

$$r^2T'' + rT' - r^2\frac{rC_p(iw)}{k}T + \frac{r^2T_m b(iw)p}{k} = 0$$

$$\downarrow$$

$$r^2T'' + rT' - r^2\left(\frac{T_m b(iw)p}{k} - \frac{rC_p(iw)}{k}T\right) = 0$$

The above equation can be solved using modified Bessel functions, and has the general solution:

$$T = AI_0(Mr) + BK_0(Mr) + C \qquad \textbf{H.5}$$

As in the wall temperature profile derivation, M is a symbol representing $\sqrt{\frac{iw}{k}}$, or $\sqrt{\frac{iwrC_p}{k}}$ when thermal conductivity is used in place of thermal diffusivity.

The particular solution can be found by assuming the solution is a constant, C. The first and second derivatives reduce to zero, and the following relationship can be used to solve for C:

$$-r^2\frac{T_m b(iw)p}{k} = -r^2\frac{rC_p(iw)}{k}T$$

Substituting C for T, and canceling the common terms:

$$-r^2\frac{T_m b(iw)p}{k} = -r^2\frac{rC_p(iw)}{k}C$$

$$\downarrow$$

$$T_m bp = rC_p C$$

$$C = \frac{T_m bp}{rC_p}$$

This particular solution is inserted into the general solution. This particular solution is used in conjunction with the cylinder wall temperature profile to solve for T_{b1}.

Three boundary conditions exist for equation Eq. **H.5**: 1) The spatial derivative of the temperature in the radial direction is zero at the origin, 2) the temperature flux through the wall is conserved, and 3) the temperature at the surface of the wall is $T_{b1,}$ as previously defined.

$$\text{B.C. \#1: } \left.\frac{\partial T}{\partial r}\right|_0 = 0$$

$$\text{B.C. \#2: } k\left.\frac{\partial T}{\partial r}\right|_{r_i} = k_s \left.\frac{\partial T_s}{\partial r}\right|_{r_i}$$

$$\text{B.C.\#3: } T\big|_{r_i} = T_{b1} = AI_0(Mr_i) + BK_0(Mr_i) + \frac{bT_m p_{acs}}{r_m C_p}$$

From boundary condition #1, the derivative of the temperature gradient at the center is zero. K_1 is non-zero at $r = 0$, therefore $B = 0$. Boundary condition #2 may be used to relate the temperature profile in the cylinder wall to the gas:

$$k\left.\frac{\partial T}{\partial r}\right|_{r_i} = AkMI_1(Mr_i)$$

$$k\left.\frac{\partial T}{\partial r}\right|_{r_i} = T_{b1} M_s k_s \frac{K_1(Mr_o)I_1(Mr_i) + I_1(Mr_o)K_1(Mr_i)}{K_1(Mr_o)I_0(Mr_i) + I_1(Mr_o)K_0(Mr_i)}$$

$$AkMI_1(Mr_i) = T_{b1} M_s k_s \frac{K_1(Mr_o)I_1(Mr_i) + I_1(Mr_o)K_1(Mr_i)}{K_1(Mr_o)I_0(Mr_i) + I_1(Mr_o)K_0(Mr_i)}$$

From boundary condition #3, another relationship is found, between A and T_{b1}:

$$T_{b1} = AI_0(Mr_i) + \frac{bT_m p_{acs}}{r_m C_p}$$

This may be substituted into the result of boundary condition #3 to solve for A. The substitution:

$$N = \left(\frac{K_1(Mr_o)I_1(Mr_i) + I_1(Mr_o)K_1(Mr_i)}{K_1(Mr_o)I_0(Mr_i) + I_1(Mr_o)K_0(Mr_i)} \right)$$

will be used to reduce the size of the equations:

$$AkMI_1(Mr_i) = M_s k_s \left(AI_0(Mr_i) + \frac{bT_m p_{acs}}{r_m C_p} \right) N$$

$$AkMI_1(Mr_i) = AM_s k_s N I_0(Mr_i) + M_s k_s N \frac{bT_m p_{acs}}{r_m C_p}$$

$$A\frac{kM}{k_s M_s}\frac{1}{N}\frac{I_1(Mr_i)}{I_0(Mr_i)} = A + \frac{bT_m p_{acs}}{I_0(Mr_i) r_m C_p}$$

$$A\left(\frac{kM}{k_s M_s}\frac{1}{N}\frac{I_1(Mr_i)}{I_0(Mr_i)} - 1 \right) = \frac{bT_m p_{acs}}{I_0(Mr_i) r_m C_p}$$

$$A = \frac{\dfrac{bT_m p_{acs}}{I_0(Mr_i) r_m C_p}}{\left(\dfrac{kM}{k_s M_s}\dfrac{1}{N}\dfrac{I_1(Mr_i)}{I_0(Mr_i)} - 1 \right)}$$

$$\frac{kM}{k_s M_s} = \frac{\sqrt{krC_p}}{\sqrt{k_s r_s C_{ps}}}$$

$$A = \frac{\dfrac{bT_m p_{acs}}{I_0(Mr_i) r_m C_p}}{\left(\dfrac{\sqrt{krC_p}}{\sqrt{k_s r_s C_{ps}}}\dfrac{1}{N}\dfrac{I_1(Mr_i)}{I_0(Mr_i)} - 1 \right)}$$

A may be substituted into the general solution to solve for the temperature profile in the gas:

$$T = \frac{bT_m p_{acs}}{(e_s - 1)} \frac{I_0(Mr)}{I_0(Mr_i) r_m C_p} + \frac{bT_m p_{acs}}{r_m C_p} \qquad \textbf{H.6}$$

The boundary temperature in Eq. **H.6** is T_{b1}, which is used in conjunction with Eq. **H.3** to solve for the temperature in the wall. Thus the temperature profile in the entire apparatus is solved for.

VITA

Timothy Merrill Marston

Ph.D Acoustics Spring 2009
The Pennsylvania State University
Dissertation: Infrasonic Pistonphone Calibration

M.S. Acoustics Fall 2006
The Pennsylvania State University
Thesis: Digital response correction and bandwidth extension of condenser microphones

B.S. Electrical Engineering Spring 2004
Seattle Pacific University
Emphasis: digital signal processing & algorithm development

First authored papers/presentations

Microphone bandwidth extension by digital correction of low-frequency roll-off [J. Acoust. Soc. Am. 119, 3378 (2006)]

Infrasonic pistonphone calibration of acoustic transducers [J. Acoust. Soc. Am. 119, 3378 (2006)]

Comparison of measurement and theory for the acoustic pressure field in an infrasonic calibrator through the isentropic-to-isothermal transition* [J. Acoust. Soc. Am. 122, 2984 (2007)]

Simulation-based response analysis of porous and non-porous infrasonic arrays [J. Acoust. Soc. Am. 122, 2960 (2007)]

Porous Hoses: Resistance measurement and subsequent implementation in an infrasonic array model (Acoustics `08, Paris, 2008)

*won best engineering student paper award